

PARTICLE AND MOMENTUM CONFINEMENT IN  
TOKAMAK PLASMAS WITH UNBALANCED NEUTRAL  
BEAM INJECTION AND STRONG ROTATION

A THESIS  
Presented to  
the Faculty of the Division  
of Graduate Studies

By  
Muhammad Afzaal Malik

In Partial Fulfilment  
of the Requirements for the Degree  
Doctor of Philosophy  
in Nuclear Engineering  
in the School of Mechanical Engineering

Georgia Institute of Technology

June, 1988.

PARTICLE AND MOMENTUM CONFINEMENT IN  
TOKAMAK PLASMAS WITH UNBALANCED NEUTRAL  
BEAM INJECTION AND STRONG ROTATION

Approved:

W.M. Stacey, Jr., Chairman

C.E. Thomas

A.V. Larson

J.N. Davidson

Date Approved by Chairman 5/19/88

To the loving memories of my parents

## TABLE OF CONTENTS

	PAGE
ACKNOWLEDGEMENTS	v
LIST OF TABLES	vii
LIST OF ILLUSTRATIONS	viii
SUMMARY	xiii
Chapter	
I. INTRODUCTION	1
II. IMPURITY AND MOMENTUM TRANSPORT THEORIES	13
2.1 Introduction	
2.2 Stacey-Sigmar Particle Transport Theory	
2.3 Burrell-Ohkawa-Wong Particle Transport Theory	
2.4 Stacey-Sigmar Extended Transport Theory	
2.5 Hogan's Momentum Transport Theory	
2.6 Stacey-Sigmar Momentum Transport Theory	
III. ANALYSIS OF INTRINSIC TUNGSTEN TRANSPORT IN PLT	52
3.1 Introduction	
3.2 PLT Experiments with Intrinsic Tungsten	
3.3 Analysis of PLT Experiments	
3.4 Summary	
IV. ANALYSIS OF INTRINSIC IRON TRANSPORT IN ISX-B	97
4.1 Introduction	
4.2 Impurity Transport Experiments	
4.3 Atomic Physics Issues	
4.4 ISX-B Data Analysis code ZORNOC	
4.5 Analysis of Co- versus Counter-Experiments	
4.6 Analysis of Two-beam Co-experiments	
4.7 Summary	

V. ANALYSIS OF INTRINSIC IRON TRANSPORT IN PLT	154
5.1 Introduction	
5.2 PLT Experiments with Intrinsic Iron	
5.3 Analysis of PLT Experiments	
5.4 Summary	
VI. ANALYSIS OF INJECTED SCANDIUM TRANSPORT IN PLT	177
6.1 Introduction	
6.2 PLT Experiments with Scandium Injection	
6.3 Analysis of PLT Experiments	
6.4 Summary	
VII. ANALYSIS OF ROTATION EXPERIMENTS	196
7.1 Introduction	
7.2 Procedure to Analyze Rotation Data	
7.3 Analysis of PLT Experiments	
7.4 Analysis of PDX Experiments	
7.5 Summary	
VIII. PREDICTIONS FOR FUTURE REACTORS	215
8.1 Introduction	
8.2 Predictions for INTOR	
8.3 Predictions for TIBER II	
8.4 Predictions for ITER	
8.5 Summary	
IX. CONCLUSIONS	242
REFERENCES	252

## ACKNOWLEDGEMENTS

I wish to express my deepest appreciation to my research advisor, Prof. W. M. Stacey, Jr., for suggesting this topic and for his continued support and guidance throughout the completion of this work. I am profoundly grateful to the members of my reading committee, Drs. C. E. Thomas, Jr., A. V. Larson, and J. N. Davidson for making their valuable time available to read the text and make useful comments. I am grateful to Dr. C. E. Thomas for being always willing and available for clarifying intricate experimental details pertinent to this work.

The success of this work depended crucially on an effective communication between theory and experiment. The experimental data needed was not always available from literature. It is not easy to recover data files for machines such as ISX-B, and PLT which have long been decommissioned. In such bleak moments, it was always reassuring to talk to Dr. R. C. Isler about ISX-B experiments. Without his willing help, a lot of work on the ISX-B tokamak would not have been possible. I am very thankful to Dr. C. E. Crume for his help on the atomic

physics aspects of this work, and for introducing me to his atomic physics code. My sincere thanks are also due to Drs. H. Howe, and A. Prinja for introducing me to the code PROCTR used in this work.

I am indebted to Drs. H. P. Eubank, S. Suckewer, and E. Hinnov for making some of the unpublished data available about the PLT tokamak. I am also thankful to Drs. von Goeler, and R. A. Hulse for making their valuable time available for some useful discussions related to the PLT tokamak.

On a personal note, I wish to express my gratitude to my wife, Gazala, for her patience, perseverance, understanding, and continued moral support during the course of this work.

This research was sponsored by the Office of Fusion Energy, U.S. Department of Energy, under Contract No. DE-AS05-78ET52025 with the Georgia Tech Research Institute.

## LIST OF TABLES

Table	Page
3.1.1 PLT data with intrinsic tungsten	53
4.1.1 ISX-B data with intrinsic iron	101
4.5.1 Iron spectral lines	116
5.1.1 PLT data with intrinsic iron	156
6.1.1 PLT data with injected scandium	179
6.2.1 Scandium transitions	180
6.2.2 Scandium densities and emissivities	182
8.2.1 INTOR reference parameters	217
8.3.1 TIBER II reference parameters	225
8.4.1 ITER reference parameters	231
8.4.2 Comparison of flows in ITER	239



## LIST OF ILLUSTRATIONS

Figure	Page
3.1.1 PLT geometry and diagnostics	54
3.2.1 Diagnostics for bolometric measurements	58
3.2.2 Tungsten density profiles in PLT with 585 kW co-injected beam power	63
3.2.3 Tungsten density profiles in PLT with 430 kW counter-injected beam power	64
3.2.4 Tungsten density fractions in PLT with 585 kW co-injected beam power	65
3.2.5 Tungsten density fractions in PLT with 430 kW counter-injected beam power	66
3.2.6 Tungsten flux profiles in PLT with 585 kW co-injected beam power	67
3.2.7 Tungsten flux profiles in PLT with 430 kW counter-injected beam power	68
3.3.1 Electron density profile in PLT	72
3.3.2 Electron temperature profiles in PLT with 585 kW co-injected beam power	73
3.3.3 Electron temperature profiles in PLT with 430 kW counter-injected beam power	74
3.3.4 Average charge-state distribution of tungsten with electron temperature	75
3.3.5 Beam deposition profile in PLT	76
3.3.6 Calculated ion temperature profile in PLT at 280 ms	80
3.3.7 Calculated ion temperature profile in PLT at 290 ms	81
3.3.8 Steady-state theory vs. experiment for PLT tungsten fluxes at 280 ms	85
3.3.9 Steady-State theory vs. experiment for PLT tungsten fluxes at 290 ms	86

3.3.10	Impurity density profile in PLT at 250 ms with co-injection	87
3.3.11	Impurity density profile in PLT at 250 ms with counter-injection	88
3.3.12	Impurity flux history in PLT at 20 cm with co-injection	89
3.3.13	Impurity flux history in PLT at 20 cm with counter-injection	90
3.3.14	Time-dependent theory vs. experiment for PLT tungsten fluxes with 585 kW co-injection	91
3.3.15	Time-dependent theory vs. experiment for PLT tungsten fluxes with 430 kW counter-injection	92
4.1.1	Cross-section of the ISX-B machine	98
4.1.2	Plan view of ISX-B with main diagnostic and auxiliary apparatus	99
4.5.1	Experimental time variation of spectral lines in ISX-B with 1 MW co-injection	117
4.5.2	Experimental time variation of spectral lines in ISX-B with 1 MW co-injection	118
4.5.3	Electron density and temperature profiles in ISX-B at 80 ms in the co-injection discharge	121
4.5.4	Electron density and temperature profiles in ISX-B at 230 ms in co-discharge	122
4.5.5	Electron density and temperature profiles in ISX-B at 120 ms in counter-discharge	123
4.5.6	Electron temperature and density profiles in ISX-B at 169 ms in counter-discharge	124
4.5.7	Beam deposition profile in ISX-B	125
4.5.8	Ion temperature profiles in ISX-B with co-injection at 80 and 230 ms	126
4.5.9	Ion temperature profiles in ISX-B with counter-injection at 120 and 169 ms	127
4.5.10	Average charge-state profiles in ISX-B with co-injection at 80 and 230 ms	128
4.5.11	Average charge-state profiles in ISX-B with counter-injection at 120 and 169 ms	129
4.5.12	Predicted iron density profile in ISX-B	

at 80 ms with 1 MW co-injection	135
4.5.13 Predicted impurity flux history in ISX-B at 27 m with 1 MW co-injection	136
4.5.14 Predicted impurity flux history in ISX-B at 27 cm with 1 MW counter-injection	137
4.5.15 Emissions during co- and counter-injection in ISX-B for theory versus experiment	138
4.6.1 Experimental time variation of spectral lines in ISX-B with 2.4 MW co-injection	140
4.6.2 Electron density and temperature profiles in ISX-B at 80 ms with two-beam co-injection	142
4.6.3 Electron density and temperature profiles in ISX-B at 250 ms with two-beam co-injection	143
4.6.4 Beam deposition profile in ISX-B with two-beam co-injection	144
4.6.5 Ion temperature profiles in ISX-B with two-beam co-injection at 80 and 230 ms	145
4.6.6 Average charge-state profiles in ISX-B with two-beam co-injection at 80 and 230 ms	146
4.6.7 Predicted iron density profile in ISX-B at 80 ms with 2.4 MW co-injection	148
4.6.8 Predicted impurity flux history in ISX-B at 27 cm with 2.4 MW co-injection	149
4.6.9 Iron emissions from two-beam co-discharge in ISX-B with theory versus experiment	150
5.2.1 Measured chordal profiles of iron radiation in PLT with 400 kW of beam injection	158
5.3.1 Electron density and temperature profiles in PLT at 400 ms in co-discharge	160
5.3.2 Electron density and temperature profiles in PLT at 500 ms in co-discharge	161
5.3.3 Electron density and temperature profiles in PLT at 400 ms in counter-discharge	162
5.3.4 Electron density and temperature profiles in PLT at 500 ms in counter-discharge	163
5.3.5 Beam deposition profile in PLT	164

5.3.6	Ion temperature profiles in PLT with co-injection at 400 and 500 ms	166
5.3.7	Ion temperature profiles in PLT with counter-injection at 400 and 500 ms	167
5.3.8	Average charge-state profiles in PLT with co-injection at 400 and 500 ms	168
5.3.9	Average charge-state profiles in PLT with counter-injection at 400 and 500 ms	169
5.3.10	Predicted iron density profile in PLT at 400 ms with 400 kW co-injection	171
5.3.11	Predicted impurity flux history in PLT at 40 cm with 400 kW co-injection	172
5.3.12	Predicted impurity flux history in PLT at 40 cm with 400 kW counter-injection	173
5.3.13	Chordal brightness profiles of iron in PLT with theory versus experiment	174
6.2.1	Measured normalized profiles of line emission from scandium and molybdenum ions in PLT	181
6.3.1	Electron density, electron temperature, and ion temperature profiles in PLT	185
6.3.2	Scandium density profiles and radial locations of scandium ions in PLT	186
6.3.3	Sensitivity of normalized emissivity profiles of scandium with scandium density	188
6.3.4	Sensitivity of normalized emissivity profiles of scandium with electron temperature	190
6.3.5	Normalized emissivity profiles of scandium ions in PLT with theory versus experiment	193
7.3.1	Neutral beam driven central toroidal rotation in PLT with theory versus experiment	204
7.4.1	Neutral beam driven central toroidal rotation in PDX with theory versus experiment	210
8.2.1	Iron flow reversal in INTOR at 100 keV beam energy	219
8.2.2	Iron flow reversal in INTOR at 200 keV beam energy	220

8.2.3	Iron flow reversal in INTOR at 500 keV beam energy	221
8.3.1	Helium flow reversal in TIBER II at 500 keV beam energy	228
8.3.2	Carbon flow reversal in TIBER II at 500 keV beam energy	229
8.4.1	Helium flow reversal in ITER at 500 keV beam energy	235
8.4.2	Helium flow reversal in ITER at 1000 keV beam energy	236
8.4.3	Helium flow reversal in ITER at 1500 keV beam energy	237

## SUMMARY

There is a self-consistent theory for the effects of neutral beam injection on impurity transport in tokamak plasmas. The theory predicts that co-injection drives impurities outward and that counter-injection enhances the normally inward flow of impurities. The theory was applied to carry out a detailed analysis of the large experimental data base from the PLT and the ISX-B tokamaks. The theory was found to generally model the experimental data quite well. It is, therefore, concluded that neutral beam co-injection can drive impurities outward to achieve clean central plasmas and a cool radiating edge. Theoretical predictions for future thermonuclear reactors such as INTOR, TIBER II, and ITER indicated that neutral beam driven flow reversal might be an effective impurity control method if the rate of beam momentum deposited per plasma ion is adequate.

The external momentum drag, which is a pivotal concept in impurity flow reversal theory, is correctly predicted by the gyroviscous theory of momentum confinement. The theory was applied to analyze experimental data from the PLT and the PDX

tokamaks with exact experimental conditions. The theory was found to be in excellent agreement with experiment over a wide range of parameters. It is, therefore, possible to formulate the impurity transport theory from first principles, without resort to empiricism.

## CHAPTER I

### INTRODUCTION

Controlled nuclear fusion in a tokamak requires confinement of plasmas at a temperature of the order of  $10^9$  K. At such extreme temperatures, the energetic plasma ions and charge-exchange neutrals can cause very high sputtering erosion rates of impurities from the first wall components. It follows from the classical transport theory [1-3] that the impurities flow inward in a closed plasma system. The neoclassical transport theories [4-8] support the classical predictions. The line radiation from even the trace levels of heavy impurities, for instance  $n_z/n_i \geq 10^{-3}$  where  $n_z$  and  $n_i$  are impurity and plasma ion densities respectively, can easily prevent ignition [9,10], or result in marked reductions in the attainable fusion power multiplication factor [11], and thus raise the threshold for fusion breakeven. While radiation from light impurities is relatively unimportant, the



additional thermal pressure of the large number of electrons that accompany impurity ions results in a reduction in the reacting ion population, and hence in fusion power output [12]. Further, the cold ions introduced into plasmas by impurities can reduce the plasma pressure, change the effective ionic charge-state, alter the radial current distribution and produce cumulative changes in particle transport that may lead to a disruption.

Some form of auxiliary heating mechanism, such as neutral beam injection, resonance excitation by electromagnetic waves, etc., is required to heat plasmas effectively to thermonuclear temperatures. The external sources affect momentum balance as in the case of neutral beam injection, and/or alter the distribution function as in the case of neutral beam injection and the radio-frequency waves. Thus it is expected that, in the presence of a particle and momentum source such as a neutral beam, the ion-impurity transport properties may be influenced significantly as compared to classical and neoclassical predictions based on the transport produced by internal ion-impurity collisions in a closed system. Further, the neutral beam injected parallel

(co-injection) or anti-parallel (counter-injection) to the plasma current may affect the transport properties differently.

Ohkawa [13] extended the two-fluid calculation used by Rutherford [6] and proposed that the inward diffusion of impurities in tokamak plasmas could be reversed by providing a source of protons on one side of the plasma and a sink on the other side. Ohkawa, however, neglected the thermal gradients in the plasma. Burrell [14] showed that the qualitative conclusions reached by Ohkawa [13] do not change when the thermal gradients are included. Chu and Rawls [15], and Wong [16] reaffirmed the conclusions reached in References [13,14].

Ohkawa [17] also noted that a source of external momentum, such as a neutral beam, would produce a radial impurity flux due to collisional momentum exchange between the impurities and the injected beam particles, and predicted that counter-injection would produce an outward impurity flux, thus causing impurity flow-reversal. El-Derini and Emmert [18] took up the the suggestion put forward by Ohkawa [17] and

showed from kinetic considerations that for circular cross-section, large aspect-ratio plasmas in arbitrary collisionality regime, the counter-injection would cause an outward flow of impurity in agreement with the conclusion reached by Ohkawa [17]. Connor and Cordey [19] calculated the energetic ion distribution as a result of high energy neutral injection and showed by introducing the effect of trapped electrons in kinetic theory that this led to a modification of the plasma current. They also showed that the diffusion of the plasma may be significantly enhanced or reduced depending upon whether the beam is directed parallel or antiparallel to the field lines. Callen, et al., [20] showed from kinetic considerations that the particle flux would be outward (inward) for co- (counter) injection.

Stacey [21] extended the earlier work [14-20] to investigate the effect of particle and heat sources upon the particle and heat fluxes in a tokamak in the collisional regime, and indicated the possibility of controlling radial particle fluxes by tailoring the parallel velocity distribution of the particle source.

Stacey and Sigmar [22,23] noted that the injected beam momentum must be balanced by a drag (i.e. the radial transfer of momentum) and showed that this allowed a unique determination of the radial electric field. They treated the momentum input, drag and the radial electric field self-consistently for arbitrary plasma cross-section, beta and collision regimes and predicted impurity flow-reversal with co-injection and enhanced inward impurity flow with counter-injection. This result is opposite to that predicted by Ohkawa [17]. However, Stacey and Sigmar [22,23] found that the direct contribution to impurity transport from beam-impurity momentum exchange was as found by Ohkawa [17], but that other effects associated with altering the flows in the flux surface and altering the radial electric field were dominant. Stacey and Sigmar [22,23] did not include the plasma rotation, temperature gradient and heat flux effects into the theory. Stacey [24] extended the theory to include temperature, heat conduction fluxes and external heat sources.

A number of experiments [25-27] were undertaken to check the predicted [22,23] flow reversal with beam injection. These experiments qualitatively agreed with the theory, that is, the central accumulation of impurities increased dramatically with counter-injection and decreased with co-injection. However, the measured rotation speeds [28-34] for the unbalanced beam injection were found to be of the order of the thermal speed of the impurities observed in these experiments, in violation of the ordering assumption of the transport theories to date.. Burrell, Ohkawa and Wong [35] pointed out that, since the measured rotation speed was of the order of the thermal speed of impurities, the inertial effects could not be ignored. They [35] included the impurity inertia terms in the momentum balance equation and showed that the ensuing poloidal variations in the impurity density over the flux surface could produce an outward impurity flux for co-injection. They, however, did not include into their theory the neutral beam momentum input, or the radial momentum transfer (drag), or self-consistently calculate the radial electric field and the toroidal and poloidal flow velocities. Using the representative experimental data, the model calculations done by Crume and Arnurius [36] show that without including the

external momentum and external drag effects, the inertial theory [35] alone can drive impurities inward with co-injection, in contrast to experimental observations. The inertial effects are also known to produce non-uniform electrostatic potential over the flux surface [37-41].

Stacey and Sigmar [42] noted that the theory developed in Reference [35] was not self-consistent with respect to the ambipolar electric field or the flows within the flux surface. They subsequently extended [42] their previous theory [22,23] in the collisional regime to include the inertial effects in a self-consistent way for particle flows in the flux surface, the radial electric field and radial particle transport. They treated the effects of beam-impurity momentum exchange, the radial transfer of toroidal momentum, and the poloidal variation in density and potential, and concluded that the co-injection reduced or reversed the inward flow of impurities.

Stacey, et al., further extended [43] their previous collisional-regime theory [42] for rotation and impurity-transport to include the banana-plateau regime. They

included a kinetic theory derivation of the parallel viscous force in the strong rotation ordering and a self-consistent formulation for calculating ion and impurity rotation velocities and radial transport fluxes, as well as the radial electric field and poloidal variation of the impurity density upon which the former strongly depend.

Several studies [36,42-46] considered the model problem calculations to compare the Stacey-Sigmar impurity flow reversal theory [42,43] with experiments. Stacey, Bennett and Sigmar [44] also treated the inertial effects, and confirmed the earlier [42] predictions of the theory. Bennett [45], and, Bennett and Stacey [46] included the temperature gradient and the heat flux effects into the impurity flow-reversal theory in the absence of the inertial effects.

The experimental data [25-27] from the PLT and the ISX-B tokamaks clearly shows that counter-injection causes a strong build-up of impurities in the plasma center, while co-injection does not cause any accumulation, or can even cause reduction in the central impurity concentration. Suckewer, et al., [47,48] found in their studies of the PLT

tokamak that co- (counter) injection led to less (more) central impurity concentration, in agreement with theory [42,43], but argued that this was due to the effects other than transport, and questioned the theoretical [22,23,42,43] and experimental [25-27] predictions. Isler, Morgan and Peacock [49] reiterated the experimental evidence that counter-injection caused preferential central accumulation of impurities whereas co-injection did not, and pointed out that the results given in [48] were inconsistent with the previous results [25] from the same device and could be interpreted differently.

The Stacey-Sigmar theory [43] includes a term to account for the radial transfer of toroidal and parallel momentum. Such a term is needed to match the rotation results from experiments. The experimental evidence [28-34] indicates that some of the momentum that is input to the center of the plasma with neutral beam injection is transferred radially outward. However, momentum confinement times inferred from toroidal rotation measurements [28-34] in tokamak plasmas with unbalanced neutral beam injection are about two orders of magnitude shorter than could be accounted for by theoretical



estimates based on standard neoclassical perpendicular viscosity [50-53] which provided the most obvious explanation. This led to the idea of an anomalous radial transport of momentum and hence anomalously reduced momentum confinement times in experiments [28-34]. Hogan [53] identified the parallel, perpendicular and drift components of the viscosity tensor and concluded that the dominant viscous force scaled directly with the collision frequency. However, his approximate evaluation of the poloidal variation of the toroidal velocity neglected order  $\epsilon = r/R$  flow variations driven by inertial forces,  $\epsilon$  being the inverse aspect ratio,  $r$  the minor radius and  $R$  the major radius. Stacey and Sigmar [54] derived the full viscosity tensor by taking into account the strong toroidal rotation and  $Q(\epsilon)$  variations in the flow velocities of plasma due to unbalanced neutral beam injection and found a good general agreement of the momentum confinement time based on gyroviscosity with the experimental values [28-34], and hence concluded that it was not necessary to postulate an anomalous mechanism for momentum confinement.

The model calculations [36,42-46,54] demonstrate that both the impurity flow reversal theory [43], and the gyroviscosity theory [54] generally show a good qualitative and semi-quantitative agreement with experiment. However, no detailed analysis was done to compare fully developed theory with experiment (Bennett and Stacey [46] had done a detailed analysis of some of the early PLT experiments using an early version of the flow reversal theory lacking inertial effects). The aim of this study is to perform a detailed analysis of a large experimental data base on the effects of neutral beam injection and rotation on impurity and momentum confinement in order to quantitatively compare the theory with experiment and to investigate the validity of theoretical predictions. The particle and the momentum transport theories are reviewed in Chapter II. The extended Stacey-Sigmar theory [43] for particle transport is applied to analyze PLT data with a tungsten limiter [25] in Chapter III, ISX-B data with iron limiter [26] in Chapter IV, PLT data with iron limiter [47] in Chapter V, and PLT data with scandium injection [48] in Chapter VI. The Stacey-Sigmar gyroviscosity theory [54] is applied in Chapter VII to analyze neutral beam driven rotation data from PLT [28,29], and PDX [30,31] tokamaks. The

application of the theory to the future reactors [55-57] is discussed in Chapter VIII. Finally, Chapter IX concludes this study.

## CHAPTER II

### IMPURITY AND MOMENTUM TRANSPORT THEORIES

#### 2.1 Introduction

The particle transport, in the historical perspective, comprises of two major theoretical developments, namely, the classical and the neoclassical theories reviewed in detail by Braginskii [3], and Hinton and Hazeltine [7] respectively. The transport of particles in both of these theories is driven by interspecies collisional momentum transfer and is thus appropriate for a system with no external sources or sinks of momentum. The classical theory deals with the cross-field transport when the magnetic field is straight and uniform as in the limit of an infinite, right circular cylinder with an axial magnetic field. The classical transport is dependent on random walk diffusion with the step size of the order of the gyroradius. The equilibrium impurity profile in the classical formulation can be written in terms of the main ion profile as  $n_z(r)/n_z(0)=[n_i(r)/n_i(0)]^2$ , which shows that the equilibrium impurity profile is more sharply peaked than the main ion

profile. When the classical diffusion is corrected for the toroidal curvature, magnetic field gradients and the trapped particle effects which are characteristic of a tokamak geometry, the result is the neoclassical theory. The neoclassical transport theory is further classified into the Pfirsch-Schluter collisional regime which treats the first two effects, and the banana-plateau collisionless regime which treats the latter effect. In a tokamak, the helical magnetic field lines form nested, toroidal flux surfaces of constant pressure, temperature and density. The Pfirsch-Schluter transport is driven by collisions between particles on the same flux surface to within a small excursion of the order of the gyroradius, and, in general, leads to an enhancement over the classical transport by a factor  $(1 + 2q^2)$  where  $q$  is the safety factor. The banana-plateau transport is driven by particle trapping in magnetic wells formed by varying magnetic field along the particle path, with the diffusion displacement step of the order of the banana-shaped orbit width, which being much larger than the toroidal gyroradius leads to an enhancement over the Pfirsch-Schluter transport by a factor  $\epsilon^{-3/2}$  where  $\epsilon$  is the inverse aspect ratio. A further type of diffusion is driven by poloidal

electrostatic fields [39-41]. All the four components of diffusion, that is, classical, Pfirsch-Schluter, banana-plateau and poloidal electrostatic diffusion may be present simultaneously in any toroidal plasma, the total diffusion being their sum, although typically the plasma conditions will make one or more of these components small [38].

The plasma transport can be studied by both microscopic and macroscopic descriptions. The microscopic, kinetic equation description in the phase space leads to an exact but rather formidable 7-dimensional integrodifferential equation which contains far more information than we normally need or possibly can handle. The plasma description can be much simplified by considering the plasma as a fluid of interpenetrating species of particles and describing the plasma behavior in terms of macroscopic parameters such as particle density, average velocity, pressure and temperature. The fluid equations may be established by considering the conservation of particles, momentum and energy across the surface of an infinitesimal volume element in the configuration space, or by evaluating the velocity moments of

the kinetic equation. The advantage of the fluid approach is its simplicity because it leads to equations in three configuration dimensions and time rather than dealing with the complicated 7-dimensional phase space. The disadvantage, however, is that the moment equations are coupled in the sense that each moment equation contains a higher order moment, and so, a constitutive relation is required to close the moment equations.

Since the trapped particles substantially change the plasma viscosity, the collisionless or the long mean free path banana-plateau regime cannot normally be treated as a fluid. The method of solution for the collisionless regime was thus restricted to the solution of the Fokker-Planck approximation of the kinetic equation in velocity space. This limitation was overcome when Hirshman [58,59] derived an averaged parallel viscosity coefficient for a collisionless plasma, which placed the long mean free path effects calculated kinetically into the fluid framework.

Hazeltine and Ware [60] applied the important concept of ambipolarity which essentially implies that the radial particle transport could not set up gross charge imbalance. Hence a radial flux of one species must be offset by an opposing radial flux of another species, so that the net charge flux is zero.

In a closed plasma system without external sources or sinks of particles and momentum, the classical [1-3] , and neoclassical [4-8] theories predict an inward impurity flow. The neoclassical banana-regime theory [4,5] predicts a temperature screening effect driven by the negative temperature gradient which inhibits or reverses the inward flow of impurities. Rutherford [6] studied hydrogen plasma containing a single type of impurity in the Pfirsch-Schluter regime in the limit of the Lorentz model and confirmed the inward flow of impurities, but did not find the temperature screening effect, rather a further contribution to the inward flow of impurities driven by a temperature gradient was found. Boley, Gelbard and Stacey [61] extended this treatment to an arbitrary number of species.



An auxiliary heating mechanism, such as neutral beam injection, is required to raise the plasma to thermonuclear temperatures. However, neutral beam injection also provides an external source of momentum, and since the toroidal flow velocity  $v_\phi$  does not continue to increase indefinitely, there must also be an external momentum sink or drag mechanism. This warrants an extension of the Hinton-Hazeltine [7] theory.

Following the suggestion by Ohkawa [17] that a source of external momentum, such as a neutral beam, could reverse the inward flow of impurities, the problem was subsequently examined by El-Derini and Emmert [18], Connor and Cordey [19], and, Callen, et al., [20]. Ohkawa [13] had earlier suggested that the radial transport could be altered by the introduction of a poloidally asymmetric particle source. This theory was further developed by Burrell [14], and Wong [16] in the Pfirsch-Schluter regime, for two species, and multiple-species respectively. Chu and Rawls [15] extended the development in Reference [20] to treat the mixed plateau-Pfirsch-Schluter regime in the presence of external particle and momentum sources.

Stacey and Sigmar [22,23] developed a self-consistent theory based on ambipolarity and Hirshman's [58,59] constitutive relation and included self-consistently the effects of external particle momentum sources and external drags. This theory is addressed in Section (2.2). Burrell, Ohkawa and Wong [35] included the plasma rotation effect into the transport theory. This inertial theory is the topic of Section (2.3) Stacey and Sigmar [42,43] extended their previous theory [22,23] to include the inertial effects self-consistently; this extended theory is discussed in Section (2.4).

The experimental evidence [28-34] and the Stacey-Sigmar [43] theory both indicate that some of the momentum that is input to the center of the plasma is transferred radially outward. It is, therefore, instructive to study the viscous drag forces to explore the momentum damping phenomenon. Braginskii [3] outlined a method to compute components of the viscous stress tensor in a magnetic field from the corresponding rate of strain tensor elements. The stress elements in this formalism can be decomposed into parallel, perpendicular and gyroviscous terms. The origin of the

viscosity coefficients relating these stress tensors was earlier discussed by Kaufman [62]. Rosenbluth, et al., [50] studied the rotation problem in the banana regime and indicated the behavior of thermal conductivity, parallel viscosity, perpendicular viscosity and plasma potential with collision frequency. Grim and Johnson [63] worked out the viscosity tensor in tokamak geometry, but considered only the parallel viscous force. Hazeltine [51] investigated toroidal rotation in the collisional regime and derived a relation between the ion parallel flow and the radial gradients of density, temperature and electrostatic potential. The momentum diffusion term was, however, neglected in Hazeltine's calculations. Tsang and Freeman [52] included the momentum diffusion term in the collision-dominated regime and found an inverse dependence of the cross-field viscosity on the ion self-collision frequency. All these neoclassical theories [50,51] invoked standard transport ordering assumptions restricting the ratio of flow velocity to sound speed to be small as compared to the ratio of the gyroradius to characteristic scale length, which violates experimental observations [28-34] on beam-heated plasmas in tokamaks. Even those theories which considered the strong rotation ordering

[35,42,43] explicitly did not explain the anomalous momentum transport. Mikhailovskii and Tsypin [64] investigated the plasma rotation and viscosity and generalized the Braginskii [3] representation of the viscosity tensor in arbitrary curvilinear coordinates.

Hogan [53] calculated the cross-field transport of toroidal momentum in the collisional regime of an axisymmetric configuration. He followed a method similar to that of Shafronov [65] for calculating the ion thermal conductivity in an axisymmetric configuration. He identified the parallel, perpendicular and drift or gyroviscosity terms. However, his approximate evaluation of the poloidal variation of  $v_\phi$  neglected inertial forces which can produce  $O(\epsilon)$  variations, where  $\epsilon$  is the inverse aspect ratio. His results are based upon smaller variations produced by viscous forces, leading him to conclude that the dominant viscous forces scaled with collision frequency. Hogan's theory of collisional transport of momentum is discussed in Section (2.5).

Stacey and Sigmar [54] considered a collisional plasma in toroidal geometry and derived the full viscosity tensor and all components of the Braginskii' stress tensor [3] including the gyroviscous tensor elements and taking into account the  $O(\epsilon)$  poloidal density variation in the strong rotation ordering. They showed that the perpendicular viscous forces which are proportional to the self-collision frequency, are too small to account for the strong rotation, but found that the gyroviscous forces, as modified by the toroidal geometry effects, are of the proper magnitude to explain the momentum confinement time inferred from experiments [28-34]. The Stacey-Sigmar momentum confinement theory based on gyroviscosity is examined in Section (2.6).

## 2.2 Stacey-Sigmar Particle Transport Theory

Stacey and Sigmar [22,23] noted that, in the presence of neutral beam injection, a more appropriate neoclassical theory should be based upon a momentum balance which explicitly includes external momentum sources and external damping or drag mechanisms. The examples of external drag are the interaction of plasma and wall via charge-exchange,

magnetic field ripple, induced toroidal electric field and viscosity. The basic equations for species  $j$  are the continuity equation

$$\partial n_j / \partial t + \nabla \cdot n_j \mathbf{v}_j = S_j , \quad (2.2.1)$$

and the momentum balance equation

$$\begin{aligned} m_j n_j \partial \mathbf{v}_j / \partial t + m_j n_j (\mathbf{v}_j \cdot \nabla) \mathbf{v}_j + \nabla p_j + \nabla \cdot \Pi_j \\ = -n_j e_j \nabla \Phi + n_j e_j (\mathbf{v}_j \times \mathbf{B}) + \mathbf{R}_j + \xi_j \end{aligned} \quad (2.2.2)$$

where, in the Lorentz representation without thermal forces, the collisional friction momentum exchange

$$\mathbf{R}_j = -m_j n_j \sum_k \nu_{jk} (\mathbf{v}_j - \mathbf{v}_k) \quad (2.2.3)$$

and the external momentum exchange

$$\xi_j = \mathbf{M}_j - m_j n_j \nu_{dj} \mathbf{v}_j \quad (2.2.4)$$

together with the charge neutrality condition

$$\sum n_j e_j = 0 \quad (2.2.5)$$

and the ambipolarity condition

$$\sum e_j \Gamma_j = 0 \quad (2.2.6)$$

In these equations, the summation is from 1 to J where J is the total number of species; m, n, e and v are the particle mass, density, charge and average velocity respectively, p is the scalar pressure and  $\Pi$  is the anisotropic shear stress tensor,  $\Phi$  is electrostatic potential, B is magnetic field, S is particle source,  $\nu_{jk}$  is the collision frequency of species j with species k, M is the external momentum input,  $\nu_d$  is the drag frequency arising from radial momentum transfer which damp the flows within the flux surface, and  $\Gamma$  represents the particle flux.

Stacey and Sigmar [22,23] considered a plasma in which the ion-impurity collisions dominate the transport so that a two species model is applicable. In the limit of the standard neoclassical transport ordering [7] used, time-dependent and inertial terms were dropped. Consequently, using the momentum balance Equation (2.2.2) for the toroidal, parallel and normal components of momentum, and the integration of the particle continuity Equation (2.2.1), the flux surface averaged radial impurity flux was shown to be driven by the interspecies collisional friction and by external momentum exchange between the injected beam and plasma ions. The parallel flows in terms of these two components contain the parallel neoclassical viscosity coefficient  $\mu$  [58,59] and the normalized drag frequency  $\beta_z = \nu_{dz} / \nu_{zi}$ , where  $z$  stands for the impurity ion and  $i$  for the main plasma ion. The radial impurity flux can be written as

$$\langle n_z v_{zr} \rangle = \langle n_z v_{zr} \rangle_{PS} + \langle n_z v_{zr} \rangle_{NC} + \langle n_z v_{zr} \rangle_S + \langle n_z v_{zr} \rangle_\Phi + \langle n_z v_{zr} \rangle_K \quad (2.2.7)$$

where  $\langle \rangle$  denotes a flux surface average, and the terms on the



right hand side are contributions respectively from Pfirsch-Schluter, neoclassical, asymptotic particle source densities, ambipolar electrostatic potential, and momentum exchange. This result was then specialized to the large aspect-ratio and low-beta approximation for which the value of  $\mu$  was used from Reference[59], valid in all collisional regimes. The external drag mechanism affects all terms in Equation (2.2.7). In the notation of Reference [23], the terms appearing in Eq. (2.2.7) can be written explicitly as shown below.

The Pfirsch-Schluter flux

$$\begin{aligned} \langle n_z v_{zr} \rangle_{PS} = & -(2n_z m_z \nu_{zi} \epsilon^2) / (Z_z e^2 B_{p0}^2) \\ & [1/(Z_z n_z) \partial p_z / \partial r (1 + \beta_z) - 1/(z_i n_i) \partial p_i / \partial r] \end{aligned} \quad (2.2.8)$$

The neoclassical flux

$$\langle n_z v_{zr} \rangle_{NC} = -1/(Z_z e^2 B_{p0}^2) \{ (n_z \mu_z / d_{zi}) [\xi_i (1 + \beta_z) + \beta_z] \}$$

$$\begin{aligned} & (1/Z_z n_z) \partial p_z / \partial r - (\mu_z / m_z \nu_{zi}) \\ & (n_i \mu_i / d_{zi}) (1/z_i n_i) \partial p_i / \partial r \} \end{aligned}$$

(2.2.9)

The flux due to asymmetric particle source densities

$$\begin{aligned} \langle n_z v_{zr} \rangle_S = & (n_z m_z \nu_{zi} \epsilon^2 R B_{\phi 0} / Z_z e B_{p0}^2) \{ [\delta_z (1 + \beta_z) / n_z - \delta_i / n_i] \\ & - \{ (n_z \mu_z / d_{zi} [\xi_i (1 + \beta_z) + \beta_z] \delta_z / n_z \\ & - (n_i \mu_i \mu_z \delta_i / d_{zi} m_z \nu_{zi} n_i) \} / (n_z m_z \nu_{zi}) \} \end{aligned}$$

(2.2.10)

The flux due to ambipolar electrostatic potential

$$\begin{aligned} \langle n_z v_{zr} \rangle_\Phi = & (-\partial \Phi / \partial r) / (Z_z e B_{p0}^2) (1 - \epsilon^2 / 2) \\ & \{ 2 n_z m_z \nu_{dz} \epsilon^2 + (n_z \mu_z / d_{zi}) [\beta_i + \beta_z (1 + \xi_i)] \} \end{aligned}$$

(2.2.11)

The flux due to internal and external momentum exchange

$$\begin{aligned}
 \langle n_z V_{zr} \rangle_K = & -(\mu_z/m_{zi} \nu_{zi}) [(1+\xi_i) K_{z\phi} + K_{i\phi}] / Z_z e B_{p0} d_{zi} \\
 & + \epsilon^2 K_{i\phi} (\mu_z/m_{zi} \nu_{zi}) / (2 Z_z e B_{p0} d_{zi}) \\
 & - \epsilon^2 K_{z\phi} [\xi_i + (\xi_z + \beta_z)(1+\xi_i)/2] / (Z_z e B_{p0} d_{zi})
 \end{aligned}
 \tag{2.2.12}$$

The radial transport flux contributions due the first three terms in Eq. (2.2.7) support the previous derivation for the usual Pfirsch-Schluter flux [6], the neoclassical flux [7], and the flux due to asymmetric particle sources [14,16], but now modified only by the drag effects. The momentum exchange term accounts for the combined effect of the inter-species collisional friction and the external momentum exchange. The direct effect of co-injection (counter-injection) due to momentum exchange is to drive impurities inward (outward). This result confirms Ohkawa's prediction [17]. This trend, however, is counter-acted by the ambipolar potential. The gradient of the ambipolar potential is produced by momentum input and by the pressure-gradient-driven drag forces. The co-injection produces a negative radial gradient in the

ambipolar potential which tends to drive impurities radially outward. The effect of counter-injection is opposite to that of co-injection. Thus the net effect of co-injection to drive impurities outward is determined by the competing influence of the direct momentum exchange and the the gradient of the ambipolar electrostatic potential. Conditions under which co-injection tends to cause impurity flow reversal in the highly collisional, mixed-collisional, and collisionless regimes for impurity flow reversal with co-injection were established in Reference [23]. It was estimated that the impurity flow reversal effects would be observable in ISX-B and PLT tokamaks, and could possibly be used to achieve impurity control in a reactor type plasma. The effects of temperature gradient and heat flux were later included [24,45,46] into the Stacey-Sigmar impurity flow reversal theory [23,24] by considering the higher order moments. Bennett [45] performed model calculations to compare the impurity flow reversal theory with experiment, and found that the theory provides a reasonable basis for interpretation of experimental results from PLT. By employing an ad hoc multiplicative factor of two to theory, the measured [25] inward impurity fluxes before injection and outward impurity

fluxes during co-injection are predicted reasonably well. A multiplicative factor of four was required to predict the enhanced inward impurity flux with counter-injection.

### 2.3 Burrell-Ohkawa-Wong Particle Transport Theory

Stacey-Sigmar theory [22,23], in the limit of the standard neoclassical transport ordering, ignored the inertial term in the momentum balance equation, and invoked an external drag mechanism to predict impurity flow reversal with co-injected neutral beam. The experiments [28-34] indicate that the rotation speeds in tokamaks with unbalance beam injection are of the order of  $10^5$  m/s. Burrell, Ohkawa and Wong [35] remarked that, since the measured rotation speeds [28-34] with unbalanced neutral beam injection are comparable to or greater than the thermal speed of the impurities observed in experiments, the impurity inertia terms could not be neglected in the momentum balance equation. They claimed that it was the rapid rotation of plasma, and not the direct beam-impurity interaction, that explained the experimental results [25-27]. Accordingly, they retained the impurity inertia term in the parallel component of the momentum balance equation without

any provision for drag and ambipolarity. They assumed the impurity ions to be in the Pfirsch-Schluter regime. Since the rotation speed [28-34] is small compared to the main ion thermal speed, the main ions were assumed to have constant density and temperature on a flux surface. Because of the strong impurity-ion temperature equilibration, the impurity temperature was also assumed to be constant on a flux surface. They specialized their results to large aspect ratio and circular cross-section geometry, and found the flux surface averaged, cross-field impurity flux to be

$$\begin{aligned} \langle n_z v_{zr} \rangle = & \mathcal{R} \{ [1 - .5(y-x)] (T_i / n_i) (\partial n_i / \partial r) \\ & + [1 - \xi + .5y(2\xi + g - 1) + .5x(1 + g)] (\partial T_i / \partial r) \} \end{aligned} \quad (2.3.1)$$

with

$$\mathcal{R} = \{ 2q^2 m_i n_i \nu_{ii} z_I [1 - .5(y-x)] \} / \{ e^2 B z_i [\delta^2 + (1-y^2)] \} \quad (2.3.2)$$

where  $i$  and  $I$  stand for the main plasma and the impurity ions

respectively, and

$$\delta = m_i \nu_{ii} z_i^2 q R v / T_i \quad (2.3.3)$$

$$v = -[T_i / (e z B_p)] [(1/n_i) (\partial n_i / \partial r) + (1+g) (\partial T_i / \partial r)] \quad (2.3.4)$$

$$y = m_i v^2 / T_i \quad (2.3.5)$$

$$x = m_i v^2 / T_i \quad (2.3.6)$$

$$v = u - v_E \quad (2.3.7)$$

and  $u$  is the experimentally measured rotation speed.

Equation (2.3.1), when written explicitly for co- and counter-injection, makes three important predictions. First, for density and temperature gradients of the usual sign, a greater influx of impurities for counter-injection, in agreement with experimental observations [25-27], is confirmed. Second, for the representative values for PLT [25], the difference in the radial convection velocities was

estimated to be in the range of 0-10 m/s as compared to the actual value of 0-4 m/s. Third, the impurity transport for discharges with only co-injection and for those with both the co- and counter-injection was found to be more similar to each other than either is to counter-injected discharge, which confirms the observation in PLT [25].

The model calculations [45] show that the inertial theory matched with the experiment quantitatively for a radial distance of 5 to 10 cm but diverged from the experiment with increasing radius to a factor of 4 at 20 cm from the minor axis. For counter-injection, the inertial theory overpredicts the experiment by a factor of 2 or less for the radial range of 5 to 15 cm, but by a factor of 4 at 20 cm. The prediction of the Burrell-Ohkawa-Wong theory combined with the prediction of the Stacey-Sigmar gradient and beam driven theory [45] showed an improved agreement with experiment for counter-injection but the agreement between the theory and the experiment was lost for co-injection. The model calculations done by Crume and Arnurius [36] with ISX-B data show that the inertial theory



alone in the absence of the external momentum and external drag effects drives the impurities inward with co-injection, contrary to the experimental evidence [25-27].

Stacey and Sigmar [42] noted that the inertial theory proposed by Burrell, Ohkawa and Wong [35] neglected a self-consistent treatment of the ambipolar potential and of the flows in the flux surface, and it also omitted the direct effects of toroidal momentum input and its radial transfer. Stacey and Sigmar [42,43] subsequently extended their previous theory [22,23] to include the inertial effects in a self-consistent theory. This extended theory is treated next.

#### 2.4 Stacey-Sigmar Extended Theory

Stacey and Sigmar [42] extended their previous impurity flow reversal theory [22,23] to explicitly include the inertial effects self-consistently and thus to calculate the particle flows in and across flux surfaces, the ambipolar potential and the poloidal variation of densities, in the strong rotation ordering  $v_\phi \geq v_{th}$  where  $v_\phi$  is the toroidal rotation speed and  $v_{th}$  is the thermal speed of the species. The

formalism was first developed [42] for plasmas in the collisional regime, and the temperature gradient effects were ignored. The essential features of the original formalism [22,23], that is, the self-consistent determination of the lowest order flows in the flux surface and of the radial electric field from particle and momentum balance equations with external momentum and viscous drag included in the momentum balance, and the presence of a transport flux component proportional to radial electric field which is outward(inward) for impurities with co(counter)-injection are retained. The extended theory predicts a radial impurity flux which is inward(outward) for co(counter)-injection with the direct momentum input. The prediction with the radial electric field is just the converse. The model calculations for ISX-B and PLT indicate that it is the radial impurity flux component due to the radial electric field that is primarily responsible for enhanced inward impurity transport with counter-injection and for reduced inward or even outward impurity transport with co-injection of a neutral beam, in the collisional regime.

The steady-state collisional regime theory [42] was further extended by Stacey and Sigmar [43] to include the plateau regime. This extended version of the theory also accommodates the important case of mixed regime in which the main ion species are nearly collisionless and the impurity species are collisional. The theoretical model is based on particle conservation Equation (2.2.1), momentum conservation Equation (2.2.2), charge neutrality condition (2.2.5), and the ambipolarity equation (2.2.6) of the cross-field particle fluxes. The extension to plateau regime requires a kinetic theory derivation of a constitutive relation for the parallel viscous force  $B \cdot \nabla \Pi$  in the strong rotation ordering ( $v_\phi \geq v_{th}$ ) to be used in the momentum balance equation. This constitutive relation was derived [43] by adopting the approach used by Shaing and Callen [66]. The model provides for incorporation of an anomalous radial transfer rate of toroidal momentum (or drag frequency) determined from experiment and relies upon neoclassical theory only for the determination of the frictional and parallel viscous forces. The model yields a self-consistent calculation of the radial electric field, poloidal and toroidal rotation velocities, poloidal density variations and

radial particle fluxes. The parallel and normal(radial) components of the momentum balance equation (2.2.2) can be combined to write the radial impurity flux as a sum of the contributions arising from different effects, that is

$$\begin{aligned} \langle n_I v_{Ir} \rangle = & \langle n_I v_{Ir} \rangle_{PS} + \langle n_I v_{Ir} \rangle_{NC} + \langle n_I v_{Ir} \rangle_M + \langle n_I v_{Ir} \rangle_I \\ & + \langle n_I v_{Ir} \rangle_{\Phi'} + \langle n_I v_{Ir} \rangle_{\Phi p} \end{aligned} \quad (2.4.1)$$

In the notation of Reference [43], the various terms in Eq. (2.4.1) may be written explicitly as shown below.

$$\begin{aligned} \langle n_I v_{Ir} \rangle_{PS} = & n_I^0 m_I \nu_{Ii}^0 \epsilon^2 / (e_I B_p^0) [ \{ (1+2q^2)/q^2 + (n_i^C/\epsilon) \} P_i' \\ & [ (1+2q^2)/q^2 + (n_I^C/\epsilon) \} (1+\beta_I) P_I' \end{aligned} \quad (2.4.2)$$

$$\begin{aligned} \langle n_I v_{Ir} \rangle_{NC} = & (n_I^0 m_I \nu_{Ii}^0 / e_I B_p^0 d) \\ & [ \{ (\mu_i \mu_I) + \epsilon^2 \mu_i \{ (1+\beta_I) (n_I^C/\epsilon) - (n_i^C/\epsilon) \} \} P_i' \\ & - [ \mu_I \{ \xi_i + \beta_I (1+\xi_i) \} + \epsilon^2 \mu_I \{ (n_i^C/\epsilon) - (n_I^C/\epsilon) \} \} P_I' ] \end{aligned} \quad (2.4.3)$$

$$\begin{aligned}
\langle n_I v_{Ir} \rangle_M = & -1/(e_I B_p^0 d) [M_{\phi I}^0 \{ \mu_I (1 + \xi_i) + e^2 (d + (1+d) \\
& (n_I^C/\epsilon) - (1 + \xi_i) (n_i^C/\epsilon) \} \\
& + M_{\phi i}^0 \{ \mu_I + e^2 ((1 + 1/2(\beta_I + \xi_I))) \\
& (n_I^C/\epsilon) - (n_i^C/\epsilon) \} ] \\
\end{aligned} \tag{2.4.4}$$

$$\begin{aligned}
\langle n_I v_{Ir} \rangle_I = & -n_I^0 m_I \nu_{Ii}^0 e^2 B_{\phi}^0 / (e_I B_p^0 (B^0)^2 d) \\
& [ (\xi_i + \beta_I (1 + \xi_i)) \langle G_I \rangle - \mu_I \langle G_i \rangle ] \\
\end{aligned} \tag{2.4.5}$$

$$\begin{aligned}
\langle n_I v_{Ir} \rangle_{\Phi} = & n_I^0 m_I \nu_{Ii}^0 / e_I B_p^0 [ \mu_I \gamma_I + e^2 \{ \beta_I (1 + 2q^2) / q^2 \\
& + (\beta_I + \gamma_I) (n_I^C/\epsilon) - \gamma_I (n_i^C/\epsilon) \} ] (E_r^0 / B_p^0) \\
\end{aligned} \tag{2.4.6}$$

$$\begin{aligned}
\langle n_I v_{Ir} \rangle_{\Phi p} = & -n_I^0 m_I \nu_{Ii}^0 e^2 / (e_I B_p^0 [ \beta_I \{ \delta_1 (n_I^C/\epsilon) + \delta_2 (n_i^C/\epsilon) \} \\
& - n_I^0 B_{\phi}^0 z T (\xi_I + \xi_i (1 + \beta_I)) / 2 (e_I (B^0)^2 (1 + a/z) d) \\
& \{ (n_I^S/\epsilon) (n_i^C/\epsilon) \\
& - (n_i^S/\epsilon) (n_I^C/\epsilon) \} ] \\
\end{aligned} \tag{2.4.7}$$

where,  $\beta$  represents the normalized drag frequency,  $\mu$

represents normalized viscosity, the symbols  $I$  and  $i$  represent the impurity and the plasma ions respectively, and

$$d = \xi_i + \xi_I(1 + \xi_i) \quad (2.4.8)$$

$$\gamma_I = [\beta_i + \beta_I(1 + \xi_i)] / [\xi_i + \xi_I(1 + \xi_i)] \quad (2.4.9)$$

The rest of the quantities appearing above are as defined in Reference [43] In Equation (2.4.1), the first two components correspond respectively to the Pfirsch-Schluter and neoclassical fluxes of the usual transport theory, but now modified to account for the radial transfer of momentum and for the variation of impurity and ion densities over the flux surface. For a negative density gradient of the main ion, both of these flux components will be inward. The third term is the transport flux resulting directly from the interaction of the beam ions with the main ions and impurities, and contributes an inward impurity flux for co-injection and outward impurity flux for counter-injection. The fourth term results from the retention of the inertial term  $nm(v \cdot \nabla)v$  in the momentum balance equation and produces an outward impurity flux for

strong co-injection and conversely for counter-injection. The fifth term is the radial impurity flux driven by the linear component of the radial electric field, and is directed outward for strong co-injection, and inward for counter-injection and weak co-injection for the normally negative main ion density gradient. The last term is the impurity transport driven by poloidal variation of potential over the flux surface, or the poloidal electric field, and is usually negligible.

In Equation (2.4.1), it is seen that the first two terms describe diffusive transport fluxes, that is, the fluxes proportional to a pressure gradient, while the rest of the terms describe convective transport fluxes arising from viscous and inertial forces and the direct momentum input. The diffusive component is similar to the usual Pfirsch-Schluter and neoclassical form, but with modified coefficients which depend upon the drag frequency and the cosine component of the impurity density variation on the flux surface. The convective component of the radial particle flux consists of contributions proportional to the direct beam momentum input, the radial electric field, and the inertial term in the

momentum balance equation all of which have coefficients that depend upon the impurity density variation on the flux surface. The diffusive impurity fluxes are inward for the normally negative main ion density gradient. The rotational and the electric field contributions to the convective flux are outward for strong co-injection and inward for counter-injection, and conversely for the direct momentum input contribution. Thus with strong co-injection, the outward impurity fluxes produced by the rotation and radial electric field compete with the inward impurity flux produced by the main ion pressure gradient. With counter injection, all three components are inward. The other flux components tend to be less significant.

The previous details are relevant to the steady-state formulation of the Stacey-Sigmar theory [42,43]. However, following the onset of unbalanced neutral beam injection, the plasma takes some time to spin up to the maximum velocity and relax to a new equilibrium. While the flows necessary to maintain radial force balance develop quickly on a short time scale due to rapid damping of the poloidal flow caused by parallel viscosity, the toroidal flow will relax to an



equilibrium on a long transport time scale. Roughly, the plasma will rotate up to an asymptotic speed on a time scale comparable to the inverse drag frequency, tens of milliseconds in machines such as PLT and ISX-B and even longer in larger devices [28-34]. It follows that for a correct modeling of the impurity transport during the first 100 ms or so of the onset of beam injection, a time dependent formulation is necessary [67].

The particle conservation for a given impurity species may be written as

$$\partial n / \partial t = -\nabla \cdot \Gamma + S \quad (2.4.10)$$

where  $n$  is impurity density,  $\Gamma$  is cross-field impurity flux, and  $S$  represents impurity sources and sinks which may include atomic processes and external inward sources. The external sources and sinks generally include impurity ion loss, recycling, and deposition in the plasma scrape-off region near the wall. Since we are primarily concerned with impurity transport and its effects in central plasmas, the details of the edge region phenomena are not included in this model. Also,

since we intend to solve Equation (2.4.10) for single species, and then use atomic physics model to unfold impurity density for different charge states, the sources and sinks due to atomic processes will not be included in Equation (2.4.10). Assuming toroidal and poloidal symmetries, the cross field radial transport can then be written as

$$\partial n / \partial t = -(1/r) \partial / \partial r (r \Gamma) \quad (2.4.11)$$

The impurity flux  $\Gamma$  predicted by impurity flow reversal theory is generally of the form

$$\Gamma = -D(r) \partial n / \partial r + v(r) n \quad (2.4.12)$$

where  $D(r)$  is the particle diffusion coefficient, and  $v(r)$  is a convective velocity. The initial and boundary conditions may be specified from the physical details of the problem. For boundary conditions, the usual choice is a zero flux on axis at  $r=0$  from symmetry consideration, and a constant density at the plasma edge.

We use an implicit conservative scheme with an implicitness parameter  $w$  to finite-difference Equation (2.4.11). The implicitness parameter  $w$  may be adjusted from  $w=0$  (fully explicit) to  $w=1$  (fully implicit), but  $w=1/2$  (Crank-Nicholson scheme) gives second order accuracy in both space and time, and also guarantees unconditional stability. The finite-differencing of Equation (2.4.11) gives a tridiagonal system of the form

$$-a_i n_{i+1,j+1} + b_i n_{i,j+1} - c_i n_{i-1,j+1} = d_i \quad (2.4.13)$$

where the subscripts  $i$  and  $j$  represent indices for space and time respectively. It is a standard procedure to solve the tridiagonal system of the form of Equation (2.4.13) by Thomas algorithm [68]. The computer simulation of the time-dependent version of the Stacey-Sigmar theory exists on the CRAY computer system of the National Magnetic Fusion Energy Computer Center (NMFECC) at the Lawrence Livermore National Laboratory. The steady-state version of the code exists on the CYBER computer system of the Georgia Institute of Technology.

## 2.5 Hogan's Momentum Transport Theory

The viscosity problem is basically related to the effect of a velocity gradient. Kaufman [62] discussed the origin of the motion of the plasma particles that leads to the viscosity tensor being related to the velocity gradient via viscosity coefficients in the presence of a magnetic field. In this formalism, the stress tensor depends only upon the symmetric traceless part of the velocity gradient. In the presence of a magnetic field, the five independent components of the traceless symmetric tensor may be grouped into three types: the first type of motion is a compression along the magnetic field, and is independent of the magnetic field itself; the second type of motion is a deformation in the transverse plane alone; and the last type of motion is a deformation in a plane containing the magnetic field direction. These motions are incompressible and irrotational.

Hogan [53] analyzed the collisional diffusion of toroidal momentum in the presence of external sources and losses of momentum. He noted that the classical viscous tensor has the

same simple structure as the heat flux. Following Braginskii [3], the viscous stress tensor may be written as

$$\Pi_{\alpha\beta} = p\delta_{\alpha\beta} - \eta_0 W_{\alpha\beta} - (\eta_1 W^1_{\alpha\beta} + \eta_2 W^2_{\alpha\beta}) + (\eta_3 W^3_{\alpha\beta} + \eta_4 W^4_{\alpha\beta}) \quad (2.5.1)$$

where  $p$  is scalar pressure,  $\alpha$  and  $\beta$  are some generalized coordinates,  $\delta$  is the kronecker delta,  $\eta$  represents viscosity coefficients, and  $W$  stands for the elements of the rate-of-strain tensor. The last three terms in Equation (2.5.1) represent the parallel, perpendicular and the drift viscosity tensors respectively. Hogan considered purely toroidal flow but did not order the toroidal velocities appearing in the stress tensor in an a priori way and found the constraints imposed by the action of the large parallel ( $\eta_0$ ) and drift ( $\eta_3, \eta_4$ ) viscosities upon the viscous diffusion across flux surfaces on the transport ( $\eta_1, \eta_2$ ) time scale. Considering  $\eta_0$ , ( $\eta_3, \eta_4$ ), and ( $\eta_1, \eta_2$ ) as  $O(1)$ ,  $O(\epsilon)$  and  $O(\epsilon^2)$  respectively, the orders of the stress tensors were found to be  $W^{(0)} = -\eta_0 W^0$ ,  $W^{(1)} = \eta_1 W^1 + \eta_4 W^4$ , and  $W^{(2)} = -\eta_1 W^1 - \eta_2 W^2$ .

The fastest relaxation occurs on the parallel viscosity time scale. The next, slower relaxation takes place on a drift viscosity time scale. Both the parallel and drift viscosities are much larger than the perpendicular viscosity, and these forces must be annihilated before the radial diffusion is important. The flux surface average of the radial diffusion equation for toroidal momentum on the slow, perpendicular diffusion time scale in the low-beta, circular cross-section, and large aspect-ratio limits leads to an effective Pfirsch-Schluter factor for the diffusion of the toroidal angular momentum

$$\eta^{\text{eff}} = \eta_i (1 + 2.31q^2) \quad (2.5.2)$$

where  $q$  is the safety factor. Thus the collisional regime cross-field momentum transport scales with the collision frequency.

The essential feature of Hogan's formalism is that the poloidal variation in  $v_\phi$  is driven by the viscosity itself and is of the order  $\delta$ , where  $\delta = r_L/L$ , with  $r_L$  = gyro-radius, and

$L$ =scale length. Thus in Hogan's formalism, the inertial forces which can produce an  $O(\epsilon)$  variation in the poloidal variation of the toroidal flow velocity, and the poloidal flow velocities were neglected. No model problem calculations were performed to check the toroidal momentum confinement time with experiment. However, the correct identification of the parallel, perpendicular and drift forces was a significant development in understanding momentum confinement in tokamak plasmas.

## 2.6 Stacey-Sigmar Momentum Transport Theory

Stacey and Sigmar [54] developed a theory to explain the rapid dissipation of momentum for a collisional, tokamak plasma with strong rotation ( $v_\phi \sim v_{th}$ ) following neutral beam injection. The theory introduces the concept of gyroviscosity to explain from first principles the momentum confinement time inferred from tokamak experiments.

Working directly with Braginskii [3] representation, the viscous stress tensor  $\Pi$  for a plasma in a magnetic field in terms of the corresponding viscosity coefficients  $\eta$ , and the

rate-of-strain tensor elements  $W$  in terms of the generalized coordinates  $\alpha$  and  $\beta$  may be written as

$$\begin{aligned}\Pi &= -\eta_0 W^0_{\alpha\beta} - (\eta_1 W^1_{\alpha\beta} + \eta_2 W^2_{\alpha\beta}) + (\eta_3 W^3_{\alpha\beta} + \eta_4 W^4_{\alpha\beta}) \\ &= \Pi^0_{\alpha\beta} + \Pi^{1,2}_{\alpha\beta} + \Pi^{3,4}_{\alpha\beta}\end{aligned}\quad (2.6.1)$$

where the terms on the right hand side of Equation (2.6.1) are respectively the parallel, perpendicular and the gyroviscous stress tensor elements. The particle motions producing these stresses were discussed by Kaufman [62]. The parallel viscosity coefficient  $\eta_0$  scales inversely with self-collision frequency, the perpendicular viscosity coefficients  $\eta^1$  and  $\eta^2$  scale directly with collision frequency, and the gyroviscous coefficients  $\eta_3$  and  $\eta_4$  are independent of the collision frequency. Assuming  $|B_\phi|/|B| \approx 1$  and  $|B_p|/|B| \ll 1$  where  $B_\phi$ ,  $B_p$  and  $B$  are respectively the toroidal, poloidal and the resultant magnetic fields, Stacey and Sigmar [54] worked out the viscosity elements explicitly. The parallel viscosity ( $\eta_0$ ) contribution to the toroidal viscous force in the flux surface average toroidal momentum balance vanishes. It was shown that if the plasma rotated as a rigid body then both perpendicular and gyroviscous forces in this representation would also



vanish. It is thus the departure from the rigid body rotation within a flux surface which drives the gyroviscous force, and, the departure from the radially uniform, rigid-body rotation which drives the perpendicular viscous force. Stacey and Sigmar thus effectively showed [43] that with strong rotation, the inertial effects drive an  $O(\epsilon)$  poloidal variation in the density, which in turn produces a higher order, poloidally asymmetric flow. Further, for  $O(\epsilon)$  poloidal variations over the flux surface, the gyroviscous force was found to be larger than the perpendicular viscous force by a factor of about 100. Since the momentum confinement times inferred from toroidal rotation measurements and momentum balance considerations have been two orders of magnitude smaller than could be accounted for by neoclassical perpendicular viscosity [28-34], the momentum confinement time based on gyroviscous force, which is about two orders of magnitude greater than the perpendicular force, is the same order of magnitude as the momentum confinement time inferred from rotation measurements. This development appears to resolve the long-standing dilemma in neutral beam injection momentum confinement experiments.

In the large aspect-ratio, low-beta and circular flux approximations, the flux-surface averaged gyroviscous force, which drives  $O(\epsilon)$  poloidal variations in toroidal velocity and density, leads to a toroidal momentum confinement time, which can be approximated to within an  $O(1)$  multiplier applicable in all collisional regimes, to

$$\tau_{\phi}^{-1} = \nu_d = T_i / (2R^2 Z e B) \quad (2.6.2)$$

where  $\tau_{\phi}$  is the toroidal momentum confinement time,  $\nu_d$  is the drag frequency [22,23,42,43],  $T_i$  is the ion temperature,  $R$  is the major radius and  $Z$  is the ionic charge-state. Preliminary calculations [54] show that the momentum confinement time predicted by Equation (2.6.2) is in good general agreement with the measured [28-34] values for ISX-B, PLT and PDX tokamaks.

## CHAPTER III

## ANALYSIS OF

## INTRINSIC TUNGSTEN TRANSPORT IN PLT

3.1 Introduction

The Princeton Large Torus (PLT) became operational in December 1975. Ohmic heating experiments emphasized the study of plasma confinement, impurity control, and MHD stability. Neutral beam experiments began in 1977. The neutral beam experiments have focussed on impurity transport studies for co- versus counter-injection. A plan view [48] of the experimental arrangement, and the toroidal location of the various diagnostics is shown in Figure (3.1.1). Some of the principal PLT parameters are listed in Table (3.1.1).

The electromagnetic radiation emitted by tokamak plasmas in the ultra-soft x-ray (USX) region ( $0.1 < h\nu < 1 \text{ keV}$ ) constitutes a significant energy loss. However, since USX radiation is primarily emitted by impurities, it can provide a

Table 3.1.1 PLT data with intrinsic tungsten

---

Major radius (m)	1.40
Minor radius (m)	0.40
$Z_{\text{eff}}$	2.5
Toroidal magnetic field (T)	3.2
Safety factor $q(0)$	1.0
Safety factor $q(a)$	4.0
Neutral beam power (kW)	585.0
Neutral beam energy (keV)	40.0
Model impurity: Tungsten	
Plasma type	: $D^+$
Beam type	: $H^0$
Beam tangency radius (m)	1.10
Beam width (m)	0.20
Beam energy components (keV)	40,20,13.3
Beam injection time (ms)	250 - 350

---

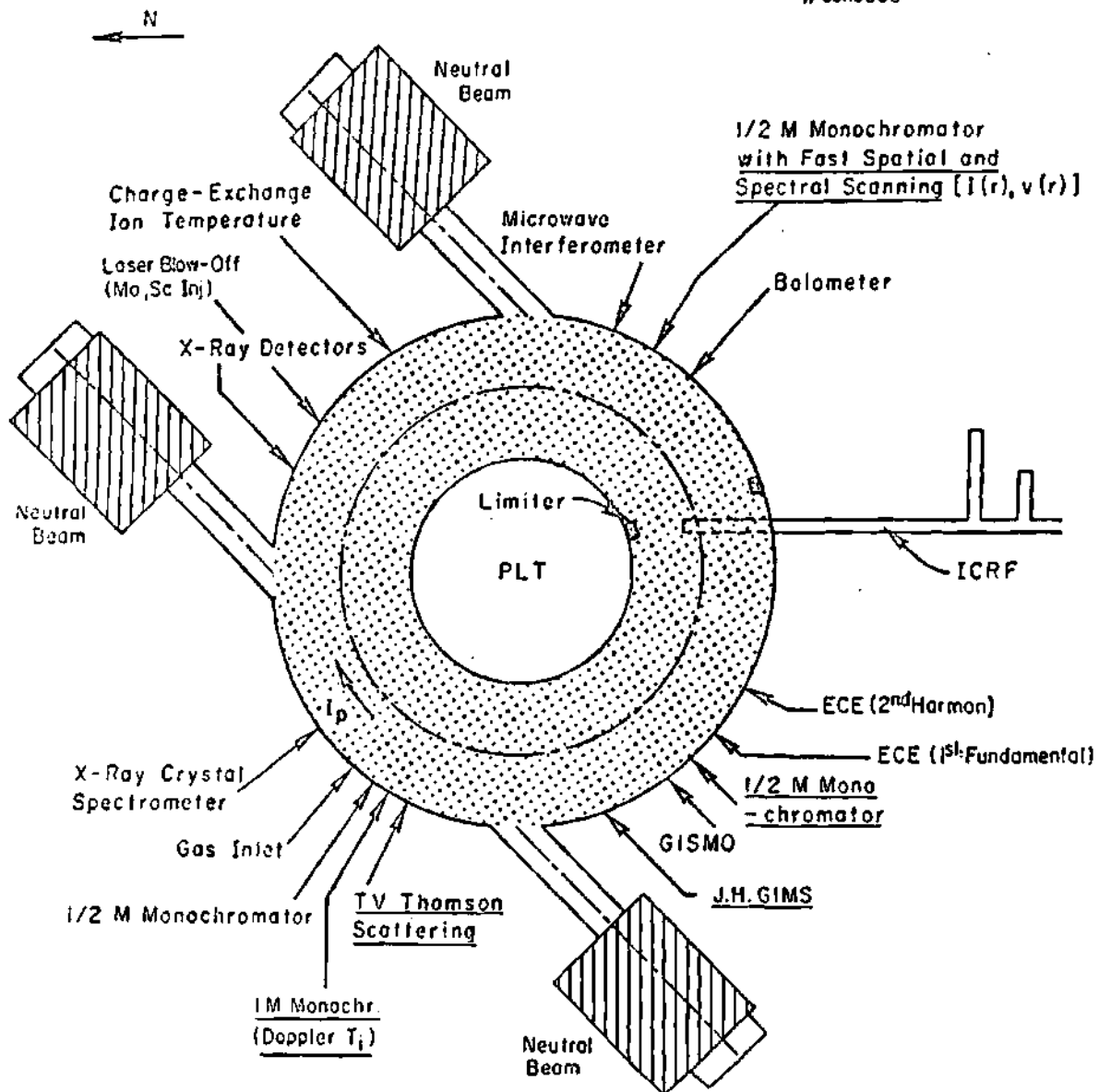


Figure 3.1.1 PLT geometry and diagnostics.

very good mechanism to study particle transport in tokamak plasmas. Eames [25] used a bolometer [69-71] to measure integrated USX radiation from intrinsic tungsten impurity in ohmic and in neutral beam heated deuterium discharges in the PLT tokamak with tungsten limiters. The tungsten limiters were later replaced with those of carbon, and stainless steel to avoid the intolerable radiation losses from tungsten. However, the data obtained with tungsten is invaluable in its own right in as much as it helps to understand the transport of impurities with beam injection. Eames' experimental work is briefly reviewed in Section (3.2). The analysis of these experiments is presented in Section (3.3).

### 3.2 PLT Experiments with Intrinsic Tungsten

Eames [25] inferred impurity fluxes from measured chordal distributions of USX radiation from the PLT deuterium discharges with tungsten limiters. The neutral beam injection took place from 250 to 350 ms after the discharge was initiated. The data were recorded for the inner 20 cm of the 40 cm discharge so that the contribution to the USX radiation from carbon and oxygen could be neglected since these impurities

would be completely stripped in this region. Three sets of data, that is, without beam injection, with 585 kW co-injection, and with 430 kW counter-injection are of particular significance since such data leads to interesting conclusions about particle transport with beam injection.

The total energy emitted by tokamak plasmas along a given chord is generally measured by bolometers [69-71]. A bolometer is basically a temperature-sensing device. The choice of a suitable temperature sensor, or thermistor depends on factors such as the level of nuclear radiation, the range of plasma temperatures, and the background noise. A thermistor may typically consist of a boron-doped, p-type silicon semiconductor film flake. However, since such thermistors cannot tolerate intense nuclear radiations and extremely high temperatures expected in a reactor environment, a modified thermistor such as the one based on a thin platinum grid may replace the semiconductor sensor in such a case. A bolometer will, of course, respond to any absorbed energy such as in the form of electromagnetic radiation, neutral atoms, and the charged particles from a plasma. With an uncollimated bolometer, we assume that the power it receives is

representative of the total power reaching the first wall by whatever means. However, with a collimated bolometer, it is usually assumed that the contribution of neutral atoms is negligible and that charged particles cannot reach the detector. Hence, in this case, we have a measurement of the electromagnetic radiation from the plasma integrated along a chord. With a set of chords fanning across a plasma column, we integrate over the column to obtain the total radiated power. In practice, the bolometric measurements usually use a stationary array that views different chords simultaneously and a separate single bolometer that scans the chords from shot to shot. The top and bottom halves of the chordal scans are first averaged, then smoothed to remove the spurious shot-to-shot irregularities. The absolute value of the measurements is usually subject to a calibration uncertainty of +50%, that is, the actual incident energy may be higher by a factor of up to (1.5). Eames [25] used a bolometer arrangement consisting of arrays of silicon surface-barrier detectors to measure integrated signal from a column of plasma 3 mm high by 35 mm wide in cross-section accessible to the detector at a given chordal length. The detector system is shown in Figure (3.2.1).



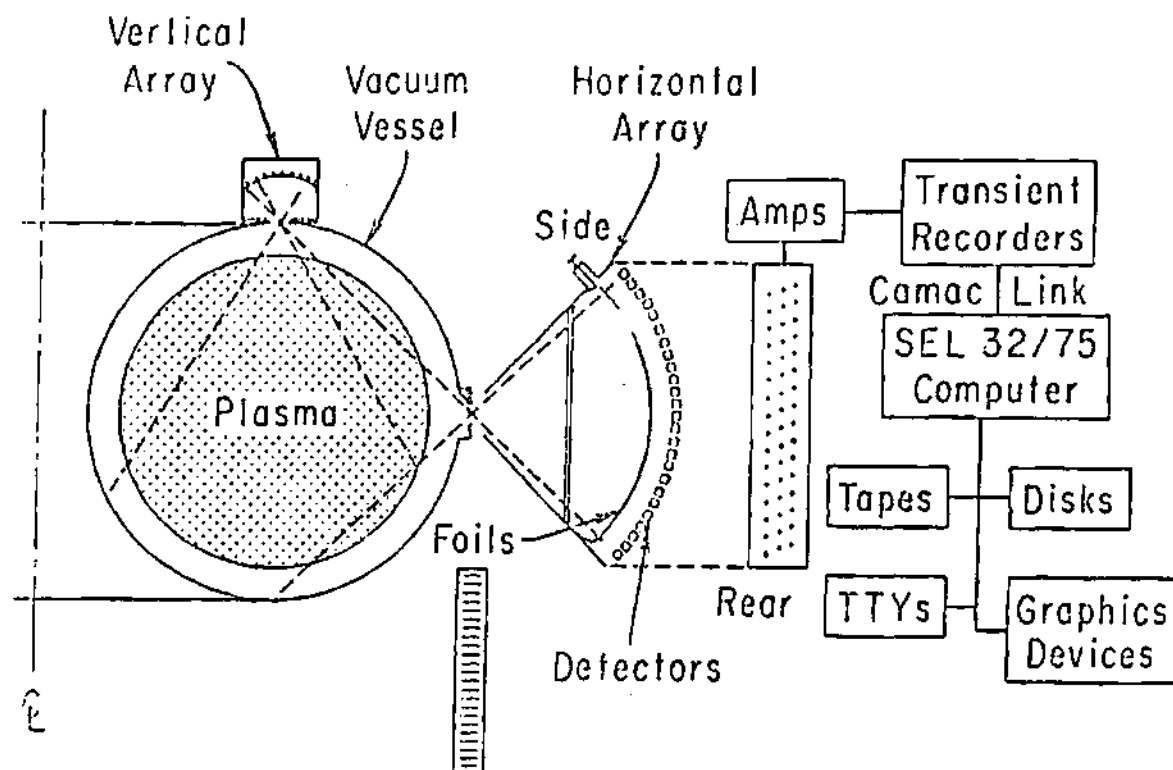


Figure 3.2.1 Diagnostics for bolometric measurements in PLT.

The bolometric measurements yield the line integrated chordal brightness (photons/cm<sup>2</sup>-s) or intensity (W/m<sup>2</sup>) along a line of sight. However, to properly interpret the experimental data, we are usually interested in the radial profiles of the radiated power density. The chordal signal can be Abel inverted [72] to get the radial profiles of emissivity, that is, power emitted per unit volume. The Abel inversion process assumes toroidal and poloidal symmetries. The actual toroidal and poloidal asymmetries can alter the radial distribution of emissivity deduced by Abel inversion. However, such asymmetries are generally peripheral and do not strongly affect the measured total power. Assuming cylindrical symmetry of the emissivity profile  $\epsilon(r)$ , the line integrated intensity along a chord intersecting the plasma at a distance  $y$  from the center is given by [72]

$$I(y) = 2 \int_y^a [\epsilon(r)/(r^2 - y^2)^{1/2}] dr \quad (3.2.1)$$

where  $a$  is minor radius. This equation is inverted to obtain the emissivity profile

$$\epsilon(r) = -(1/\pi) \int_r^a [I(y)/(y^2 - r^2)^{1/2}] dy \quad (3.2.2)$$

Assuming coronal equilibrium [73], the radial emissivity

profile inferred from measured chordal intensity can then be used to unfold the radial profile of the radiating impurity density.

The coronal equilibrium [73] results when electron collisional ionization is exactly balanced by total recombination rate. For the coronal equilibrium model to be valid, it is generally assumed that: 1) the plasmas are optically thin to the emitted radiation so that all photoabsorption processes may be neglected, 2) the collision times of interest are much longer than the decay times of most excited atomic states so that each ion may be assumed to be in its ground state at the start of any collisional process. Thus, the coronal model essentially implies that excitation and ionization are due to electron collisions in the ground state, and de-excitation is only radiative. At the high temperatures ( .001 - 100 keV ) and low densities (  $\leq 10^{16} \text{ cm}^{-3}$  ), which are characteristic of tokamak plasmas, the coronal equilibrium model is generally a good starting approximation.

The chordal distribution of the USX radiation was Abel inverted [72] by Eames [25] to determine the power density  $P_W$  radiated by tungsten. Assuming coronal equilibrium [73], the power  $P_W$  radiated by tungsten per unit volume can be written as

$$P_W = n_e n_W f(T_e) \quad (3.2.3)$$

where  $n_e$  and  $n_W$  represent electron and tungsten densities respectively, and  $f$  is the coronal equilibrium function of the electron temperature  $T_e$ . The coronal equilibrium assumption was justified on the basis of the short equilibration times estimated. The measured values of  $P_W$  [25],  $n_e$  [74], and the calculated value of the coronal equilibrium function  $f$  [75] were then used to unfold the tungsten density  $n_W$  (Figs. 3.2.2-3) using Equation (3.2.1). The tungsten flux was then inferred from the tungsten density and the known geometry of the experiment. The total amount of tungsten at time  $t$ , inside a radius  $r$  was written by Eames [25] as

$$N(r, t) = \int_0^r 2\pi r n_W(r) dr \quad (3.2.4)$$

The tungsten flux is then given by [25]

$$\Gamma_z(r, t) = 1/(2\pi r) \partial/\partial t N(r, t), \quad (3.2.5)$$

with

$$\Gamma_z(r=0, t) = 0 \quad (3.2.6)$$

Eames [25] found significant differences in impurity transport for co- versus counter-injection. The co-injection was found to cause only a 30 % increase in the central power loss, while for counter-injection the central power loss increased by a factor of 6. During co-injection, the tungsten density profiles were quite flat out to 20 cm radius at all times. However, during counter-injection, the tungsten density profile became peaked with a factor of 6 increase as compared to pre-injection. The tungsten density fraction  $n_W/n_e$  (Figs. 3.2.3-4) may indicate whether or not tungsten shows a preferential accumulation at any part of the cross-section. The tungsten density fraction for co-injection was quite flat, but counter-injection showed a factor of 4 increase near center as compared to that at  $r=20$  cm. The general tendency of the tungsten flux for co-injection (Fig. 3.2.6) is to change from an inward to an outward direction. The tungsten flux for counter-injection (Fig. 3.2.7) is always directed inward, is an order of magnitude greater than the flux during co-injection, and increases substantially with time. Eames [25] noted that the increased amount of tungsten with counter-injection could be attributed to the fact that more particle orbits intersect the limiter with counter-injection

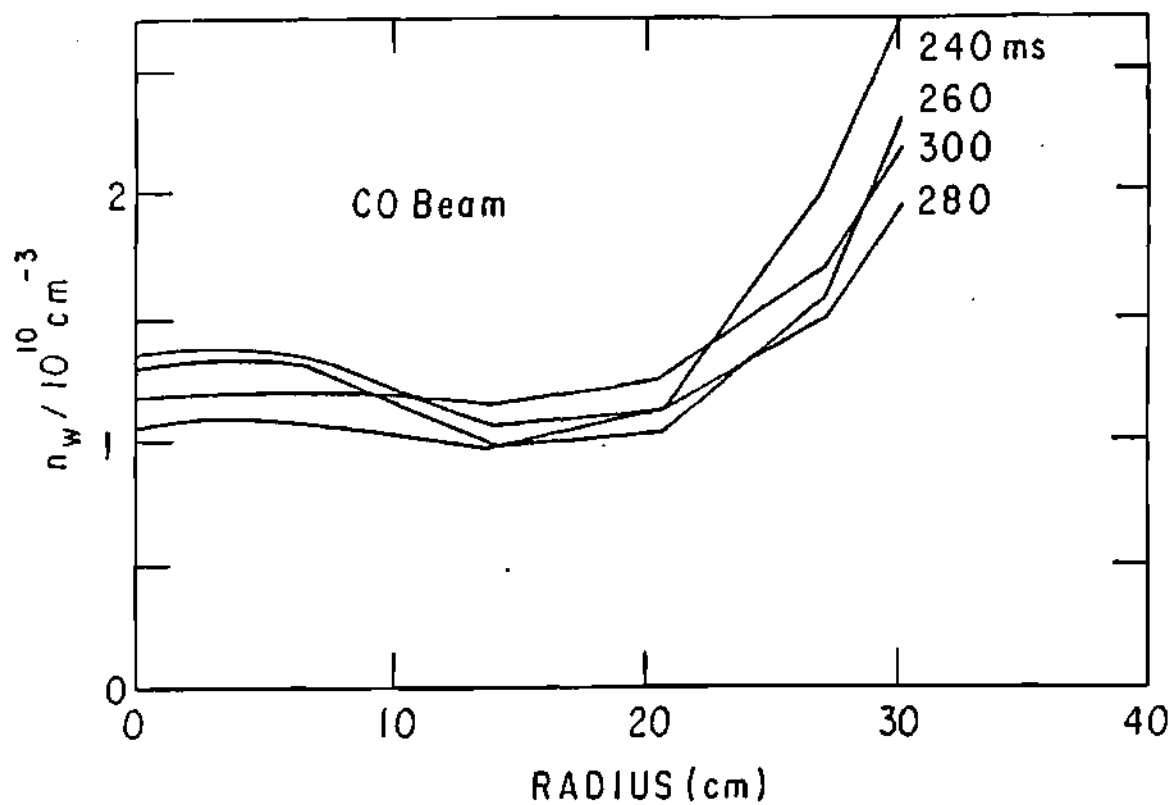


Figure 3.2.2 Experimental density profiles for tungsten in PLT with 585 kW of neutral beam co-injection.

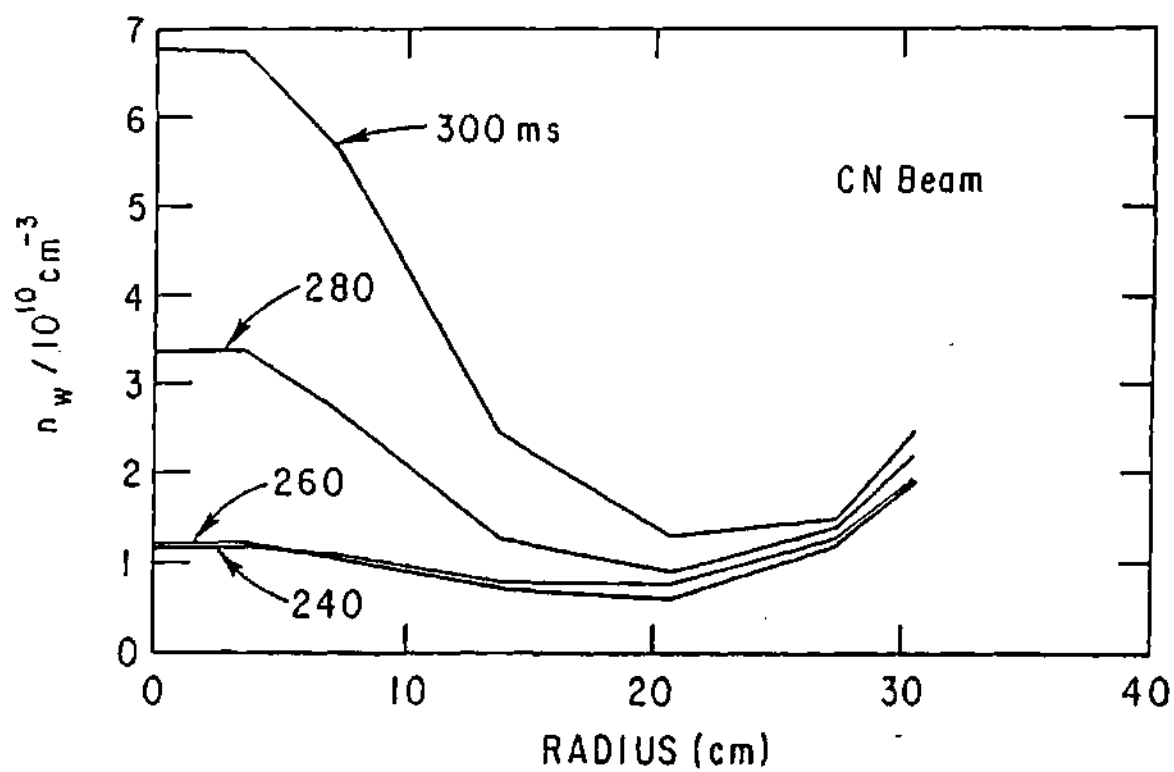


Figure 3.2.3 Experimental density profiles for tungsten in PLT with 430 kW of neutral beam counter-injection.

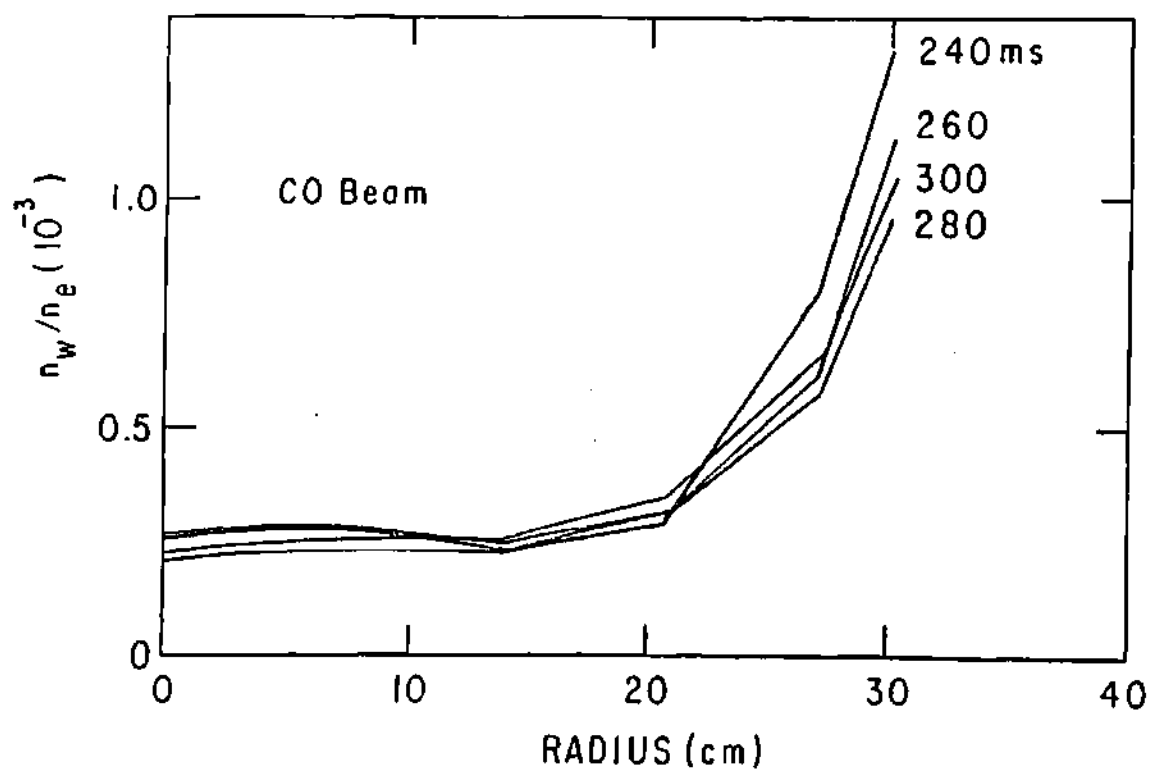


Figure 3.2.4 Tungsten density fraction in PLT with 585 kW of neutral beam co-injection.



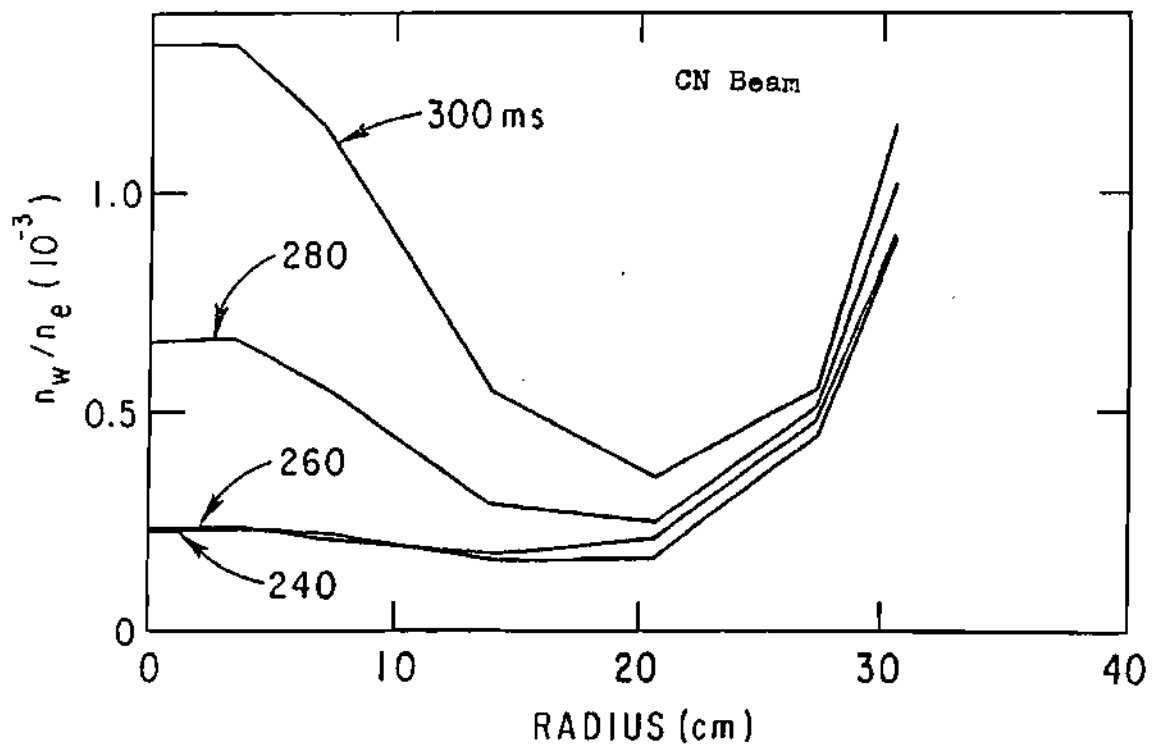


Figure 3.2.5 Tungsten density fraction in PLT with 430 kW of neutral beam counter-injection.

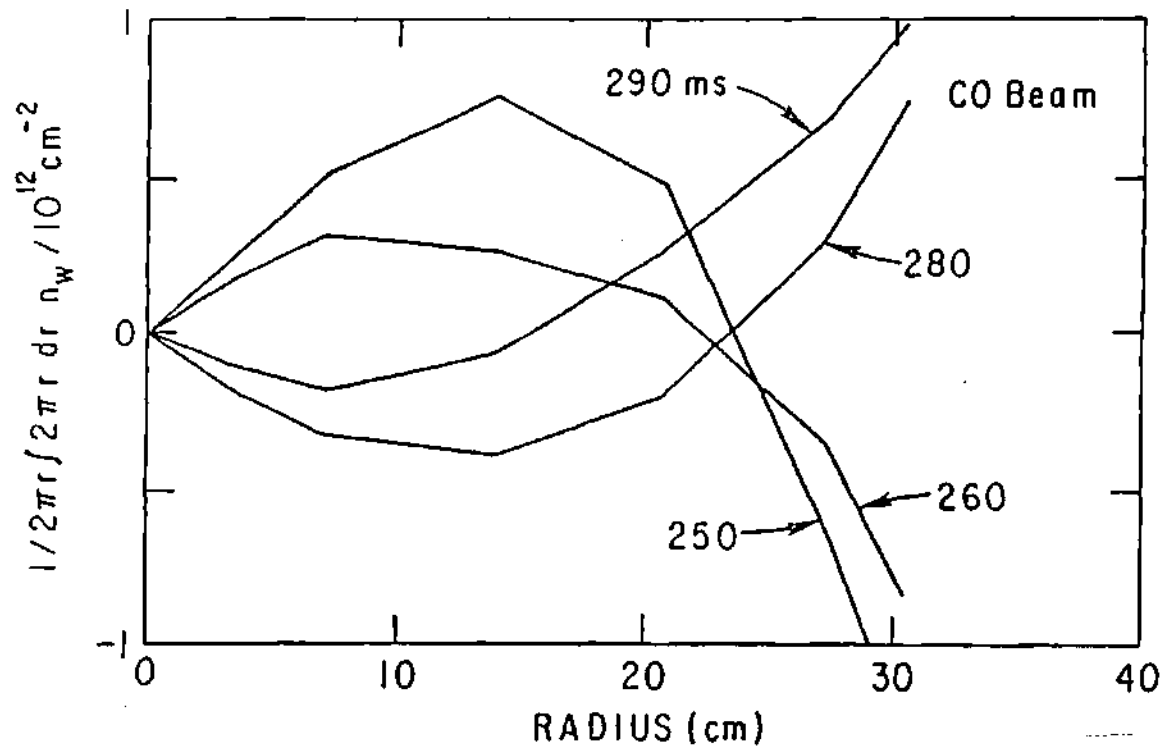


Figure 3.2.6 Experimental flux profiles for tungsten in PLT with 585 kW of neutral beam co-injection.

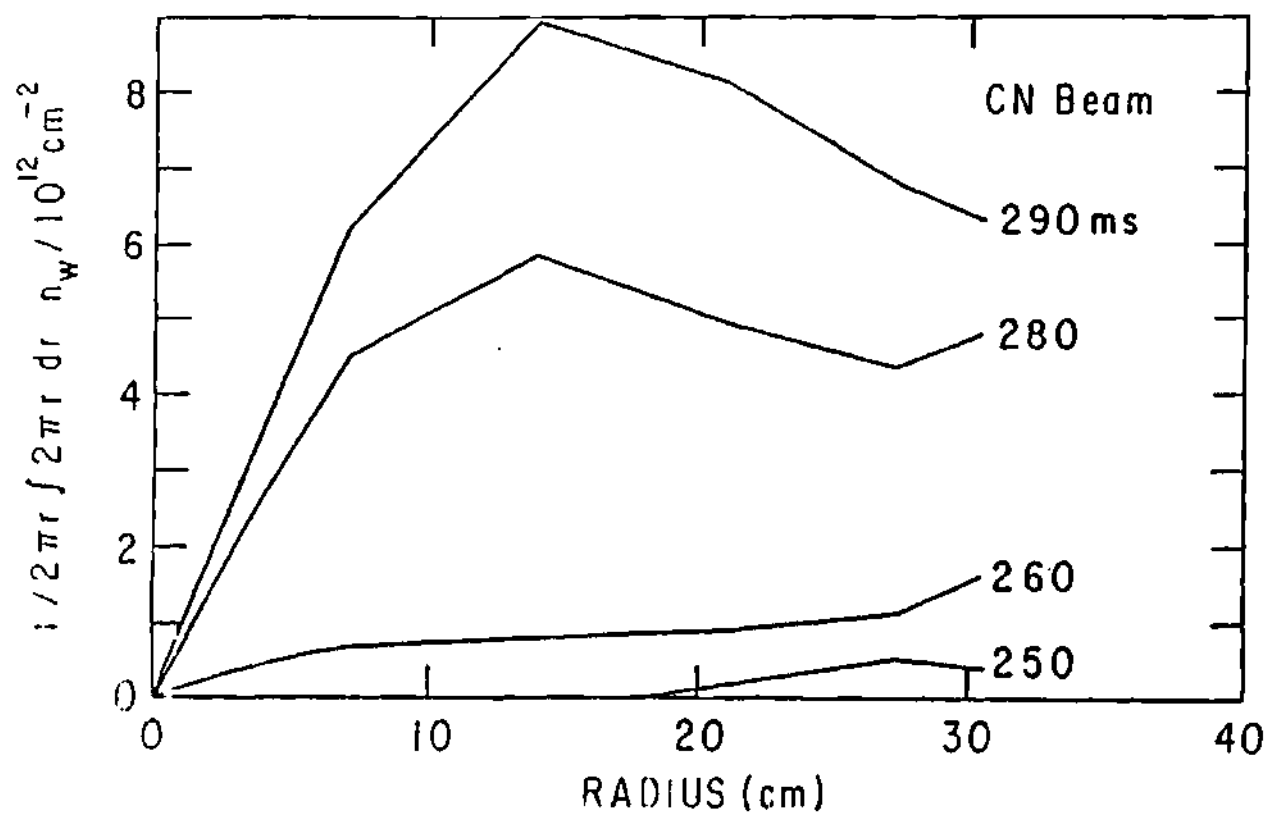


Figure 3.2.7 Experimental flux profiles for tungsten in PLT with 430 kW of neutral beam counter-injection.

but concluded that this would not explain the tungsten peaking with counter-injection. It was further observed that the co-plus counter-discharges were similar to co-discharges instead of to counter-discharges. If the counter-beam were responsible for an increased tungsten density due only to knocking tungsten off the limiter, then co-plus counter-discharges should have at least as much tungsten as in the counter-injection discharge. All of these observations indicate that impurity transport is very sensitive to the direction of beam injection.

### 3.3 Analysis of PLT Experiments

To correctly model the experimental conditions, measured data were used as far as possible for the relevant physical quantities such as density and temperature. However, measured data for every quantity of interest was not always available for a given shot. In such a situation, the relevant information was obtained either by extrapolation or by numerical modeling. The measured electron density profile shown in Figure (3.3.1) was based on Reference [74], and was assumed to be constant in time and identical for both co- and counter-injection. The

plasma ion density distribution was assumed to be same as the electron density. The experimental values of the space- and time-resolved electron temperature profiles [74] determined from the fundamental cyclotron radiation are shown in Figures (3.3.2) and (3.3.3) for co- and counter-injection respectively. The typical profiles of the safety factor were taken from Reference [76].

The values of the average charge state  $\langle z \rangle = \sum_i z_i n_i$ , where  $n_i$  is the fraction of the ions in charge state  $i$  with charge  $z_i$ , at different locations and times are required to model the transport calculations for a given charge state. The average ion model [77] based on coronal equilibrium [73] was used to estimate the average values of the tungsten charge states. The average ion model based on coronal approximation replaces the different ionic species for each element by an average ion which is a statistical average of all possible charge states of the element. A set of coupled nonlinear time-dependent rate equations are iterated numerically till a steady-state solution is achieved. The coronal equilibrium values for the radiation and mean charge state are determined at this stage. The average charge state for an impurity species depends only

on the local electron temperature. The variation of the average charge state for tungsten with electron temperature is shown in Figure (3.3.4).

The code PROCTR [78] was used to compute the beam deposition profile  $H(r)$  needed to evaluate the beam momentum deposition. The deposition profile  $H(r)$  is a shape factor whose volume average represents the percentage of the fast neutrals that are absorbed and confined in the plasma [79]. The code models the thermalization of the fast ions by solving the Fokker Planck equation by moments method. The beam shape factor is shown in Figure (3.3.5).

An important element in the impurity flow reversal theory [42,43] is the radial transfer of neutral beam momentum to a flux surface by an external drag. The Stacey-Sigmar gyroviscous theory [54] for momentum confinement was used to infer external drag for the PLT parameters. According to gyroviscous theory [54], the drag frequency is given to within a constant of order unity by

$$\nu_d = T_i / (2R^2 Z_e B) \quad (3.3.1)$$

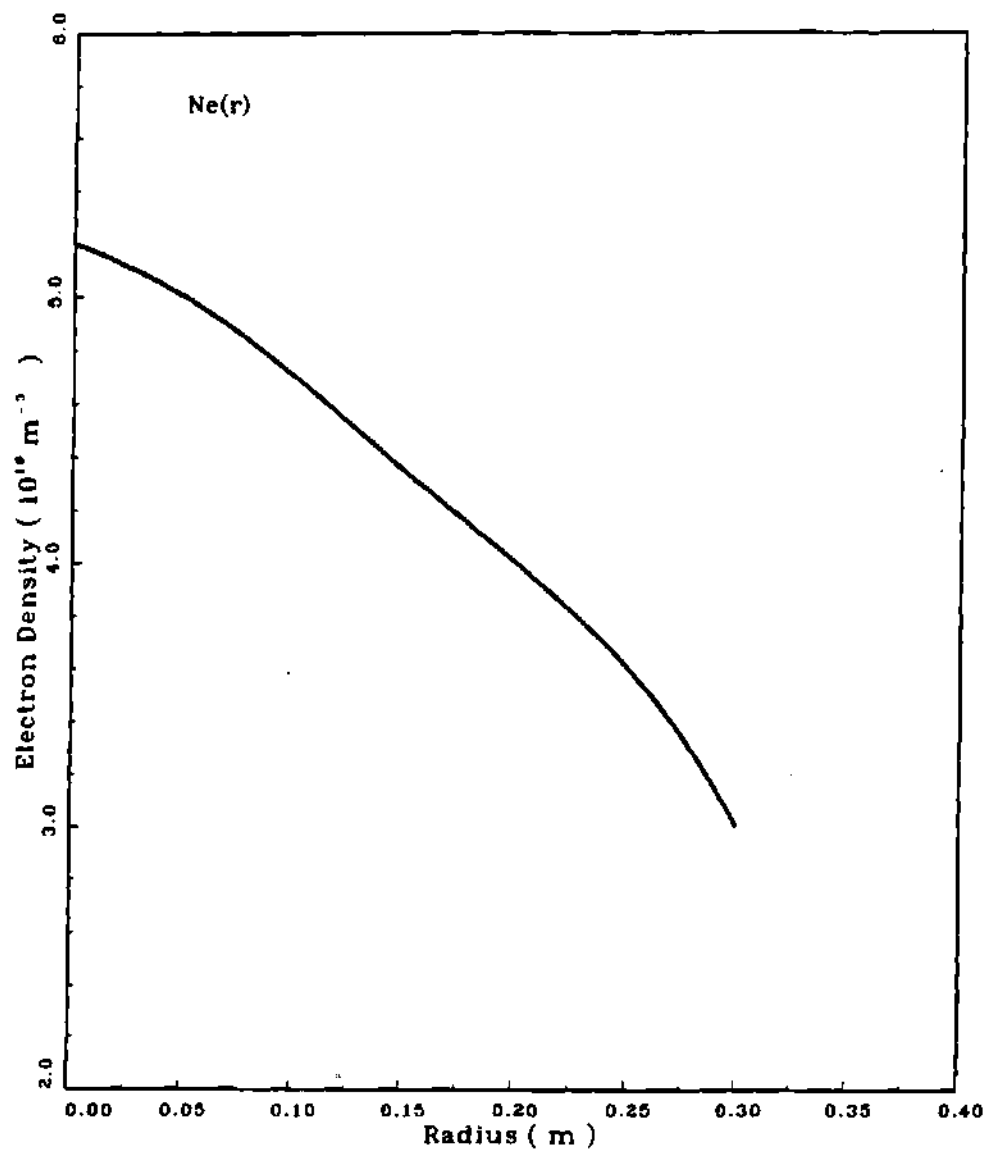


Figure 3.3.1. Electron density profile in PLT.

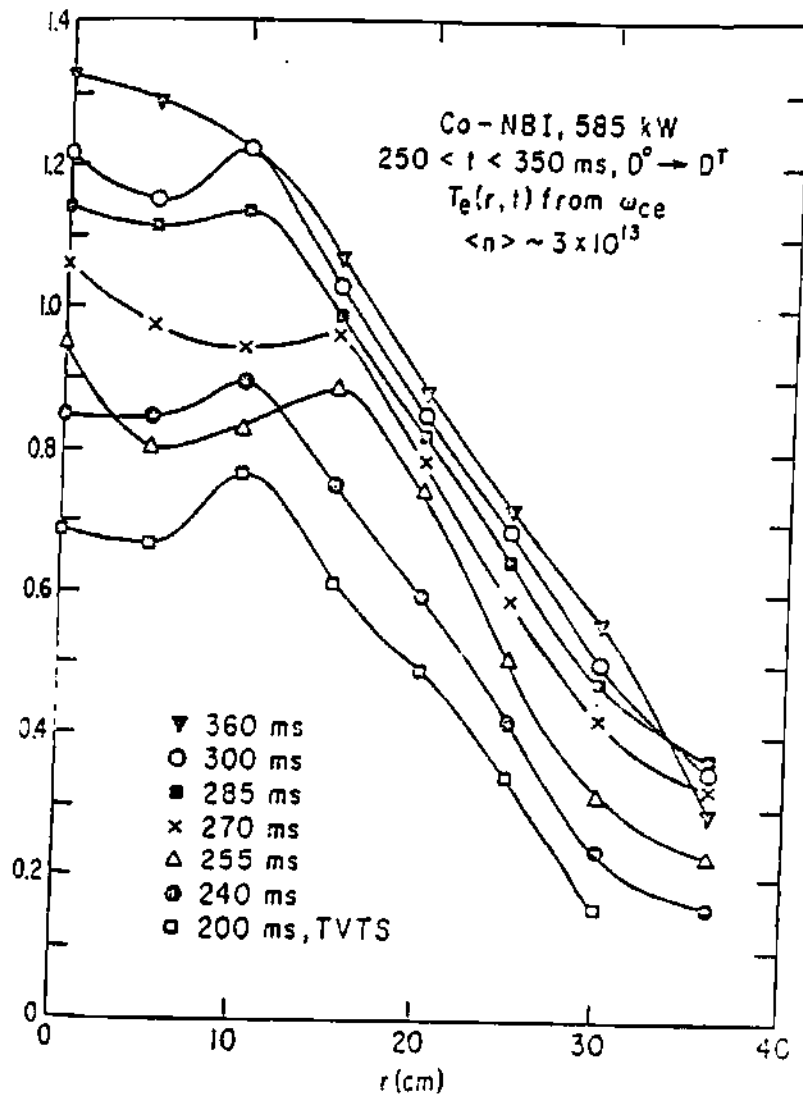


Figure 3.3.2 Measured profiles of electron temperature in PLT with 585 kW co-injection.



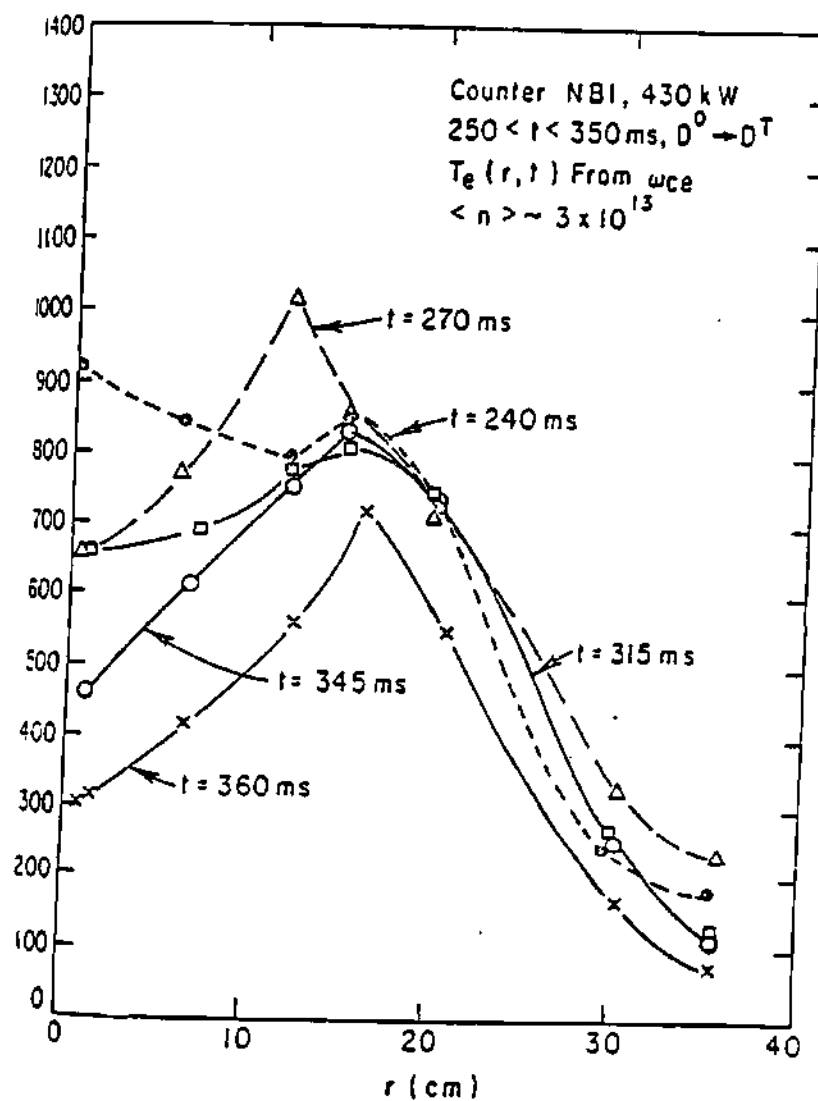


Figure 3.3.3 Measured profiles of electron temperature in PLT with 430 kW counter-injection.

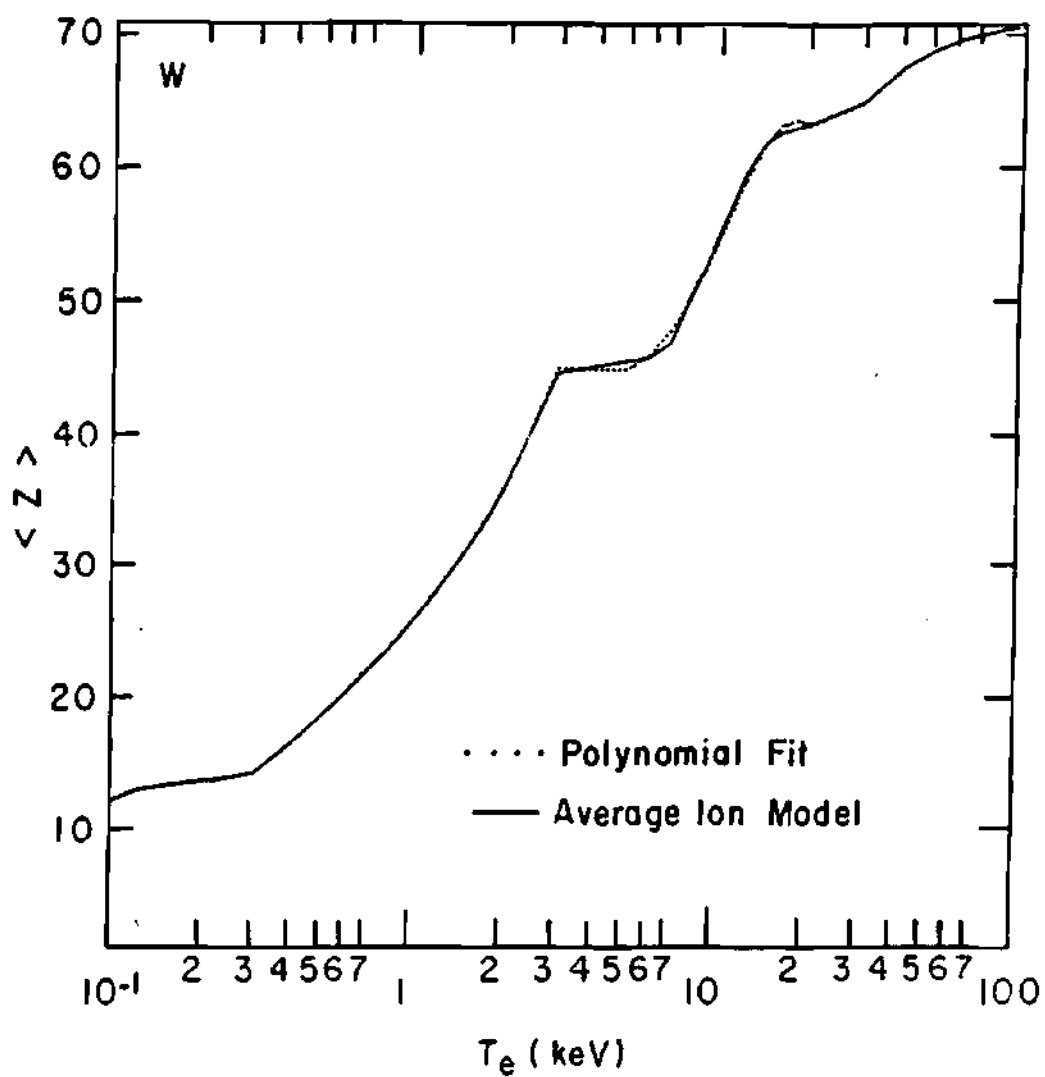


Figure 3.3.4 Coronal equilibrium charge state distribution of tungsten with electron temperature.

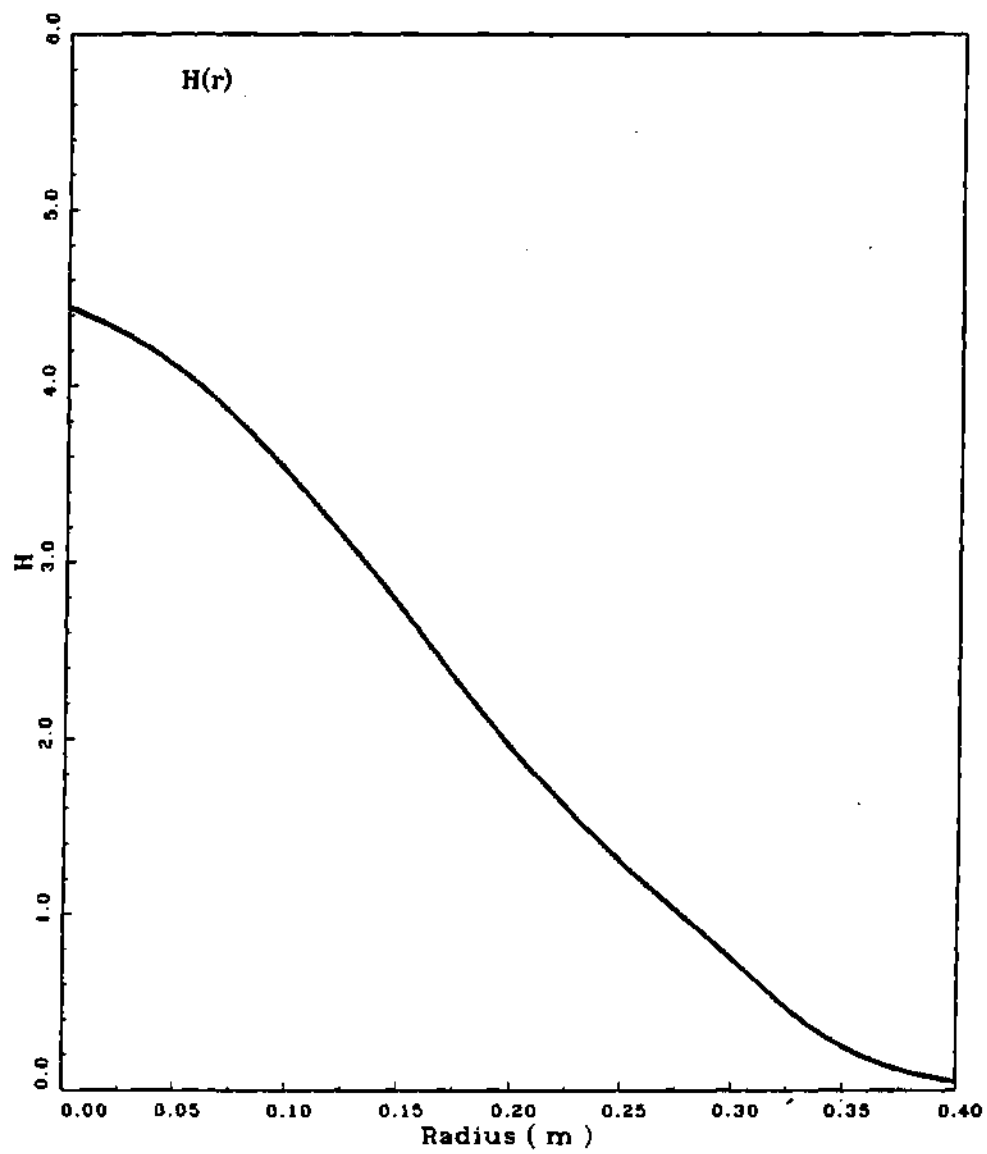


Figure 3.3.5 Beam deposition profile in PLT.

where  $R$  is major radius,  $Z$  is the effective ionic charge,  $e$  is electronic charge,  $B$  is magnetic field, and  $T_i$  is the ion temperature.

The ion temperature was not measured for these experiments. Since ion temperature is of fundamental importance in estimating drag frequency from Eq.(3.3.1), and since drag is an important element in the flow reversal theory [42,43], we have carefully estimated the ion temperature from the ion power balance equation [80]

$$\partial E_i / \partial t = P_b + P_{ei} + P_{iz} - P_{tc} - P_{pd} - P_{cx} \quad (3.3.2)$$

where  $E_i$  is ion energy, and the terms on the right side of Eq.(3.3.2) represent respectively the power components due to beam injection, electron-ion coupling, ionization of neutrals, thermal conduction, particle diffusion to the colder plasma edge, and electron charge-exchange with cold neutrals. The ion power balance studies [81,82] on PLT show that the neutral-beam-heated plasmas with a beam power of 2.1 MW, and a low plasma density of  $n_e \approx 2.3 \times 10^{13} \text{ cm}^{-3}$ , are characterized by a low ion-energy confinement time of  $\tau_{Ei} \approx 25$  ms as compared to  $\tau_{Ei} \approx 95$  ms for higher density plasmas with

$n_e \approx 3.5 \times 10^{13} \text{ cm}^{-3}$ . This difference in  $\tau_{ei}$  is due to the enhanced role of charge-exchange and convective losses at the high ion temperatures and steep temperature gradients which occur with beam heated, low density plasmas [81,82]. It is generally agreed [81-84] that in the case of neutral beam injection into high density ( $n_e \approx 3.5 \times 10^{13} \text{ cm}^{-3}$ ) plasmas, charge-exchange and convective losses in PLT are reduced and the ion-electron coupling becomes the dominant term in the ion energy flow. At the moderate plasma density of  $n_e \approx 3.0 \times 10^{13} \text{ cm}^{-3}$  considered in this analysis of the PLT data [25], and the beam power ranging from 0.430 to 0.585 MW for which the beam driven losses are assumed to be further reduced, charge-exchange and convective losses are assumed to be of no major consequence. Also, since the plasma ion density is assumed to be constant in time, Eq. (3.3.2) reduces to

$$(3/2)n_i \partial T_i / \partial t = P_b + P_{ei} - \nabla \cdot q_i \quad (3.3.3)$$

with

$$P_{ei} = (3m_e n_e / m_i \tau_{ei}) (T_e - T_i) \quad (3.3.4)$$

$$\tau_{ei} = 3\sqrt{m_e} T_e^{3/2} / (4\sqrt{2\pi} e^4 n_e \ln \lambda_e) \quad (3.3.5)$$

$$q_i(r) = -\chi_i n_i \partial T_i / \partial r \quad (3.3.6)$$

where  $m_i$ ,  $n_i$ ,  $T_i$ ,  $q_i$ , and  $\chi_i$  represent the plasma ion mass, density, temperature, conductive heat flux, and thermal diffusivity respectively;  $e$ ,  $m_e$ ,  $n_e$ ,  $T_e$ ,  $\tau_{ei}$ , and  $\lambda_e$  are electron charge, mass, density, temperature, characteristic scattering time, and coulomb logarithm, respectively.  $P_b$  represents neutral beam power. Thus Eq. (3.3.3) assumes the form

$$\begin{aligned} (3/2)n_i \partial T_i / \partial t = P_b + (3m_e n_e / m_i \tau_{ei})(T_e - T_i) \\ + \nabla \cdot (\chi_i n_i \partial T_i / \partial r) \end{aligned} \quad (3.3.7)$$

The ion energy loss due to neoclassical thermal conduction in PLT remains a small fraction of the total energy flow [82]. With the estimated [85] values of  $\chi_i$ , our calculations show that the conduction loss term was negligible as compared to electron-ion coupling term. Thus the conduction term was dropped from Eq.(3.3.7) and the resulting equation was solved numerically using the experimentally determined electron temperature and density. The computed ion temperature profiles for co- and counter-injection at 280 and 290 ms are shown in Figures (3.3.6) and (3.3.7), respectively. The volume averaged ion temperatures computed from these profiles were found to be

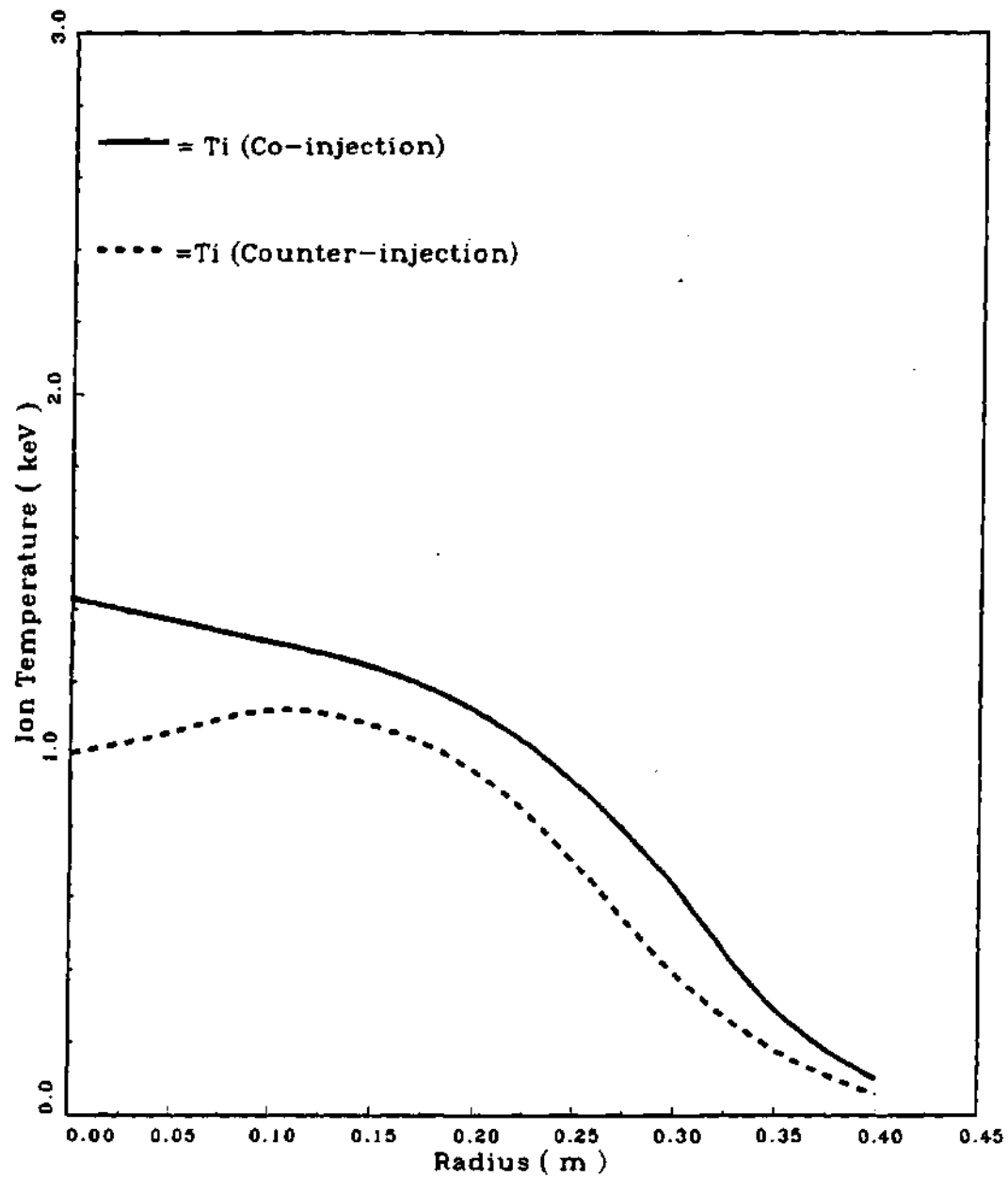


Figure 3.3.6. Calculated ion temperature profiles in PLT at 280 ms.

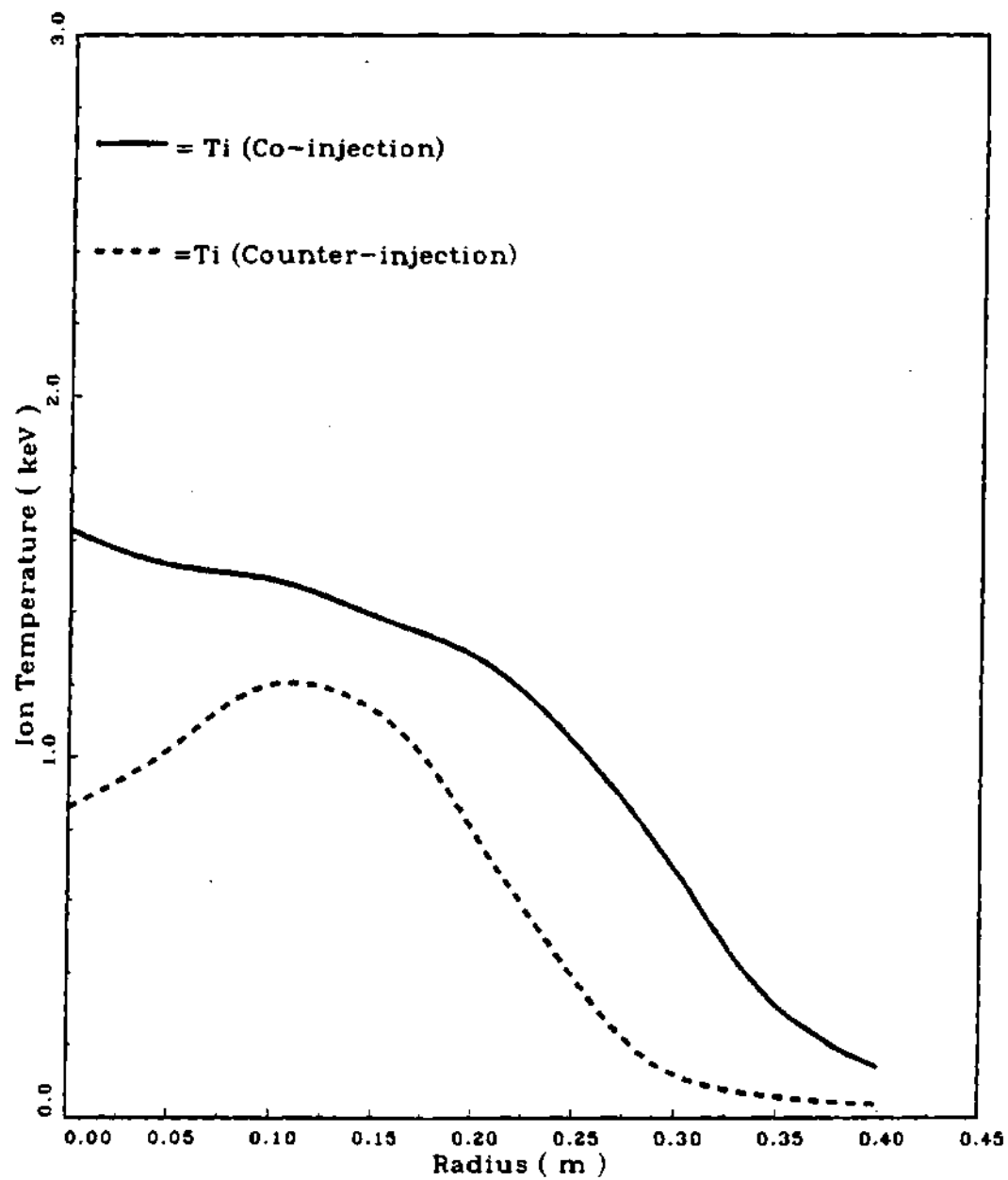


Figure 3.3.7 Calculated ion temperature profiles in PLT at 290 ms.



$$T_i^{CO}(t=280 \text{ ms})=0.833 \text{ keV}$$

$$T_i^{CN}(t=280 \text{ ms})=0.624 \text{ keV}$$

$$T_i^{CO}(t=290 \text{ ms})=0.936 \text{ keV}$$

$$T_i^{CN}(t=290 \text{ ms})=0.478 \text{ keV}$$

$$T_i^{OH}(t=250 \text{ ms})=0.740 \text{ keV}$$

With the average ion temperatures and the representative parameters as above, Eq. (5) yields the following values of the average drag frequency

$$\nu_d^{CO}(t=280 \text{ ms})=31. \text{ s}^{-1}$$

$$\nu_d^{CN}(t=280 \text{ ms})=23. \text{ s}^{-1}$$

$$\nu_d^{CO}(t=290 \text{ ms})=35. \text{ s}^{-1}$$

$$\nu_d^{CN}(t=290 \text{ ms})=17. \text{ s}^{-1}$$

$$\nu_d^{OH}(t=250 \text{ ms})=27. \text{ s}^{-1}$$

The above values of the drag frequency computed from the gyroviscous theory [54], and the representative data for PLT were then used in the steady-state model of the Stacey-Sigmar impurity flow reversal theory [42,43] to compute the impurity flux. The flux-surface averaged impurity fluxes for different

flux-surfaces are not coupled since flux is computed from the input data independent for each flux-surface. In addition to the plasma densities, temperatures, and impurity charge states, the impurity density is also an input parameter via the impurity concentration parameter  $a = z^2 n_z/n_i$ . The radial profiles of  $z^2$  were computed from the average ion model [77] in terms of the measured [74] electron temperature. Assuming  $n_i = n_e$ , the radial profiles of  $n_z/n_i$  were determined from measured [25] radial profiles of  $n_z/n_e$  (Figs. 3.2.4-5). The steady-state formulation computes impurity flux as a sum of several components as shown in Equation (2.4.1). With the experimental values of  $n_e$  (Figs. 3.3.1) and  $T_e$  (Figs. 3.3.2-3), the computed values of  $T_i$  (Figs. 3.3.6-7), and the other parameters of interest determined as shown above, the impurity flux as predicted by theory [42,43] and the experimental values [25] for ohmic-heating at 250 ms, and co- and counter-injection at 280 and 290 ms respectively, are shown in Figures (3.3.8) and (3.3.9).

In the time-dependent model, the impurity fluxes are coupled for various flux-surfaces. However, there is no coupling of the flux-surfaces for quantities such as plasma

densities, temperatures, and charge states which are input quantities at the initial and the final points in time, with the intermediate values obtained from interpolation. The initial and the boundary conditions determined from experiment [25] are shown in Figures (3.3.8) through (3.3.11). Starting with  $n_z(r, t=250)$  (Figs. 3.3.10-11) from experiment [25], the impurities were transported using the measured [25] values of  $\Gamma_z(r=20 \text{ cm}, t)$  (Figs. 3.3.12-13), the measured values [74] of electron density and temperature (Figs. 3.3.1-3), computed values of the ion temperature (Figs. 3.3.6-7), and other parameters determined as shown above. After starting with the initial and the boundary conditions, and the input data for the quantities of interest, the solution advances in time by computing the flows, electric potential, perturbations, impurity densities, and the flux-surface averaged impurity flux for each flux-surface. The drag was computed at each time level using the volume-average value of the ion temperature in Equation (2.6.2) of the gyroviscous theory [54]. The impurity flux computed from the time-dependent model, and the experimental values for co- and counter-injection are compared in Figures (3.3.14) and (3.3.15) respectively. The steady-state as well as the

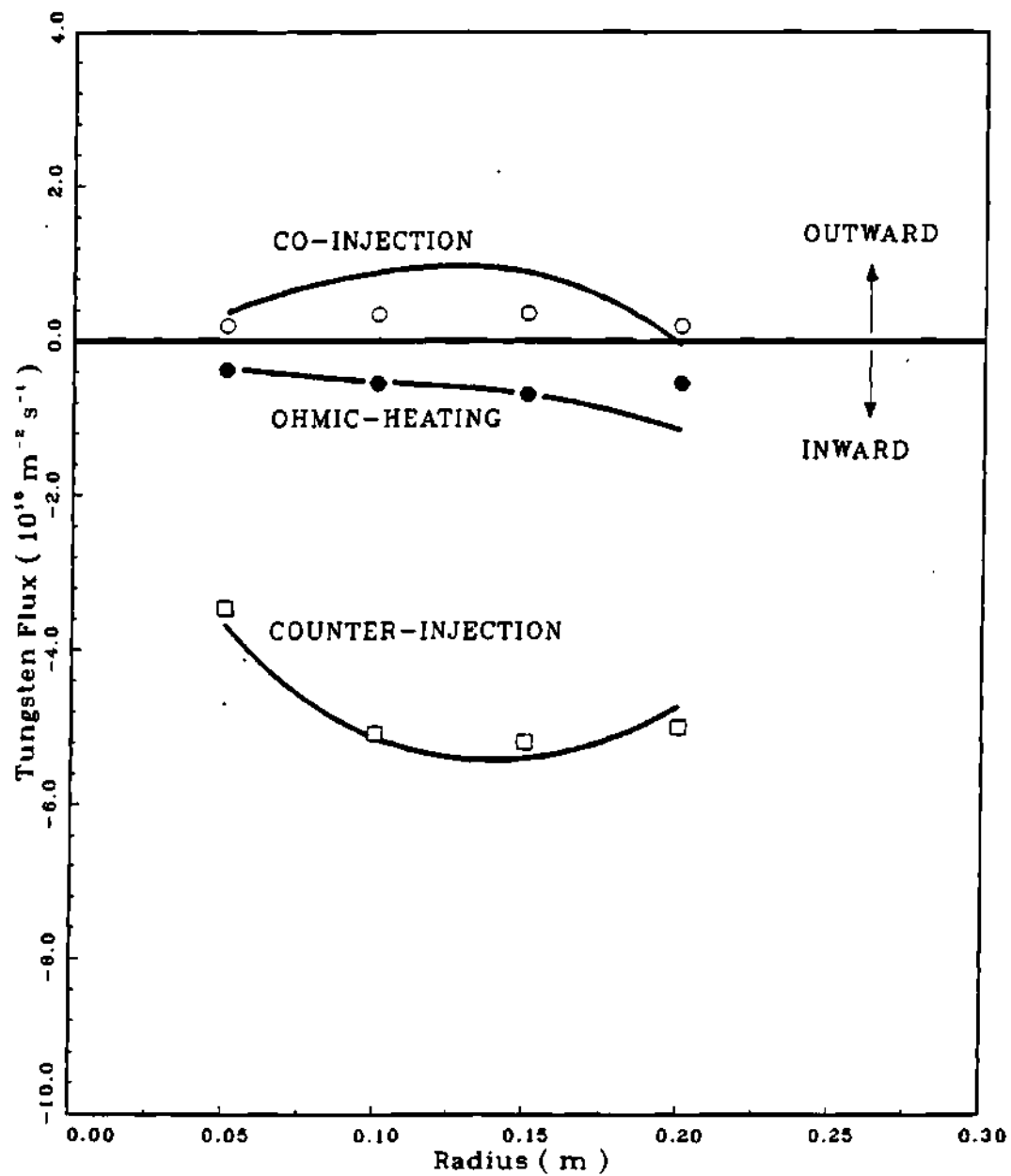


Figure 3.3.8 Steady-state theory (solid line) vs. experiment ( $\bullet$ ,  $\circ$ ,  $\square$ ) for PLT tungsten fluxes at 280 ms.

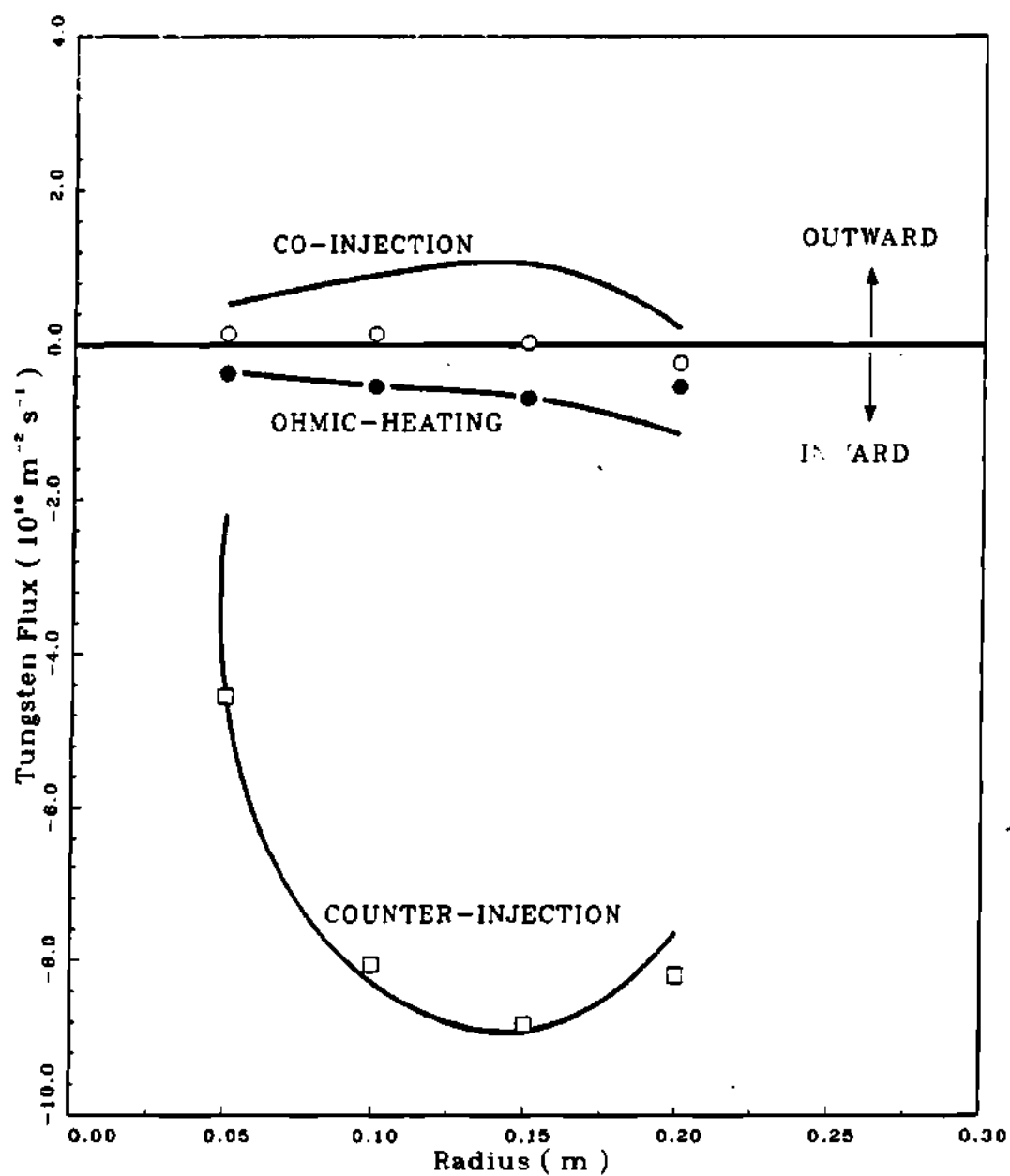


Figure 3.3.9 Steady-state theory (solid line) vs. experiment(●,○,□) for PLT tungsten fluxes at 290 ms.

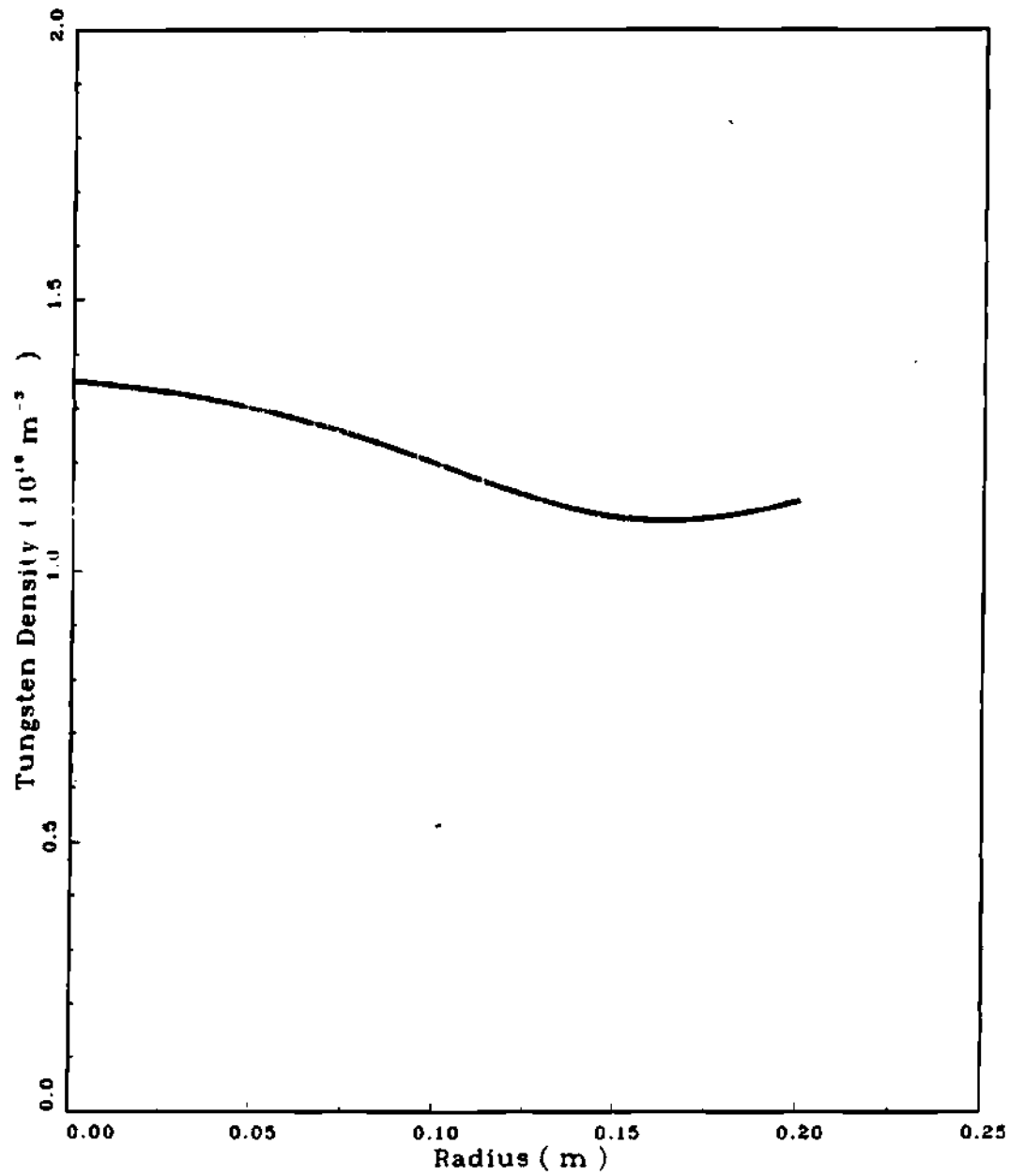


Figure 3.3.10 Measured impurity density profile in PLT at 250 ms in co-discharge.

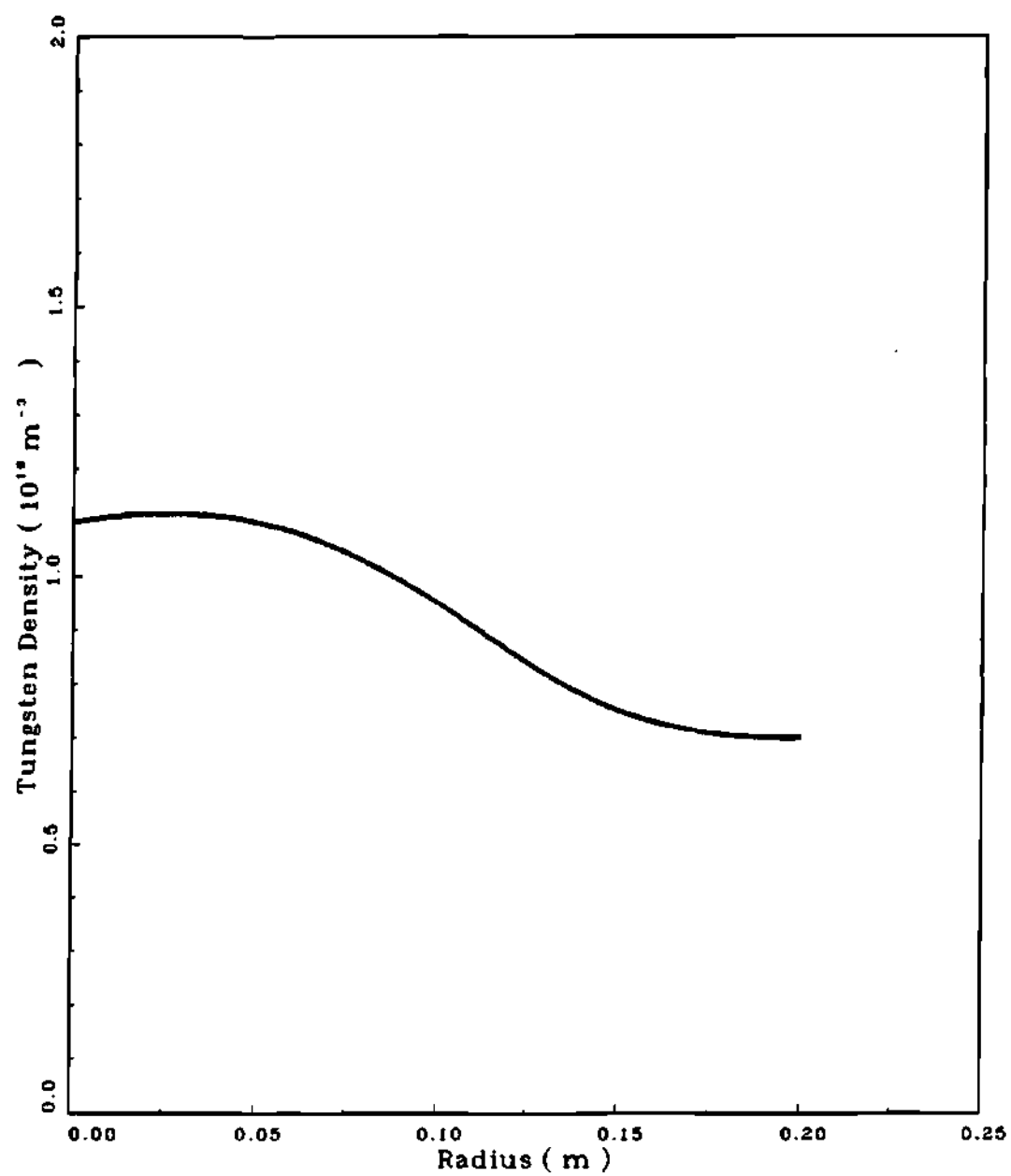


Figure 3.3.11 Measured impurity density profile in PLT at 250 ms in counter-discharge.

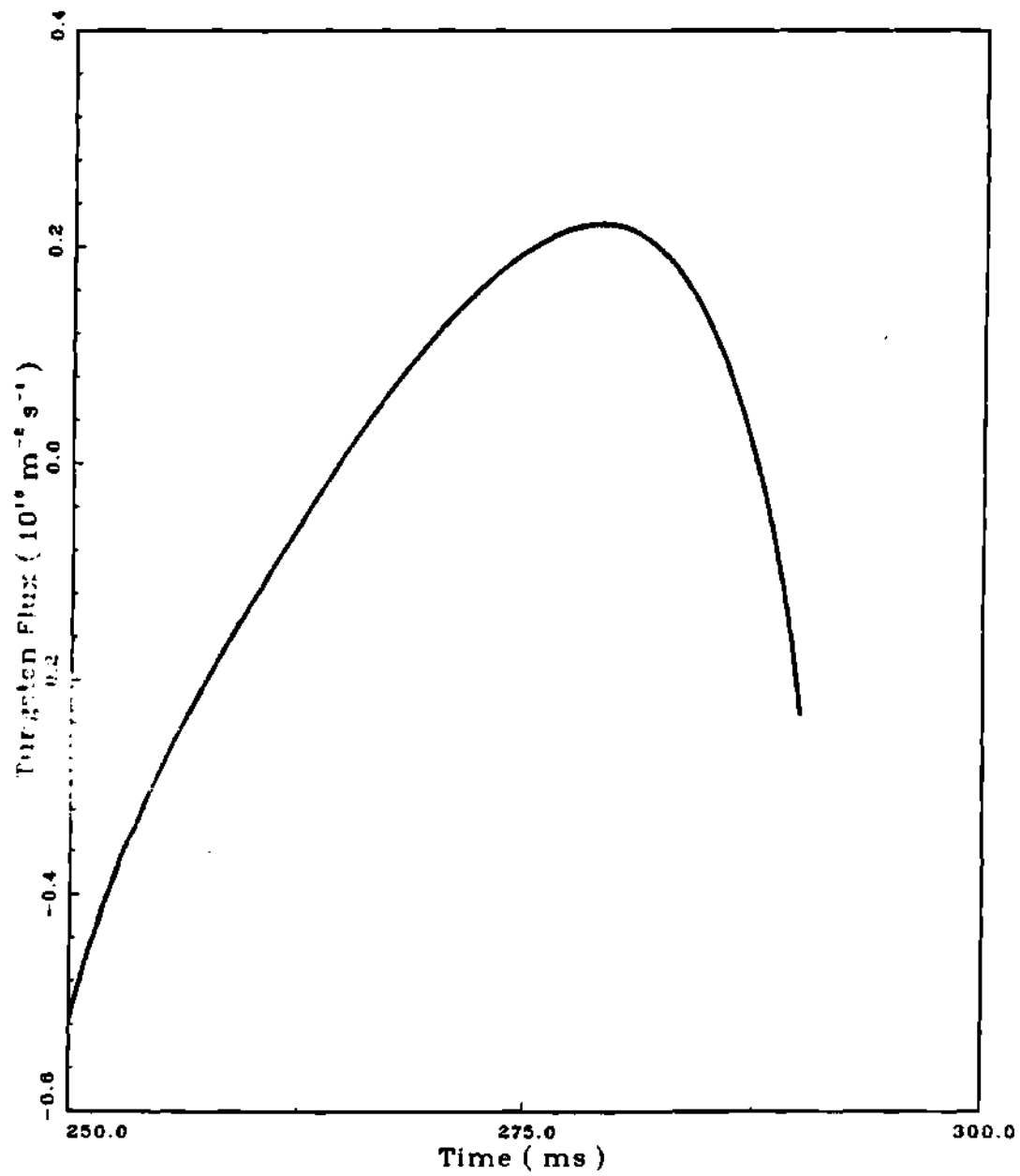


Figure 3.3.12 Measured impurity flux history in PLT at 20 cm with co-injection.



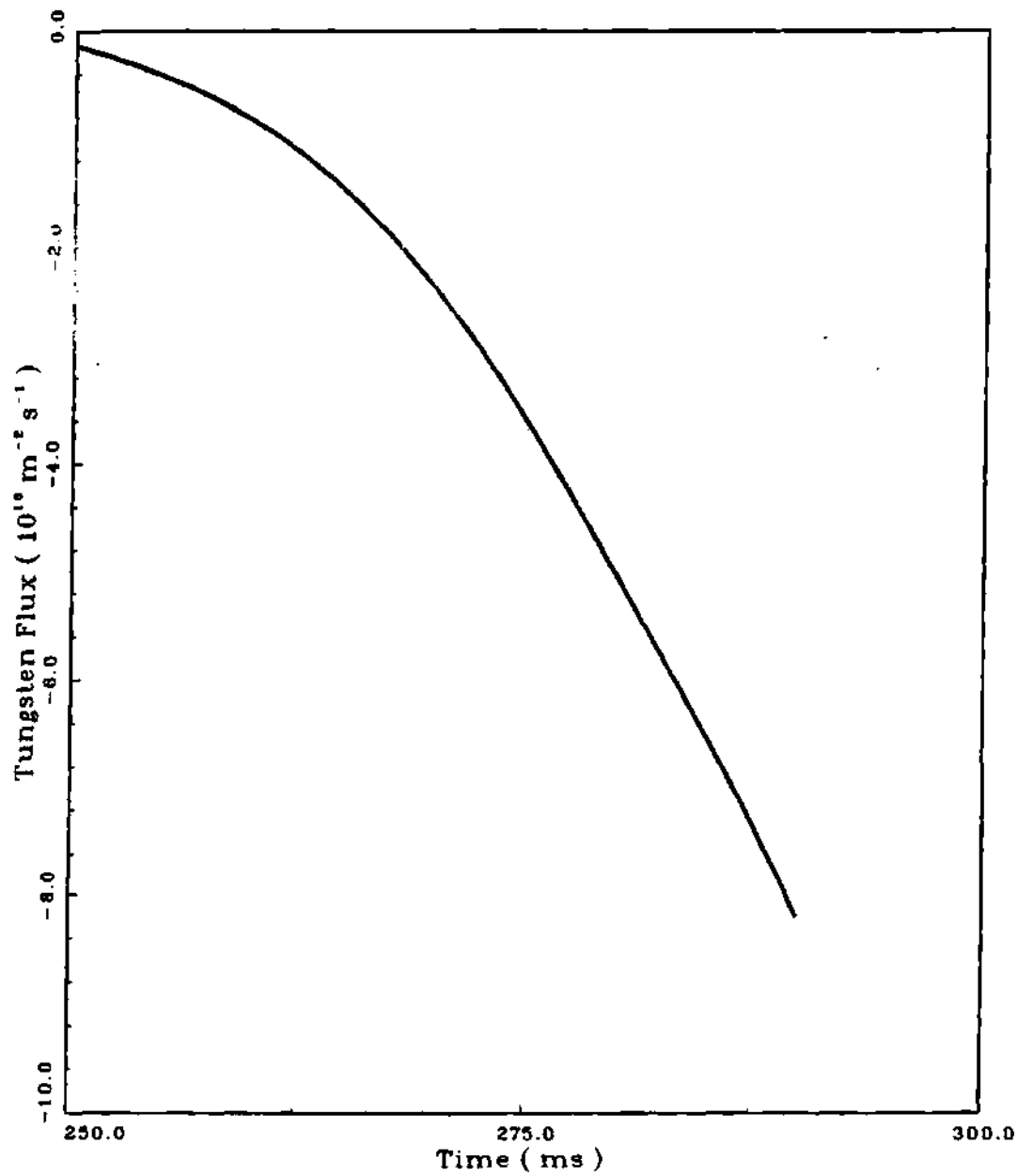


Figure 3.3.13 Measured impurity flux history in PLT at 20 cm with counter-injection.

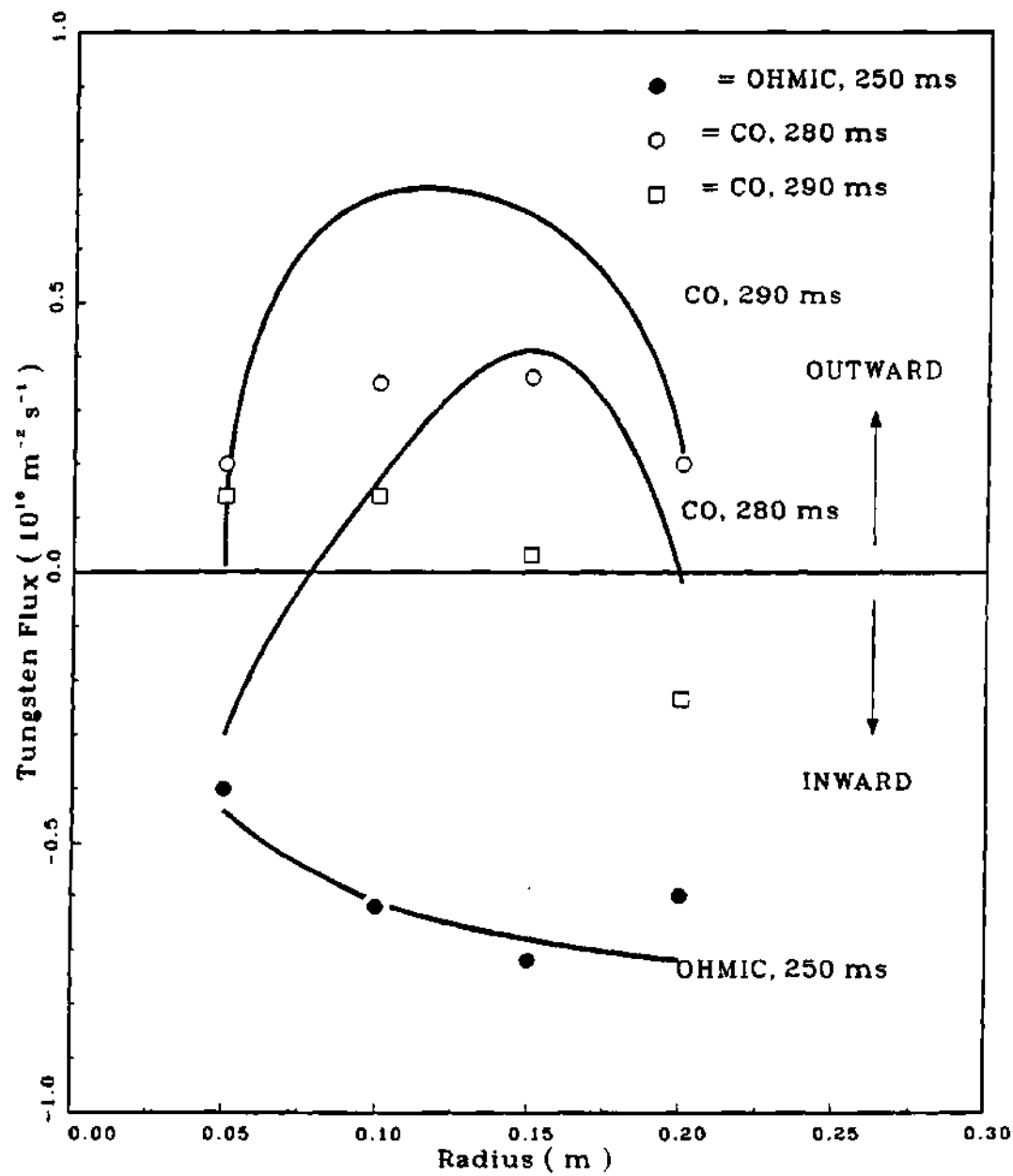


Figure 3.3.14 Time-dependent theory (solid line) vs. experiment(●,○,□) for PLT tungsten fluxes with 585 kW co-injection beginning at 250 ms.

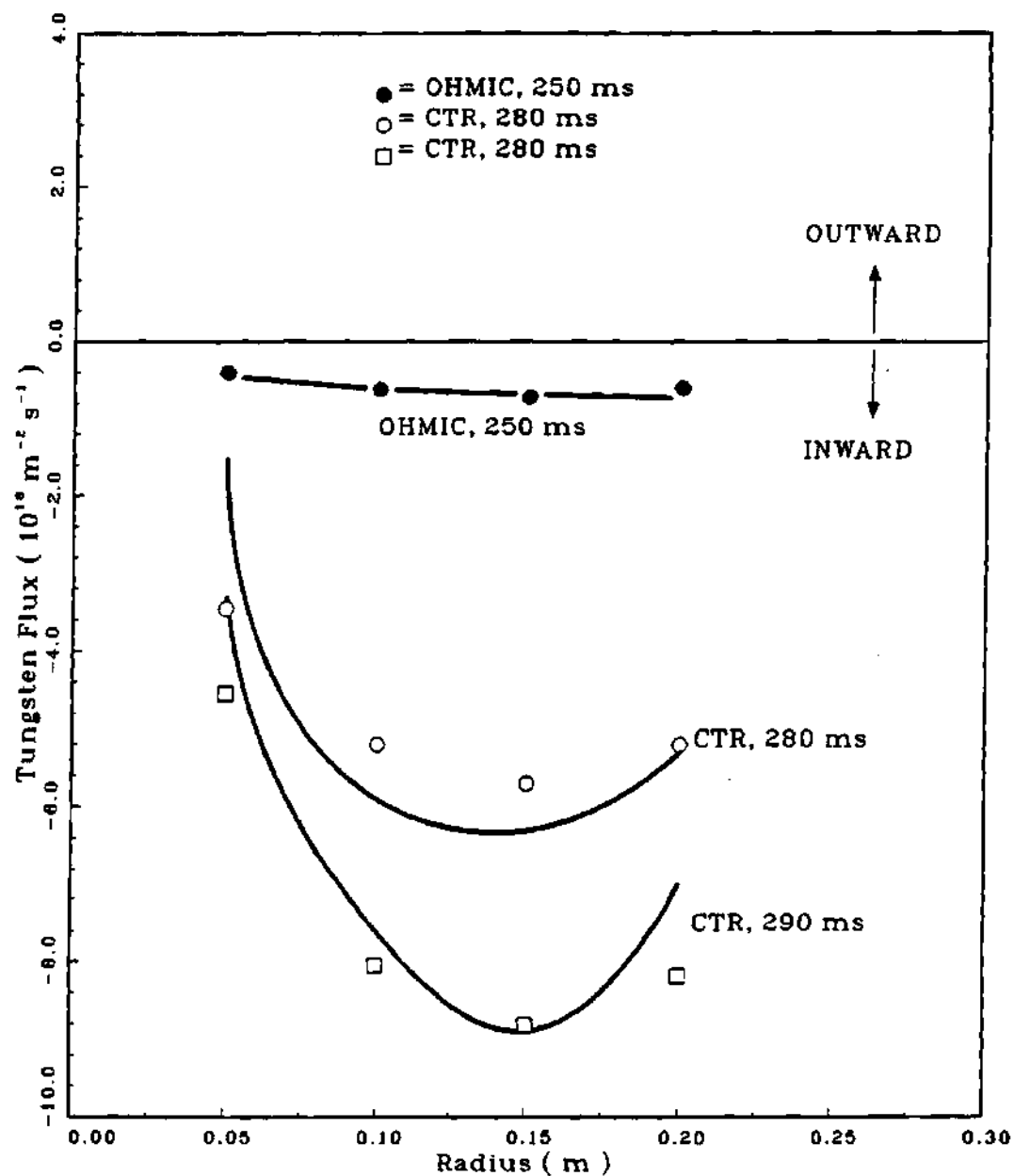


Figure 3.3.15 Time-dependent theory (solid line) vs. experiment(●,○,□) for PLT tungsten fluxes with 430 kW counter-injection beginning at 250 ms.

time-dependent versions of the impurity flow reversal theory [42,43] model experimental data remarkably well. Both theory and experiment show an inward flow of impurities with ohmic heating and counter-injection, but the inward flow of impurities with counter-injection is greatly enhanced. On the contrary, co-injection leads to a net outward flow of impurities.

The agreement of the impurity flow reversal theory [42,43] with experiment also gives confidence in gyroviscous theory [54] of momentum confinement since the latter was used to compute external drag needed in the flow reversal theory. The fact that the computed central toroidal velocity ( $5.0 \times 10^4$  m/s) matches the measured [29] value ( $4.5 \times 10^4$  m/s), further strengthens the validity of using gyroviscous theory to predict external drag in the impurity flow reversal theory.

### 3.4 Summary

The impurity flow reversal theory was applied to analyze the effects of neutral beam injection on transport of intrinsic tungsten impurity in the PLT tokamak.

The neutral beam injection took place from 250 to 350 ms in deuterium discharge, with 585 kW of co and 430 kW of counter-injected beam power. The experimental results show that radiated power, impurity density, and impurity flux profiles are very sensitive to neutral beam direction. The co-injection caused only 30% increase in the central power loss as compared to a factor of six increase in case of counter-injection. The tungsten density profiles were generally flat in case of co-injection, whereas counter-injection led to sharp peaking with a factor of six increase. The tungsten density fraction  $n_W/n_e$  for co-injection was quite flat, but counter-injection caused a factor of four increase near center. The tungsten flux generally changed from inward to outward direction with co-injection. However, with counter-injection, the tungsten flux was always directed

inward, increased substantially with time, and was an order of magnitude greater than the flux during co-injection. The observation that co- plus counter-discharges were similar to co-discharges instead of to counter-discharges, indicated that impurity flow reversal was indeed due to the effects of neutral beam injection on the transport properties irrespective of the differences in the edge source rate of impurities. Thus the experimental observations indicate that intrinsic tungsten transport in the PLT tokamak is very sensitive to the direction of neutral beam injection.

The steady-state as well as the time-dependent formulations of the flow reversal theory were applied to model experimental conditions using the measured quantities as far as possible. With the measured values of the electron densities and temperatures, and other data inferred from experimental conditions, the steady-state theory was seen to model measured impurity fluxes quite well.

For the time-dependent calculations, the solution started with the initial condition from experiment, and transported the impurities using the measured values of the incident

impurity flux, measured values of electron densities and temperatures, and the values of other parameters inferred from experimental conditions. The theory generally shows a good agreement with experiment.

Thus, in conclusion, the theory was seen to model experimental data quite well. Both theory and experiment show that counter-injection causes a central accumulation of impurities, whereas co-injection can drive impurities outward. Thus, an effective impurity control is possible with neutral beam co-injection in tokamak plasmas.

CHAPTER IV

ANALYSIS OF

INTRINSIC IRON TRANSPORT IN ISX-B

4.1 Introduction

The Impurity Study Experiment (ISX-B) at the Oak Ridge National Laboratory (ORNL) was designed for the study of high-beta plasmas [86]. The experimental program has concentrated on the study of impurity transport with neutral beam injection. The auxiliary heating was initially supplied by two neutral beam lines. A later upgrade increased the number of beam lines to three. The third beam line was directed opposite to the first two, allowing the investigation of momentum effects in terms of co- versus counter-injection. The machine had a rectangular cross-section vacuum vessel, but a poloidal field system allowed elliptic, D-shaped, and circular configurations of plasmas to be investigated. A cross-section [86] of the machine is shown in Figure (4.1.1). A plan view [86] is shown in Figure (4.1.2) with the main diagnostic and auxiliary apparatus labeled. The ISX-B plasmas



FED/VU 78-263R10

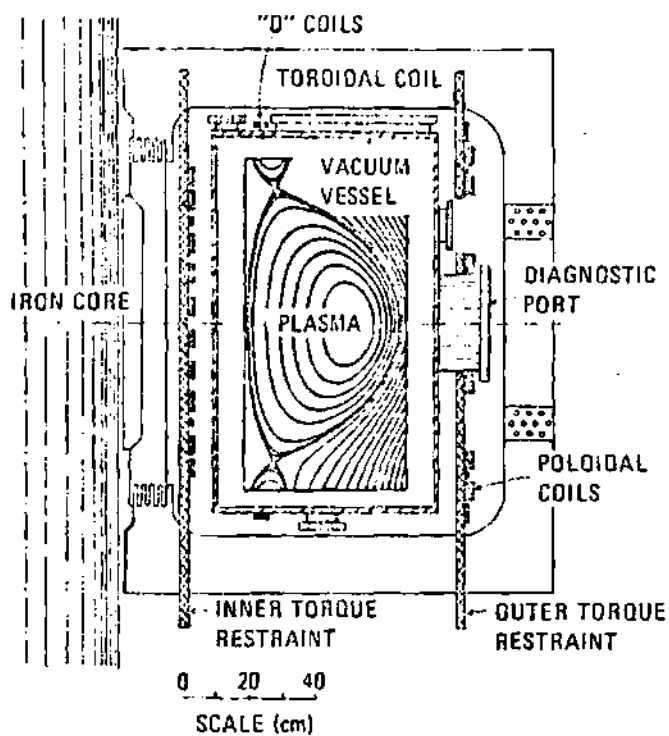


Figure 4.1.1 Cross section of the ISX-B machine.

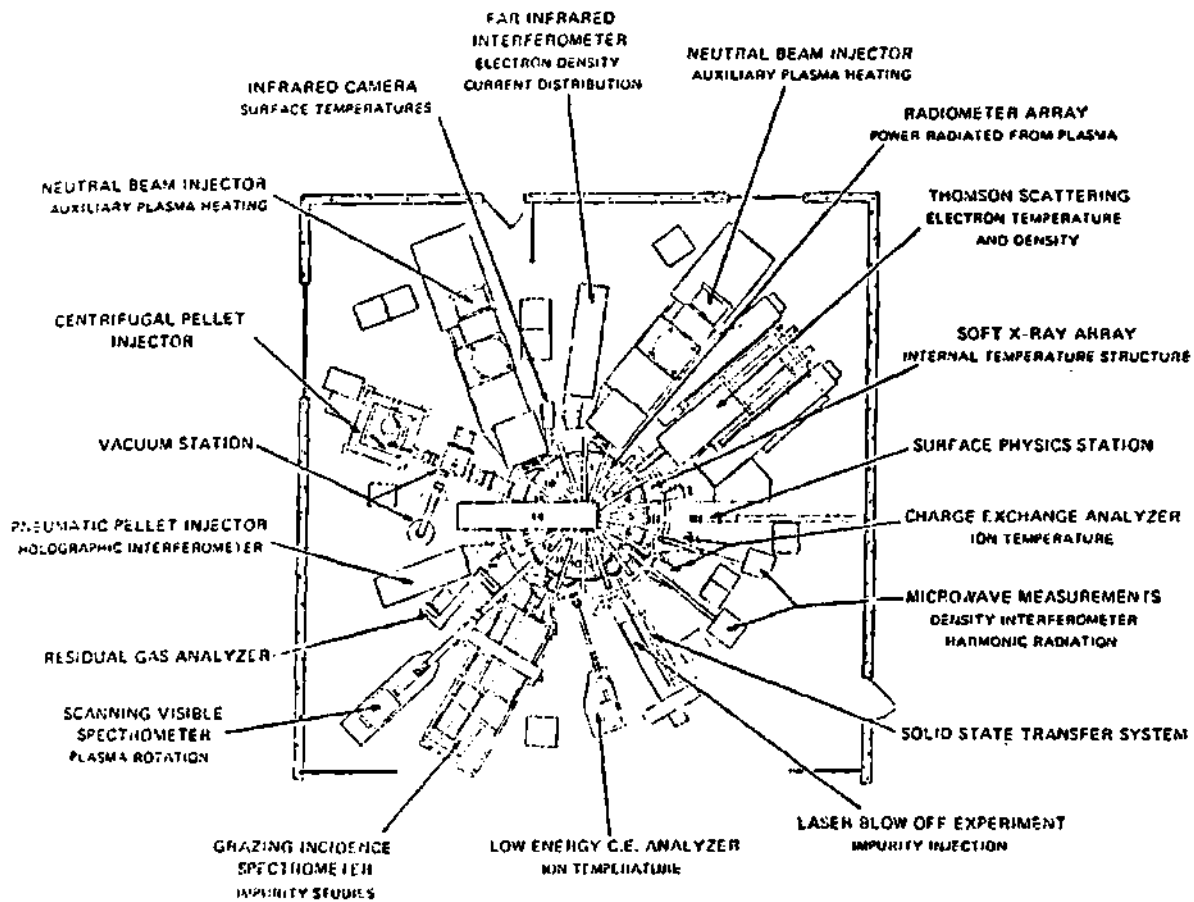


Figure 4.1.2 Plan view of ISX-B tokamak with main diagnostic and auxiliary apparatus.

were typically operated with a major and minor radii of 93 and 27 cm respectively in the ohmically heated discharges. With beam-injection, the major radius of the magnetic axis shifted by as much as 2 cm [32]. The experiments were generally performed using a vertical stainless steel bar for the inner limiter and a mushroom shaped outer limiter constructed from stainless steel or from TiC-coated graphite. The vacuum vessel was not gettered until February, 1981, but thereafter, titanium gettering was regularly employed to condition the walls. The reference parameters of interest for ISX-B are shown in Table (4.1.1).

The ISX-B impurity transport experiments are described in section 4.2. These experiments generally report emission rates from impurities. An understanding of the underlying atomic physics is essential to theoretically model such experiments. The relevant atomic physics issues are reviewed in section (4.3). The data base for ISX-B is generally based on the data analysis code ZORNOC [87]. A brief description of the code is given in Section (4.4). The analysis of the ISX-B experiments with intrinsic iron impurity for co- versus counter-injection is carried out in section 4.5. The

Table 4.1.1 ISX-B data with intrinsic iron

---

Major radius (m)	0.93
Minor radius (m)	0.27
$Z_{\text{eff}}$	2.5
Toroidal magnetic field (T)	0.93
Safety factor $q(0)$	1.0
Safety factor $q(a)$	4.0
Neutral beam power (MW)	1.2 - 2.4
Neutral beam energy (keV)	32.0
Model impurity: Iron	
Plasma type	: $D^+$
Beam type	: $H^0$
Beam tangency radius (m)	0.75
Beam width (m)	0.20
Beam energy components (keV)	32,16,10.67

---

experiments with two-beam co-injection with intrinsic iron impurity are analyzed in section 4.6.

#### 4.2 Impurity Transport Experiments

The ISX-B experiments [26,27,32,86-91] provided a wealth of information about impurity transport in tokamak plasmas with both the intrinsic and the injected impurities. The characteristics of the intrinsic impurity behavior in ohmically heated discharges for both hydrogen and deuterium discharges are described in Reference [88], and the transport of argon as a test impurity is illustrated in Reference [86]. The confinement of laser-ablated impurities have been reported in References [32,88]. The spectral observations in an ohmic discharge show that under basically the same operating conditions, impurities accumulate in the central region throughout the deuterium discharges but not during hydrogen discharges [32,88]. The central iron concentration in deuterium discharge is at least five times higher relative to the peripheral concentration than it is in hydrogen discharge [32]. The continual growth of the soft x-ray signal in deuterium discharge supports spectral indications of

intrinsic impurity accumulations except when the MHD signals dominate [32]. The laser-ablated silicon introduced into ohmic discharge shows a confinement time of 70 ms [88]. The confinement time for laser-ablated titanium appears to be much greater than 100 ms [32]. Thus the impurities that have reservoirs in the edge of the plasmas continually accumulate during the quasi-steady part of the discharge; those that are introduced in toto in the interior of the discharge by laser-ablation appear to have characteristic confinement time much greater than 100 ms [32]. The impurity accumulation and long confinement times are characteristic of ohmically heated deuterium discharges, but not of hydrogen discharges for which anomalous transport mechanisms are supposed to be dominant [32,88].

The impurity confinement studies with both co- and counter-injection using intrinsic as well as test impurities such as argon and titanium show that the results are very sensitive to beam direction. The emissions from intrinsic titanium show that after an initial rise following the onset of co-injection, the radiated power remains almost constant rather than increasing as it does during ohmic heating.

Usually 10-20% of the input power is radiated during co-injection and spatial profiles show that most of it comes from the periphery. The radiated power does not reach a steady level during counter-injection; it increases much more rapidly than it does in ohmically heated discharges, and the spatial profiles indicate that a strong peak occurs at the magnetic axis [27,32]. The soft x-ray signals, which reflect the central impurity, have temporal developments similar to the radiated power. They increase initially during co-injection because of plasma heating and impurity influx, but then maintain a relatively constant average value throughout the remainder of the shot. During counter-injection, however, the signals rise rapidly until about 5 ms before a disruption occurs, then they begin to decrease [32]. When laser-ablated titanium is introduced into counter-injected discharges, its presence becomes completely obscured late in time by the build-up of intrinsic titanium. This build-up occurs preferentially in the interior of the plasma as evidenced by the rapid increases appearing first in the highest ionization stages. If the strong increases in the signals were the result of additional influxes, they would appear initially in the lower stages located near the edge of

the plasmas and later show up in the higher stages as the impurities diffuse inward [32,88]. Thus the strong rise of the interior emissions result from accumulation. This accumulation becomes so severe that the plasma disrupts and hence cools rapidly from radiation losses. But seeding co-injection discharges with laser-ablated titanium shows that the characteristic confinement time for the highest ionization stages is only 10-20 ms, in contrast to times of well over 100 ms that were deduced from ohmically heated discharges. Thus the impurities do not accumulate during co-injection and the confinement is similar to that of the main plasma ions [32].

The radiation from intrinsic oxygen [26,32] follows the same pattern as that of the metallic impurities. The radiation from the most interior, fully-ionized ion, O VIII, is observed by charge-exchange recombination spectroscopy. The spectrometer used for these measurements detects the emitted radiation originating from within 6 cm of the plasma center. The beam pulse lasts from 100 ms to the end of the shot during co-injection, and the signal is almost constant throughout this period, indicating a quasi-steady level of oxygen.



However, following the onset of counter-injection at 100 ms, the  $O^{8+}$  density rises rapidly to five times the co-injection level until a disruption occurs at about 180 ms; the beam is turned off at 185 ms. Thus the central oxygen content grows rapidly during counter-injection leading to a disruption while co-injection maintains a quasi-steady level of oxygen.

The study of argon as a test impurity is particularly useful in confirming that the differences between co- and counter-injection depend upon transport and not upon plasma/material interactions since these processes do not appreciably affect the rare-gas ions [32]. Some experimental studies [32,89,90] used argon as a test impurity in short 4- to 7-ms bursts at 90 ms after the discharge began. In the ohmically heated case, the intensity of Ar XVI continually builds up until the shot terminates, while the peripheral radiation slowly decreases, thus showing that the argon accumulates in the interior while it gets depleted from the scrape-off region [92]. The argon behavior in the two injection cases is distinctly different from each other and from that of the ohmically heated plasma. No accumulation is observed during co-injection. Reference [89] reports that the

argon from the exterior of the plasma is halted or reversed during co-injection. However, during counter-injection, the accumulation of argon is so rapid that the plasma disrupts within 30 ms, with an emissivity of about  $1.4 \text{ W/cm}^3$  [27], thus causing an extreme cooling in the center [86].

The temporal evolution of emission rates for iron ions was analyzed in References [26,32] to compare the effect of co-versus counter-injection. For the co-injection case, the iron concentration of all ionization states rose for about 30 ms after the beams were turned on. This interval was followed by a period of relatively constant radiation until the discharge terminated at 200 ms. In contrast, the emission from Fe XIX continues to rise very rapidly for about 40 ms following counter-injection, and then starts to drop after 165 ms as a result of the impurity accumulation and rapid radiation cooling. The lower ionization stages attain peak intensities at successively later times and a disruption occurs at 174 ms. The sequential peaking of the emission from the highest to the lowest ionization stages reflects the rapid cooling of the plasma after 160 ms. When Fe XVI and Fe XVIII signals are normalized to Fe IX emission, they are 18-50 times greater for

counter-injection as compared to those for co-injection. The experiments [32] with intrinsic iron using two-beam co-injection strongly support the above conclusions for co-injected discharges.

Thus, impurity transport in ISX-B plasmas differs distinctly among ohmic, co-injection, and counter-injection cases in deuterium discharges. The ohmic heated discharge is characterized by accumulation of impurities with relatively long confinement times. During counter-injection discharges, the accumulation is much more rapid than in ohmically heated discharges leading to a disruption and extreme cooling of the plasma center. The co-injection counter-acts the accumulation trend and causes depletion of central impurities with a suitable power level of the injected beam.

#### 4.3 Atomic Physics Issues

The analysis of impurity concentrations and transport from spectral data in thermonuclear devices requires a knowledge of excitation, ionization and recombination rate coefficients of highly stripped ions [26]. Since measured data for the atomic

rate coefficients are very limited, theoretical formulations are generally used to evaluate the coefficients. Depending on the model used, the evaluated rate coefficients may not be identical in the impurity transport studies that use such models. The atomic physics data of interest in this study were based on the computer code from ORNL [92]. The code uses the general formulation described by Breton, et al. [93] to compute the ionization rate coefficient  $S_z$ , the recombination rate coefficients  $a_z$ , and the excitation rate coefficients  $X_z$  for an impurity of charge  $z$ .

The time evolution of the density  $n_j(r,t)$  of the ground state of an ion of charge  $j$  is given by a set of coupled rate equations [94,95]

$$\partial n_j / \partial t = n_e (n_{j-1} S_{j-1} + n_{j+1} a_{j+1} - n_j S_j - n_j a_j) \quad (4.3.1)$$

where  $n_e(r,t)$  is the electron density. It is important to note that the rate coefficients in Equation (4.3.1) must apply to the ground state populations, otherwise, we would have one equation for each excited state that would enormously increase the number of equations to be solved. Thus, for a given

element, there are  $(z+1)$  coupled equations, and  $j$  ranges in integral steps from  $j=1$  (atoms) to  $j=z+1$  (fully ionized ion, i.e., the bare nucleus).

The ionization rate coefficients  $S_j(T_e)$  for the ion of charge  $j$  is the moment of the product of the ionization cross-section  $\sigma_i(v)$  with the relative velocity  $v$  over the assumed Maxwellian electron distribution  $f_{e0}(T_e)$ ; that is

$$S_j(T_e) = (1/n_e) \int d^3v \sigma_i(v) v f_{e0}(T_e) \quad (4.3.2)$$

The recombination rate coefficient  $\alpha_j(T_e)$  is a similar moment of the recombination cross-section  $\sigma_r(v)$ . The ionization process generally includes direct electron impact ionization, and auto-ionization. The recombination of an ion typically includes radiative, dielectronic, and charge-exchange rates.

For tokamak plasmas, the rather detailed calculations may not be necessary, and the simple coronal model described in Section (3.2) may generally be sufficient [93]. The coronal model assumes that excitation and ionization are due to collisions in the ground state, and de-excitation is only radiative. Assuming steady-state coronal equilibrium,

Equation (4.3.1) reduces to

$$n_j S_j = n_{j+1} a_{j+1} \quad (4.3.3)$$

The resulting balance between ionization and recombination rates is primarily a function of the electron temperature  $T_e$ , with the only density dependence occurring via the dielectronic recombination rate [75].

The ionization and recombination rate coefficients are used in Equation (4.3.3) to determine the coronal equilibrium fractional abundance, or the charge state fraction [75,93]

$$f_j = n_j / \sum_j n_j = n_j / n_z \quad (4.3.4)$$

where  $j=1, \dots, z+1$ .

The charge-state fraction is needed to determine the radiation loss from a given charge state  $j$ . The dominant radiation loss is generally the line radiation due to de-excitation of an excited state. The local emission rate  $\epsilon$  (photons/cm<sup>3</sup>-s) due to line radiation from a given charge-state  $j$  may be written as

$$\epsilon(r) = n_e(r) n_j(r) X_{j,k} \quad (4.3.5)$$

where  $n_e(r)$  is the local electron density,  $n_j(r)$  is the local

density of the impurity charge-state  $j$ , and  $X_{j,k}(T_e)$  is the electron collisional excitation rate for the  $k$ th energy level. Here,  $n_j(r)$  is determined from Equation (4.3.4), given the local impurity density  $n_z$ . The power density (eV/cm<sup>3</sup>-s) due to line radiation is given by

$$P_L = n_e(r) \sum_j \sum_k n_j(r) X_{j,k}(T_e) E_{j,k} \quad (4.3.6)$$

where  $E_{j,k}$  is the transition energy in eV between the  $k$ th energy level and the ground state of the  $j$ th charge-state.

The volume-integrated power (eV/s) is given by

$$P = 4\pi^2 R f_0^a n_e(r) n_j(r) E_{j,k}(T_e) X_{j,k}(T_e) r \, dr \quad (4.3.7)$$

where  $R$  is the major radius, and  $a$  is the minor radius of the torus.

It may be noted that Equation (4.3.1) does not account for sources and sinks which may arise from particle transport, or from external sources such as wall sources of neutrals. The particle transport can be accounted for in a simple manner by adding a term  $(-n_j/\tau_j)$  to Equation (4.3.1), where  $\tau_j(r,t)$  is an appropriate decay time [75,95]. If  $\tau_j$  is positive the term represents a sink if negative, a source. However, neither a

term of this type nor the external source was included in Equation (4.3.1) of the atomic physics model [92] because of its anticipated use with the impurity transport theory [42,43].

The choice of the rate coefficients is generally problem-dependent. The rate coefficients may be well known from experiment for low atomic number elements. For elements with intermediate and high atomic number, the experimental data may be scant, or simply unavailable, making it necessary to use semi-empirical, or model calculations to determine the rate coefficients.

#### 4.4 ISX-B Data Analysis Code ZORNOC

The ISX-B data used in this study is generally based on data stored in files produced by the ZORNOC [87] code from the basic experimental measurements. The ZORNOC [87] is a static 1 1/2-D tokamak data analysis code. The code starts with the gross plasma parameters, the Thomson scattering profiles for electron temperature and density, and the central value of the charge exchange ion temperature. The poloidal dependence of



the plasma variables is ignored by assuming that quantities such as densities and temperatures are constant on given poloidal flux surfaces, or by taking flux surface averages for quantities such as the plasma current and the poloidal magnetic field that are not symmetric poloidally.

The MHD equilibrium flux surface geometry is determined in ZORNOC by solving the Grad-Shafranov equation based on: (1) the shape of the outermost flux surface, deduced from the magnetic loop probes (2) a pressure profile, deduced by means of Thomson scattering data for electrons, charge exchange data for ions, and a Fokker-Planck model for fast ions and (3) a safety factor profile, determined from the experimental data using a simple model based on a constant  $Z_{\text{eff}}$ . The initial guess for the shape of the flux surface is based on the shape of the outermost surface deduced from the magnetic loop probes. The flux surface shapes are determined consequently from the poloidal magnetic flux function contours determined from the plasma equilibrium considerations. The ion temperature profiles are assumed to have the same shape as that of the electron temperature profile, with the central ion temperature obtained directly from the charge exchange data.

The code uses the average ion model [77] based on a single impurity species coronal model to take into account the  $Z_{\text{eff}}$  deduced from conductivity. The code then calculates various confinement parameters such as average values of densities and temperatures. The code solves the electron power balance equation for ohmically heated and beam-heated discharges. The beam deposition profile is determined as a function of the poloidal flux function using the Monte Carlo code NFREYA [96]. However, the slowing down of the fast ions is studied by moments method based on an approximate analytical solution of the Fokker-Planck equation.

#### 4.5 Analysis of Co- versus Counter-discharges

Isler et al., [26] have documented extensively the sensitivity of the intrinsic iron impurity transport to the direction of neutral beam injection in the ISX-B tokamak. The iron spectral lines studied are shown in Table (4.5.1). The neutral beam injection took place from 80 - 240 ms for co-injection and from 125 - 240 ms for counter-injection, with 1 MW neutral beam power in each case. The measured emission profiles for co- and counter-injection (Figs. 4.5.1-2) show

Table 4.5.1 Iron spectral lines

Ion	Wavelength (Å)	Ground state
		configuration
Fe IX	171	$1s^2 2s^2 2p^6 3s^2 3p^6$
Fe XV	284	$1s^2 2s^2 2p^6 3s^2$
Fe XVI	361	$1s^2 2s^2 2p^6 3s$
Fe XVIII	94	$1s^2 2s^2 2p^5$
Fe XIX	108	$1s^2 2s^2 2p^4$
XIX	423	$3s^2-3s3p$

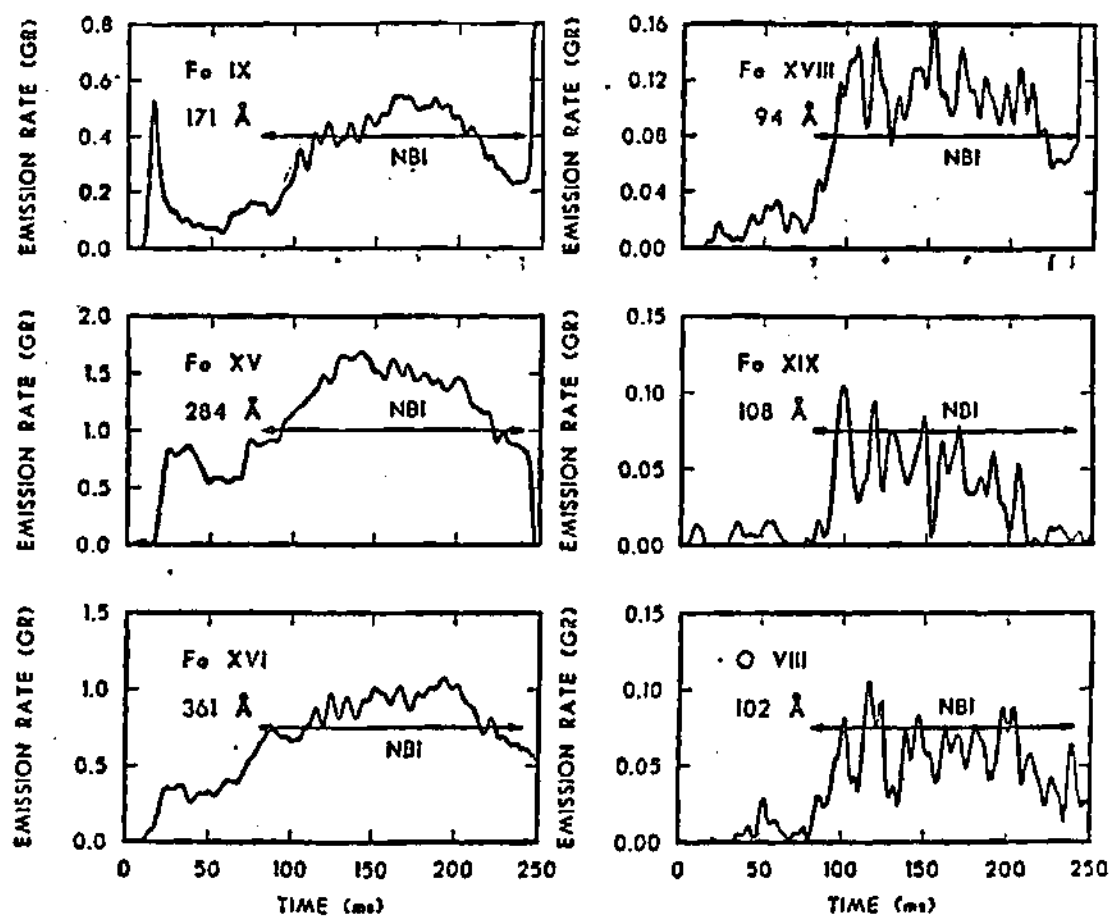


Figure 4.5.1 Experimental time variation of spectral emissions of iron in ISX-B with 1 MW co-injection.

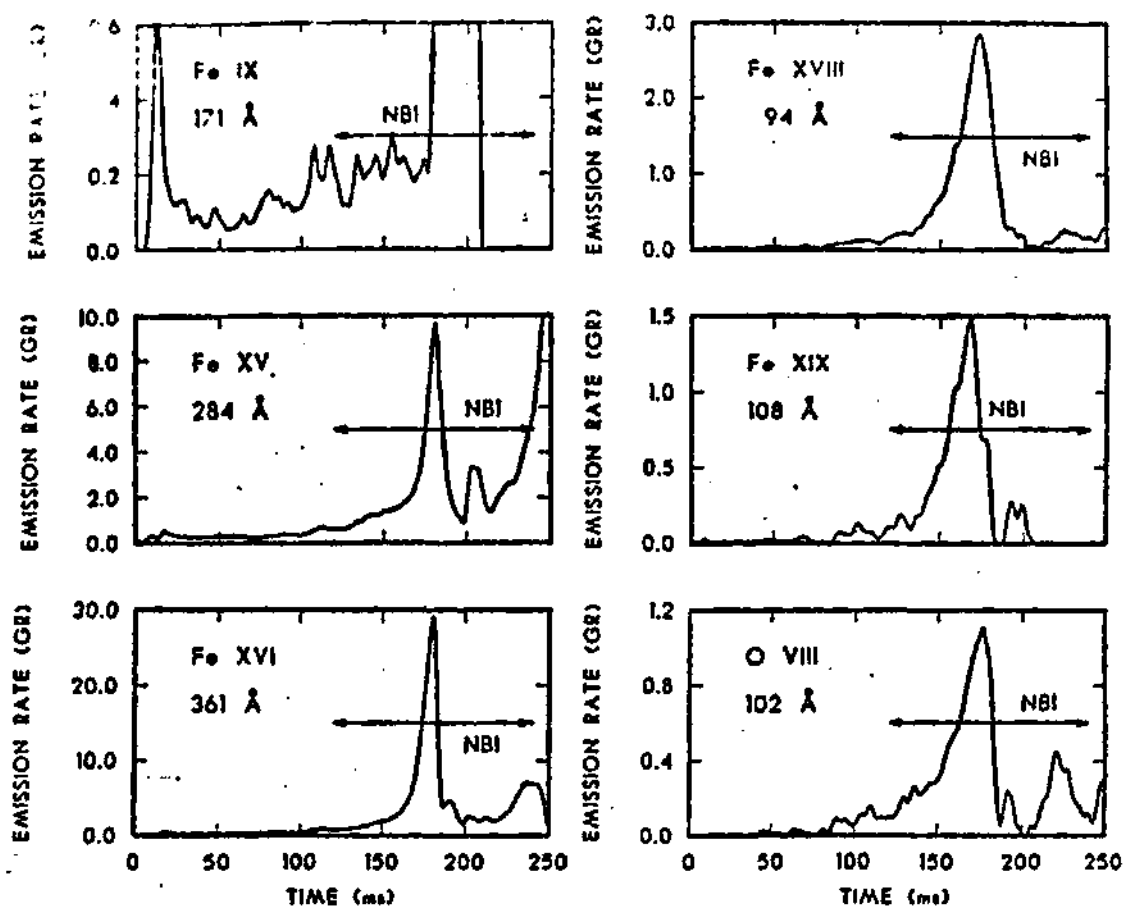


Figure 4.5.2 Experimental time variation of spectral emissions of iron in ISX-B with 1 MW counter-injection.

that in the case of co-injection, after an initial rise of iron concentration for about 30 ms after the beams are turned on, the temporal emission profile remains relatively constant until the discharge terminates at 200 ms. In contrast, the emission profiles generally rise very rapidly following counter-injection until the discharge disrupts around 174 ms due to impurity accumulation and rapid cooling. An increase by a factor of 10 - 30 of central ion radiation with counter-injection as compared to co-injection is evident from the experimental curves.

To model the measured emission profiles, the information about the experimental conditions was generally derived from the ZORNOC [87] data files. The initial and the final profiles for electron density and temperature for co-injection are shown in Figures (4.5.3) and (4.5.4) respectively. The space resolved profiles for plasma density and temperature for counter-injection were not available from the ZORNOC data files at the initial time. To get such profile information, the following procedure was adopted.

Assuming a profile of the form

$$X=X_0[1-(r/a)^2]^a \quad (4.5.1)$$

where  $X$  is a physical quantity such as density or temperature, it can be shown that

$$\langle X \rangle = X_0/(1+a) \quad (4.5.2)$$

where  $\langle X \rangle$  represents the volume average value of  $X$ . With the given information about the volume average value of plasma density and temperature from ZORNOC files, the spatial profiles were unfolded from equation (4.5.1) assuming parabolic profiles. The initial profiles for electron density and temperature for counter-injection are shown in Figure (4.5.5). The final profiles for electron density and temperature for counter-injection based on ZORNOC data files are shown in Figure (4.5.6).

We also need profile information about beam momentum deposition, ion temperature, and charge state distribution to correctly model the transport calculations. The beam momentum was computed from the beam shape factor  $H(r)$  given in the ZORNOC data files, and is shown in Figure (4.5.7). The beam shape factor was assumed to be the same for both co- and

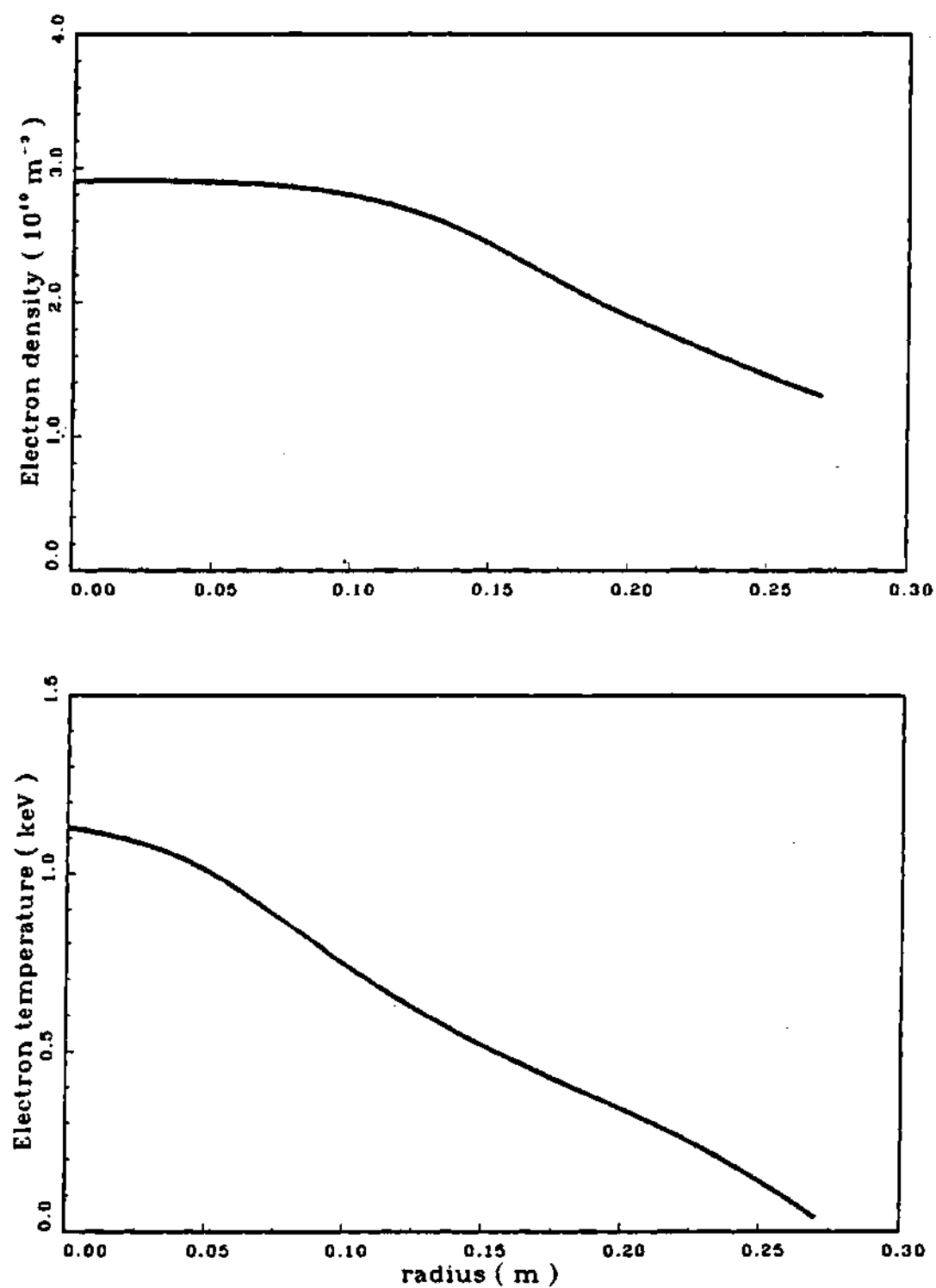


Figure 4.5.3 Electron density and temperature profiles in ISX-B at 80 ms in the co-injection discharge.



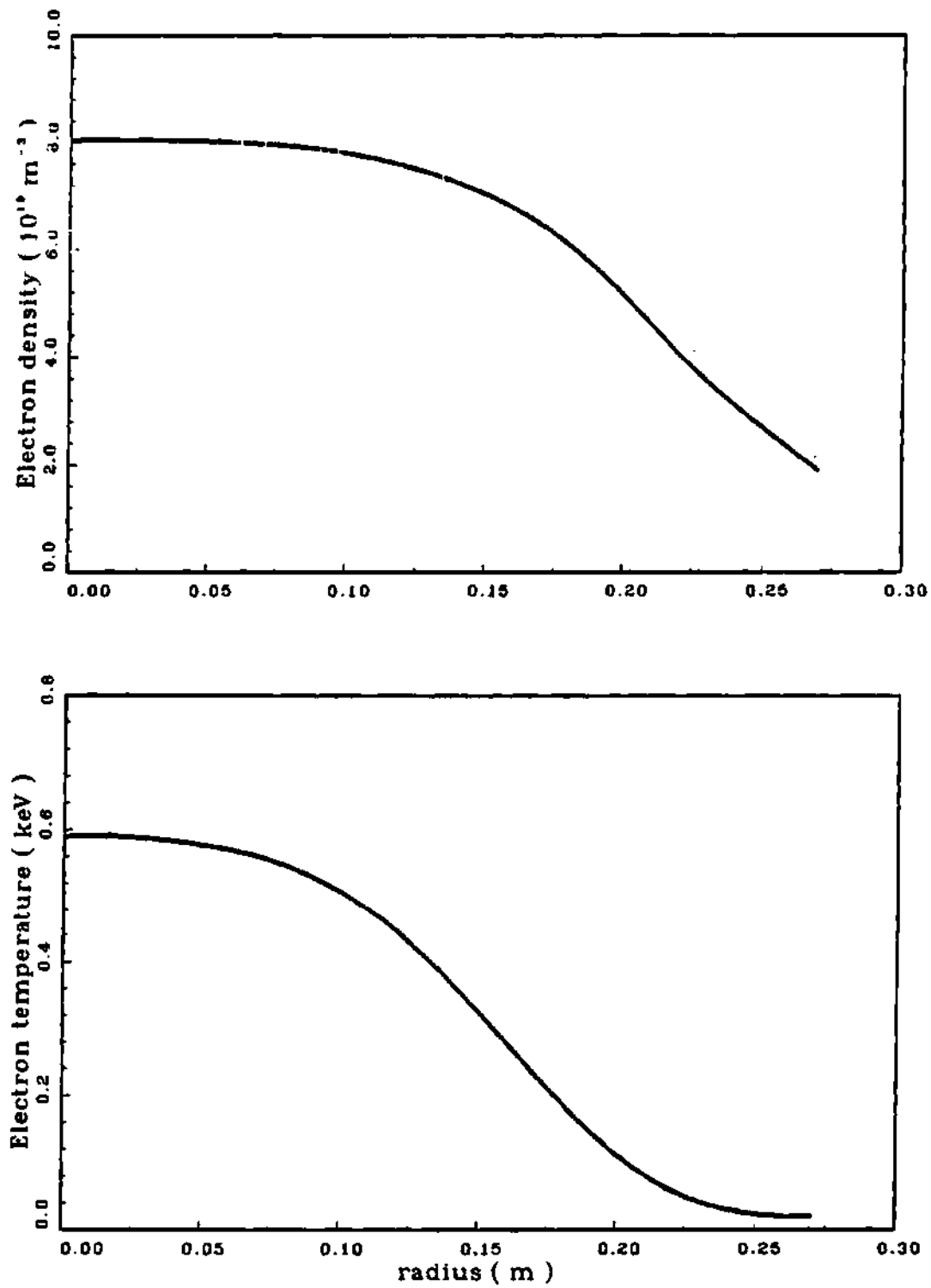


Figure 4.5.4 Electron density and temperature profiles in ISX-B at 230 ms in the co-injection discharge.

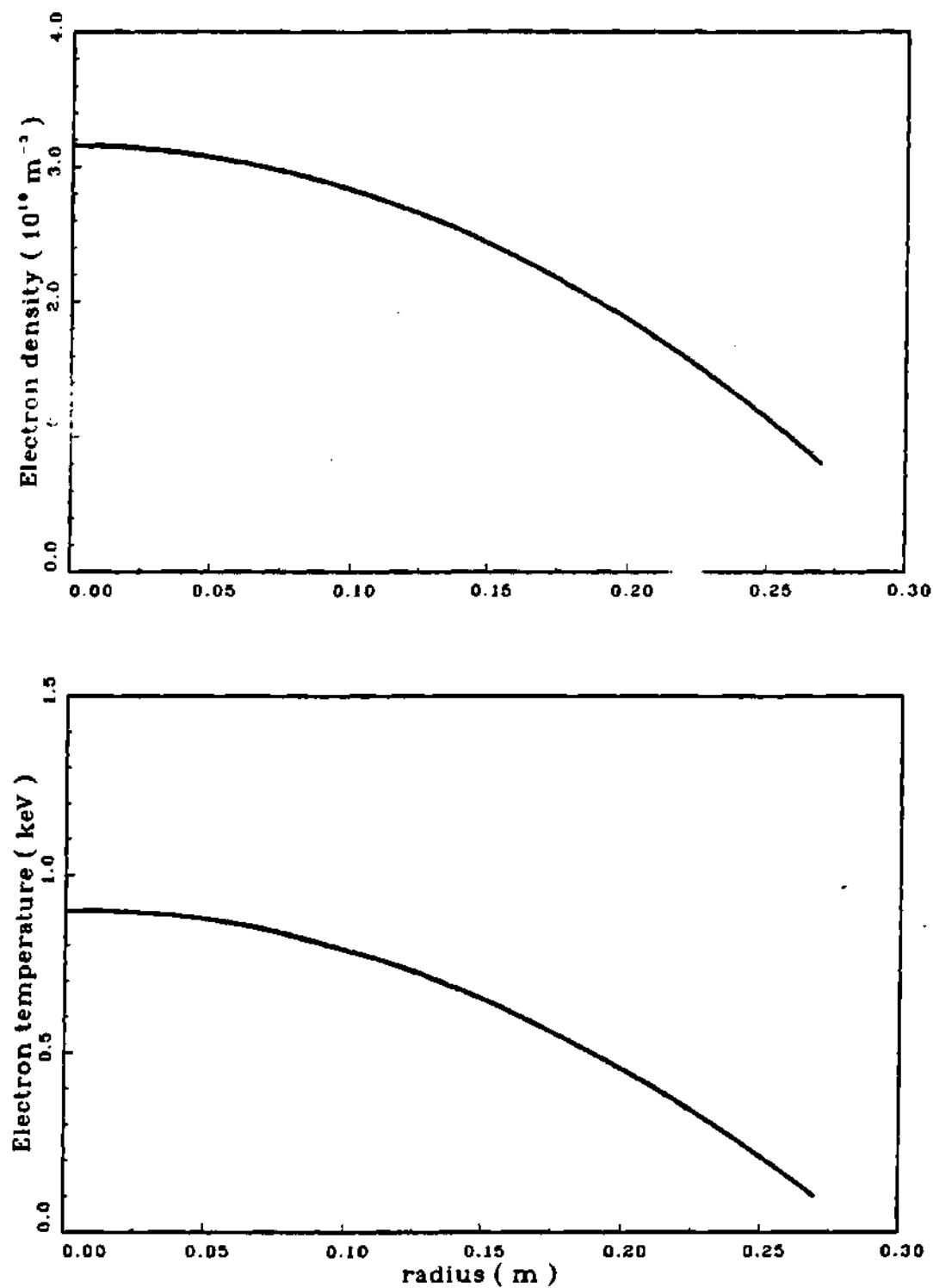


Figure 4.5.5 Electron density and temperature profiles in ISX-B at 120 ms in the counter-injection discharge.

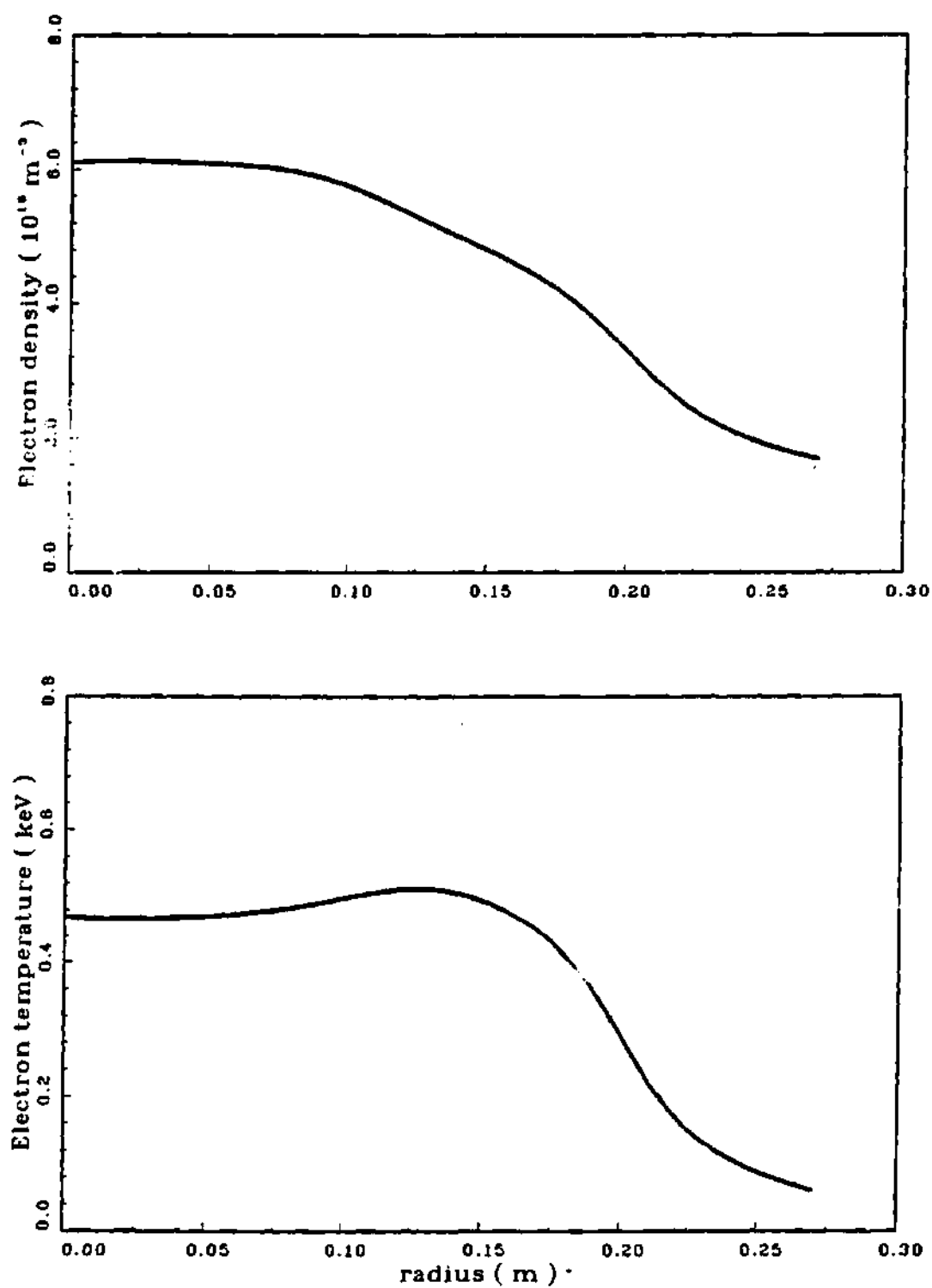


Figure 4.5.6 Electron density and temperature profiles in ISX-B at 169 ms in the counter-injection discharge.

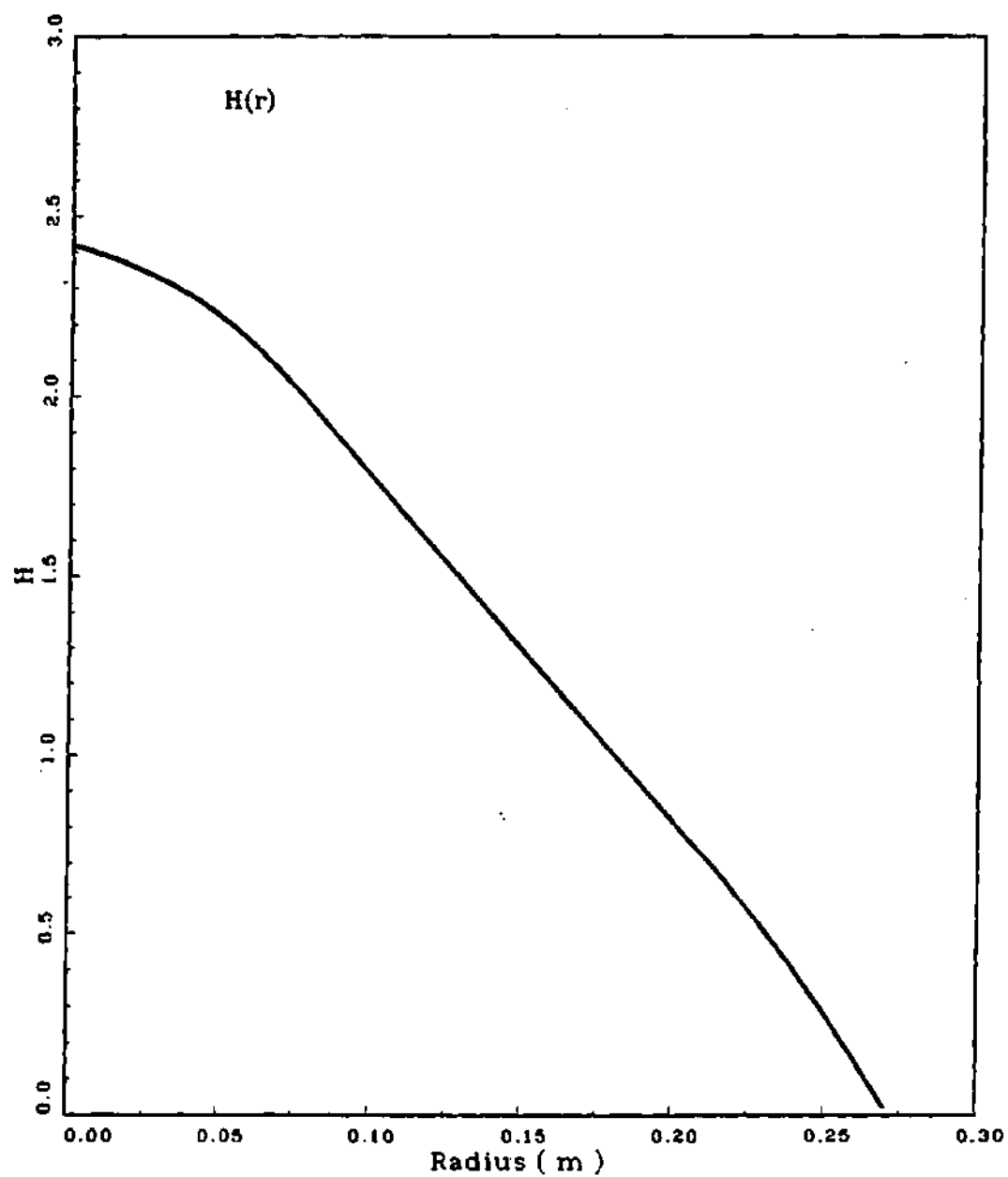


Figure 4.5.7 Beam deposition profile in ISX-B.

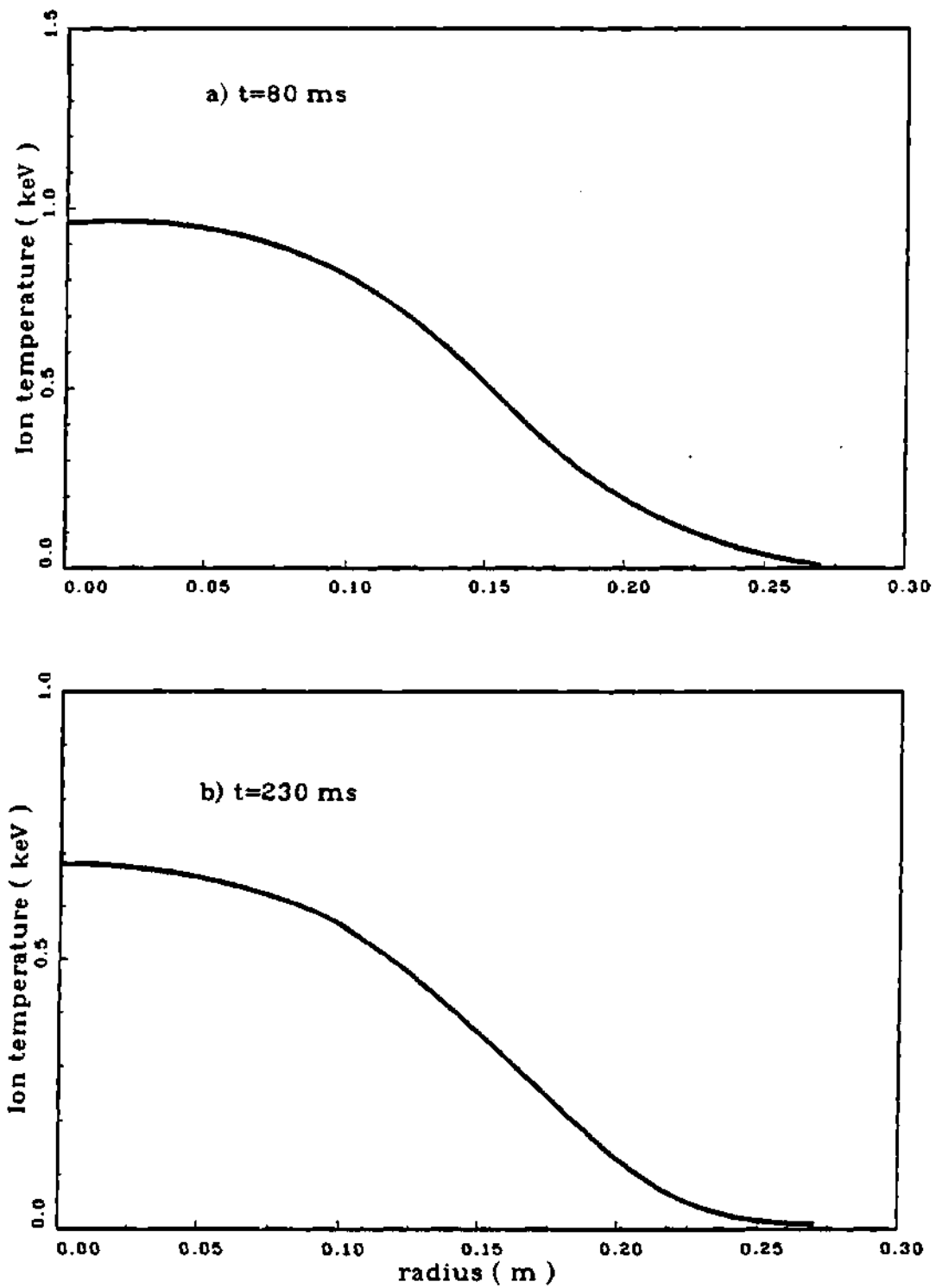


Figure 4.5.8 Ion temperature profiles in ISX-B with co-injection at 80 and 230 ms.

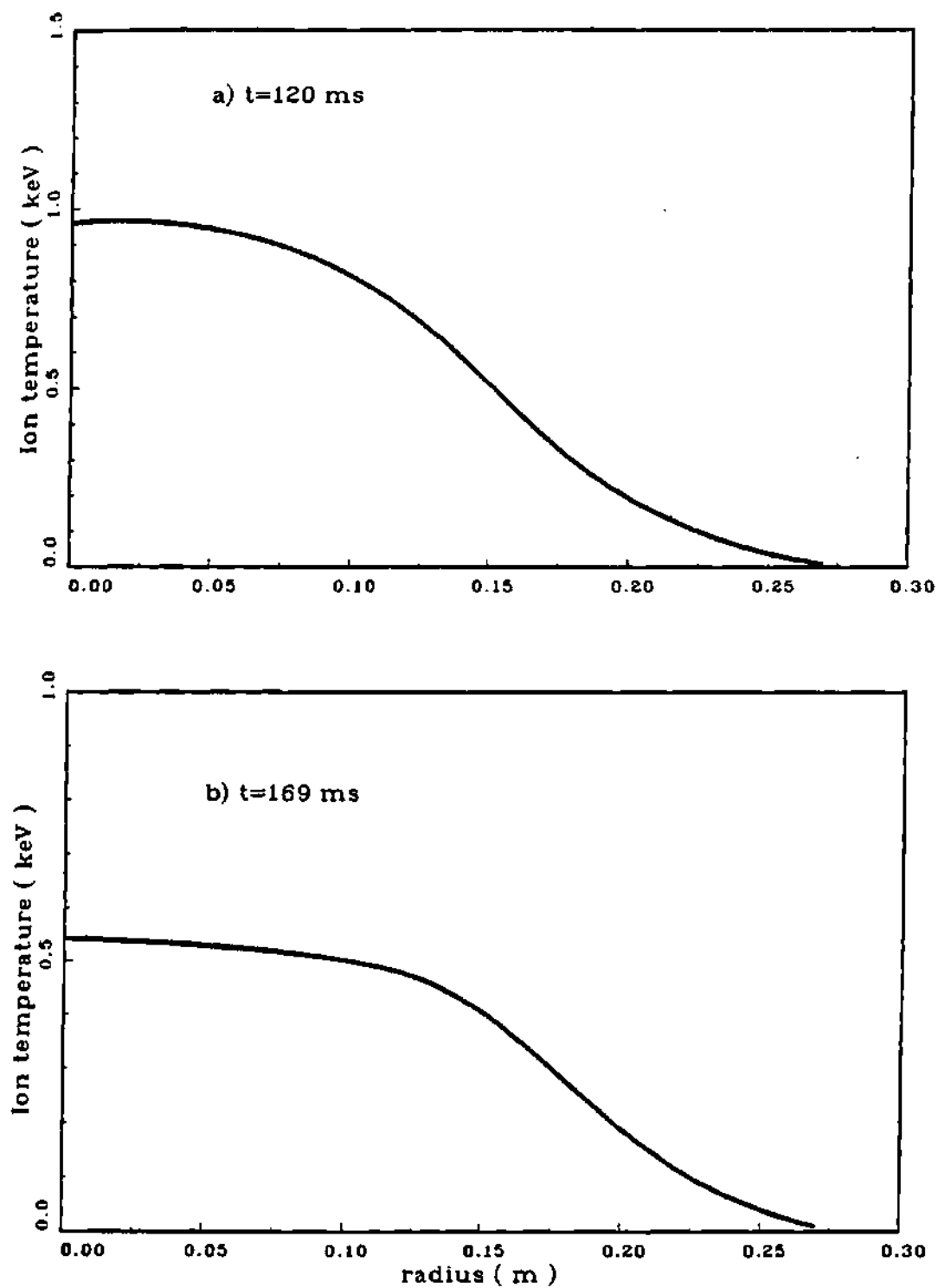


Figure 4.5.9 Ion temperature profiles in ISX-B with counter-injection at 120 and 169 ms.

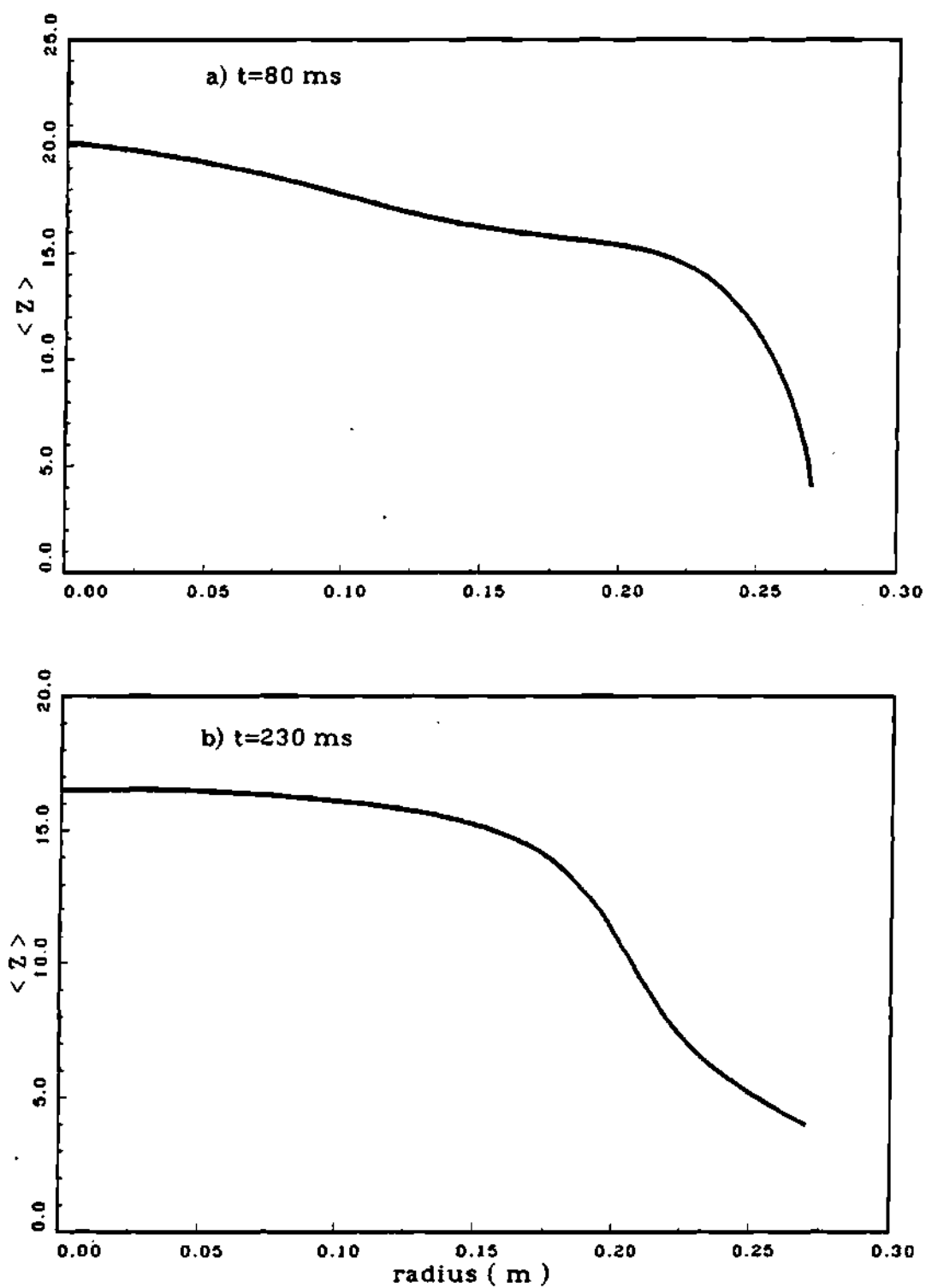


Figure 4.5.10 Average charge state profiles in ISX-B with co-injection

at 80 and 230 ms.

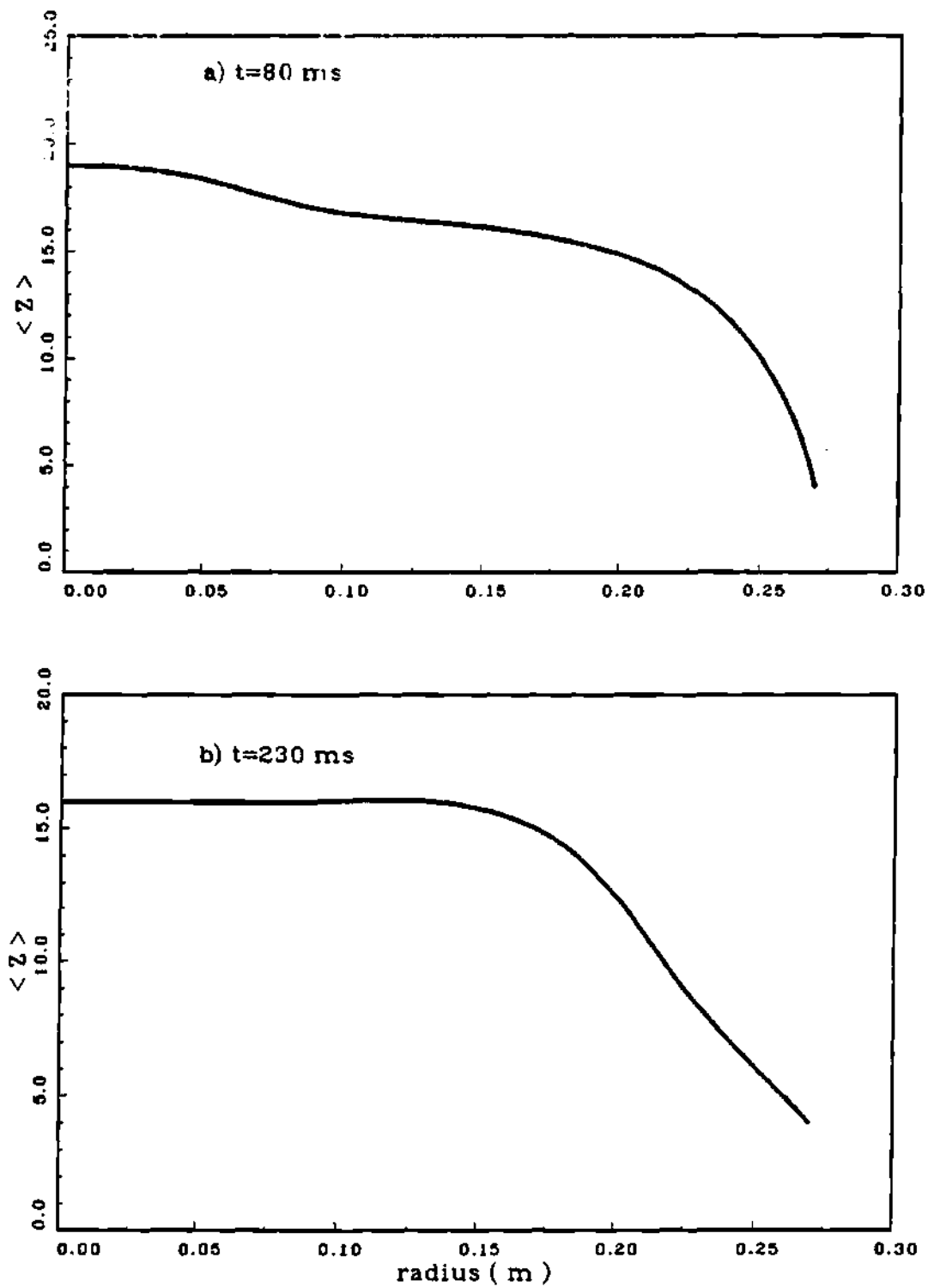


Figure 4.5.11 Average charge state profiles in ISX-B with counter-injection at 120 and 169 ms.



counter-injection. The ion temperature profiles for co-injection based on ZORNOC data files at the initial and final times are shown in Figure (4.5.8). For counter-injection, the initial ion temperature computed as explained in Section (3.3), and the final ion temperature based on ZORNOC data files and shown in Figure (4.5.9). The spatial charge state distribution with co-injection based on ZORNOC data files, at the initial and the final points in time is shown in Figure (4.5.10). For counter-injection, the initial charge state distribution, based on the average ion model in Reference [77], and the final distribution based on ZORNOC data files, is shown in Figure (4.5.11).

The information about the initial and the boundary conditions is required to solve the time-dependent impurity transport problem. In addition to an initial guess and the usual zero density gradient at the center, the outer boundary condition is required to complete the solution. The outer boundary condition can be estimated from the edge conditions by solving the particle diffusion equation [97].

$$\partial n / \partial t = -(1/r) \partial / \partial r (r \Gamma) + S \quad (4.5.3)$$

where  $n$  is particle density,  $\Gamma$  is the cross-field particle flux,  $S$  is the sum of the particle sources,  $r$  is the radial coordinate, and  $t$  is time. The equation (4.5.3) can be solved approximately by integrating it over the plasma volume inside the limiter radius and by writing the diffusive loss of ions at the edge as  $S_D = N/\tau_p$ , the total source rate as a sum of the external gas feed rate  $S_g$  and the recycling rate  $S_R = R N/\tau_p$  as

$$dN/dt = S_g + S_R - S_D \quad (4.5.4)$$

or,

$$dN/dt = S_g + R N/\tau_p - N/\tau_p \quad (4.5.5)$$

or,

$$dN/dt = S_g - N/\tau_p^* \quad (4.5.6)$$

where  $N$  is the integrated number of particles,  $\tau_p$  is the global particle confinement time,  $R$  is the global recycle coefficient, and

$$\tau_p^* = \tau_p / (1 - R) \quad (4.5.7)$$

is the effective particle confinement time, or the density decay time constant measured in the absence of external fueling. Due to desorption and backscattering from the wall, the effective particle confinement time is usually much longer

than the inherent confinement time [98]. In steady state, Eq. (4.5.6) leads to

$$S_g = N/\tau_p^* \quad (4.5.8)$$

Thus, for a given steady-state density, large recycling fractions reduce the required rate of external fueling. The ISX-B simulations [97] indicate that 50 Torr l/s of H<sub>2</sub> gas is required to maintain a steady-state. Experimentally it is found that a gas feed rate of 10 Torr l/s will support a net density increase [97]. These values suggest an overall recycle fraction greater than 85%. The wall source

$$S_w = N/\tau_p = S_g/(1-R) \quad (4.5.9)$$

is then determined mostly by recycling rather than the gas feed rate. Since physical sputtering is mostly responsible for heavy impurity introduction at the edge, a knowledge of the source rate from Eq. (4.5.9), and the sputtering yield at the typical edge temperatures can be used to determine the impurity flux from the wall. The computed impurity flux from wall compares favorably to the value  $2.5 \times 10^{13}/\text{cm}^2\text{-s}$  [88] obtained from the measured neutral deuterium flux to the wall at a sputter yield of  $10^{-3}$ . This information was subsequently

used to estimate the boundary condition needed to predict the emission rates from the iron charge-states radiating from different radial locations.

To estimate the radial locations of the iron charge-states, the atomic physics model [92] was used to predict the maximum coronal equilibrium fractions for the charge-states investigated experimentally [26]. Since the coronal equilibrium fraction is essentially a function of the electron temperature only, the electron temperature corresponding to the maximum coronal fractions was then used to estimate the most probable radial location of the charge-states in the 27-cm discharge. This procedure shows that the theoretically investigated charge-states, Fe XVI, Fe XVIII, and Fe XIX are located somewhere around 24, 16, and 13 cm respectively in the 27-cm discharge.

We do not know impurity level or distribution at the end of the ohmic phase, so we adjusted  $n_z(r, t=0)$  to match the predicted emission rates with experiment for all charge-states at  $t=0$ . The incident impurity flux was then adjusted to match the predicted Fe XVI emissions with

experiment. Since Fe XVI is located around  $r=24$  cm, this procedure is equivalent to indirectly determining experimentally the edge boundary condition on the impurity flux. The fact that the time histories of the other emission rates from the radial locations 16 and 13 cm are predicted well, indicates that the calculated rate of impurity transport is consistent with the observations for both co- and counter-injection. The initial and the edge boundary conditions for co- and counter-injection are shown in Figures (4.5.12) through (4.5.14). The emission rates predicted by theory (dotted curve), and the measured values (solid curve) are compared in Figure (4.5.15). The theory is seen to model the experimental data quite well.

Since the value of external drag needed in flow reversal calculations was computed from the gyroviscous theory [54], the agreement between theory and experiment also confirms the validity of the gyroviscous theory. It may also be noticed that the predicted central rotation velocity ( $2.3 \times 10^5$  m/s) at  $P_b=1$  MW was found to be in good agreement with the measured [32,33] central velocity ( $1.2 \times 10^5$  m/s), supporting again the use of

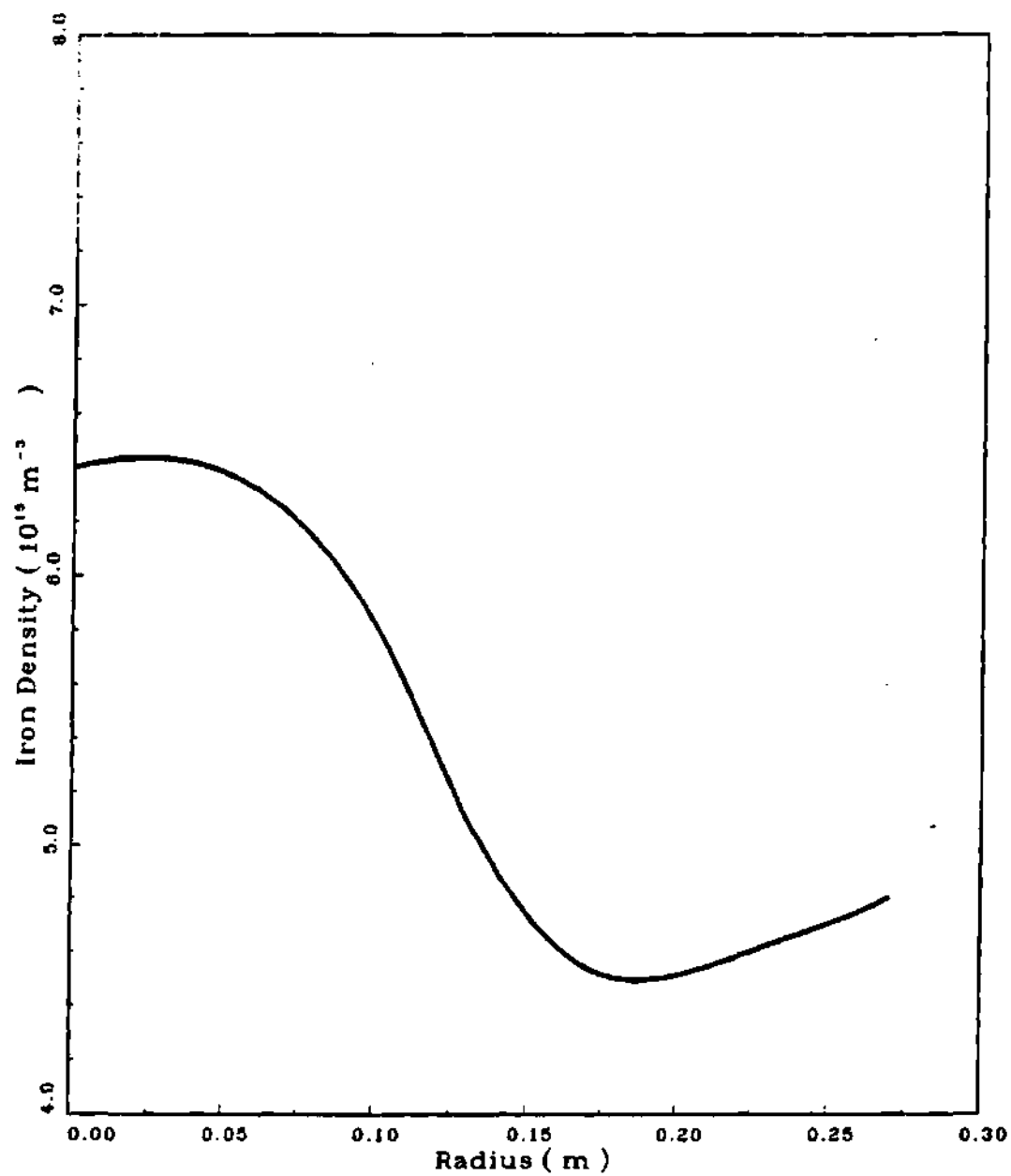


Figure 4.5.12 Theoretical impurity density profile in ISX-B at

80 ms in co-discharge.

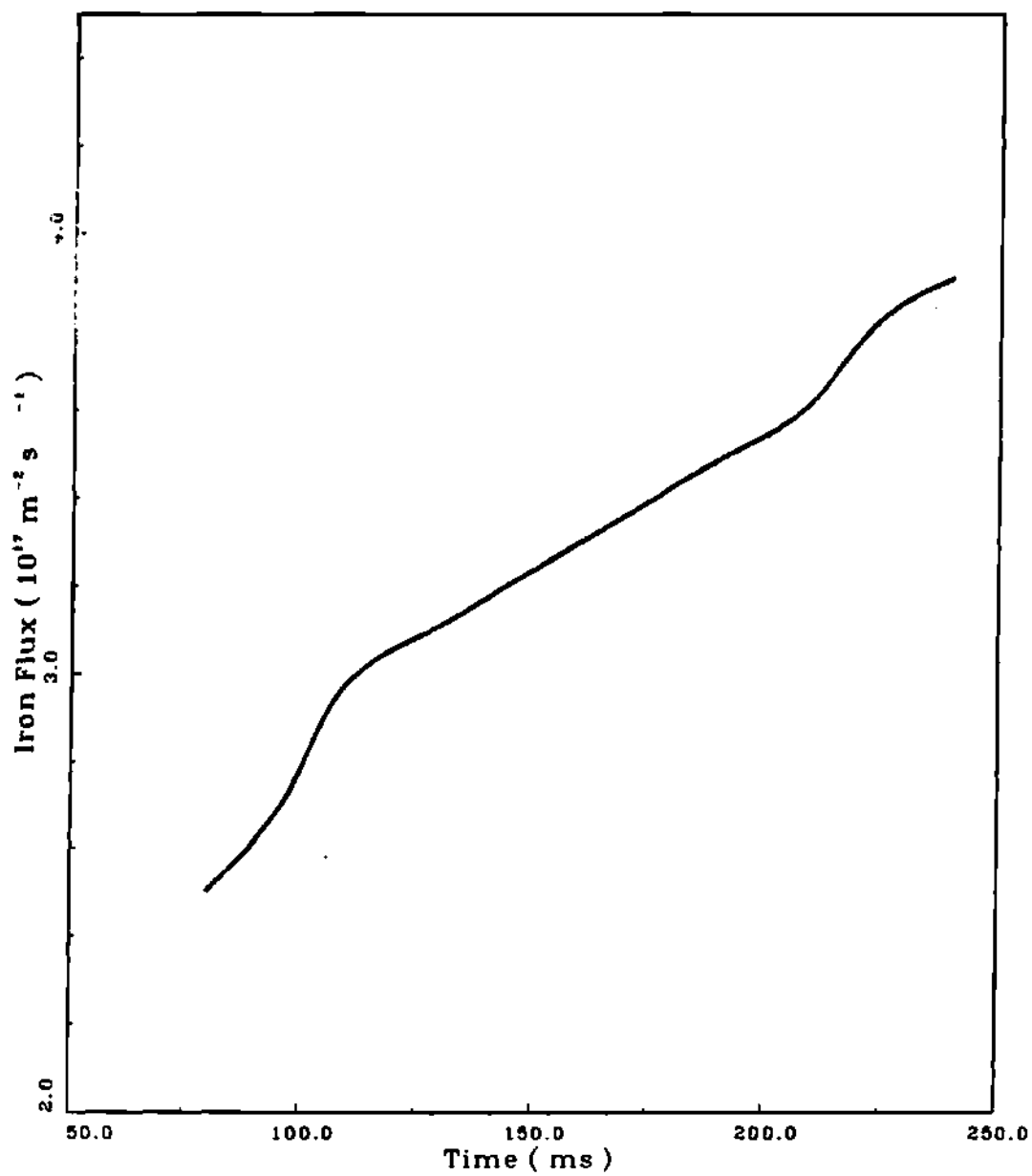


Figure 4.5.13 Theoretical impurity flux history in ISX-B  
at 27 cm with co-injection.

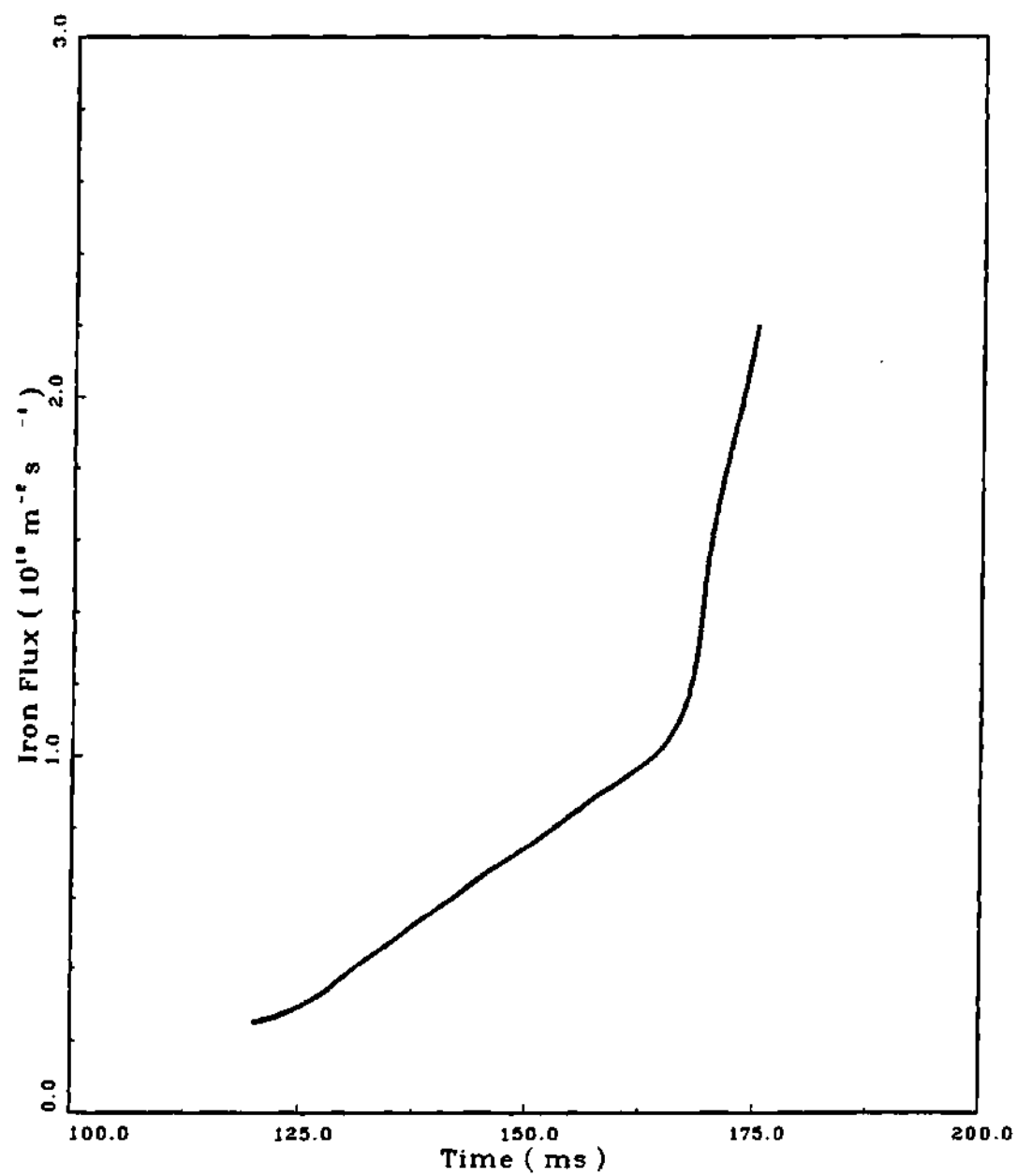


Figure 4.5.14 Theoretical impurity flux history in ISX-B at 27 cm with counter-injection.



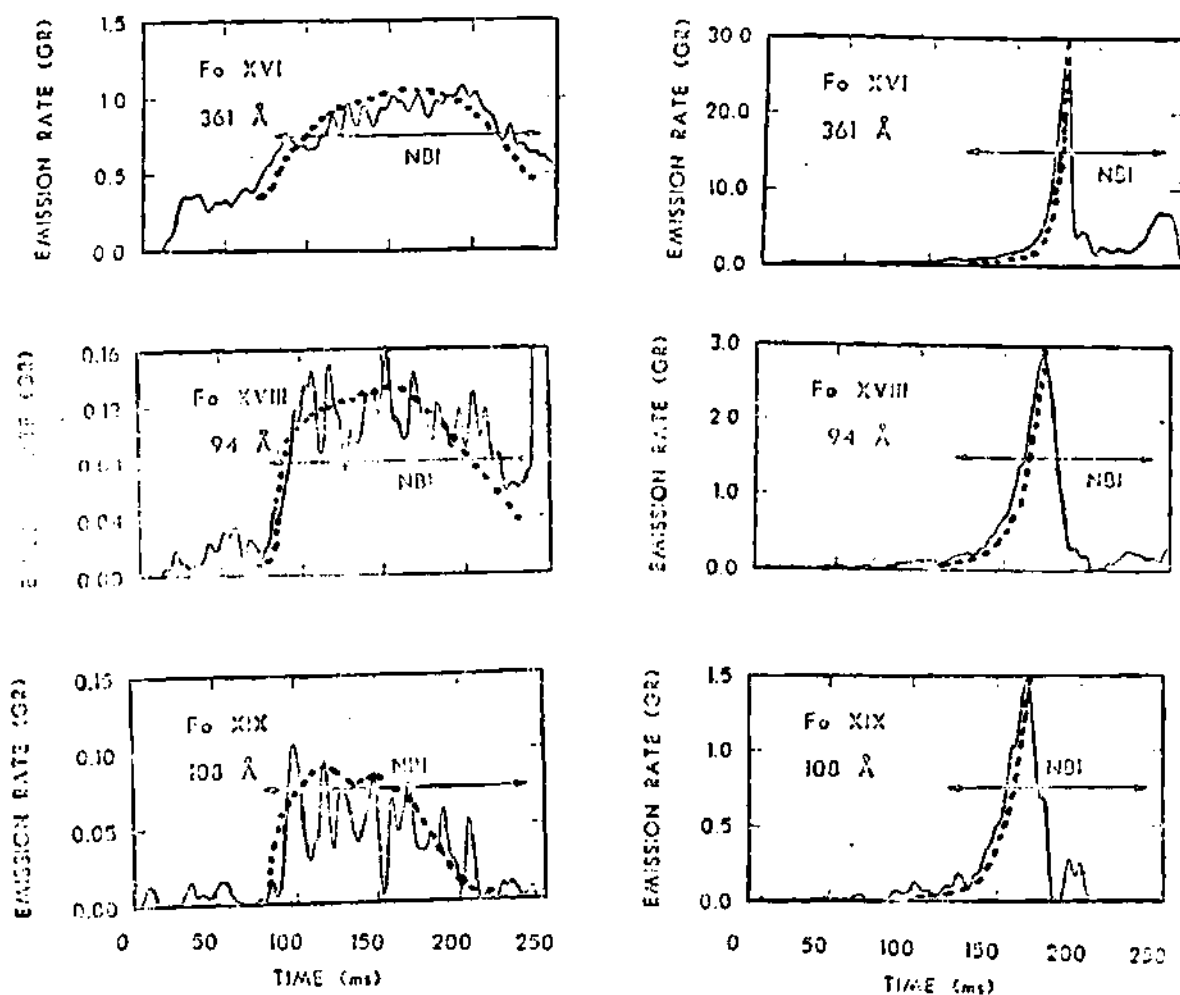


Figure 4.5.15 Comparison of the measured (solid curve) and theoretical (dotted curve) time variation of spectral emissions of iron in ISX-B with co- and counter-injection, with 1 MW power in each case.

gyroviscous theory in predicting drag for use in the flow reversal calculations.

#### 4.6 Analysis of Two-beam Co-discharge

Isler et al. [32] have recorded a set of experiments performed in the ISX-B tokamak to study intrinsic iron impurity in deuterium discharge with two-beam co-injection that clearly demonstrates [Fig. 4.6.1] that the beam-induced transport effects can overwhelm the increases in the edge source rates. Two neutral beams, each with 1.2 MW power, were injected sequentially in deuterium plasmas. The first beam was turned on at 80 ms and the second at 160 ms. A typical increase of the iron influx is observed from the Fe IX and Fe XVI after the onset of injection at 80 ms, and signals from Fe XVIII and Fe XIX became prominent both from the influx and from electron heating. When the second beam was turned on, however, the radiation from these ions decreased to 40% and 25% of the maximum values respectively. The decreases in the signals from Fe IX and Fe XVI were much smaller. The central temperature at 250 ms was only 750 eV, which is too low for Fe XVIII and Fe XIX

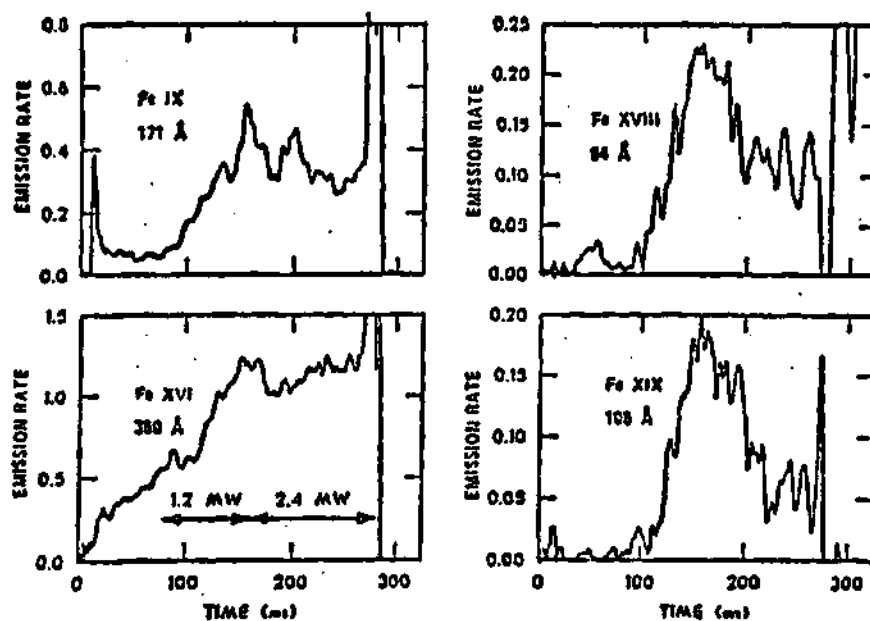


Figure 4.6.1 Experimental time variation of spectral emissions of iron in ISX-B with two-beam sequential co-injection, with 1.2 MW power in each case.

to exhibit burn-out to higher ionization stages. The decrease in concentration of the interior iron after the second beam was turned on was very prominent.

The electron density and temperature profiles at the start of neutral beam injection were not available for these experiments. The parabolic profiles were used for these quantities with the central values obtained from reference [32]. These profiles are shown in Figure (4.6.2). The final profiles were obtained from the ZORNOC data files and are shown in Figure (4.6.3). The beam deposition profile shown in Figure (4.6.4) was computed using the code PROCTR [78]. The ion temperature profiles at the initial and the final points in time obtained from the modeling calculations as explained in Section (3.3), are shown in Figure (4.6.5). The average charge distributions based on Reference [77] are shown in Figure (4.6.6).

The atomic physics model was used to estimate the radial locations of the radiating charge-states in the experiment, as explained in Section (4.5). The electron temperatures corresponding to the maximum coronal equilibrium abundances

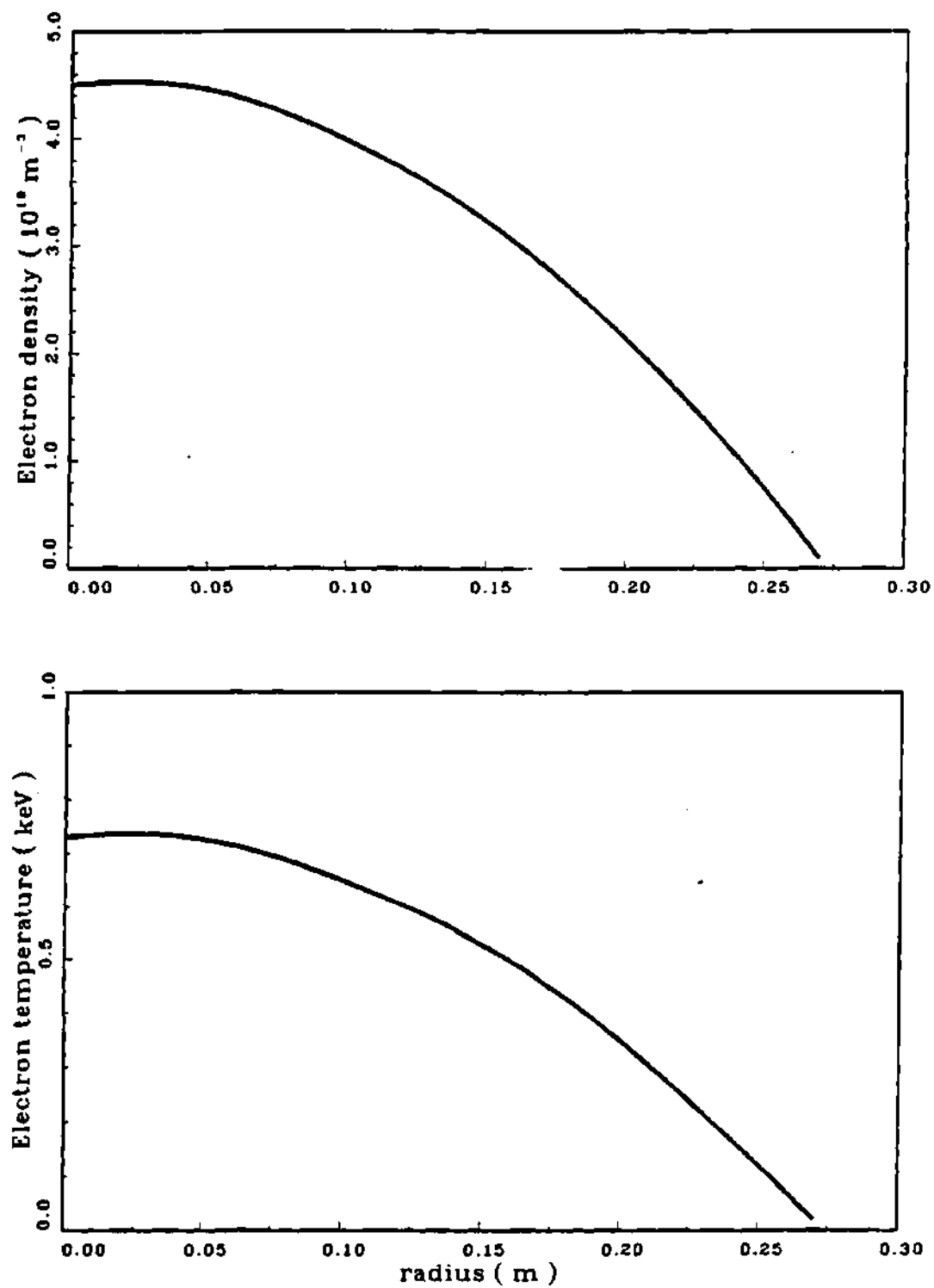


Figure 4.6.2 Electron density and temperature profiles in ISX-B at 80 ms in two-beam co-injection discharge.

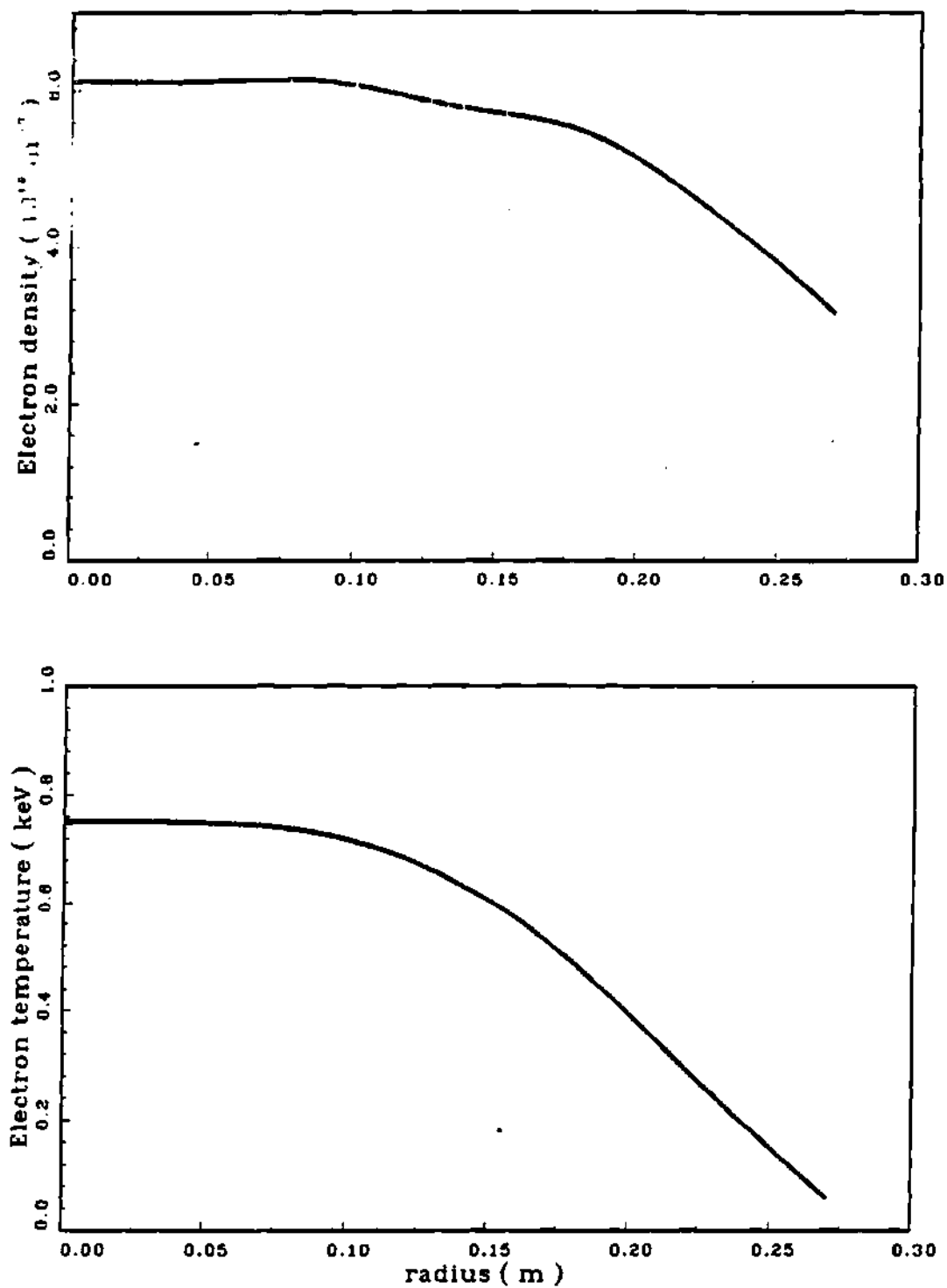


Figure 4.6.3 Electron density and temperature profiles in ISX-B at 250 ms in two-beam co-injection discharge.

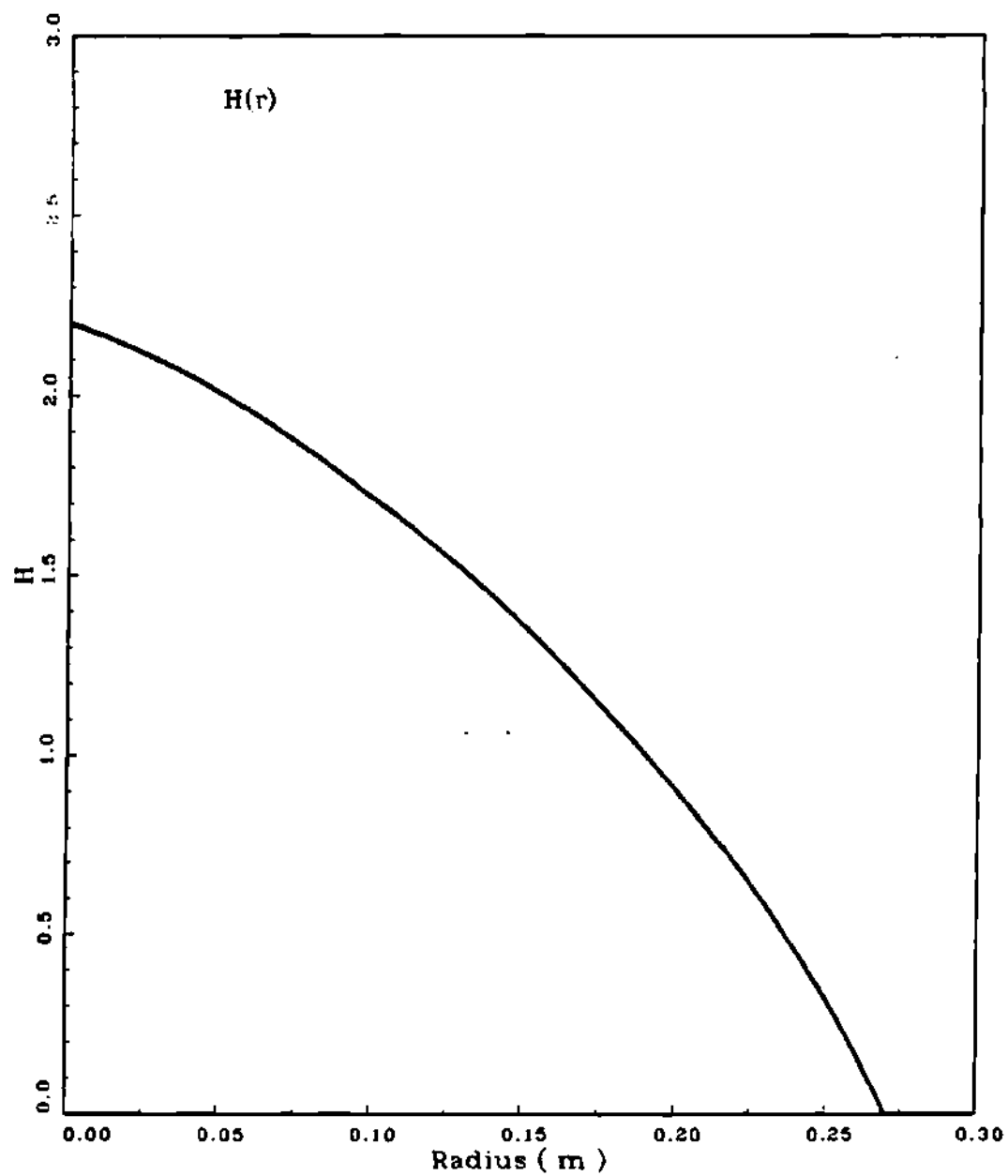


Figure 4.6.4 Beam shape factor in ISX-B with two-beam co-injection.

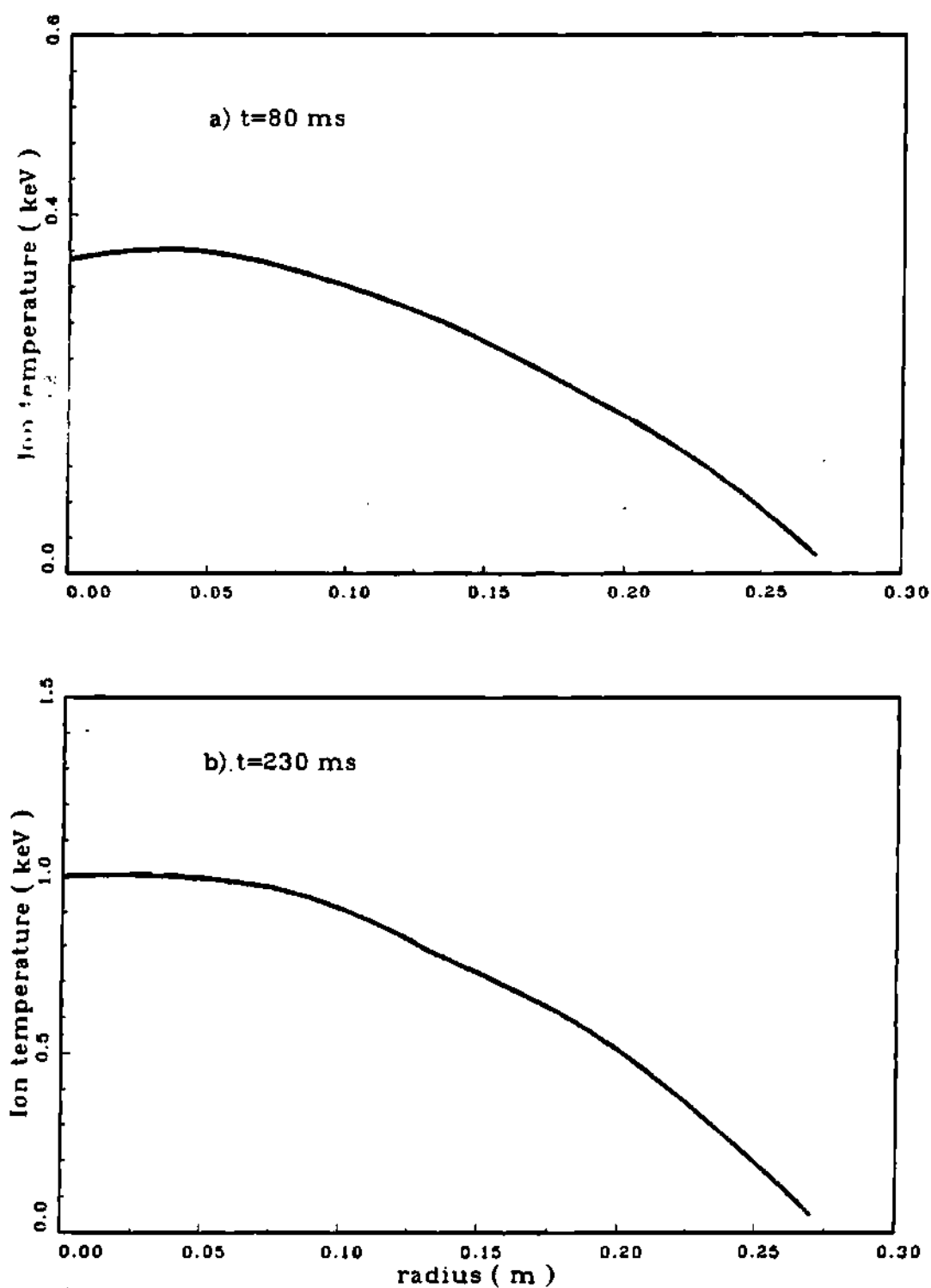


Figure 4.6.5 Ion temperature profiles in ISX-B with two beam co-injection at 80 and 230 ms.



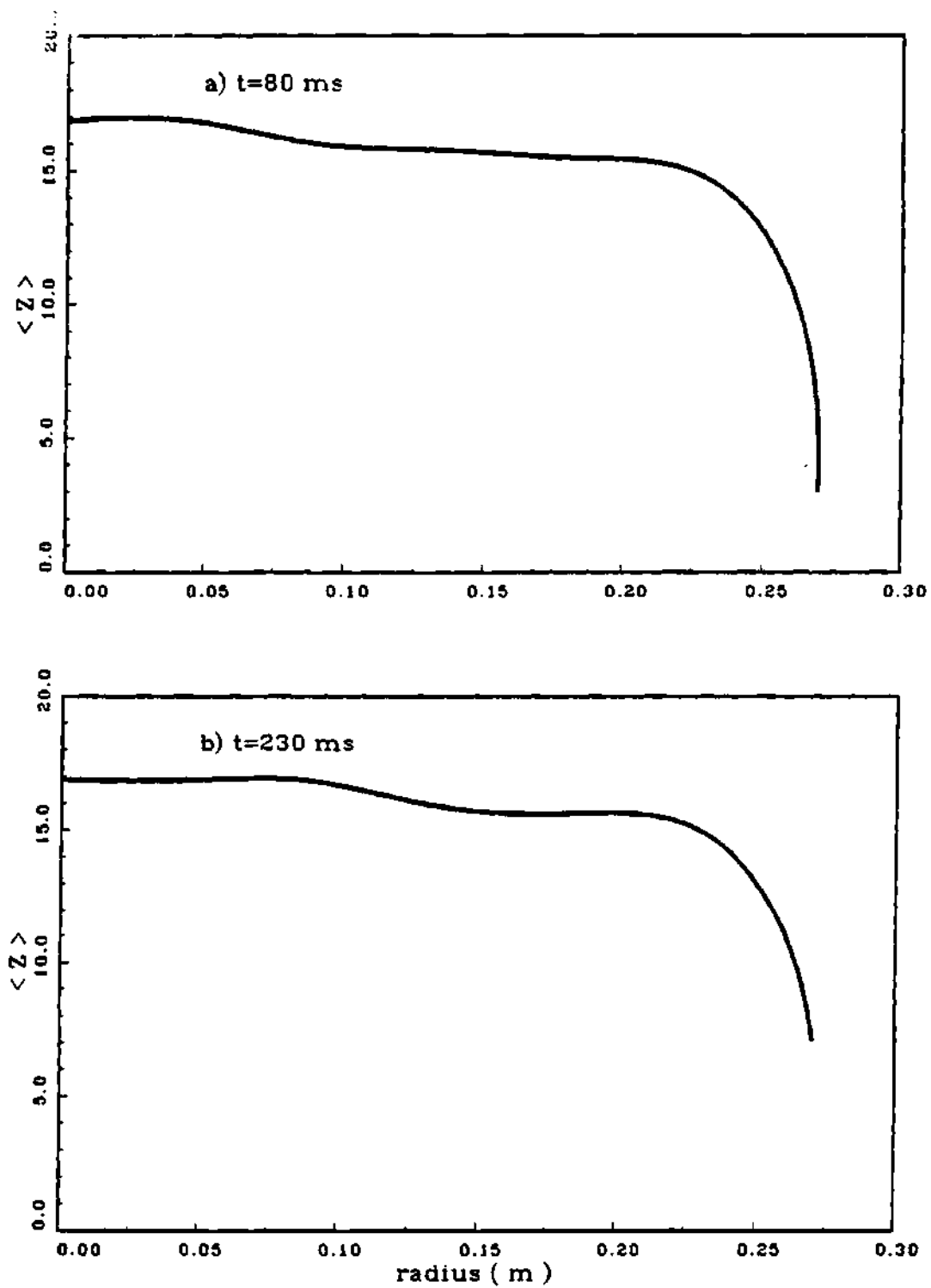


Figure 4.6.6 average charge state profiles in ISX-B with two-beam co-injection at 80 and 230 ms.

shows that Fe XVI, Fe XVIII, and Fe XIX investigated in this study, radiate from the neighborhood of 20, 14 and 10 cm respectively.

The source rate was estimated as described above in Section (4.5). Since the impurity level or the distribution is unknown from experimental conditions at the time of injection,  $n_z(r, t=0)$  was adjusted to match the predicted emission rates with experiment for all charge-states at  $t=0$ . The incident impurity flux was then adjusted to match the predicted Fe XVI emissions with experiment. Since Fe XVI is located near  $r=24$  cm in the 27-cm discharge, this procedure is equivalent to indirectly determining the edge boundary condition on the impurity flux. Since the time histories of the other emission rates from the radial locations indicated above, are predicted well, the calculated rate of impurity transport is consistent with the observations. The initial and the edge boundary conditions are shown in Figures (4.6.7) and (4.6.8).

With the initial and the edge boundary conditions as estimated above, and the experimental values of the electron density and temperatures, and other experimental data where

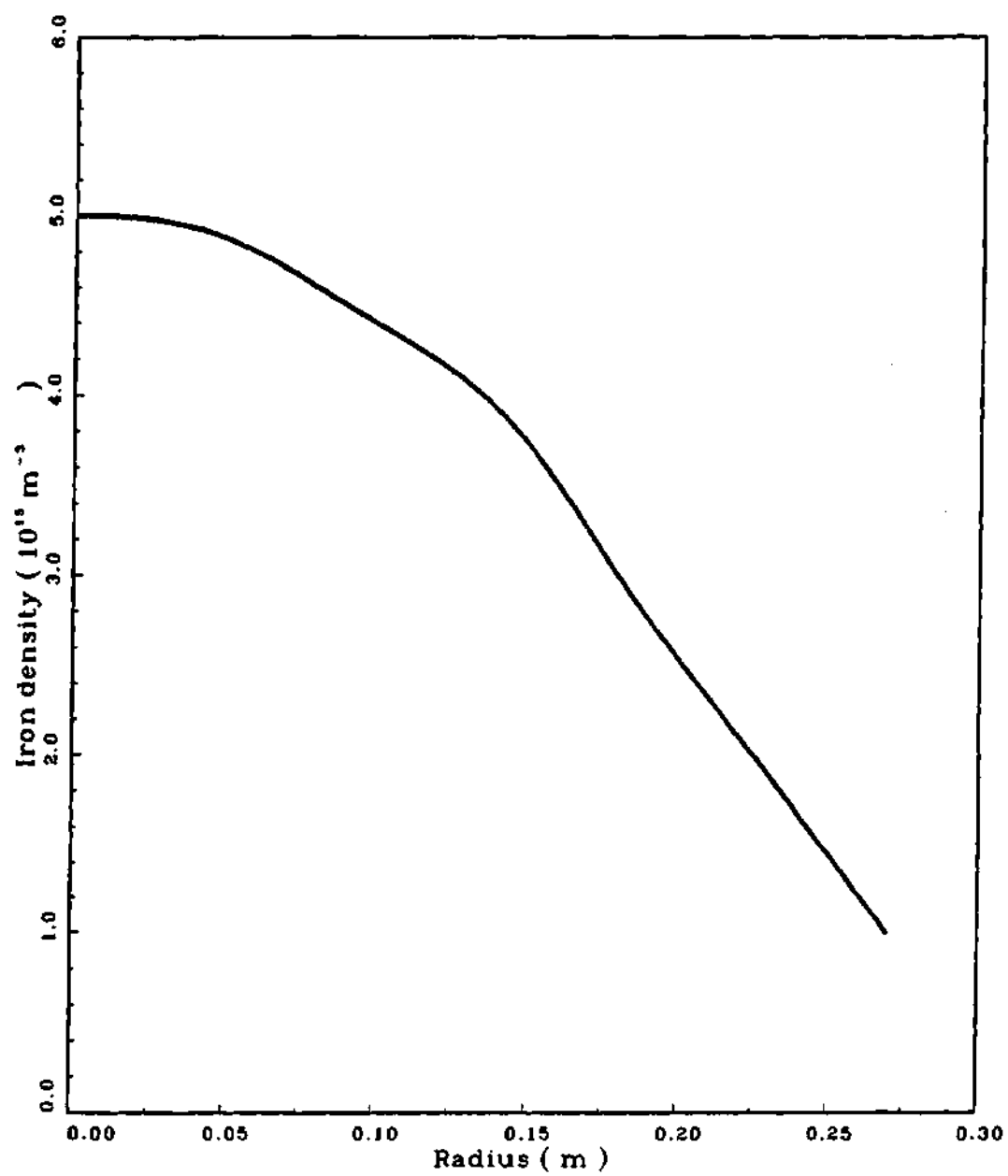


Figure 4.6.7 Theoretical impurity density profile in ISX-B at 80 ms.

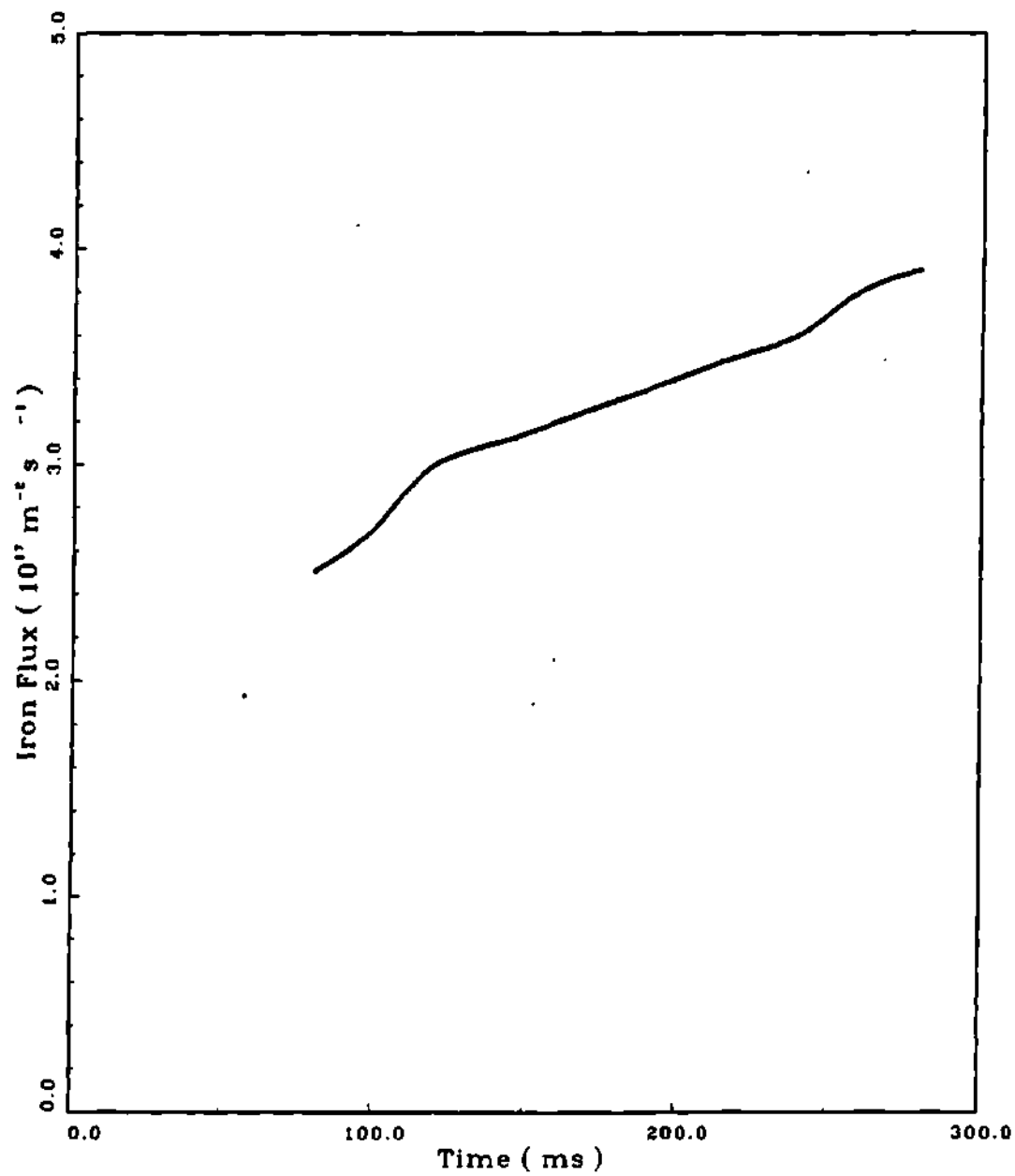


Figure 4.6.8 Theoretical impurity flux history in ISX-B at 27 cm with two-beam co-injection.

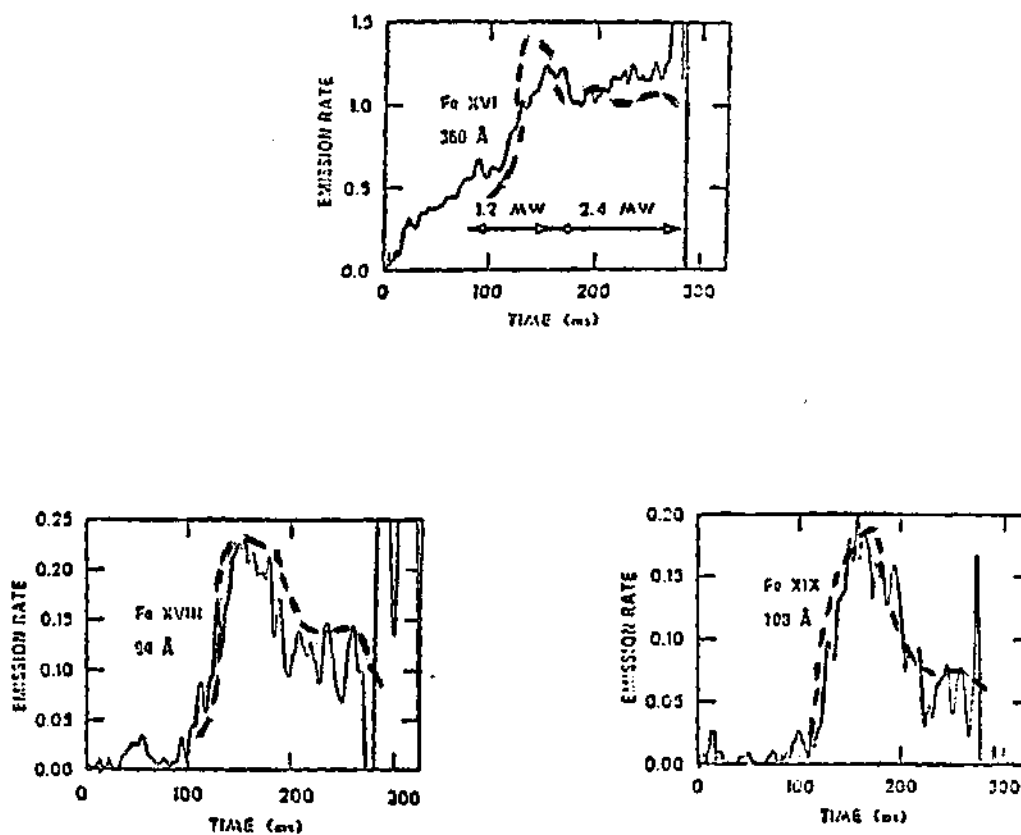


Figure 4.6.9 Comparison of measured (solid curve) and theoretical (dotted curve) time variation of spectral emissions of iron in ISX-B with two-beam sequential co-injection, each case with 1.2 MW beam power.

available, the predicted emission rates (dotted curves) are compared with the measured emission rates (solid curves) in Figure (4.6.9). The agreement between the theory and the experiment is generally remarkable. Thus, the neutral beam co-injection with two beams triggered sequentially clearly demonstrates that the increased source can be offset by impurity flow reversal caused by neutral beam co-injection.

It is instructive to compare the predicted and the measured rotation velocities. The predicted central rotation velocity ( $1.2 \times 10^5$  m/s) is in very good agreement with the measured [32,33] central velocity ( $1.5 \times 10^5$  m/s) at  $P_D = 2.4$  MW. This justifies the use of gyroviscous theory in predicting external drag in impurity flow reversal calculations.

#### 4.7 Summary

The neutral beam driven impurity flow reversal was investigated with intrinsic iron impurity in the ISX-B tokamak.

There is a vast collection of measured data on the effects of neutral beam injection on the transport of intrinsic as well as injected impurities in the ISX-B plasmas. Two sets of experiments were investigated in this chapter. The first type of experiments consider the effects of co- versus counter-injection on the transport of intrinsic iron in the ISX-B tokamak. The second set of experiments study the effects of two co-injected neutral beams triggered sequentially.

In the first type of experiments, neutral beam injection took place from 80 to 240 ms in the co-injection case, and from 125 to 240 ms in the counter-injection case, with 1 MW of neutral beam power in each case. The temporal emission profiles remain relatively flat in co-discharge. In contrast, the emissions generally rise very rapidly in the counter-injection case, and the discharge disrupts soon around 174 ms due to impurity accumulation and rapid cooling. The increase in the central ion radiation was 10 to 30 times higher in the case of counter-injection as compared to that in the co-discharge. Thus, impurity transport is very sensitive to the neutral beam direction.

The second type of experiments used two beams, each with 1.2 MW power, injected sequentially. The emission rate from various charge states decreased as soon as the second beam was turned on. Thus, the two-beam co-discharge demonstrates very clearly that the beam induced transport effects can overwhelm the increased edge source rate and actually drive impurities out of the center of the plasmas.

The time-dependent impurity flow reversal theory was applied to analyze the iron emission rates with co- versus counter-injection, and the two-beam co-injection experiments. The experimental conditions were used where available. The predicted emission rates were found to be a good representation of the experimental results. Both theory and experiment show central accumulation of impurity with counter-injection, and a decrease in accumulation, or a reversal in the impurity flow in case of co-injection. Thus, neutral beam co-injection can provide an effective mechanism to control impurities in tokamak plasmas.



CHAPTER V

ANALYSIS OF

INTRINSIC IRON TRANSPORT IN PLT

5.1 Introduction

The PLT tokamak has been extensively operated with neutral beam injection, and has provided useful data for impurity transport with co- versus counter-injection. Suckewer, et al., [47] measured the effects of co- versus counter-injection on the transport of iron impurity in the PLT tokamak. A schematic view of the PLT tokamak and the principal diagnostic equipment is shown in Figure (3.1.1). The quasi-steady part of the ohmically heated target plasma lasts for about 0.7 s, and usually toward the latter part of the interval, the neutral beam power is turned on for about 150 ms, which is sufficient to produce a new quasi-steady condition. The limiter is either graphite or stainless steel in these experiments. The vacuum vessel is stainless steel, with titanium evaporated on it at several toroidal locations for the purpose of trapping oxygen

and carbon, and providing greater flexibility of gas inlet programming. The reference parameters of interest in the PLT tokamak relevant to experiments analyzed in this chapter are shown in Table (5.1.1).

The experimental results [47] on the effects of co- versus counter-injection on the transport of iron impurity is reviewed in Section (5.2). The analysis of these experimental results using the impurity flow reversal model [42,43] is presented in Section (5.3).

## 5.2 PLT Experiments with Intrinsic Iron

Suckewer, et al., [47] inferred chordal brightness from the measured spectral signals from the PLT deuterium discharges with iron limiter. The neutral beam injection lasted from 400 to 500 ms. The neutral beam power was approximately 400 kW in each of the co- and counter-injection cases. The actual measured quantity [99] in all cases was the photomultiplier current of a grazing incidence bichromator, with a field of view approximately 2 cm in vertical, 10 cm in horizontal (along the field) direction. The view was changed from shot to shot in

Table 5.1.1 PLT data with intrinsic iron

---

Major radius (m)	1.40
Minor radius (m)	0.40
$Z_{\text{eff}}$	2.5
Toroidal magnetic field (T)	3.1
Safety factor $q(0)$	1.0
Safety factor $q(a)$	4.0
Neutral beam power (kW)	400.0
Neutral beam energy (keV)	40.0
Model impurity: Iron	
Plasma type	: $D^+$
Beam type	: $H^0$
Beam tangency radius (m)	1.10
Beam width (m)	0.20
Beam energy components (keV)	40,20,13.3
Beam injection time (ms)	400 - 500

---

about 2.5 cm steps vertically until the edge of the vertical magnetic field coil limited the scan mechanically to about 17 cm. The background radiation was subtracted from each signal. The remainder was then converted to brightness (photons/cm<sup>2</sup>-s) by means of a calibration curve constructed from branching ratios of certain line pairs [100-102]. The measurements were believed to be accurate in absolute terms to about 30%.

The chordal brightness distribution of Fe XV and Fe XXIII ions was measured with co- and counter-injection. The Fe XXIII radiates from near center, and Fe XV intensity was estimated to be located in the neighborhood of 25 cm in the 40 cm discharge. The chordal brightness is proportional to the ion concentration along the line of sight in the experiment [47]. The experimental results (Fig. 5.2.1) clearly indicate a substantial difference in the iron concentrations between the co- and counter-injection cases, being roughly double in the latter case. The soft x-ray signals from these discharges indicate only a small increase with the co-beam, but roughly a double increase with the counter-beam. The bolometric measurements [103,104] indicate a substantial central peaking

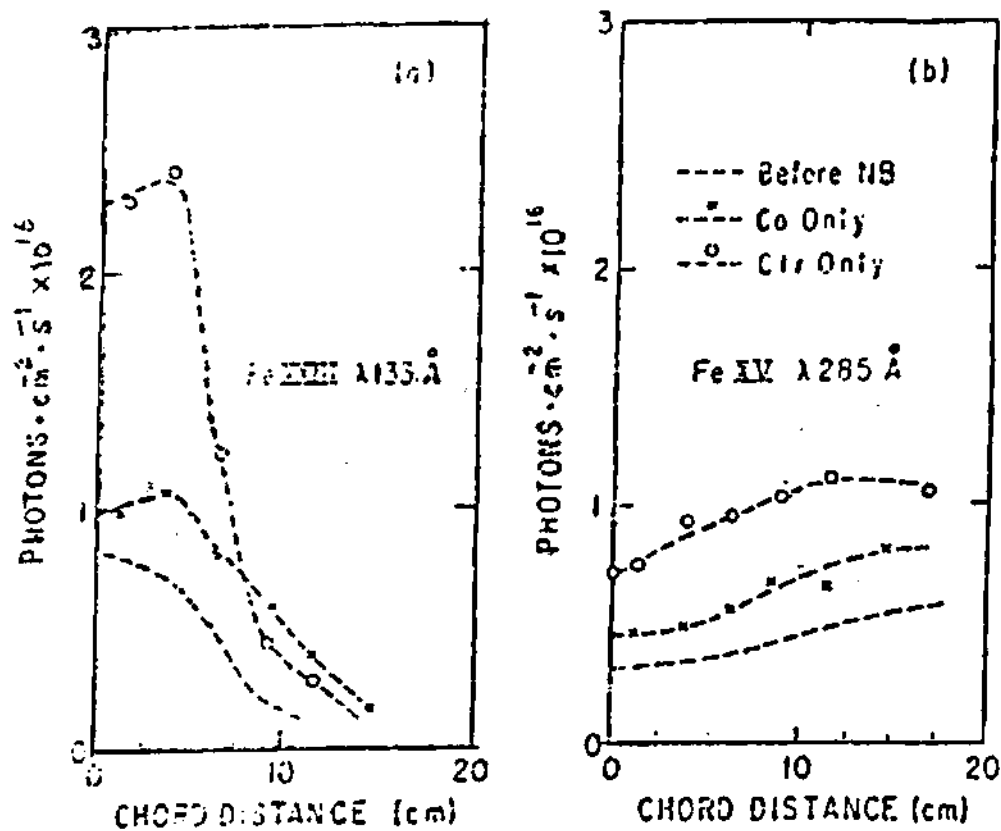


Figure 5.2.1 Measured chordal profiles of iron radiation in PLT with co- and counter-injection, with 400 kW power in each case.

with counter-injection, but a fairly broad distribution with co-injection. The experimental investigation [47] concludes that counter-injection produces significantly higher radiation losses than either co-injection or simultaneous co- and counter-injection at the same power level.

### 5.3 Analysis of PLT Experiments

The necessary information about the measured electron density and temperature profiles required to model the measured chordal brightness is given in Reference [47]. These profiles were deduced from Thomson scattering measurements [104]. The electron density and temperature profiles for co- and counter-injection, based on Reference [47] are given in Figures. (5.3.1) through (5.3.4) at the initial and the final times of beam injection. The beam shape factor  $H(r)$  computed from the code PROCTR [78] is shown in Figure (5.3.5). and is assumed to be same for both co- and counter-injection. The code treats the fast ion thermalization by solving the Fokker-Planck equation by the moments method. The ion temperature was modeled as explained in Section (3.3). The computed ion temperature profiles are given in Figures.

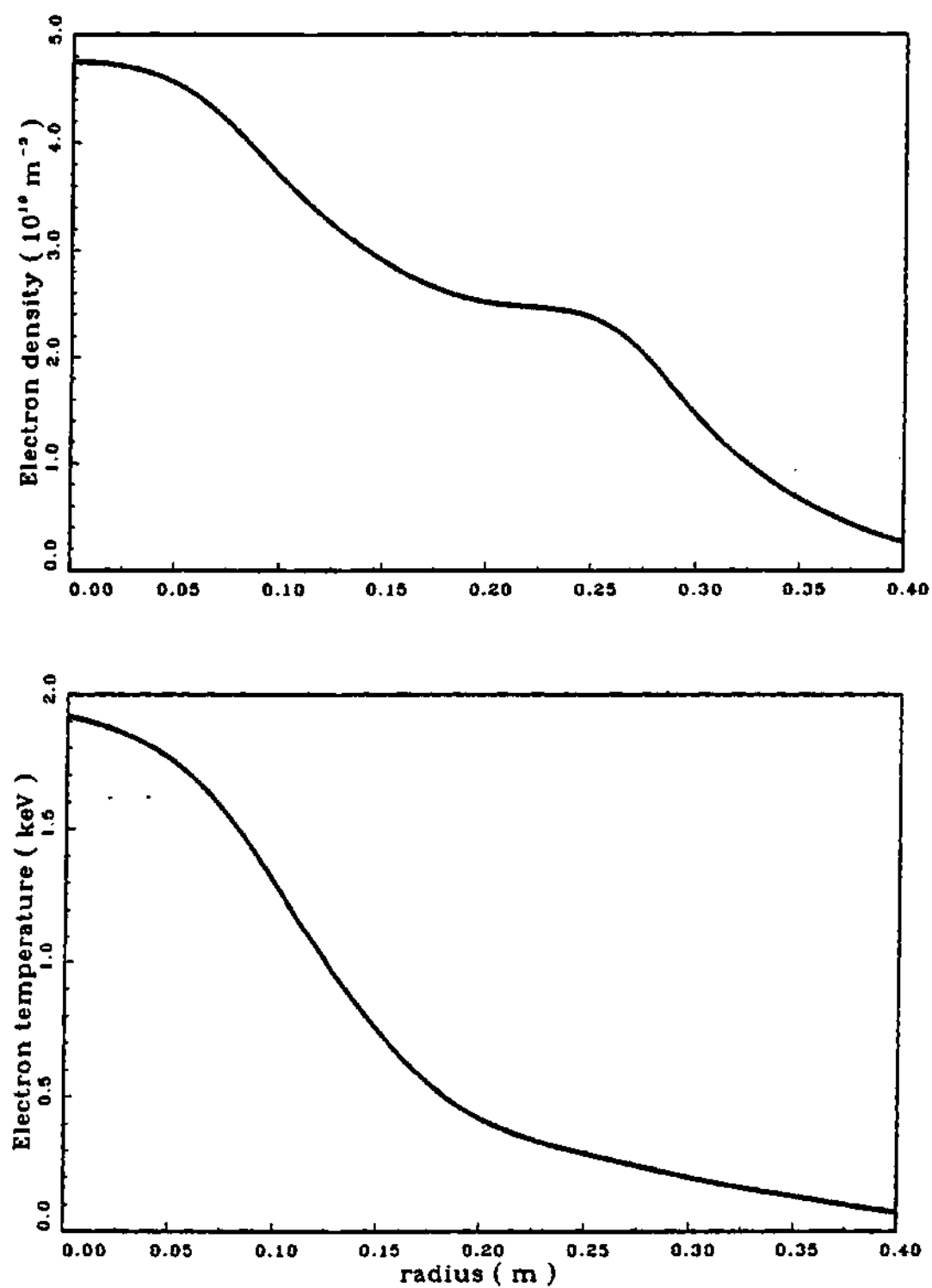


Figure 5.3.1 Electron density and temperature profiles in PLT at 400 ms in the co-injection discharge.

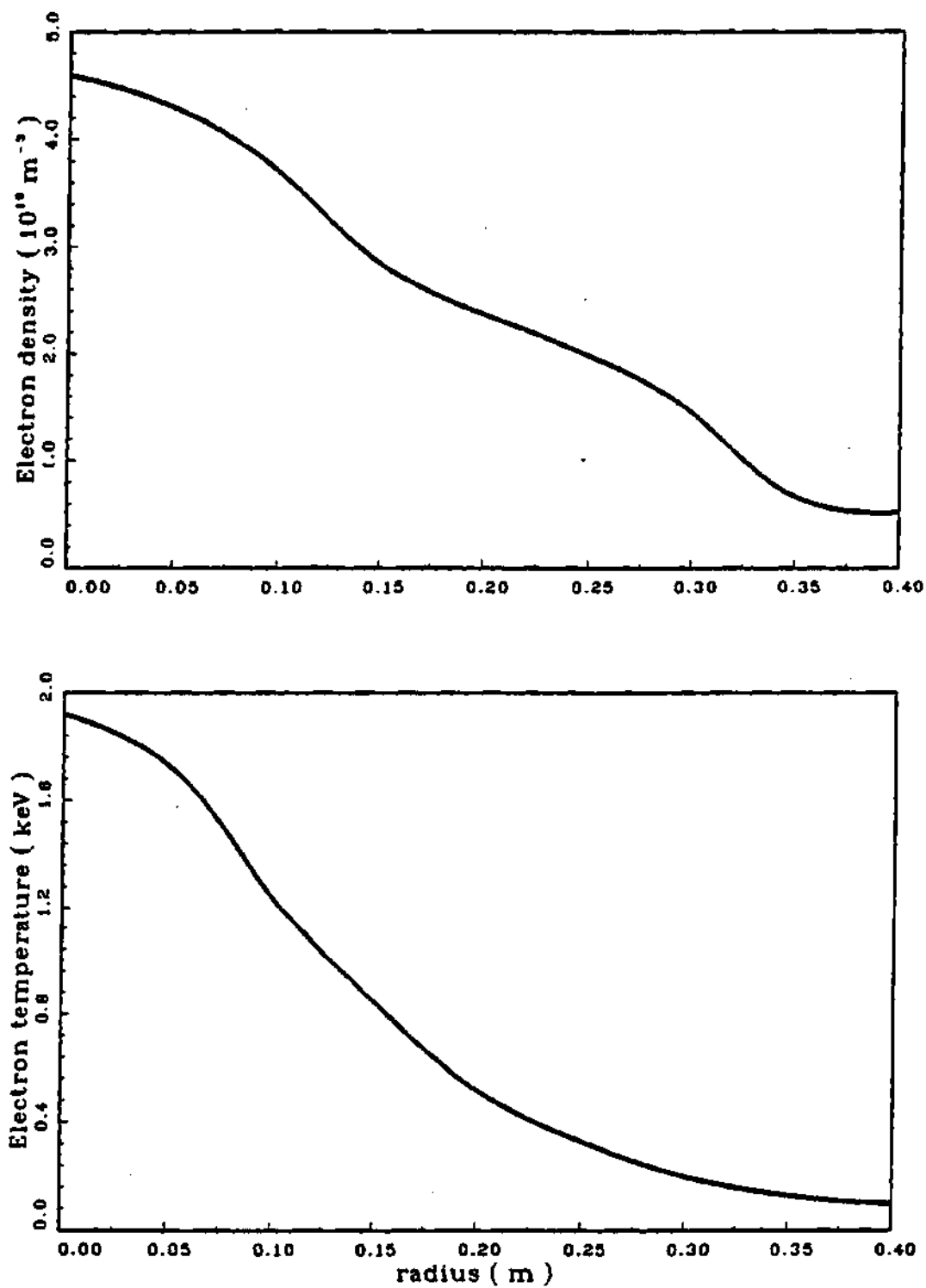


Figure 5.3.2 Electron density and temperature profiles in PLT at 500 ms in the co-injection discharge.



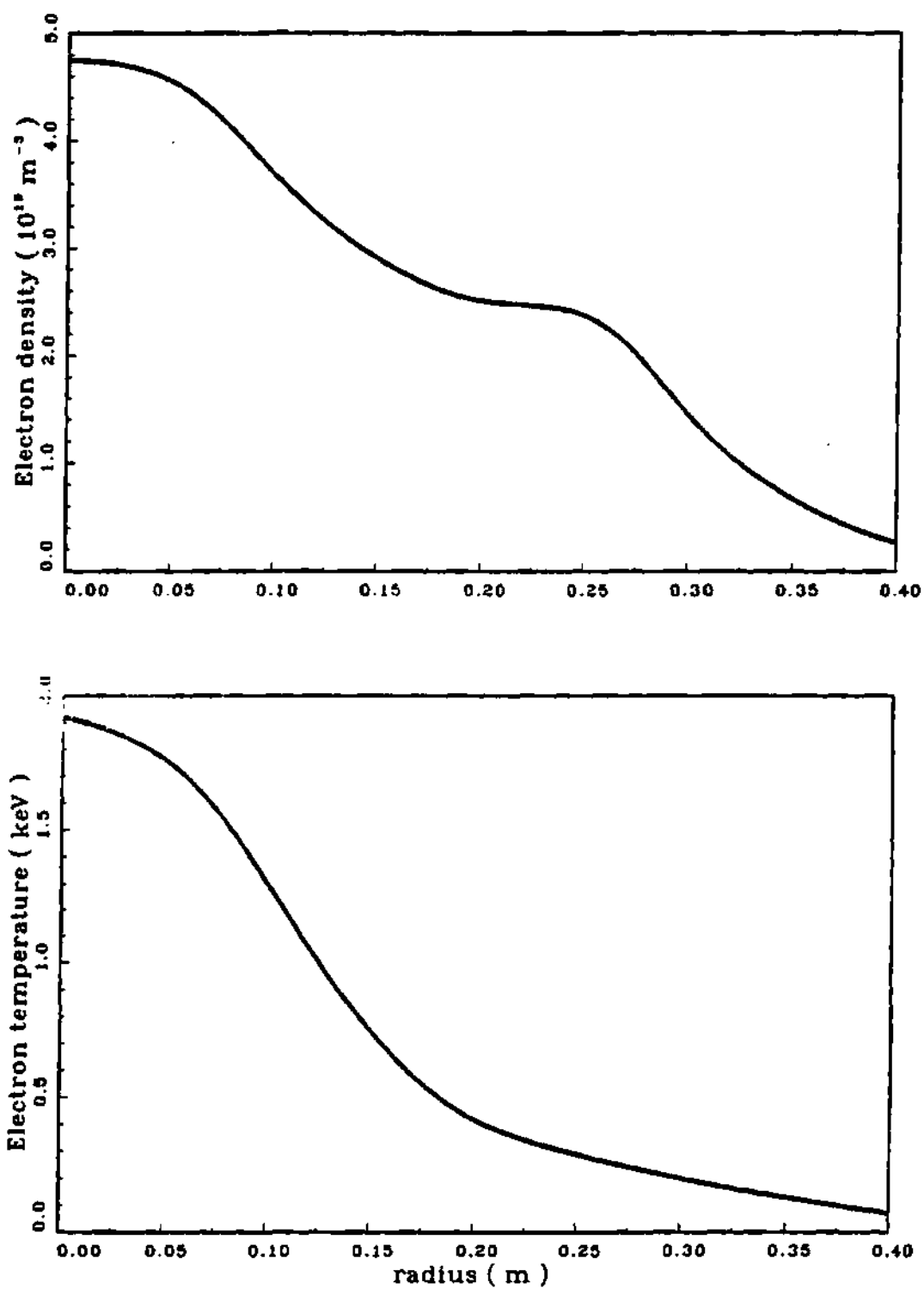


Figure 5.3.3 Electron density and temperature profiles in PLT at 400 ms in the counter-injection discharge.

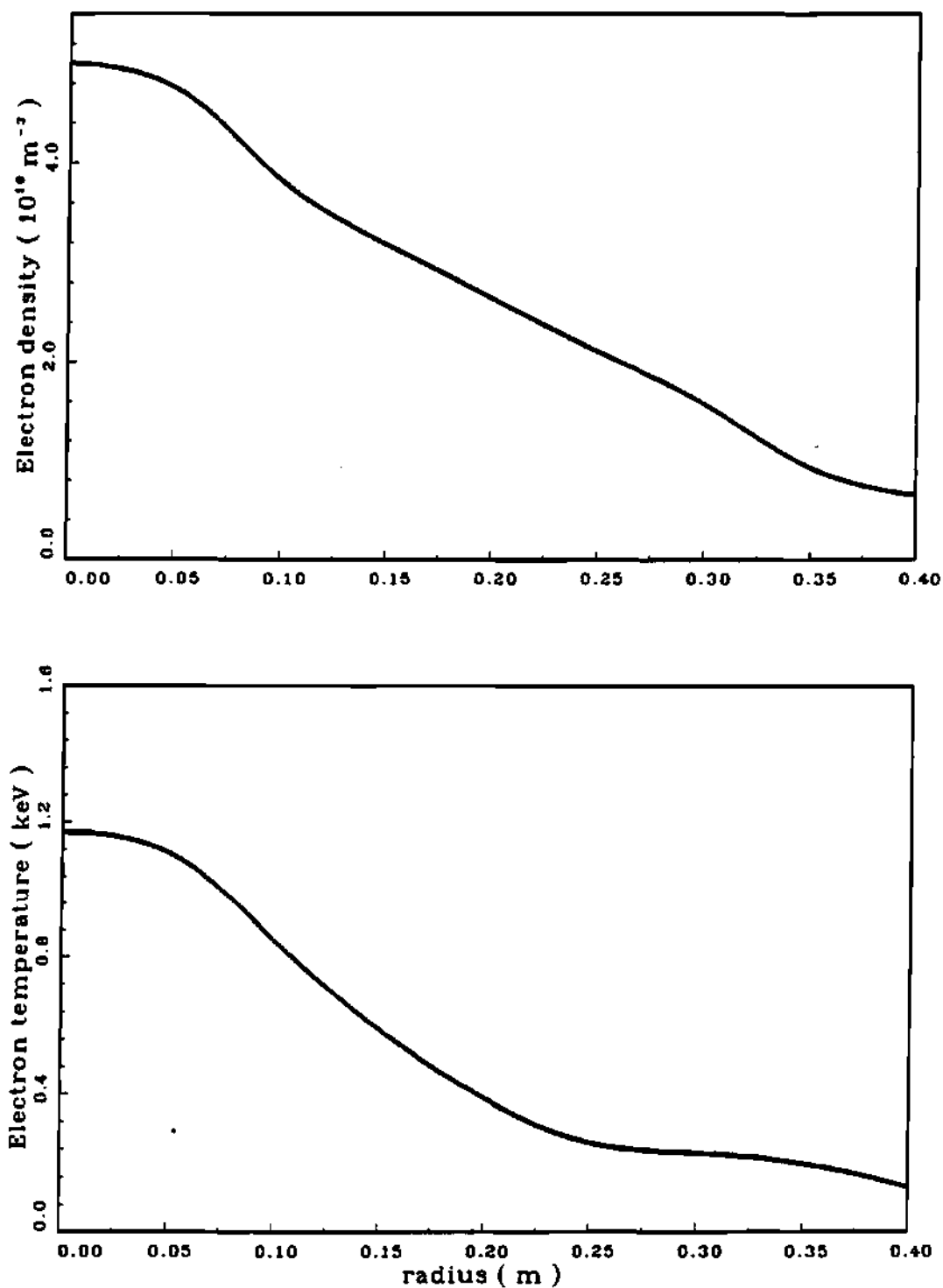


Figure 5.3.4. Electron density and temperature profiles in PLT at 500 ms in the counter-injection discharge.

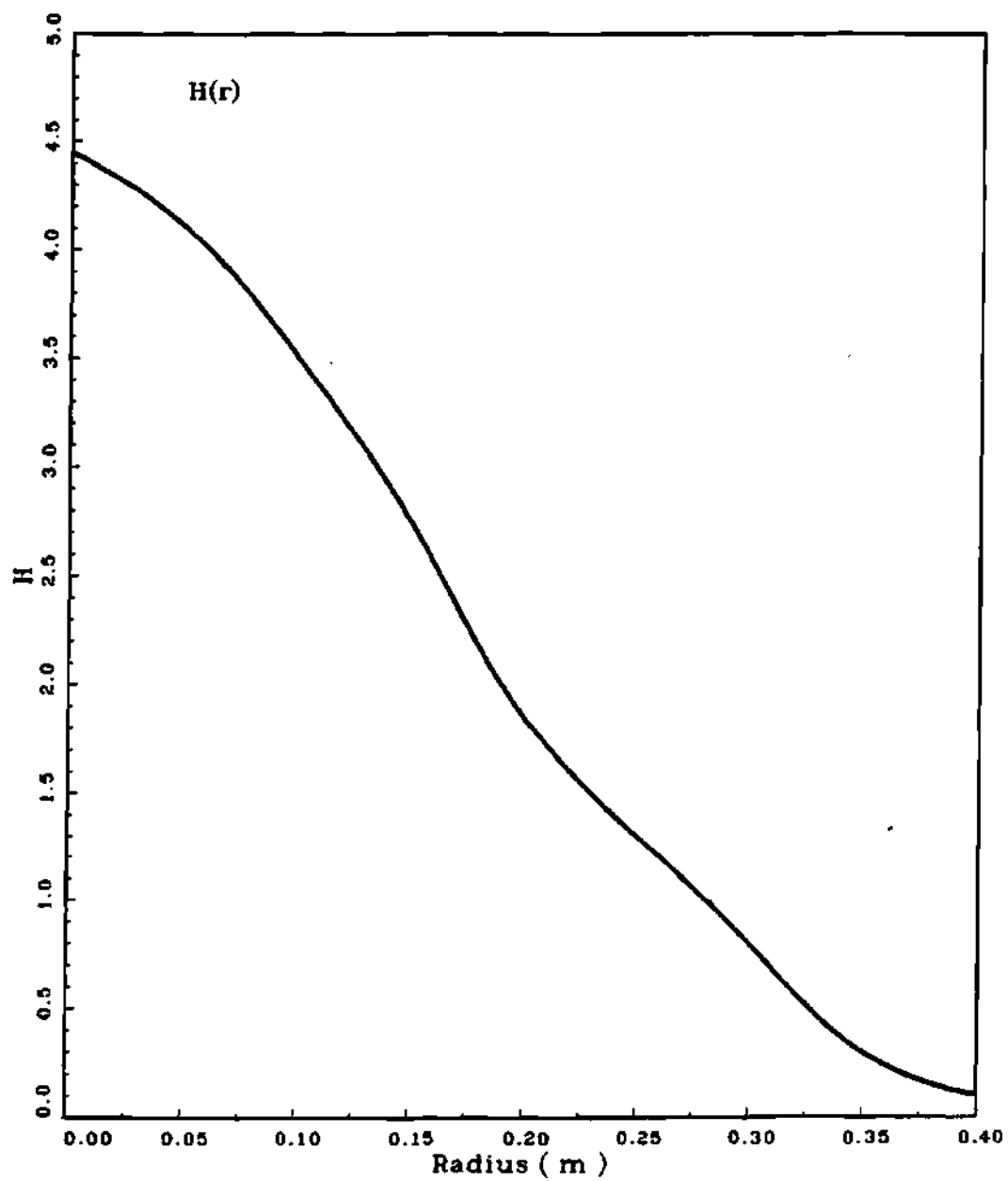


Figure 5.3.5 Beam deposition profile in PLT.

(5.3.6) and (5.3.7) for co- and counter-injection respectively at the initial and the final times. The average charge charge distribution profiles obtained from the average ion model [77] are shown in Figures. (5.3.8) and (5.3.9) respectively for co- and counter-injection at the initial and the final times of the beam injection.

The impurity flow reversal theory [42,43] predicts the radial profiles of impurity density, and impurity fluxes at different points in time. However, the measured quantity in the above set of experiments was the chordal distribution of brightness. To establish proper basis for comparison of theory with experiment. the impurity density predicted by the impurity flow reversal theory [42,43] is used in the atomic physics model [92], described in Section (4.3), to compute the emissivity profile  $\epsilon(r)$ . With this emissivity profile, equation (3.2.1) is integrated to obtain the predicted chordal brightness distribution which is then compared with the measured chordal brightness distribution.

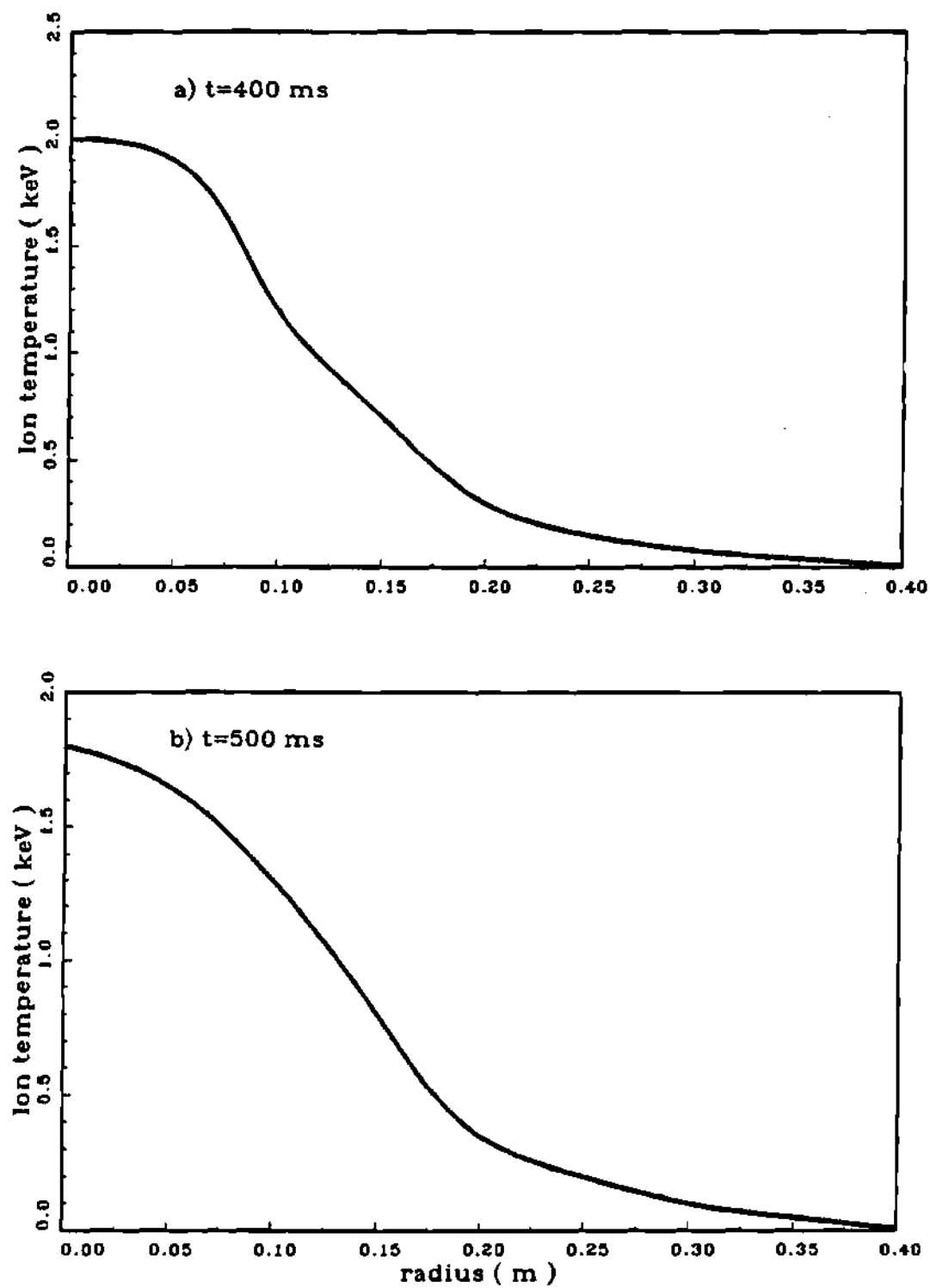


Figure 5.3.6 Ion temperature profiles in PLT with co-injection at 400 and 500 ms.

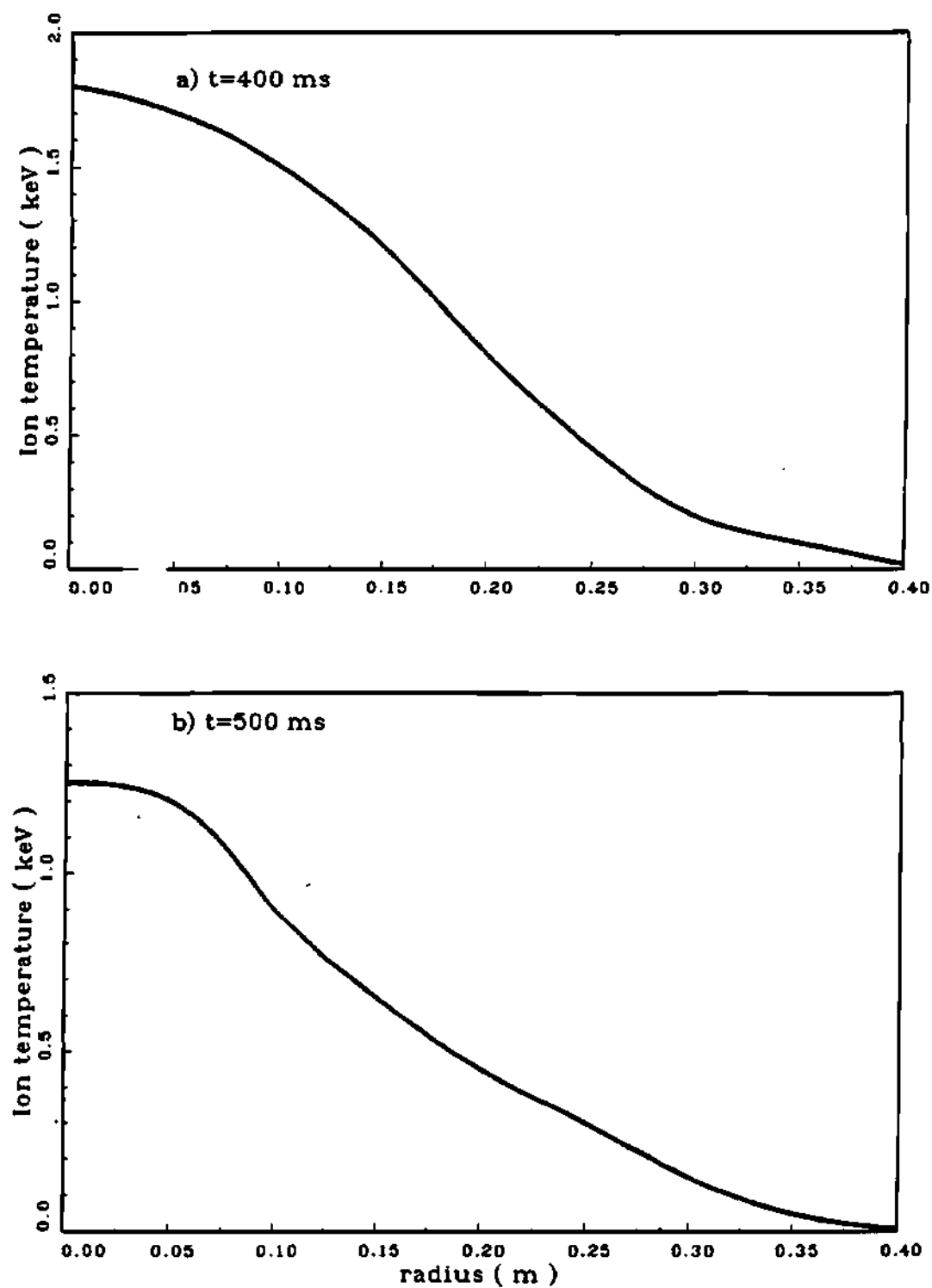


Figure 5.3.7 Ion temperature profiles in PLT with counter-injection at 400 and 500 ms.

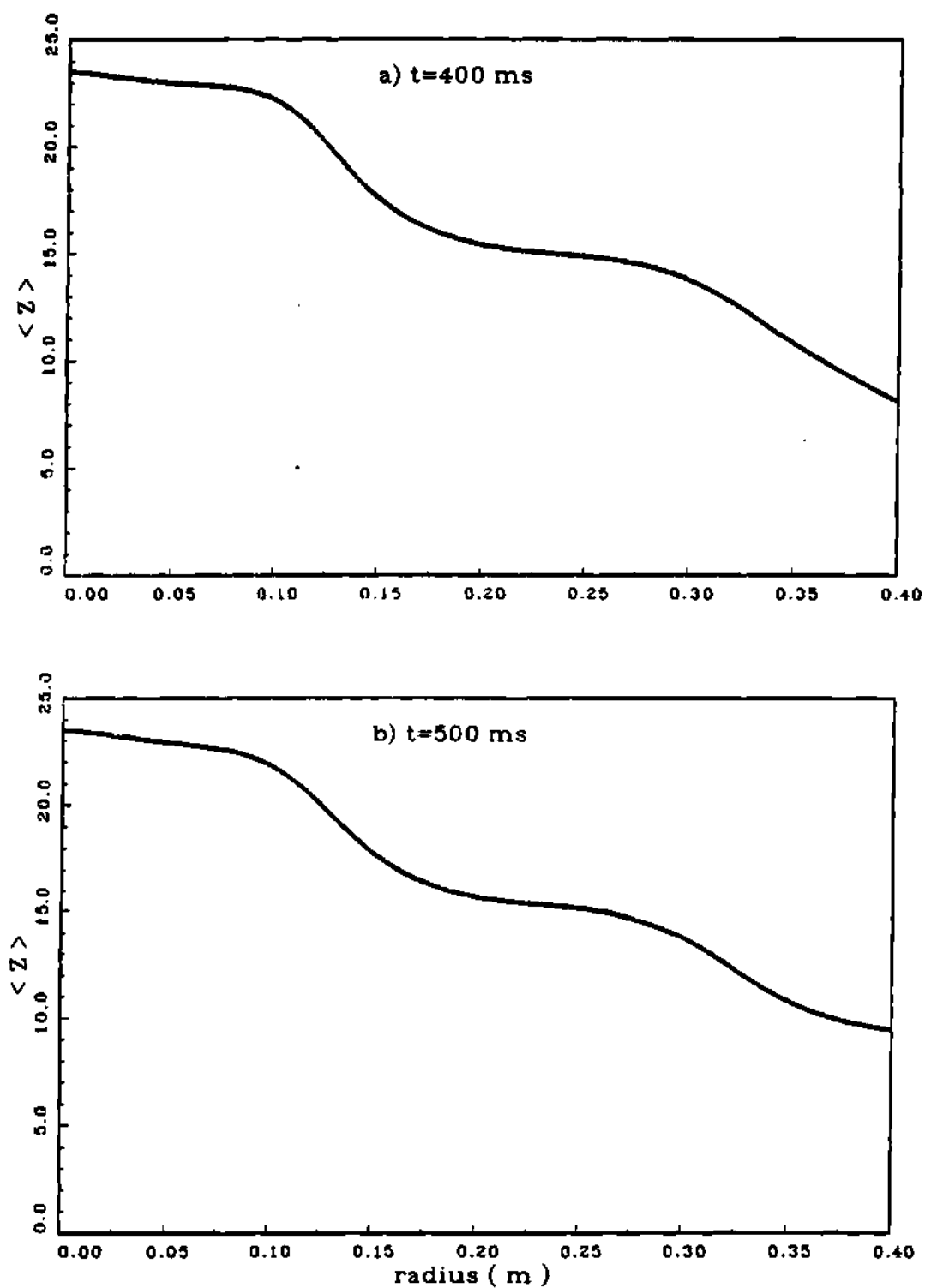


Figure 5.3.8 Average charge state profiles in PLT with co-injection at 400 and 500 ms.

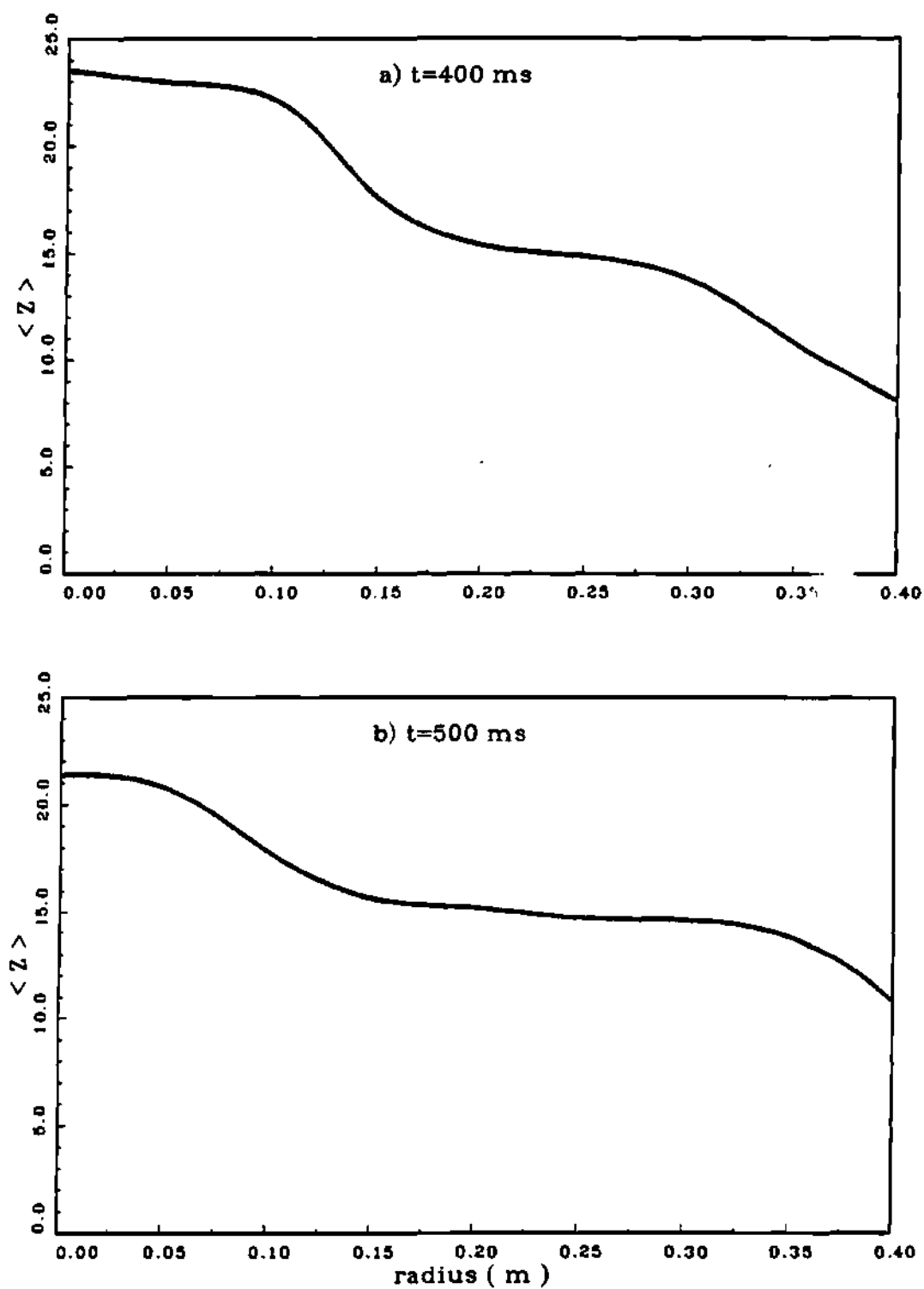


Figure 5.3.9 Average charge state profiles in PLT with counter-injection at 400 and 500 ms.



The information about the initial and the boundary conditions is required to model the impurity flow reversal theory [42,43]. However, the impurity level or distribution at the instant of beam injection is not known from the experimental conditions. The source rate was estimated as detailed in Section (3.3). The initial condition  $n_z(r,t=0)$  was adjusted to match the measured, pre-injection chordal profile [47] for both charge-states at  $t=0$ . The incident impurity flux was then adjusted to match the Fe XV emission. Since Fe XV is located in the neighborhood of 25 cm [47] in the 40-cm discharge, this procedure is equivalent to indirectly determining experimentally the edge boundary condition. Since the chordal brightness of Fe XXIII is predicted well with this procedure, the calculated rate impurity transport is consistent with the observations for both co- and counter-injection. With the estimated initial and boundary conditions (Figs. 5.3.10-12), and the measured data where available, the predicted and the measured chordal profiles are shown in Figure (5.3.13). The theory is seen to model the experimental data quite well. The theory as well as experiment clearly demonstrate that impurity transport is sensitive to the direction of the neutral beam injection.

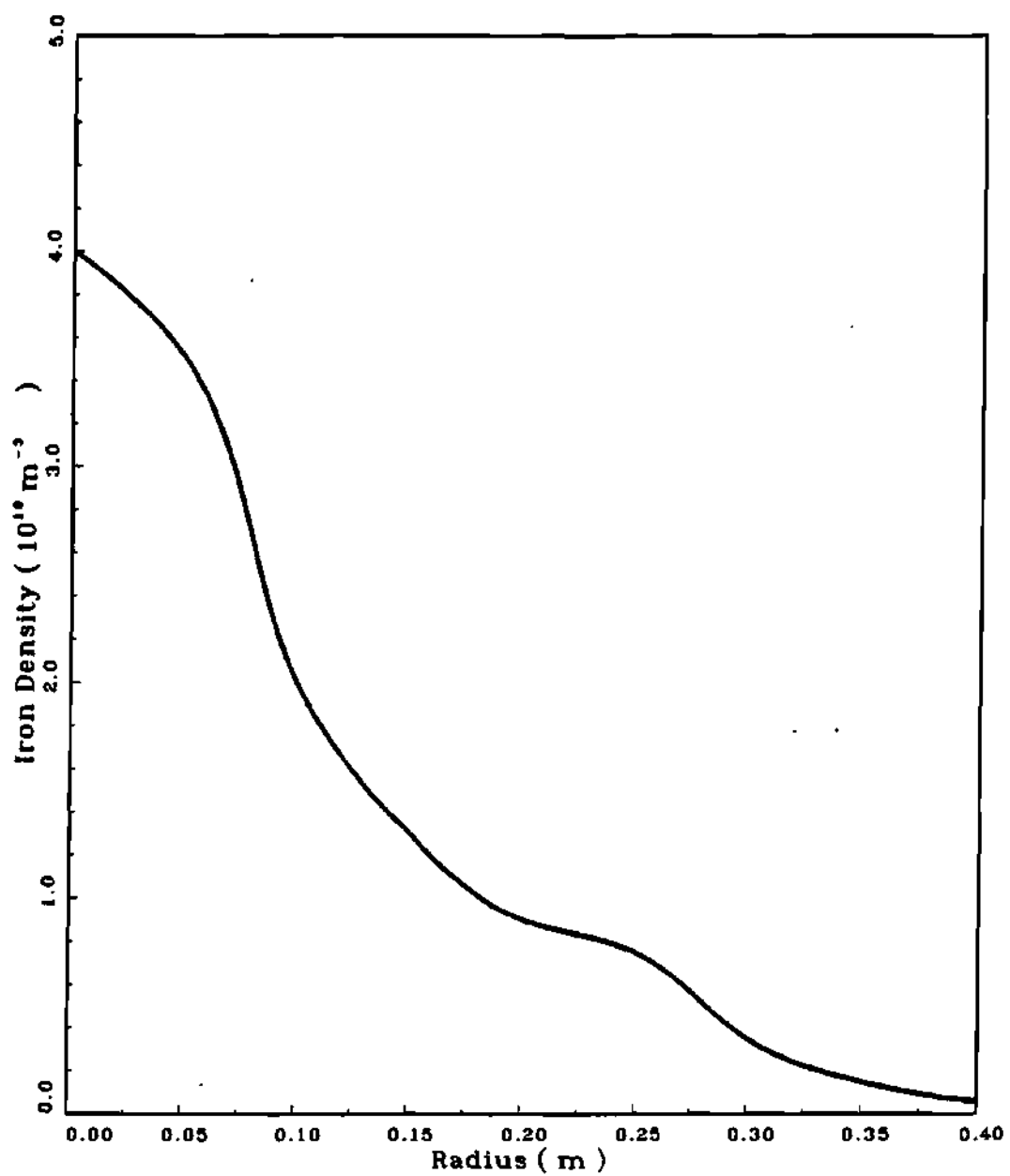


Figure 5.3.10 Theoretical impurity density profile in PLT at 400 ms.

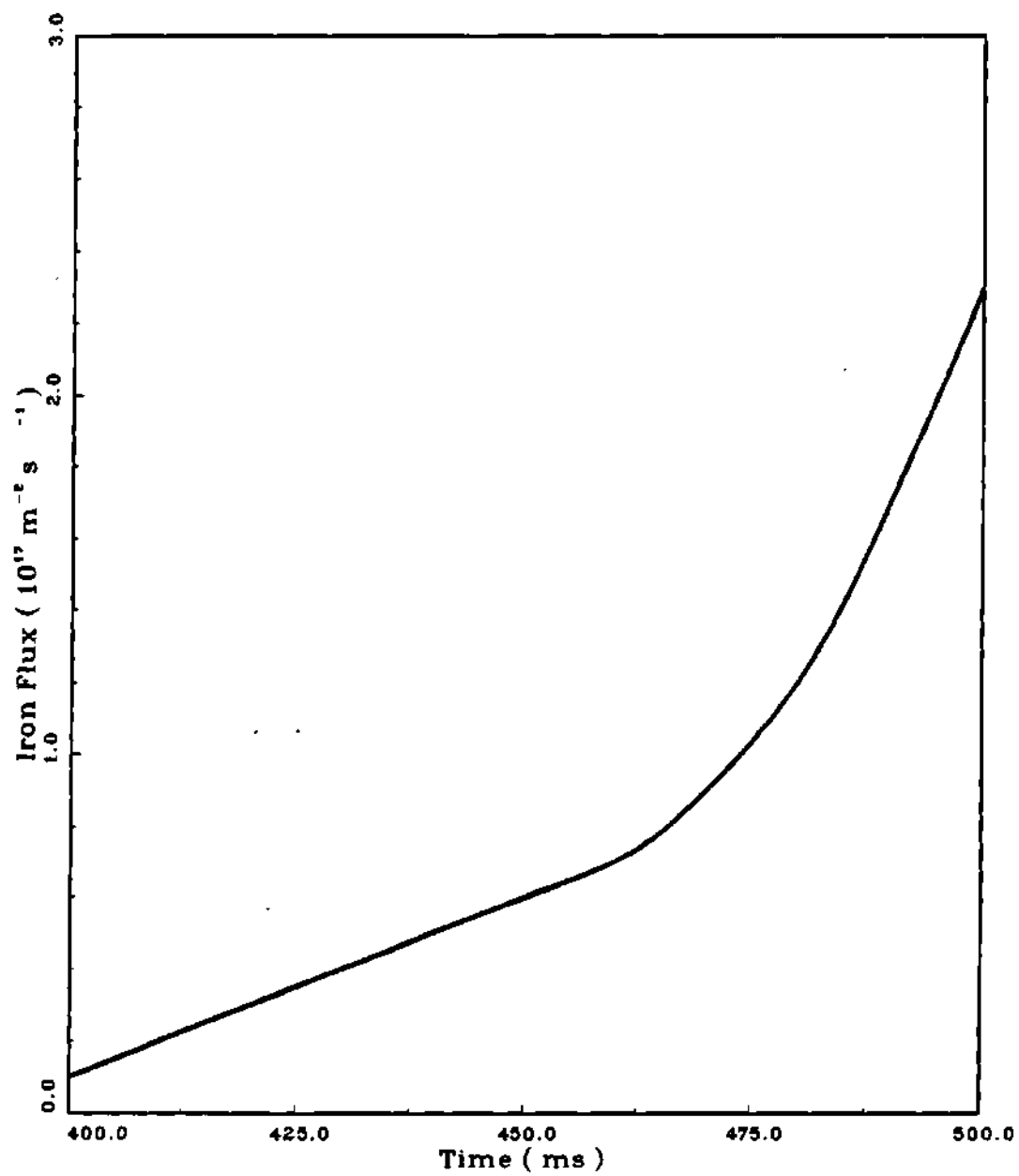


Figure 5.3.11 Theoretical impurity flux history in PLT at 40 cm with co-injection.

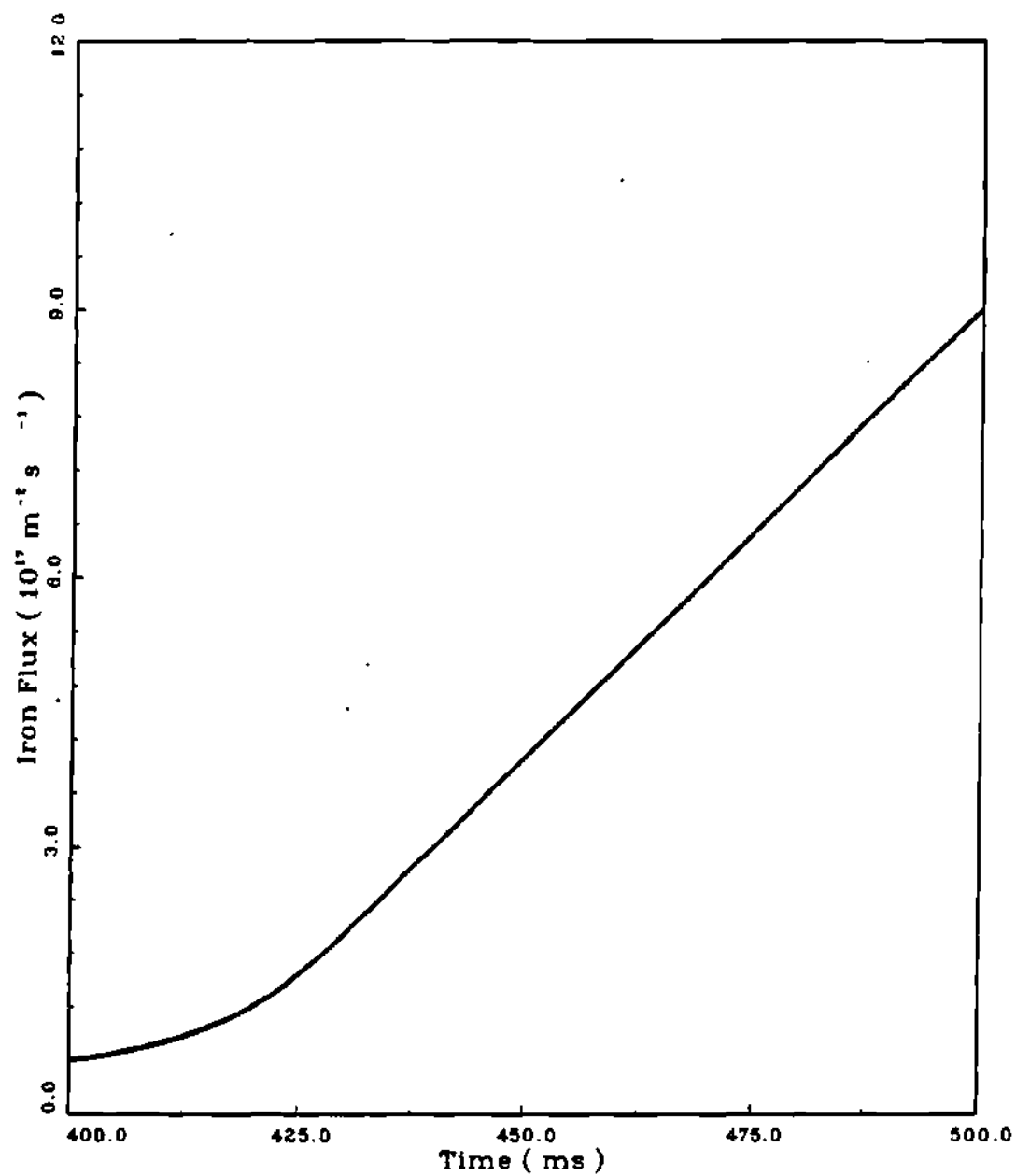


Figure 5.3.12 Theoretical impurity flux history in PLT at 20 cm with counter-injection.

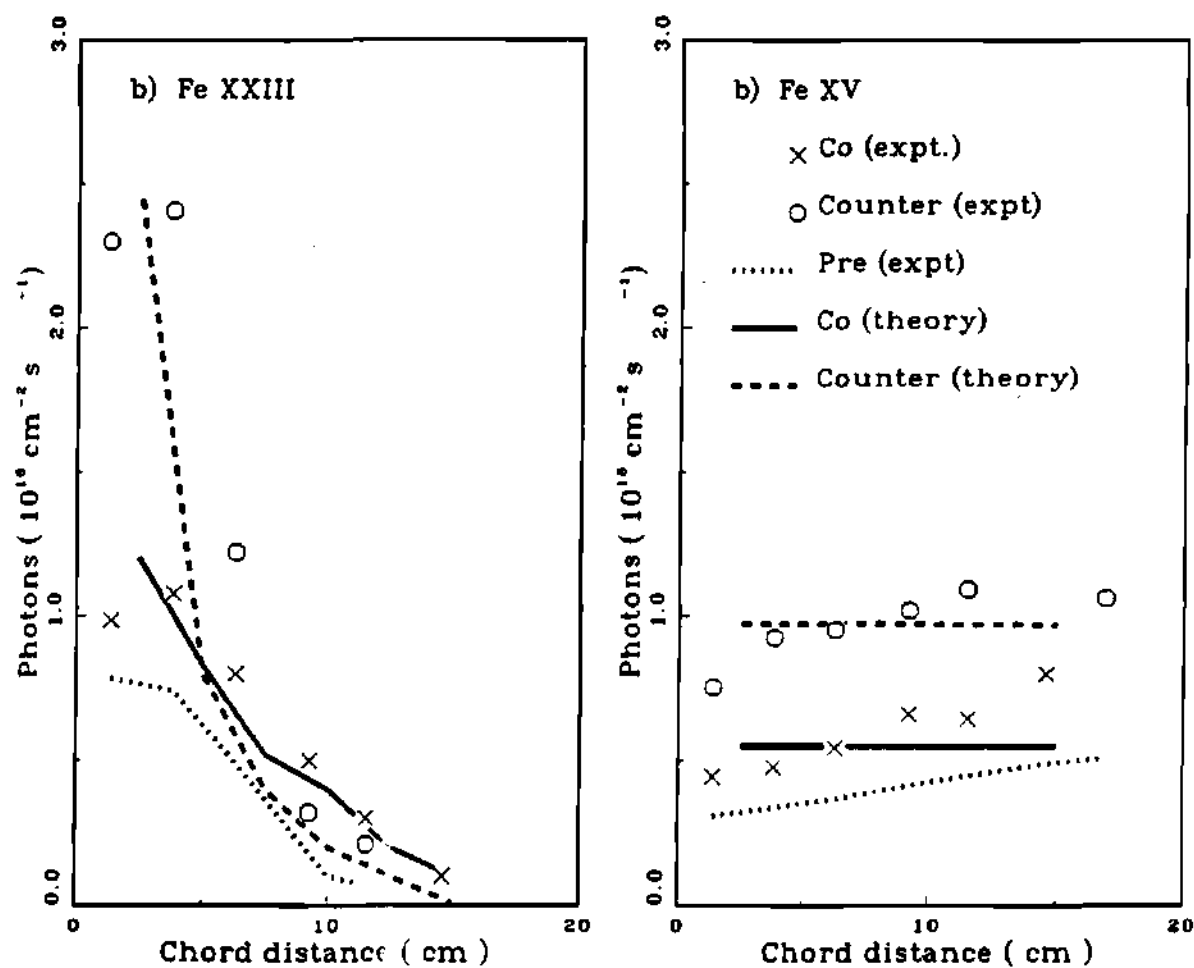


Figure 5.3.13 Brightness distribution of Fe XXIII and Fe XV resonance lines before and during neutral beam co- and counter-injections.

The predicted central toroidal rotation velocity ( $8.9 \times 10^4$  m/s) at  $P_b = 400$  kW compares favorably with the measured [29] central velocity ( $3.8 \times 10^4$  m/s). Thus the use of the gyroviscous theory to compute external drag in impurity flow reversal [42,43] calculations.

#### 5.4 Summary

The impurity flow reversal theory was applied to analyze spectral signals from intrinsic iron impurity in the PLT deuterium discharges with neutral beam injection.

The neutral beam power was approximately 400 kW in each of the co- and counter-discharges, and the beam was on from 400 to 500 ms. The chordal brightness distribution was measured for Fe XV and Fe XXIII in the experiments investigated. The Fe XXIII ion is representative of central radiation, and Fe XV radiates from the radial location in the 25 to 40 cm range in the 40 cm discharge. The spectral measurements demonstrate that the central impurity ion concentration was more than twice in counter-discharge as compared to co-discharge. The soft x-ray signals, and the bolometric measurements support

the experimental conclusion that counter-injection caused substantial central peaking of impurity, in contrast to fairly broad distribution with co-injection. The experimental study also concludes that counter-injection produces a significantly higher radiation losses than either co-injection or simultaneous co- and counter-injection at the same power level. This last observation seems to invalidate the speculation [48] that the substantial central peaking of impurity in the counter-discharges may be due to higher edge source rate of impurity in such discharges.

With the estimated initial and boundary conditions, and the measured data where available, the impurity flow reversal theory was applied to model experimental observations. The chordal brightness distribution predicted by theory clearly matches the measured distribution. Thus, both theory and experiment demonstrate that counter-injection causes a substantial central peaking, whereas a fairly broad distribution is maintained with counter-injection. The quantitative agreement is very good.

CHAPTER VI

ANALYSIS OF

INJECTED SCANDIUM TRANSPORT IN PLT

6.1 Introduction

Suckewer, et al., [48] investigated experimentally the effects of neutral beam injection on impurity transport of the laser-ablated scandium and molybdenum impurities in the PLT tokamak. There are certain advantages in studying impurity transport by deliberately introducing the trace impurities into tokamak plasmas by laser blow-off techniques. The variations in source rates due to intrinsic impurities can lead to ambiguities and uncertainties in impurity transport modeling. The controlled use of impurities can obviate such problems. Also, with controlled use of impurities, the source rate alongwith its location and time of introduction into plasmas are known. With trace impurities, the perturbation effects can be minimized.



The geometry of the experiment and the toroidal location of the various diagnostics are same as shown in Figures (3.1.1). The principal parameters of interest in this study of the PLT tokamak are shown in Table (6.1.1). The experimental results modeled in this study are reviewed in Section (6.2). The analysis of these experiments in relevance to impurity flow reversal theory [42,43] is carried out in Section (6.3).

## 6.2 PLT Experiments with Scandium Injection

The experimental study [48] of impurity transport with neutral beam injection using trace elements scandium and molybdenum has come up with some novel but interesting conclusions. Due to atomic physics complications with molybdenum, we shall consider only scandium for analysis in this work. Even for scandium, the measured data for ionization, recombination, and excitation rates is not available, and at best we have to be content with semi-empirical and scaling results. However, the choice for scandium study is not expected to alter the essential

Table 6.1.1 PLT data with injected scandium

---

Major radius (m)	1.40
Minor radius (m)	0.40
$z_{\text{eff}}$	2.5
Toroidal magnetic field (T)	3.1
Safety factor $q(0)$	1.0
Safety factor $q(a)$	4.0
Neutral beam power (kW)	900.0
Neutral beam energy (keV)	40.0
Model impurity: Scandium	
Plasma type	: $D^+$
Beam type	: $H^0$
Beam tangency radius (m)	1.10
Beam width (m)	0.20
Beam energy components (keV)	40,20,13.3
Beam injection time (ms)	400 - 550
Impurity injection time (ms)	450

---

Table 6.2.1 Scandium transitions

Ion	Wavelength (Å)	Transition
Sc XIX	326(280)	2s-2p
XVIII	180	2s <sup>2</sup> -2s2p
	2908	2s2p( <sup>3</sup> p)
XVII	2190	2s <sup>2</sup> 2p( <sup>2</sup> p)
	193	2s <sup>2</sup> 2p-2s2p <sup>2</sup>
XVI	4354	2s <sup>2</sup> 2p <sup>2</sup> ( <sup>3</sup> p)
XIV	3206	2s <sup>2</sup> 2p <sup>4</sup> ( <sup>3</sup> p)
XVIII	2627	2s <sup>2</sup> 2p <sup>5</sup> ( <sup>3</sup> p)
XIX	505(522)	3s-3p
XIX	423	3s <sup>2</sup> -3s3p

#83X0069

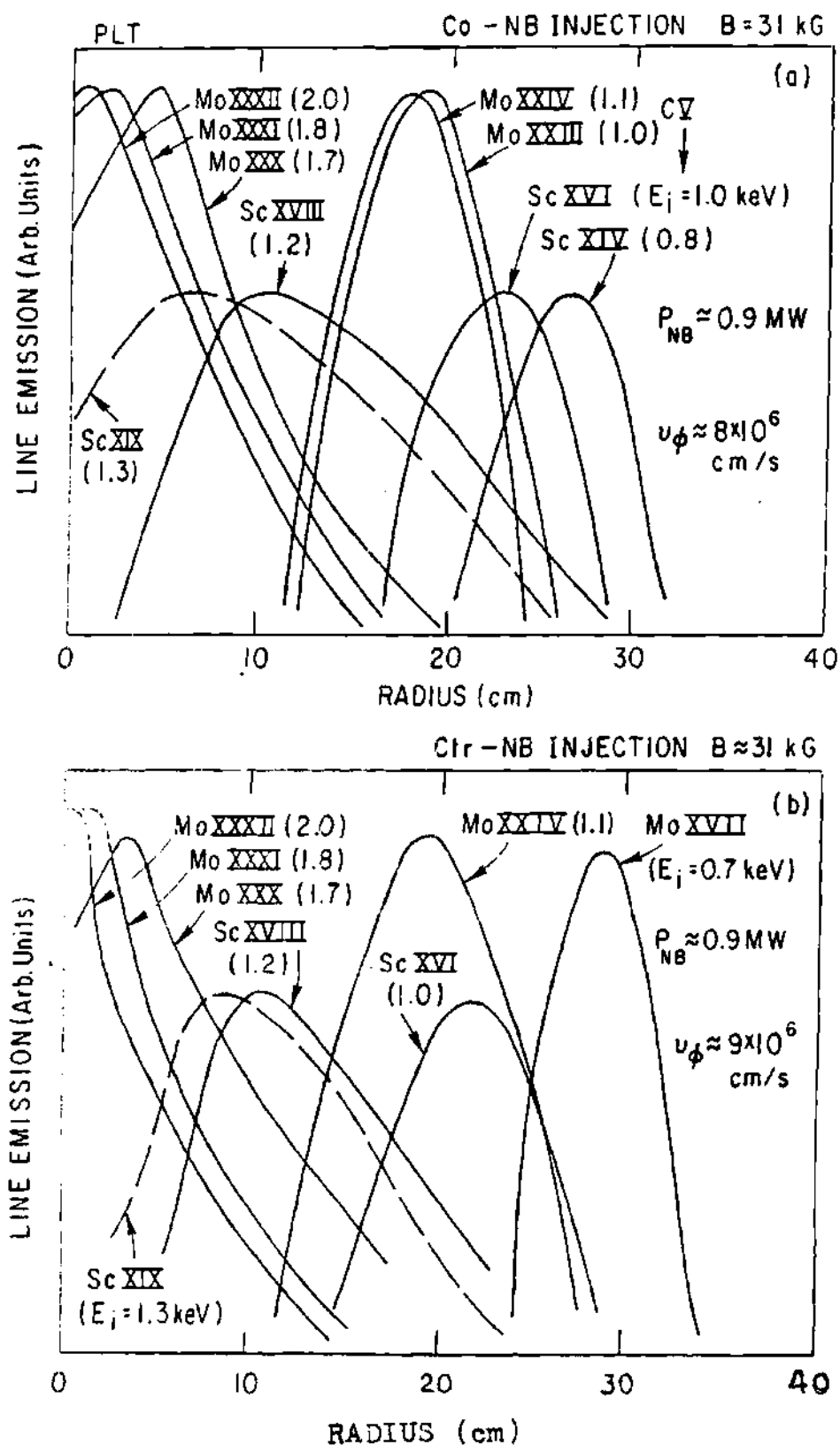


Figure 6.2.1 Measured normalized profiles of line emission from scandium and molybdenum ions in PLT with co- and counter-injection, with 900 kW beam power in each case.

Table 6.2.2 Scandium densities and emissivities [106].

Ion	Wavelength (A)	$n_i(\text{max})$ $\text{m}^{-3}$	Emissivity (max) (photons/ $\text{m}^3\text{-s}$ )	Co/Ctr
Sc XIX	280	$3.2 \times 10^{16}$	$9.4 \times 10^{20}$	Co
		$4.2 \times 10^{16}$	$1.5 \times 10^{21}$	Ctr
Sc XVI	4354	$3.5 \times 10^{16}$	$1.9 \times 10^{18}$	Co
		$3.6 \times 10^{16}$	$2.1 \times 10^{18}$	Ctr
Sc XIV	3206		$1.7 \times 10^{18}$	Co
			$1.2 \times 10^{18}$	Co

plasmas were found to be two to three times larger in the counter-injected case as compared to those with co-injection. This observation was, however, attributed [48] to peripheral plasma conditions, and hence was assumed to be of no consequence in terms of the impact of neutral beam direction on impurity transport. However, the data in terms of absolute measurements was not published. Some of the measured data [106] on absolute measurements of emissivity, and impurity density are given in Table (6.2.2).

### 6.3 Analysis of PLT Experiments

The measured values of density and temperature profiles are known [48] for this study of emission from scandium trace impurity in deuterium plasmas. The electron temperature and density were determined from Thomson scattering measurements, and their time variation from the multi-channel electron cyclotron emission and the microwave interferometer, respectively. The total radiated power was monitored with a fast pyroelectric radiation detector., and the short wavelength emission separately with a soft x-ray fluxmeter. The ion temperature profiles were measured from Doppler

broadening of various intrinsic and injected impurity ion lines, and separately from neutral hydrogen charge-exchange spectra. The measured [48] electron density, electron temperature, and ion temperature profiles are shown in Figure (6.3.1).

We begin by investigating the sensitivity of the normalized emissivity profiles on impurity density in terms of atomic physics alone in the absence of the transport details of the impurity flow reversal theory. The coronal equilibrium model discussed in Section (4.3) was modified to take into account the atomic physics data for scandium. Four very different scandium density profiles including a parabolic profile, and three profiles that peak figure are the experimental electron temperature profiles for co- and counter-injection. The most probable locations of the scandium ions of interest predicted by coronal equilibrium model in terms of electron temperature are also indicated in Figure (6.3.2). With the assumed impurity density profiles (Fig. 6.3.2), and the measured values of the electron density and temperature (Fig. 6.3.1), the normalized emissivity profiles for Sc XVI, Sc XVIII, and Sc XIX predicted by the coronal equilibrium model in terms of the

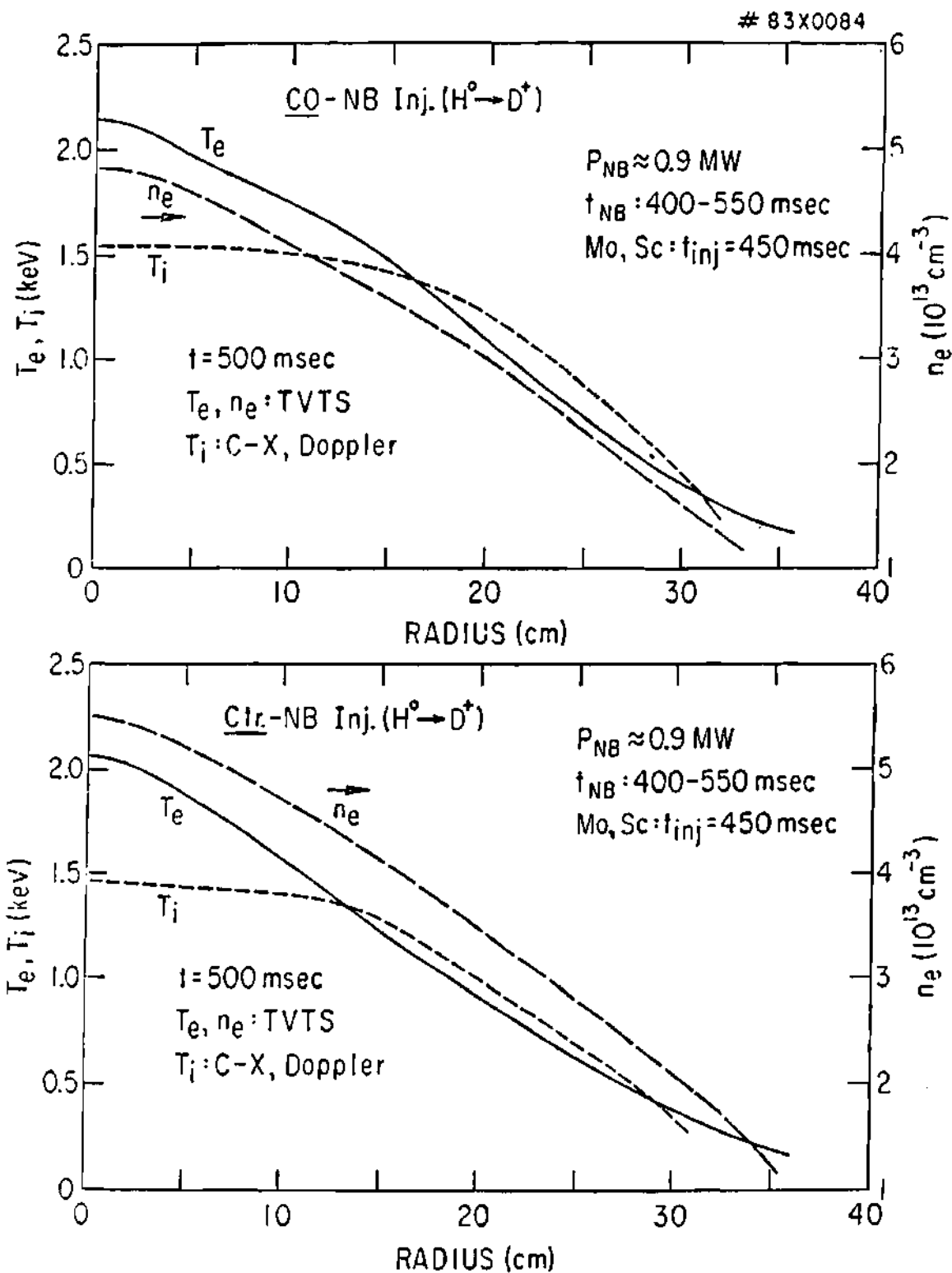


Figure 6.3.1 Measured profiles of electron temperature, electron density, and ion temperature with co- and counter-injection in PLT, with 900 kW power in each case.



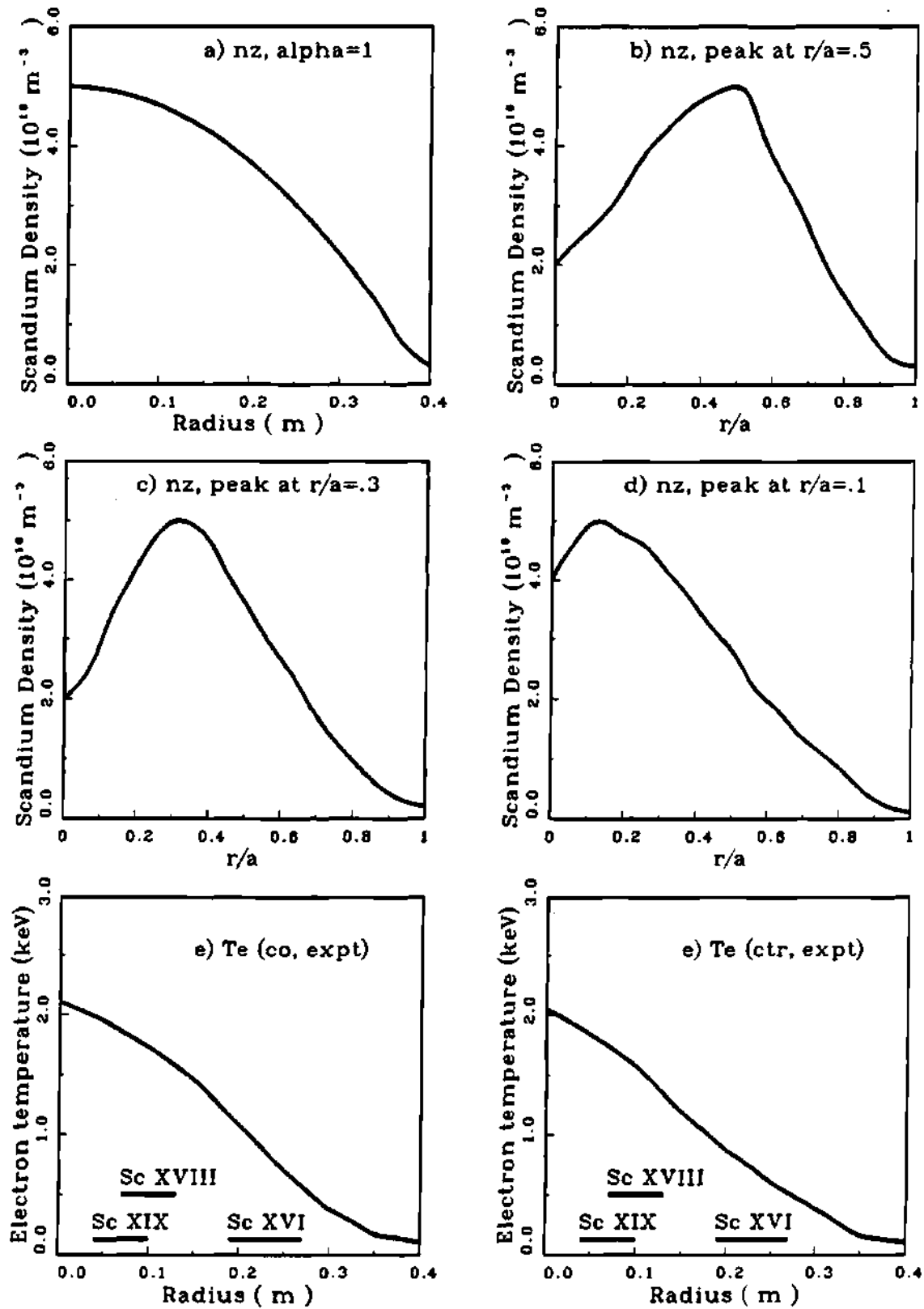


Figure 6.3.2 Assumed impurity density and experimental electron temperature profiles used in scandium sensitivity studies in PLT.

atomic physics data alone are compared with the experimental normalized emissivity profiles in Figure (6.3.3) for both co- and counter-injection. In all cases shown in Figure (6.3.3), the normalized emissivity profiles are not very different from one another. The very different impurity density profiles used demonstrate that the normalized emissivity profiles are not very sensitive to impurity density profile. It is noteworthy that the normalized emissivity profiles are not only rather insensitive to impurity density profile, but are almost identical for both co- and counter-injection under the prevailing experimental conditions in the given set of experiments in agreement with the views expressed in Ref. [48].

The sensitivity of the normalized emissivity profiles for scandium ions to electron temperature was studied next, again only in terms of the atomic physics model without introducing the details of the impurity flow reversal theory [42,43] into these calculations. Three electron temperature profiles including the experimental, the parabolic, and the parabolic-cubed were used for this purpose. The impurity density profile used in the three cases was a parabolic profile

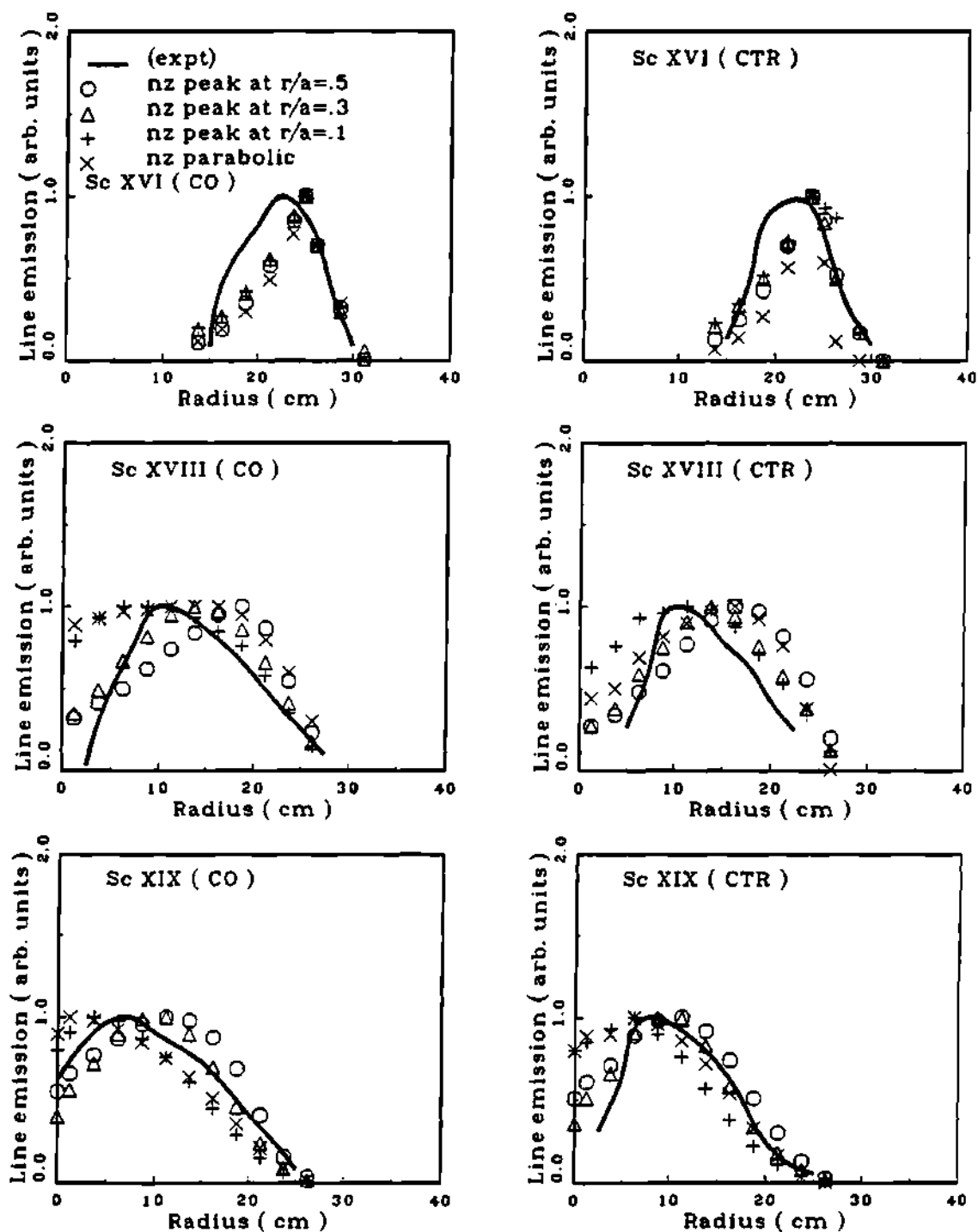


Figure 6.3.3 Sensitivity of normalized emissivity profiles of scandium ions with scandium density profiles in PLT.

with the central value set arbitrarily equal to  $5.0 \times 10^{16} \text{m}^{-3}$ . The experimental [48] and the predicted normalized emissivity profiles are shown in Figure (6.3.4). The results are clearly very sensitive to the assumed electron temperature profiles.

The results shown in Figures (6.3.3-4) demonstrate clearly that the normalized emissivity profiles of scandium depend primarily upon  $T_e(r)$  and only weakly upon  $n_z(r)$ , hence providing a rather poor test of transport effects since the trace impurities have no effect upon  $T_e(r)$ .

We finally applied the impurity flow reversal theory [42,43] in combination with the coronal equilibrium model to analyze the experimental observations. The calculational details are similar to those explained in Chapter IV. The measured data [48] for electron density, electron temperature, and ion temperature shown in Figure (6.3.1) were used in this investigation. The values of the average charge-state in terms of electron temperature were determined from the average ion model [77]. The beam shape factor was

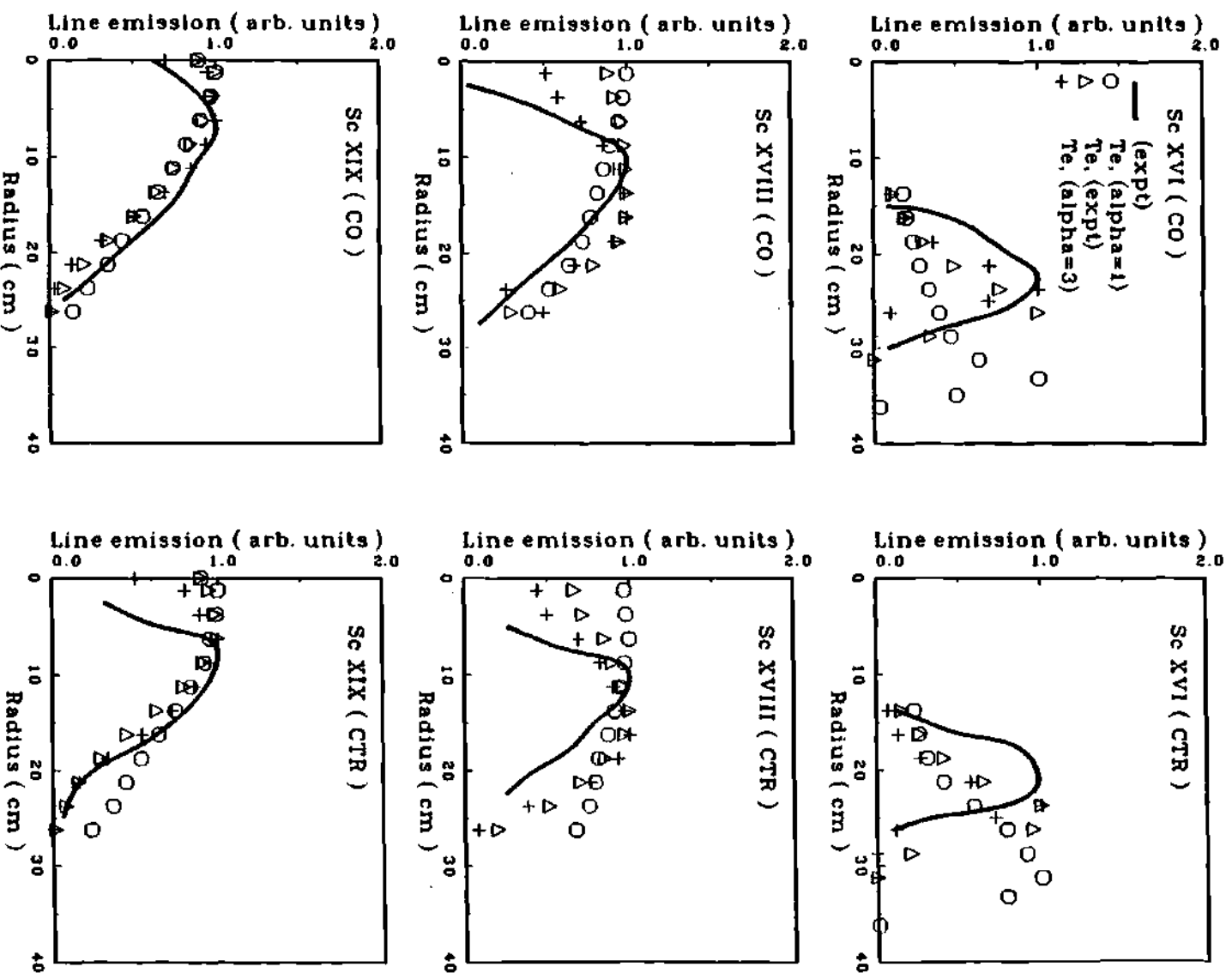


Figure 6.3.4 Sensitivity of normalized emissivity profiles of scandium ions with electron temperature profiles in PLT.

computed using the code PROCTR [78]. The gyroviscous theory [54] of momentum transport was used to predict external drag required in the impurity flow reversal calculations [42,43].

The impurity level or distribution before or during beam injection is not reported in the experiments [48] being investigated. This obviously makes the task of using an impurity transport model to analyze experimental data very difficult. In the model used, the initial impurity distribution at the instant of impurity injection was taken to be negligible. To model the contribution of a source to impurity density at edge, we assumed

$$n_z(r=a,t) \approx n_z(r=a,t=0)e^{-t/\tau} \quad (6.3.1)$$

The value of  $n_z(r,t)$  can be made to represent an instantaneous source by a suitable choice of  $\tau$  to simulate injected impurities. For a fixed  $\tau=1$  ms, the value of  $n_z(r=a,t=0)$  was adjusted to reproduce at 20 ms after impurity injection the measured [106] values of the maximum impurity densities for Sc XVI and Sc XIX shown in Table (6.2.2). With this value of  $n_z(r=a,t=0)$ , Equation (6.3.1) was assumed to be a true representation of the injected source. The impurity flow

reversal theory [42,43] was then used to predict the normalized emissivity profiles of scandium ions. The predicted and the measured [48] normalized emissivity profiles are shown in Figure (6.3.5). The agreement between the theory and the experiment is remarkable.

The gyroviscous theory [54] theory was used in the transport calculations to predict external drag. The fact that the predicted rotation velocity  $v_{\phi,i}(\text{theory})=1.4 \times 10^5$  m/s compares favorably with the measured [29] rotation velocity  $v_{\phi,i}(\text{experiment})=0.8 \times 10^5$  m/s, justifies the use of gyroviscous theory to predict external drag for use in calculations based on impurity flow reversal theory [42,43].

#### 6.4 Summary

This chapter was devoted to study spectral measurements from injected scandium impurity in neutral beam injected deuterium discharges.

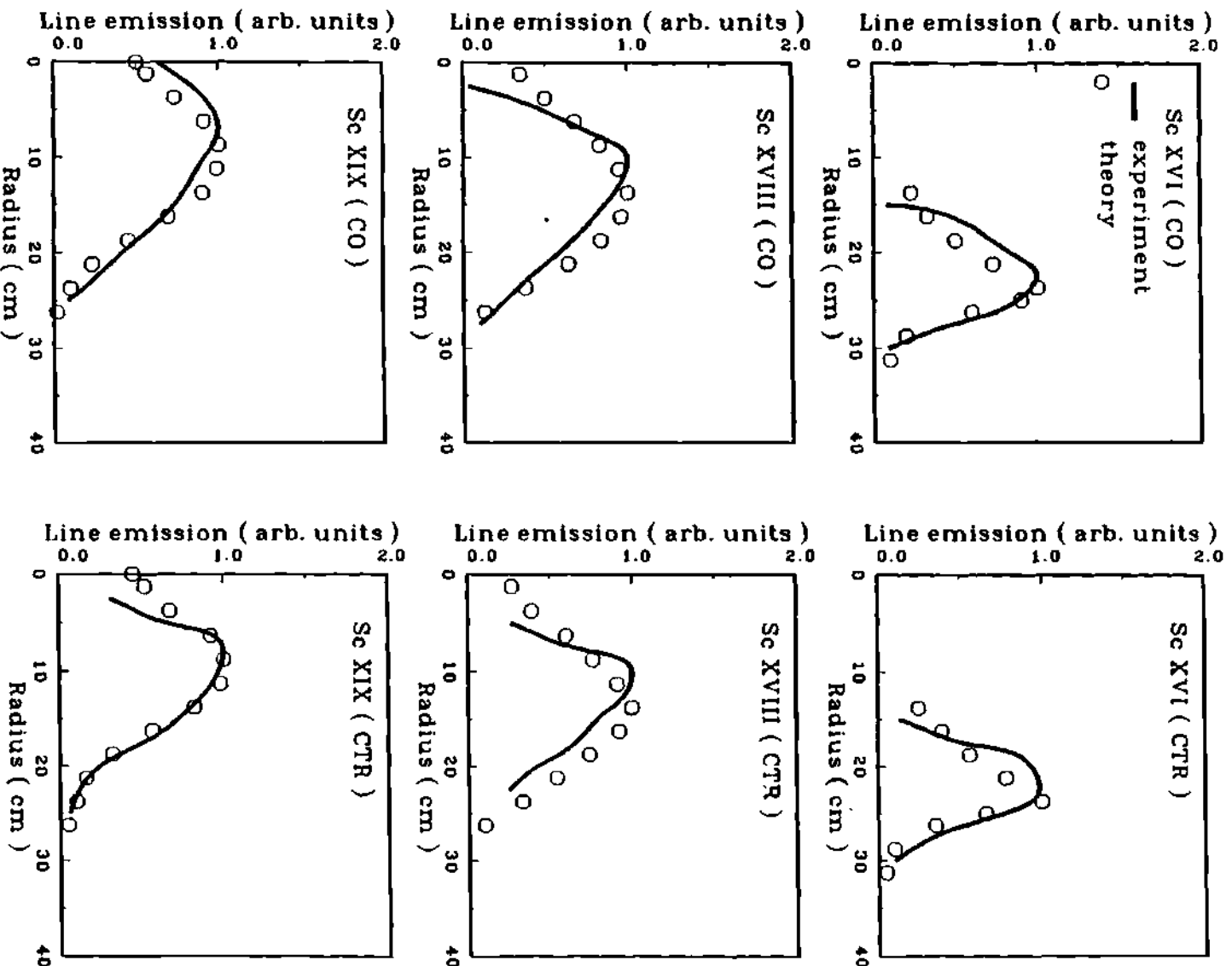


Figure 6.3.5 Comparison of measured and predicted normalized emissivity profiles of scandium ions in PLT.



The experimental group [48] found the individually normalized emissivity profiles of scandium and molybdenum ions to be similar with both co- and counter-injection. This observation was used in Reference [48] to conclude that impurity transport was insensitive to neutral beam direction. However, significant and reproducible quantitative differences were found with co- versus counter-injection. The counter-injection was found to cause a factor of three larger central concentration of impurity ions as compared to that in the co-injection case. However, the absolute measurements were not reported in any detail.

As a first step to investigate the experimental results, the sensitivity of these results was studied in terms of the atomic physics alone. Very different impurity profiles used did not show any appreciable effect on the normalized emission profiles. This indicates that the way that the experimental results are normalized makes them insensitive to impurity density, and hence a poor reflection of impurity transport. In contrast to rather poor sensitivity of the normalized emissivity profiles to impurity density, the results were found to be very sensitive to electron temperature. Since

trace impurities do not change electron temperature, the normalized emissivity profiles provide a rather poor test of the transport effects. The theory was shown to calculate the normalized results rather well.

Since measured electron temperature profiles are not very different in the co- and counter-discharges, it is not surprising that atomic physics considerations would lead to similar normalized emission profiles irrespective of the beam direction as was indeed observed in these experiments. However, in the absence of more detailed measurements under less restrictive conditions, it does not seem to be justified to conclude that impurity transport is insensitive to neutral beam direction.

## CHAPTER VII

### ANALYSIS OF ROTATION EXPERIMENTS

#### 7.1 Introduction

The momentum confinement times inferred from toroidal rotation measurements in the PLT [28,29,107], PDX [30,31,107], and ISX-B [32,33,108] tokamaks are one to two orders of magnitude shorter than would be predicted on the basis of the neoclassical perpendicular viscosity [109]. This situation led to the impression that an anomalous phenomenon was responsible for the momentum confinement times in the experiments. Stacey and Sigmar [54] proposed a theory based upon the neoclassical gyroviscosity and showed that the gyroviscous force is of the right order of magnitude to correctly explain the measured momentum confinement time. The gyroviscous theory was reviewed in Chapter II. The theory is applied in this chapter to analyze rotation data from the PLT, and the PDX tokamaks. The procedure adopted to analyze the rotation data is explained in Section (7.2). The analysis of

the rotation data from the PLT and the PDX tokamaks is presented in Sections (7.3) and (7.4) respectively.

## 7.2 Procedure to Analyze Rotation Data

According to gyroviscous theory [54], the toroidal momentum confinement time can be approximated to within an  $O(1)$  multiplier to

$$\tau_{\phi}^{-1} = \nu_d = T_i / (2R^2 Z e B) \quad (7.2.1)$$

where  $\tau_{\phi}$  is the toroidal momentum confinement time,  $\nu_d$  is the drag frequency [22,23,42,43],  $T_i$  is the ion temperature,  $R$  is the major radius and  $Z$  is the ionic charge-state.

The procedure to compare momentum confinement time predicted by gyroviscous theory with that inferred from experiment is explained in Reference [110]. When unbalanced neutral beam injection is applied in the co- or counter-direction to a tokamak plasma, a toroidal rotation of the bulk plasma is observed to take place in the direction of the neutral beam momentum input. When the beam is turned on,

the toroidal rotation builds up to an asymptotic value; and when the beam is then turned off, the toroidal rotation velocity decays more or less exponentially. The toroidal rotation velocity is usually measured from the Doppler shift of spectral lines from intrinsic or injected impurities. The toroidal confinement time can be inferred from the asymptotic rotation velocity during beam injection, as well as from the decay of the rotation velocity after beam termination. Both of these procedures are explored in this analysis of the rotation data.

In interpreting the rotation, the experimentalists use a toroidal momentum balance on ion species  $j$  of the form

$$n_j m_j \partial v_{j\phi} / \partial t = M_{j\phi} - n_j m_j v_{j\phi} / \tau_{j\phi} - n_j m_j \sum_k \nu_{jk} (v_{j\phi} - v_{k\phi}) \quad (7.2.2)$$

where  $n_j$  and  $m_j$  are the ion density and mass,  $v_{j\phi}$  is the toroidal rotation velocity,  $M_{j\phi}$  is the toroidal momentum input from the beam,  $\tau_{j\phi}$  is the toroidal momentum confinement time, and  $\nu_{jk}$  is the interspecies collision frequency between species  $j$  and  $k$ . The second term on the right side of Equation (7.2.1) represents loss of toroidal momentum of species  $j$  due

to radial transport, and the third term represents loss of toroidal momentum of species  $j$  due to transfer to species  $k$ . To make contact with the theory, we shall use Equation (7.1.1) to associate the  $\tau_{j\phi}$  with the gyroviscous force.

### 7.2.1 Steady-state Rotation Velocity Measurement

One experimental technique for determining the momentum confinement time is to measure the asymptotic, steady-state rotation velocity for an impurity species, then assume that all species have the same rotation velocity and perform a momentum balance on the bulk plasma. Using the steady-state version of Equation (7.2.2), together with the assumption  $v_{j\phi} \sim v_{\phi}^{\text{exp}}$  for all species, and summing over species yields

$$\begin{aligned} M_{\phi} &= \sum_j M_{j\phi} = \sum_j n_j m_j v_{j\phi} / \tau_{j\phi} \\ &\approx \sum_j n_j m_j v_{\phi}^{\text{exp}} \equiv n_p m_p v_{\phi}^{\text{exp}} / \tau_{\phi}^{\text{exp}} \end{aligned} \quad (7.2.3)$$

where

$$n_p m_p \equiv \sum_j n_j m_j$$

Thus, the  $\tau_{\phi}^{\text{exp}}$  inferred experimentally in this manner is an effective momentum confinement time for the bulk plasma. In comparing with this  $\tau_{\phi}^{\text{exp}}$ , Equation (7.2.1) should be regarded as applying to a bulk plasma with effective ionic charge  $Z_{\text{eff}}$ ,

$$\tau_{\phi}^{\text{th}} = 2R^2 Z_{\text{eff}} e B^0 / T \quad (7.2.4)$$

The directly measured quantity is the rotation velocity. The corresponding theoretical expression is found by using Equation (7.2.1) in the steady-state momentum balance on the bulk plasma,

$$v_{\phi}(r) = f_{\text{peak}}(r) P_b (2R^2 Z_{\text{eff}} e B^0) / (2m_b / E_b) / (m_p V_p n_p(r) T(r)) \quad (7.2.5)$$

where  $P_b$ ,  $E_b$  and  $m_b$  are the total beam power, the energy and the mass of the beam particles, respectively,  $V_p$  is the plasma volume, and  $f_{\text{peak}}$  is the local-to-average beam momentum deposition peaking factor.

The central ion temperature in a beam-heated tokamak plasma can usually be represented by

$$T_i(0) = T_{OH}(0) + CP_b/n_e \quad (7.2.6)$$

where  $C$  is the heating efficiency.

Combining Equations (7.2.5) and (7.2.6) leads to an equation for the central toroidal rotation velocity:

$$v_\phi(0) = f_{peak}(0) n_e (\sqrt{(2m_b/E_b)} (2R^2 e Z_{eff} B^0) [(P_b/n_e)/(T_{OH}(0) + C(P_b/n_e))] / (v_p n_p(0) m_p) \quad (7.2.7)$$

### 7.2.2 Decay of Rotation Velocity after Beam Turn-off

The decay of the toroidal rotation velocity after termination of neutral beam injection provides another means for determining the momentum confinement time by fitting the decay of the measured rotation velocity for an impurity species with the exponential form  $\exp(-t/\tau_\phi)$ .



To interpret this measurement in terms of the momentum balance, we set  $M_{j\phi}=0$  in Equation (7.2.2) because the beam injection is terminated. If we further make the plausible assumption that it is the beam injection which drives any significant difference in toroidal rotation velocities among the different ion species, then the friction term in Equation (7.2.2) can be neglected, and the reduced equation has a solution

$$v_{j\phi}(t) = v_{j\phi}(0) \exp(-t/\tau_{j\phi}) \quad (7.2.8)$$

of the form to fit the experimental data to infer a momentum confinement time.

In this case, the theoretical formula for  $\tau_{\phi}$  of Equation (7.2.1) clearly should be evaluated by using  $z_j$  corresponding to the charge state of the ion species for which the rotation velocity is being measured,

$$\tau_{\phi}^{th} = 2R^2 z_j e B^0 / T \quad (7.2.9)$$

We note that the temperature will also decay after the beam

injection is terminated, so that a strictly exponential decay would not be expected.

### 7.3 Analysis of PLT Experiments

The first systematic study of toroidal rotation driven by unbalanced neutral beam injection was carried out in PLT [28,29,107]. The PLT parameters are:  $R=130$  cm,  $a=40$  cm,  $B^0=2.5$  T,  $Z_{\text{eff}}=2.5$ . Generally,  $n_e \cong 3 \times 10^{13} \text{ cm}^{-3}$  and  $I_p \cong 450$  kA. The estimated accuracy of the rotation measurements was  $\pm 1.5 \times 10^4 \text{ ms}^{-1}$ . Co- and counter-injected discharges with  $E_b=40$  keV and beam power up to  $P_b=1.2$  MW were studied.

#### 7.3.1 Dependence of $v_\phi(0)$ on Injected Power

An essentially linear increase in steady-state central toroidal rotation velocity versus momentum input was observed for neutral beam power up to  $\sim 1$  MW. When normalized to the same beam power, the magnitude of the toroidal rotation velocity was identical for co- and counter-injection. The measured central rotation velocity versus momentum input is shown in Figure (7.3.1) for  $D^0 \rightarrow H^+$ .

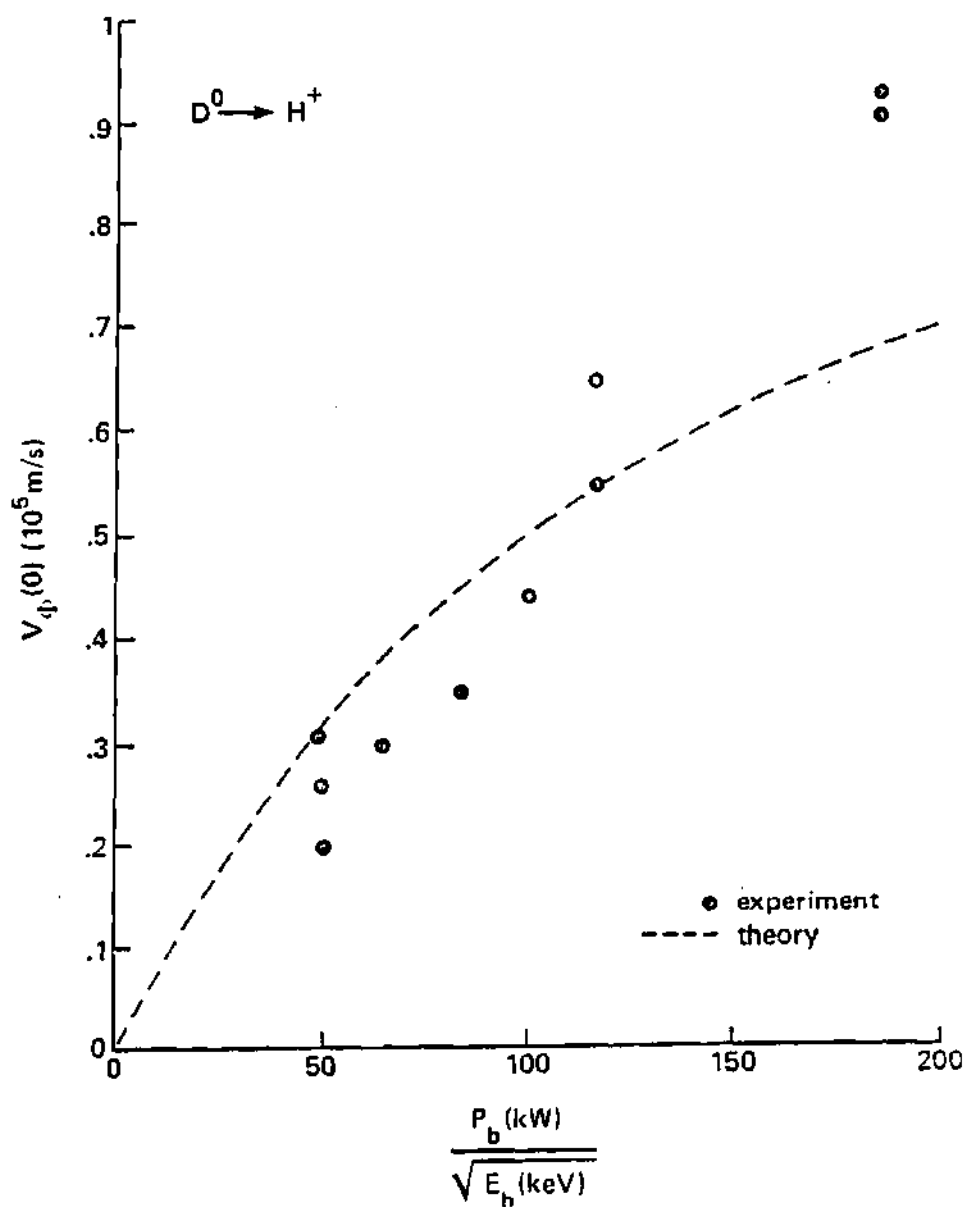


Figure 7.3.1 Comparison of neutral beam driven experimental and theoretical central toroidal rotation velocity in PLT.

The corresponding theoretical prediction is given by Equation (3.2.7). The beam momentum peaking factor was calculated [78] to be  $f_{\text{peak}}(0)=4.38$ . The central ion temperature was calculated from Equation (3.2.6) by using  $T_{\text{OH}}=1.1$  keV [111], and a heating efficiency [112] for  $\text{D}^0 \rightarrow \text{H}^+$  of  $C=4.5 \times 10^{-19}$  keV.MW.m<sup>-3</sup>. As is shown in Figure (7.3.1), the theoretical prediction matches the experimental results quite well, except at the highest beam power where the theoretical result begins to show a saturation of  $v_{\phi}(0)$  versus  $P_b$ .

Since the heating efficiency is the same for co- and counter-injection in PLT [29], Equation (7.2.7) would predict that the magnitude of the rotation velocity for a given beam power input would be identical for co- and counter-injection, consistent with the experimental observation. Central toroidal rotation velocities of  $v_{\phi}^{\text{exp}}(0)=6.5 \times 10^4$  m.s<sup>-1</sup> and  $v_{\phi}^{\text{exp}}(0)=-1.1 \times 10^5$  m.s<sup>-1</sup> were measured for 400 kW of co-injection and 500 kW of counter-injection, respectively ( $\text{H}^0 \rightarrow \text{D}^+$ ). Taking into account an observed central rotation velocity of  $-1.5 \times 10^4$  m.s<sup>-1</sup> before neutral beam injection,

Equation (7.2.7) predicts  $v_{\phi}^{\text{exp}}(0) = 4.7 \times 10^4 \text{ m.s}^{-1}$  and  $v_{\phi}^{\text{th}}(0) = -8.5 \times 10^4 \text{ m.s}^{-1}$  for co- and counter-injection, respectively.

A steady-state central toroidal rotation velocity of  $v_{\phi}^{\text{exp}}(0) = -4.5 \times 10^4 \text{ m.s}^{-1}$  was measured when 380 kW of co-directed beam power and 520 kW of counter-directed beam power ( $\text{H}^0 \rightarrow \text{D}^+$ ) were injected. Using  $P_b = 900 \text{ kW}$  to evaluate the central temperature, but using  $P_b^{\text{net}} = -140 \text{ kW}$  to evaluate the momentum input in Equation (7.2.7), and taking into account the observed  $-1.5 \times 10^4 \text{ m.s}^{-1}$  rotation before injection, leads to a prediction of  $v_{\phi}^{\text{th}}(0) = -3.0 \times 10^4 \text{ m.s}^{-1}$ .

### 7.3.2 Dependence of $v_{\phi}(0)$ on Density

Steady-state central toroidal rotation velocities were measured for  $P_b \approx 1 \text{ MW}$  in  $\text{D}^0 \rightarrow \text{H}^+$  and  $\text{H}^0 \rightarrow \text{D}^+$  discharges for densities over the range  $1.5 < n_e < 4 \times 10^{13} \text{ cm}^{-3}$ . The experimental results show that  $v_{\phi}(0)$  decreases gradually with increasing  $n_e$ , but much less rapidly than  $1/n_e$ , which implies a density dependence of the momentum confinement time.

A 65% increase in  $n_e$  ( $1.7 \rightarrow 2.8 \times 10^{13} \text{ cm}^{-3}$ ) resulted in about a 10% decrease in the measured central rotation in both the  $\text{H}^0 \rightarrow \text{D}^+$  and  $\text{D}^0 \rightarrow \text{H}^+$  discharges. Equation (7.2.7) predicts about a 20% decrease in both types of discharge, which is in agreement with the measurements to within the experimental error.

### 7.3.3 Difference of $v_\phi(0)$ Between $\text{H}^0 \rightarrow \text{D}^+$ and $\text{D}^0 \rightarrow \text{H}^+$

The steady-state toroidal rotation velocity for  $\text{D}^0 \rightarrow \text{H}^+$  was higher than for  $\text{H}^0 \rightarrow \text{D}^+$ , for  $P_b \approx 1 \text{ MW}$  in both cases, by about 20%. This difference in velocities is not as large as would be expected solely on the basis of the difference in momentum input per unit plasma mass, however, implying a larger momentum confinement time for  $\text{D}^+$  plasmas than for  $\text{H}^+$  plasmas.

Since the heating efficiency is greater [112] for  $\text{D}^0 \rightarrow \text{H}^+$  ( $C = 4.5 \times 10^{-19} \text{ keV.MW}^{-1} \cdot \text{m}^{-3}$ ) than for  $\text{H}^0 \rightarrow \text{D}^+$  ( $C = 4.0 \times 10^{-19} \text{ keV.MW}^{-1} \cdot \text{m}^{-3}$ ), equations (7.2.4) and (7.2.6) would lead to the prediction of a larger momentum confinement time for  $\text{H}^0 \rightarrow \text{D}^+$  than for  $\text{D}^0 \rightarrow \text{H}^+$  plasmas, for the same beam power. When this difference in heating efficiency, as well as the difference in momentum input, is taken into account, Equation (7.2.7)

predicts that the steady-state central rotation velocity is about 30% greater for  $P_{D=1} \text{ MW}$ ,  $D^0 \rightarrow H^+$  than for  $H^0 \rightarrow D^+$ , which agrees with the measured result to within the experimental error.

#### 7.3.4 Global Momentum Confinement Time

The global momentum confinement time inferred for PLT was in the range 10-30 ms for the cases studied. Using Equation (7.2.6) for the central ion temperature and measured [111] ion temperature profiles to evaluate an average ion temperature for the entire plasma leads to a prediction, from Equation (7.2.4), of 27 ms for the global momentum confinement time, in excellent agreement with experiment.

#### 7.4 Analysis of PDX Experiments

Several toroidal rotation measurements, encompassing steady-state and decay observations, have been carried out in PDX [30,31,107]. The PDX parameters are:  $R=143 \text{ cm}$ ,  $a=43 \text{ cm}$  (circular),  $B^0=2.2 \text{ T}$ . The value of  $Z_{\text{eff}}$  in PDX depends upon the beam power [113] and varies from somewhat less than two to

somewhat more than four. Both  $D^0 \rightarrow H^+$  and  $H^0 \rightarrow D^+$  discharges were studied, with  $E_b=50$  keV and  $P_b$  up to about 5 MW.

#### 7.4.1 Dependence OF $v_\phi(0)$ on Injected Power

Measured steady-state central toroidal rotation velocity for  $D^0 \rightarrow H^+$  plasmas are shown in Figure (7.4.1) as a function of  $P_b/n_e$ . Since the heating efficiency in PDX increases with plasma current, the interpretation of these results is not straightforward. We use  $C=4.0 \times 10^{-19}$  keV.MW<sup>-1</sup> .m<sup>-3</sup> for  $D^0 \rightarrow H^+$  heating efficiency [112],  $T_{OH}(0)=0.71$  keV [114] and  $f_{peak}(0)=5.0$  for the momentum deposition peaking factor [30] to evaluate Equation (7.2.7). The result is plotted in Figure (7.4.1), and provides a reasonable agreement with the rather scattered experimental data.

#### 7.4.2 Decay Measurements

The decay of the toroidal rotation velocity after termination of the beam was measured for Ti XXI ( $r=0$ ) and Ti XVII ( $r=20 - 25$  cm). Momentum confinement times of 80 - 100 ms and 160 - 180 ms, respectively were inferred by fitting the data to Equation (7.2.8).



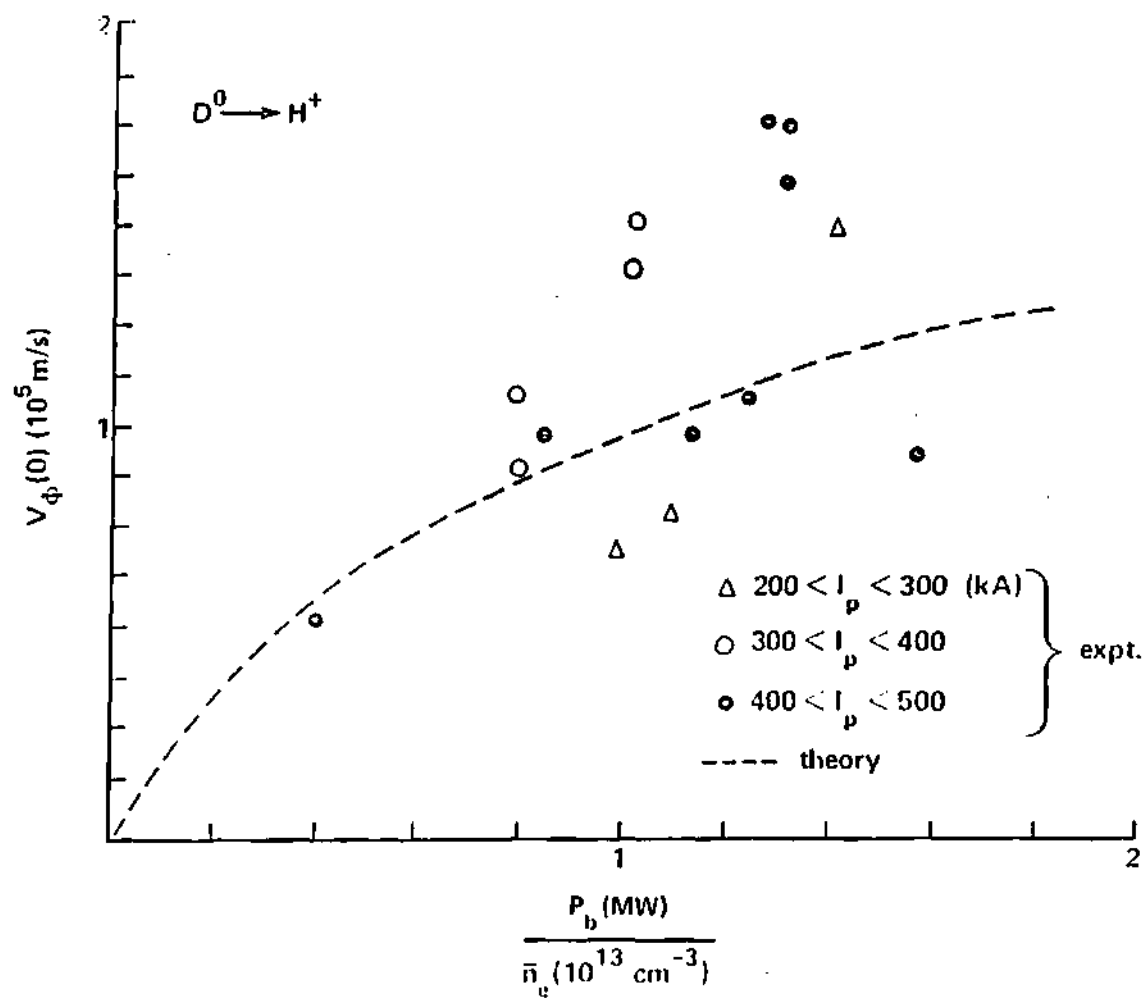


Figure 7.4.1 Comparison of experimental and theoretical central toroidal rotation velocity in PDX.

Theoretical values of the corresponding momentum confinement times were calculated from Equation (7.2.9). Over the time of the rotation decay, the temperature also decays. The maximum ion temperature during injection and after the decay back to the ohmic discharge were determined from the data in References [114,115]. The median values  $T_i(0)=1.8$  keV,  $T_i(20 \text{ cm})=1.1$  keV and  $T_i(25 \text{ cm})=0.96$  keV were then used in Equation (7.2.9) to calculate  $\tau_\phi^{\text{th}}(r=0)=98$  ms and  $\tau_\phi^{\text{th}}(r=20 - 25)=135 - 190$  ms. These predictions agree quite well with the experimental values.

#### 7.4.3 Dependence of $v_\phi(0)$ on $n_e$ and $B_\phi^0$

Steady-state central rotation velocities of  $v_\phi^{\text{exp}}(0)=0.97 \times 10^5 \text{ m.s}^{-1}$  were measured in  $D^0 \rightarrow H^+$  discharges with  $(P_b=3.5 \text{ MW}, I=480 \text{ kA}, B^0=2.2 \text{ T}, n_e=2.9 \times 10^{13} \text{ cm}^{-3})$ , and  $(P_b=3.1 \text{ MW}, I=370 \text{ kA}, B^0=1.5 \text{ T}, n_e=4.8 \times 10^{13} \text{ cm}^{-3})$ . Using  $T_{\text{OH}}(0)=0.71$  keV and a heating efficiency  $C=4.0 \times 10^{-19} \text{ keV.MW}^{-1}.\text{m}^{-3}$ , central ion temperatures of 5.5 keV and 3.3 keV were calculated and used in Equation (7.2.7) to predict  $v_\phi^{\text{th}}$

$(0)=1.0 \times 10^5 \text{ m.s}^{-1}$  and  $0.61 \times 10^5 \text{ m.s}^{-1}$ , respectively, in good agreement with the measured results.

#### 7.4.4 Dependence of $v_\phi(0)$ on Plasma Current

The data in Reference [31] were interpreted by the authors as indicating that  $v_\phi(0)$  was independent of plasma current, although the scatter in the data leaves open other possible interpretations. On the other hand, data in ref. [107] indicate that  $v_\phi(0)$  increases by almost a factor of two as the plasma current increases from 300 to 500 kA. If we assumed that the heating efficiency increased with plasma current [107], then Equation (7.2.7) would predict a decrease in  $v_\phi(0)$  with increasing plasma current, unless the beam momentum transfer efficiency also increases with plasma current, as is speculated in Reference [111]. In any case, the data are insufficient to draw any conclusions in this regard.

### 7.5 Summary

The gyroviscous theory of momentum confinement predicts the right order of magnitude gyroviscous force to explain the momentum confinement times inferred from experiment with unbalanced neutral beam injection. The theory was applied to analyze the momentum confinement data from the PLT and the PDX tokamaks. Both the steady-state and the decay measurements of the toroidal rotation velocity were modeled. The theory is found to model the experimental data quite well over the wide range of the parameters considered. The theory has also been shown to match the steady-state and the decay rotation measurements in the ISX-B tokamak [114]. It is concluded that the gyroviscous theory correctly explains the measured momentum confinement time. The theory, therefore, obviates the necessity of any assumptions of anomalous processes to explain the momentum confinement time inferred from experiments in the tokamak plasmas. The agreement of the

theory with experiment provides confidence for using the gyroviscous theory of momentum confinement to compute  $\nu_d = \tau_\phi^{-1}$  in the impurity flow reversal theory.

## CHAPTER VIII

## PREDICTIONS FOR FUTURE REACTORS

8.1 Introduction

The analysis of impurity transport data from the PLT and the ISX-B tokamaks shows that co-injected neutral beams can be effectively used to drive impurities outward and thus possibly achieve clean central plasmas with a cool radiating edge. Thus co-injected neutral beams can be very useful in reducing the central radiation losses. These results provide sufficient motivation to explore the possibility of using neutral beam injection to control impurities in the future reactors. Three designs have been chosen for such exploratory and predictive studies. The reactors studied include the International Tokamak Reactor (INTOR), the Tokamak Ignition/Burn Experimental Reactor II (TIBER II), and the International Thermonuclear Test Reactor (ITER). Neutral beams may offer a backup, or alternative mechanism to rf-heating, can be used to control burn dynamics, and can also provide a potential

current drive mechanism in the future thermonuclear reactors. Thus, the choice of neutral beams for impurity control does not pose any additional economic constraints. The predictions for INTOR, TIBER II, and ITER are covered in Sections (8.2), (8.3), and (8.4) respectively.

## 8.2 Predictions for INTOR

The International Tokamak Reactor (INTOR) [55] is a collaborative effort among the European Community, Japan, the USSR, and the United States. The INTOR workshop studies are conducted under the auspices of the International Atomic Energy Agency (IAEA), in terms of reference defined by the International Fusion Research Council (IFRC), an advisory body to the director general of the IAEA, which supervises the INTOR workshop. The broad objectives of the INTOR activity are to identify the next major experiment beyond the present generation of tokamaks, to develop the design, and to construct and operate it on an international basis. The characteristic design parameters for INTOR are given in References [55]. Some of these reference parameters relevant to this study are shown in Table (8.2.1).

Table 8.2.1 INTOR reference parameters

---

Major radius (m)	5.0
Minor radius (m)	1.2
Elongation	1.2
$Z_{\text{eff}}$	2.5
Toroidal magnetic field (T)	5.5
Safety factor $q(0)$	1.1
Safety factor $q(a)$	2.0
Model impurity: Iron	
Plasma type : D-T	
Beam type : D <sup>-</sup>	
Neutral beam power (MW)	75.0
Neutral beam energy (keV)	750
Beam tangency radius (m)	4.3
Beam width (m)	0.40

---



The details of the space- and time-resolved profiles for the physical quantities of interest such as density and temperature are not available for the INTOR plasmas. Since the INTOR is similar in size and design parameters to the Fusion Engineering Device [116], the density and temperature profiles for FED [116] were adopted for the INTOR model calculations. Because the first wall reference material is stainless steel, the model impurity used in this study is iron with a concentration  $\alpha = z^2 n_z / n_i = 5\%$ . The safety factor was assumed to vary from  $q(r=0)=1$  to  $q(r=a)=2$ , which is in accordance with the INTOR design parameters [55]. The momentum deposition profile was computed by model calculations based on the beam part of the code PROCTR [78]. With the average ion temperature equal to 10 keV and the representative values for other parameters for INTOR shown in Table (8.2.1). Equation (2.6.2) based on the gyroviscous theory [54] of momentum confinement gives an average drag frequency equal to  $14 \text{ s}^{-1}$ .

The value of the drag frequency computed from the gyroviscous theory [54] of momentum confinement, the representative values for reference parameters for INTOR, and the space- and time-resolved profiles of the physical

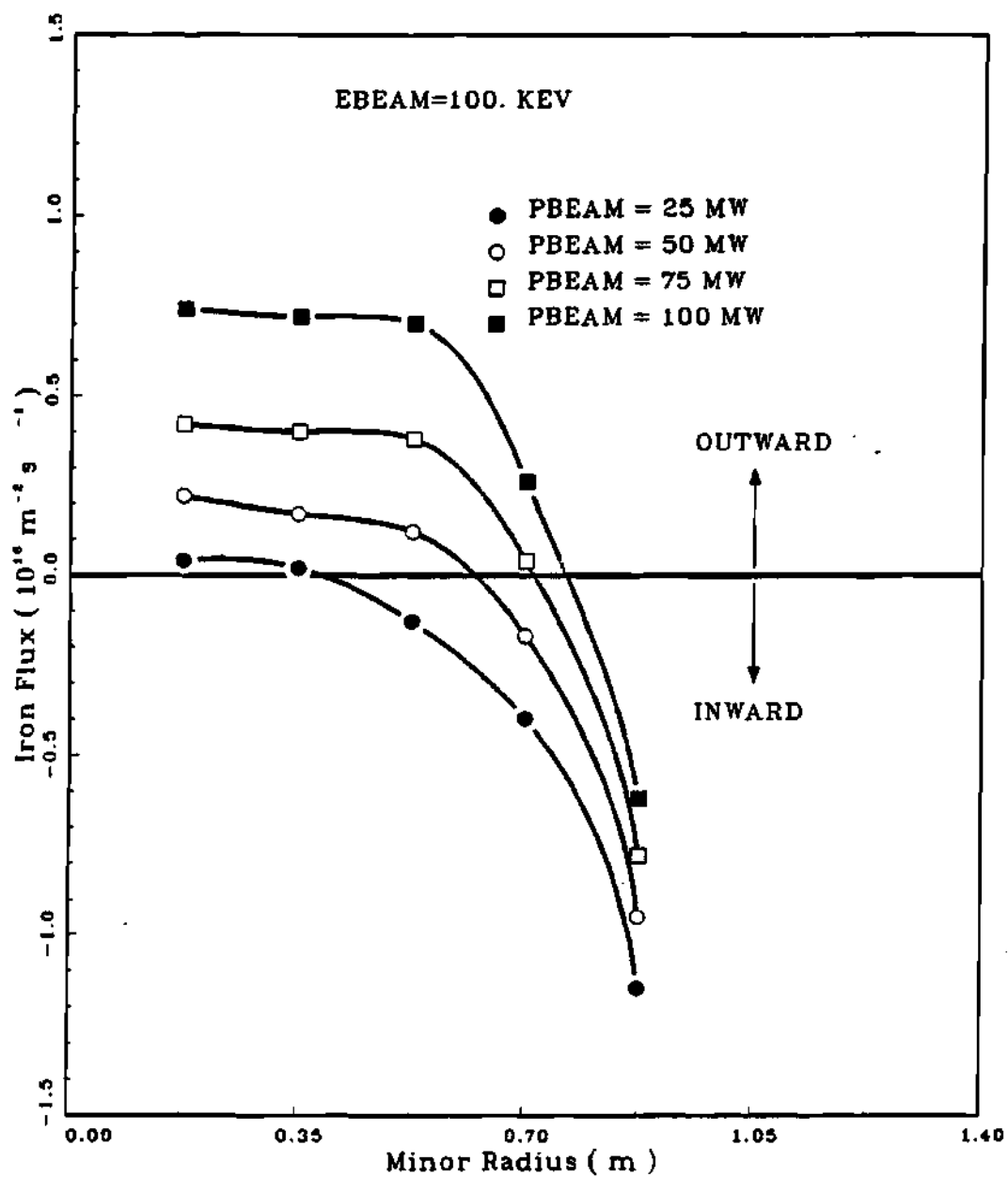


Figure 8.2.1 Impurity flow reversal in INTOR at 100 keV beam energy.

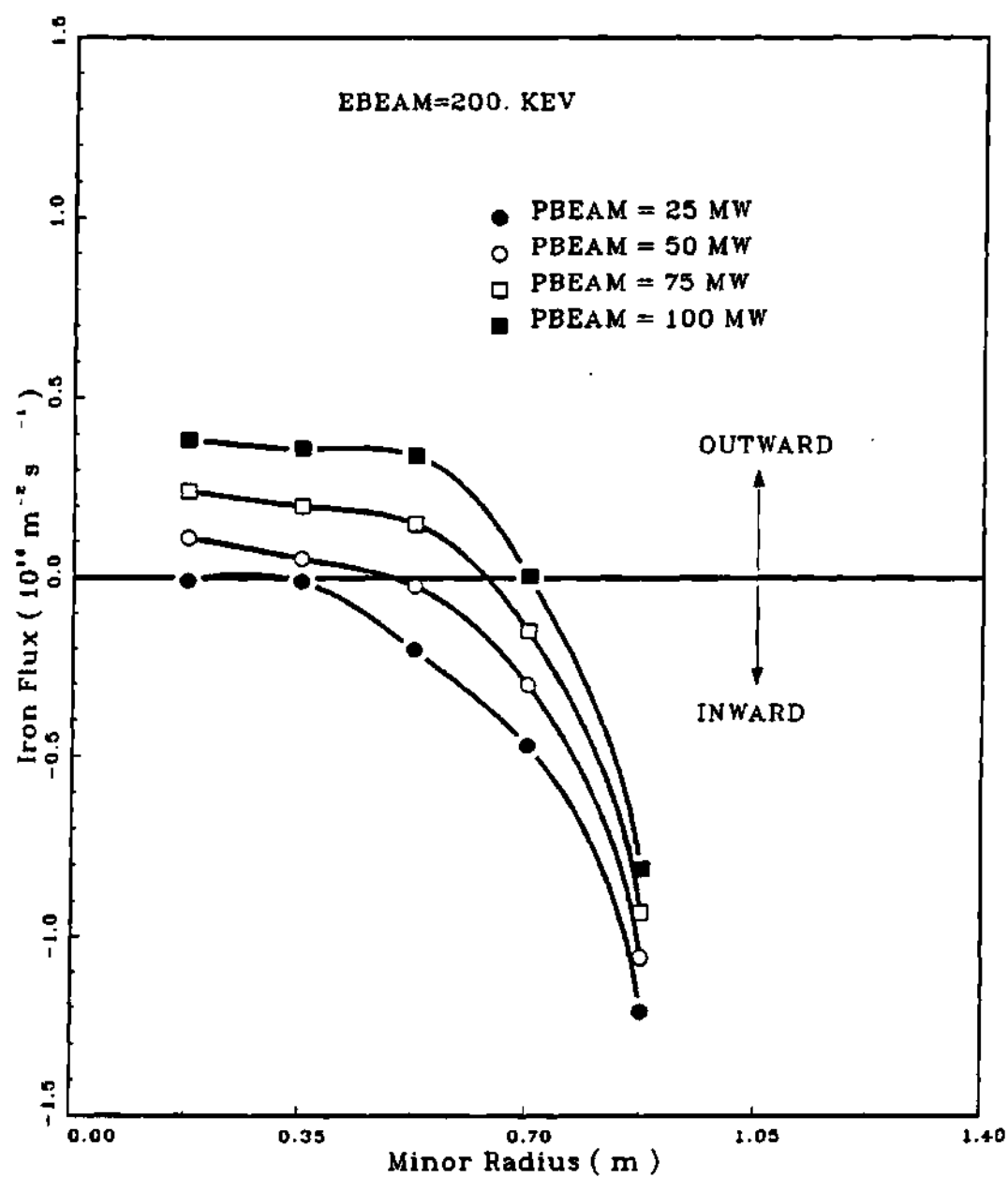


Figure 8.2.2 Impurity flow reversal in INTOR at 200 keV beam energy.

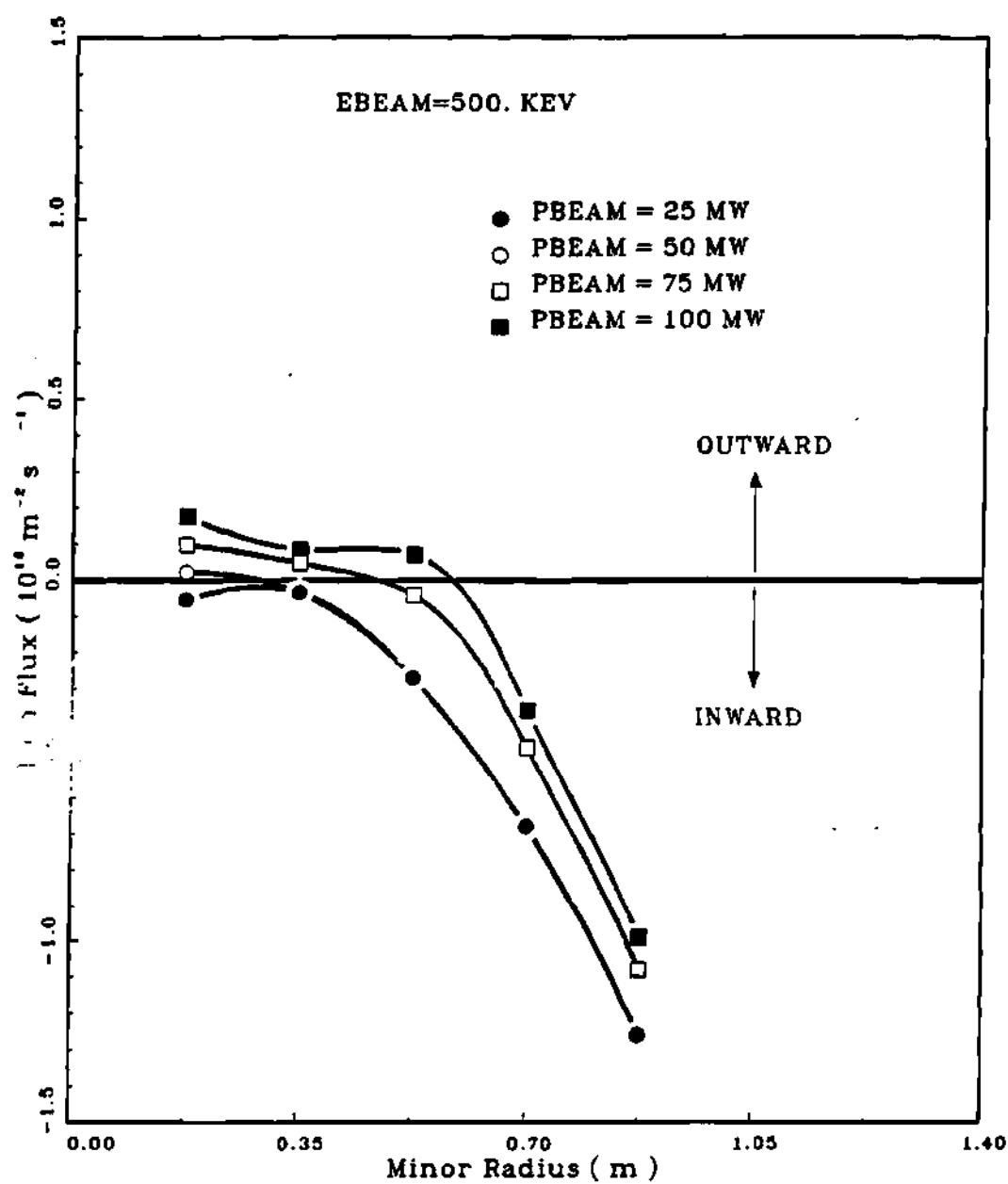


Figure 8.2.3 Impurity flow reversal in INTOR at 500 keV beam energy.

quantities of interest as estimated above were then used in the steady-state model of the Stacey-Sigmar theory [42,43] to compute the flux-surface averaged impurity flux for a range of co-injected neutral beam powers and energies. The impurity flux for beam power values of 25, 50, 75, and 100 MW and beam energies of 100, 200, and 500 keV are shown in Figures (8.2.1) through (8.2.3). It is clear from these figures that neutral beam co-injection can prevent the accumulation of impurities in the INTOR central plasmas. The low energy (100 keV) beam seems to be much more effective (per unit power) at reversing impurity influx than the high energy (500 KeV) beam. For example, 50 MW of 100 keV neutral beam should prevent penetration of impurities, whereas 100 MW of 500 KeV neutral beam would be needed. This, unfortunately, runs counter to the trend for neutral beam current drive.

### 8.3 Predictions for TIBER II

The tokamak Ignition/Burn Experimental Reactor (TIBER) is the U.S. option for an international Engineering Test Reactor (ETR) [56]. This reactor concept evolved from earlier work on the Tokamak Fusion Core Experiment (TFCX) [117] to develop a

small, ignited tokamak. While the copper-coil version of TFCX became the short-pulsed, 1.23-m radius, Compact Ignition Tokamak (CIT) [118], the superconducting TIBER [56] with long pulse or steady-state and a 2.6-m radius became a candidate for international collaboration. The TIBER design was updated to TIBER II to accomodate the conservative Kaye-Goldston confinement scaling, double poloidal divertors for impurity control, steady-state current drive, and nuclear testing.

The characteristic design parameters of interest for TIBER II are based on Refs. [1-3,5], and the design information files maintained on the CRAY computer system of the National Magnetic Fusion Energy Computational Center (NMFECC) of the Lawrence Livermore National Laboratory. The design parameters relevant to this study are shown in Table (8.3.1). The Stacey-Sigmar impurity flow reversal theory [42,43] is applied to study the helium and carbon transport in TIBER II.

Table 8.3.1 TIBER II reference parameters

---

Major radius (m)	3.0
Minor radius (m)	0.834
Elongation	2.4
$Z_{\text{eff}}$	2.085
Toroidal magnetic field (T)	5.55
Safety factor $q(0)$	1.268
Safety factor $q(a)$	3.945
Model impurity: Carbon	
Plasma type	: D-T
Beam type	: $D^+$
Neutral beam power (MW)	45.0
Neutral beam energy (keV)	500
Beam tangency radius (m)	2.6, 3.0
Beam width (m)	0.40

---

### 8.3.1 Helium Transport in TIBER II

The removal of helium ash (thermalized alpha particles) is an important problem in the design of tokamak reactors. The accumulation of thermal alphas at the center can interfere with the burning process and degrade the performance of the reactor. To model helium transport using the Stacey-Sigmar theory [42,43], the radial density and temperature profiles for the ions and electrons were assumed to be of the form given in Equation (4.5.1), that is

$$X(r)=X_0[1-(r/a)^2]^a \quad (8.3.1)$$

where  $X$  represents either density or temperature, and  $X_0$  is the value at the center. The exponents  $a_n$  and  $a_T$  for the main ion density and temperature respectively were taken to be 1.02 and 0.58. Using the gyroviscous theory, the average drag frequency for the main ions was found to be  $80 \text{ s}^{-1}$ . The rest of the TIBER II parameters, some of which are shown in Table (8.3.1), were taken from the ETR files maintained on the NMFECC system.



The fast ion deposition profile needed for the calculation of the neutral beam momentum deposition was computed with the code PROCTR [78]. The helium profile was also assumed to be of the form given in Equation (8.3.1). Since the exact spatial distribution of the thermalized alpha particles is not known, three different values of the exponent  $\alpha_n$ , 1.0, 1.5, and 2.0 were considered. The central value of the helium density was calculated in such a way that the volume averaged helium density was 5% of the volume averaged ion density.

The results of the numerical simulation are shown in Figure (8.3.1). The flux-surface averaged helium flux is plotted versus the minor radius for different beam powers for the three different helium profiles. It is clear that the results are sensitive to the assumed helium profile. Flow reversal occurs at lower beam power when the profile is more peaked. This can be explained if we note that the diffusive impurity fluxes in Equation (2.4.1) which are driven by the main ion and impurity ion density gradients and are normally inward, for low  $z$  impurities like helium and peaked impurity profiles relative to the ion profile can be outward. The same behavior was observed in the case of strong profile coupling where the

thermal alpha profile was proportional to the fusion reaction rate  $n^2 \langle \sigma_f v \rangle$ , in agreement with similar observations made by Sigmar, et al., [119]. If the helium profile were the same as the main ion profile Figure (8.3.1b), one would need 75 MW or higher of co-injected beam power to drive the impurities out of the center. For more peaked profiles, which are probably more realistic, 25 to 50 MW would be adequate to drive the helium out of the center Figure (8.3.1-c,d).

### 8.3.2 Carbon Transport in TIBER II

The reference wall material in TIBER II is carbon. To study the effect of impurity flow reversal theory [42,43] on carbon impurity in TIBER II, the carbon profile was assumed to be of the same shape as that of the main ion, and the carbon concentration  $\alpha = z^2 n_z / n_i$  was assumed to be 5%.

The results are shown in Figure (8.3.2, a-b). The flux-surface averaged carbon flux is plotted versus the minor radius for different beam powers. It can be seen that 50 MW of co-injected beam power would be adequate to drive the carbon impurities out of the center.

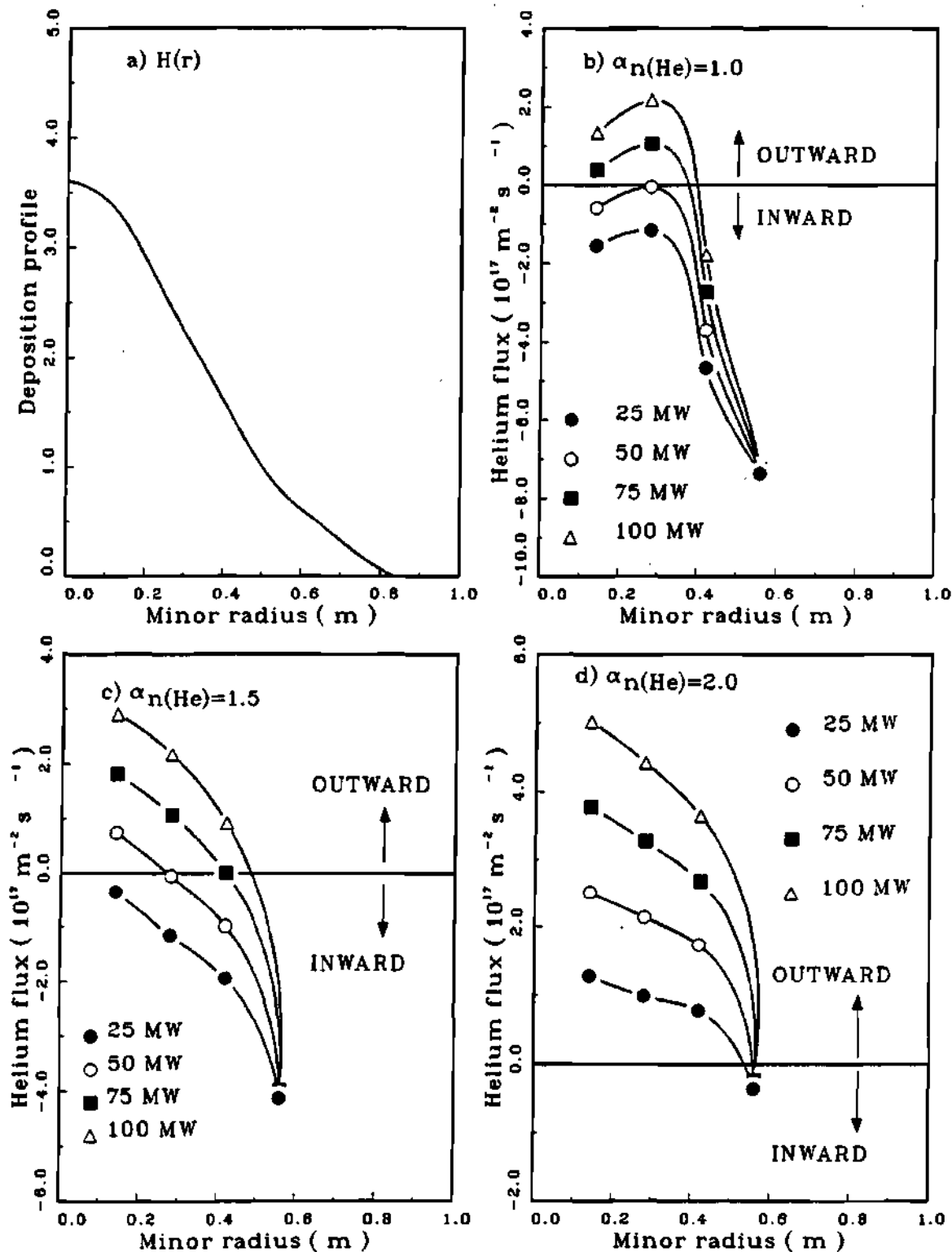


Figure 8.3.1 Neutral beam deposition profile (a), and beam driven flow reversal (b-d) for different helium profiles in TIBER II with 500 keV beam energy.

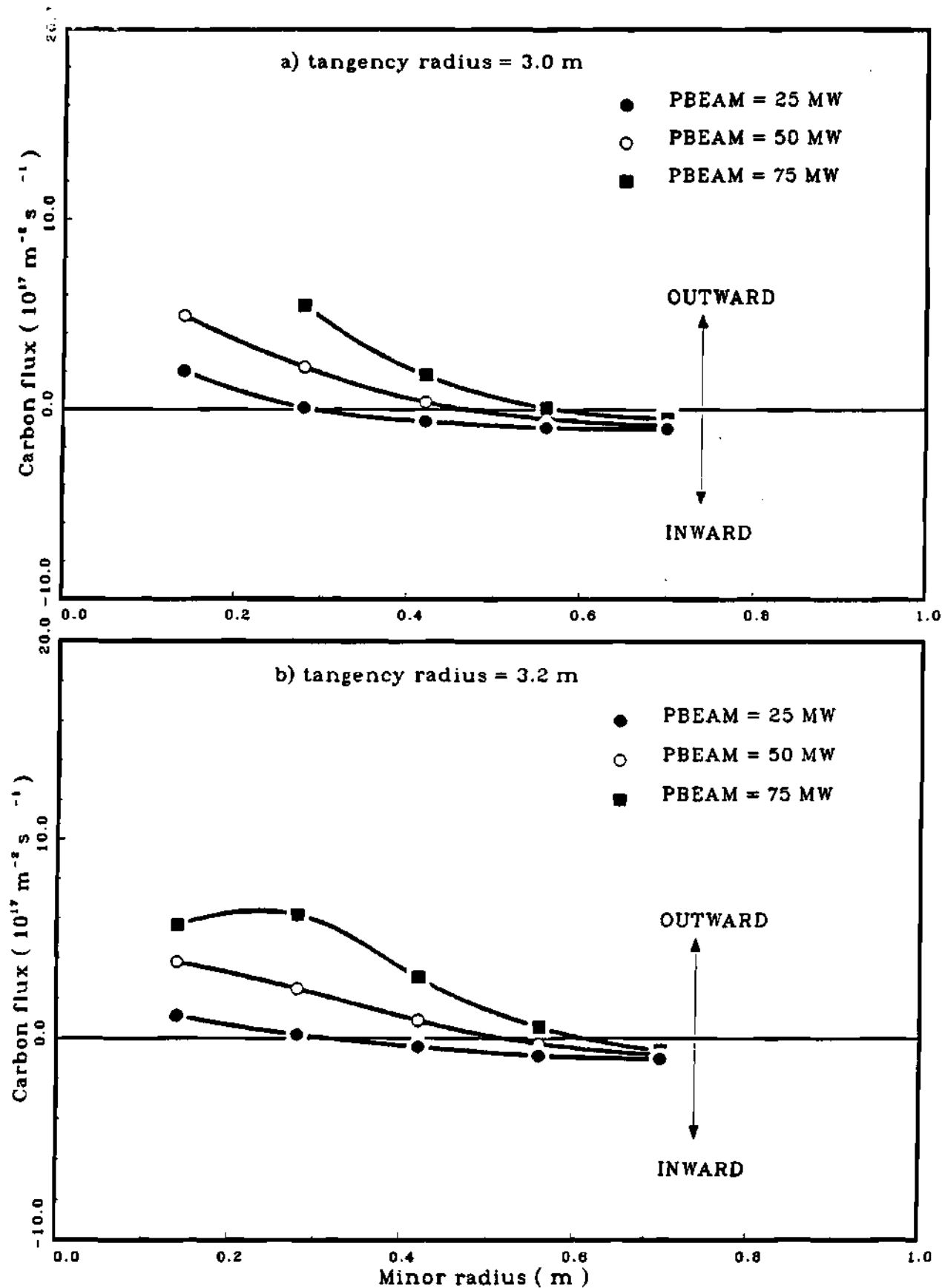


Figure 8.3.2. Carbon flow reversal in TIBER II with reference profiles, at 500 keV neutral beam energy and beam tangency radius of (a) 3.0 m, (b) 3.2 m.

To study the sensitivity of the calculations to the beam deposition profile, the tangency radius of the outer beamline was changed from 3.0 m to 3.2 m. This results in a less peaked deposition profile and hence in less momentum being deposited in the center. The results are shown in Fig. (8.3.2,b). Although the impurity fluxes are now smaller for the same beam power, flow reversal still occurs for co-injected beam power of 50 MW.

#### 8.4 Predictions for ITER

The steady-state impurity transport theory is applied in this section to predict the impurity transport trends in the U.S. option for the International Thermonuclear Reactor (ITER-US). The characteristic design parameters for the ITER-US are generally based on the data files maintained on the CRAY computer system of the National Magnetic Fusion Energy Computational Center, Lawrence Livermore National Laboratory. The impurities modeled in this study are iron, carbon, and helium. The reference parameters for ITER-US are shown in Table (8.4.1).

Table 8.4.1 ITER reference parameters

---

Major radius (m)	4.04
Minor radius (m)	1.41
Elongation	2.3
$Z_{\text{eff}}$	1.5
Toroidal magnetic field (T)	4.98
Safety factor $q(0)$	1.539
Safety factor $q(a)$	2.490
Model impurities: iron, carbon, helium	
Plasma type	: D-T
Beam type	: $D^-$
Neutral beam power (MW)	60.0
Neutral beam energy (keV)	1600
Beam tangency radius (m)	3.68
Beam width (m)	0.40

---

The radial profiles of plasma density and temperature are assumed to be of the form

$$X(r)=X_0[1-(r/a)^2]^a \quad (8.3.1)$$

where  $X$  represents either density or temperature, and  $X_0$  is the value at the center. The reference values for the exponents are  $a_n=1.0$ , and  $a_T=0.5$ . The central values used in this study based on the reference design parameters are  $n_{i0}=1.305 \times 10^{20} \text{m}^{-3}$ ,  $T_{i0}=22.8 \text{ keV}$ , and  $T_{e0}=25.74 \text{ keV}$ . The impurity temperature was assumed to be the same as the main ion temperature. The impurity density gradients were computed by assuming  $n_z/n_i=.05$ ,  $.01$ , and  $.01$  respectively for iron, carbon, and helium. The safety factor profile was obtained by interpolating between the reference values at the center and at the edge. The gyroviscous theory [54] of momentum confinement was used to compute the external drag. Corresponding to the reference value of the average ion temperature  $\langle T_i \rangle = 15.20 \text{ keV}$ , the computed external drag was  $\nu_{di}=62 \text{ s}^{-1}$ .

The neutral beam shape factor  $H(r)$  is needed to compute the beam momentum deposition profile. The  $H(r)$  profile was computed using the beam section of the PROCTR [78] code. The code uses the moments solution of the Fokker-Planck equation. A single neutral beam-line in the co-direction using negative deuterium ions, with 60 MW of 1.6 MeV beam energy, and 3.68 m beam tangency radius was assumed. The beam was assumed to be circular in cross-section with a width of 0.40 m.

Using the reference design parameters for ITER-US, the external drag computed from the gyroviscosity theory [54], and the neutral beam shape factor computed from the code PROCTR [78] code, the steady-state impurity flow reversal theory [42,43] was applied to predict the flux-surface averaged flux for iron, carbon, and helium using neutral beam energy values of 500, 1000, and 1500 keV over the beam power range of 25, 50, 75, and 100 MW. The flow reversal did not take place in case of iron and carbon impurities. The flow reversal did take place for helium, though the effect is only small. The results for helium in the range of parameters considered are shown in



Figures (8.4.1-3). It is estimated that 75 to 100 MW of neutral beam power can cause helium flow reversal in the central region of the ITER plasmas with the range of beam energies considered.

The predicted impurity transport in ITER-US can be explained from the neutral beam momentum deposition considerations. As indicated in Section (7.2.1), the rate of momentum deposition per plasma ion in the toroidal direction normalized to the beam shape factor can be written as

$$M_{\phi} = P_b / (n_p V_p) \sqrt{(2m_b / E_b)} \quad (8.4.1)$$

where the subscripts p and b imply plasma and beam respectively, and the rest of the symbols are as described in Section (7.2.1). Since impurity flow reversal effects were quite pronounced in the case of the PLT tokamak, it is instructive to compare the rate of the neutral beam momentum deposition per plasma ion in ITER with that in PLT. With the ITER reference parameters,  $M_{\phi}(\text{ITER}) = 6.9 \times 10^{-22}$  N/s. The corresponding value for PLT was estimated to be  $M_{\phi}(\text{PLT}) = 3.2 \times 10^{-21}$  N/s. Thus, the rate of momentum deposition

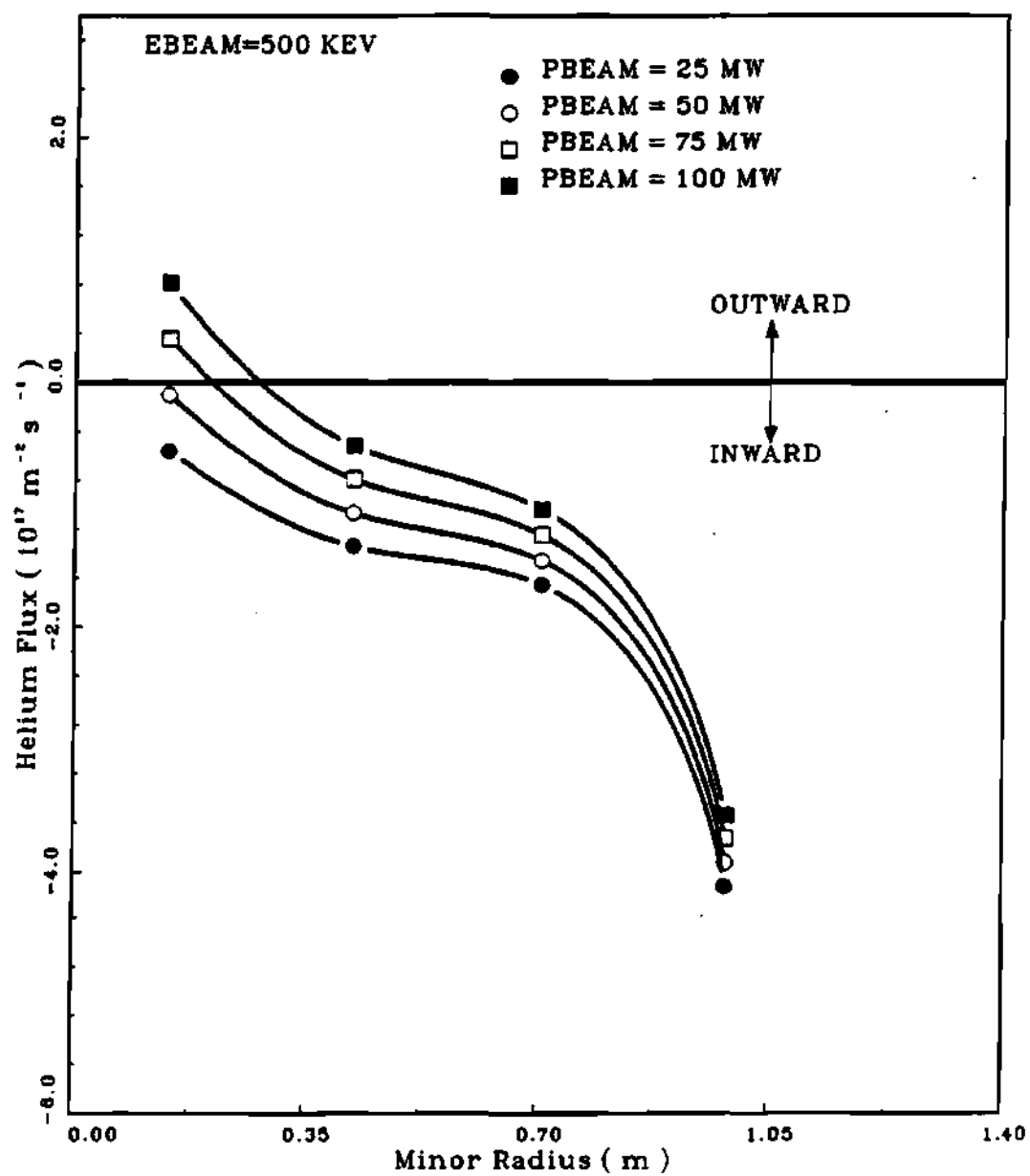


Figure 8.4.1 Impurity flow reversal in ITER at 500 keV beam energy.

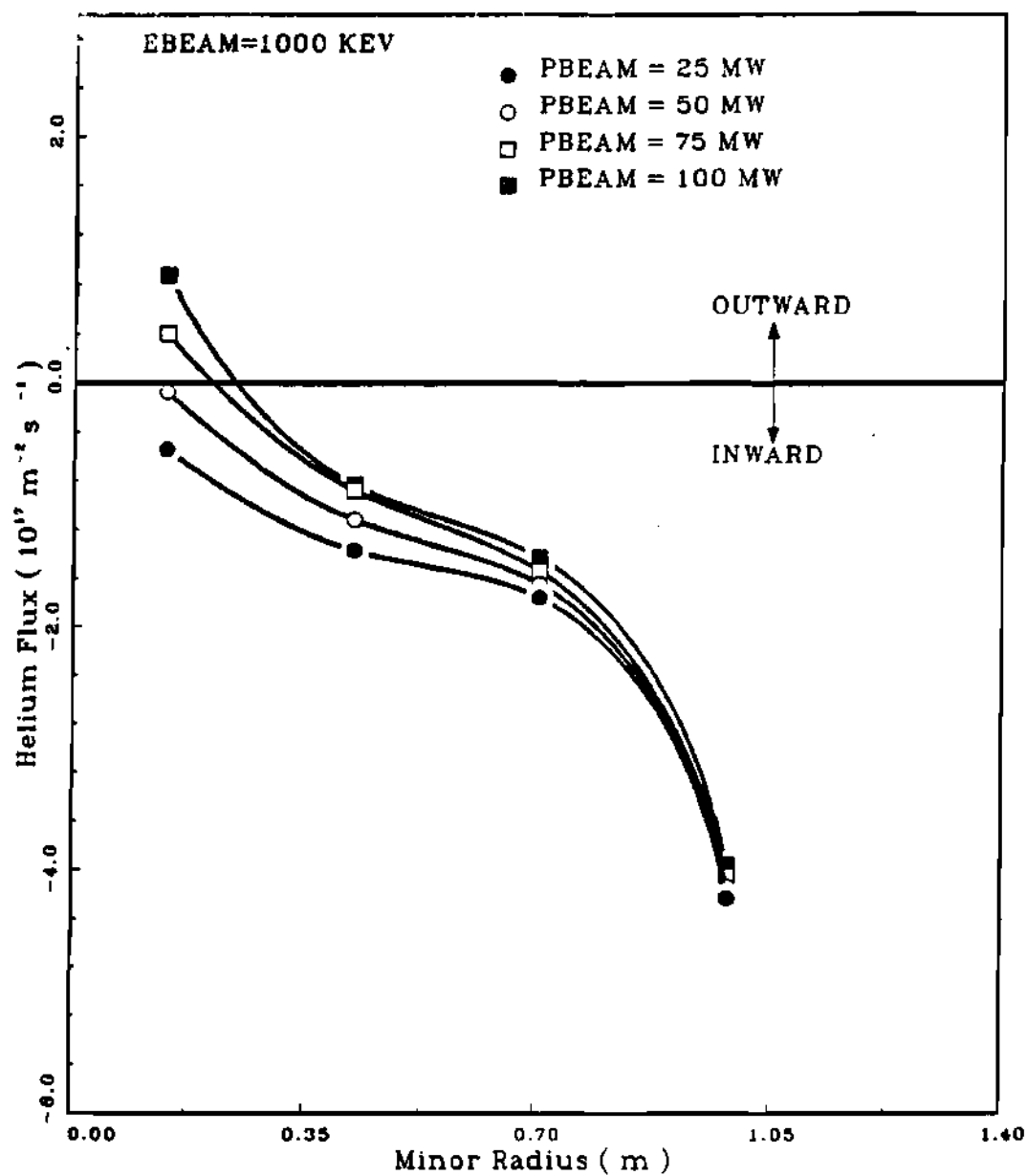


Figure 8.4.2 Impurity flow reversal in ITER at 1000 keV beam energy.

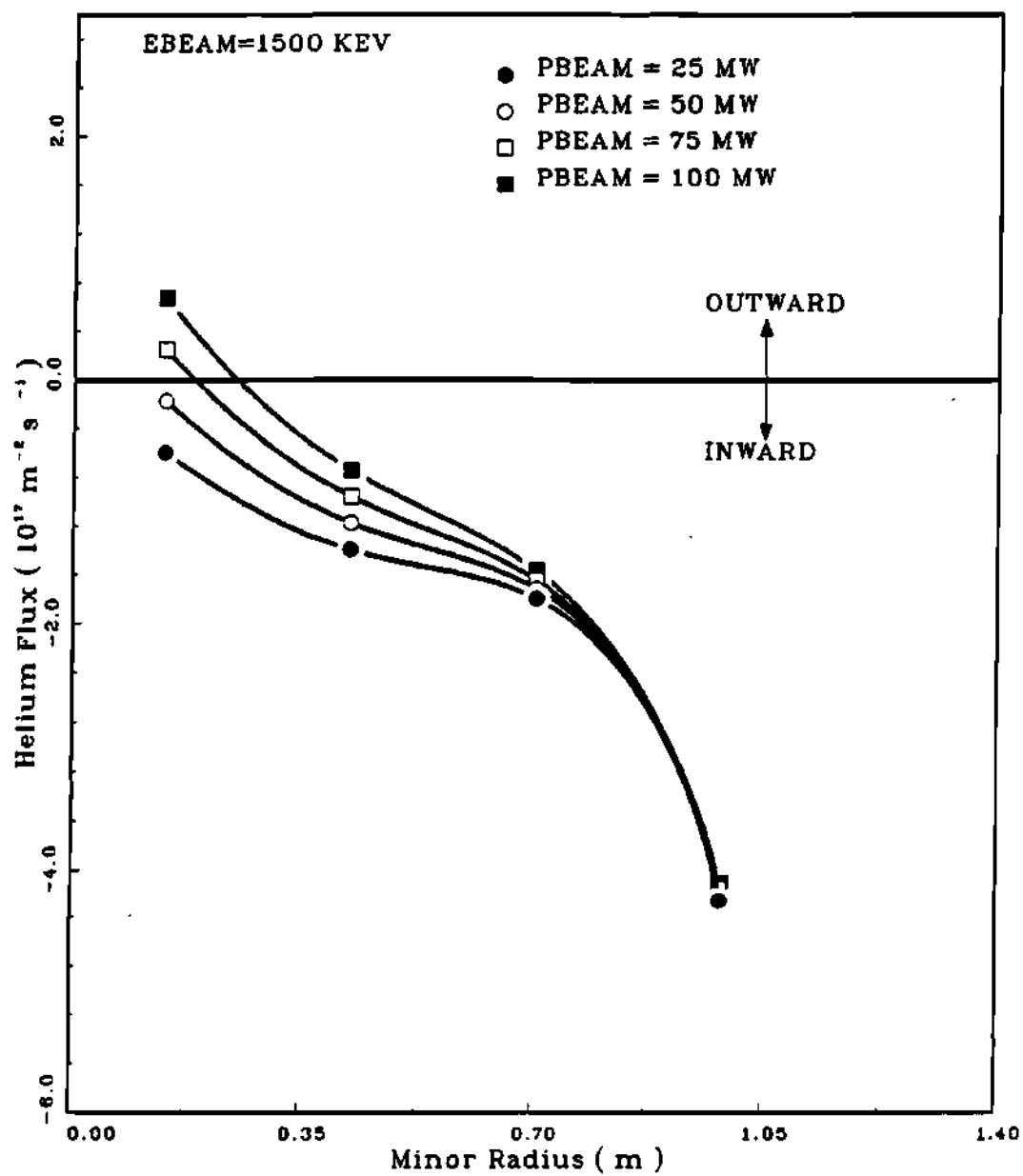


Figure 8.4.3 Impurity flow reversal in ITER at 1500 keV beam energy.

per ion in ITER is only 1/5 th of that in PLT. Hence, it is not surprising that the neutral beam driven impurity flow reversal is not a dominant effect with the ITER reference parameters.

The above point can further be illustrated by comparing the toroidal rotation velocities with the thermal velocities shown in Table (8.4.2). It may be noticed that plasma rotation velocity is about two orders of magnitude smaller as compared to the main ion thermal velocity. Hence, the inertial effects are negligible with the ITER reference parameters with the result that the plasmas do not rotate sufficiently to cause impurity flow reversal. This situation can again be compared with that in PLT for which the rotation speed was comparable to the main ion thermal speed, and hence the impurity flow reversal was quite pronounced in the case of the PLT tokamak. The impurity flow reversal in ITER in the case of helium (Figs. 8.4.1-3) is mainly because of the diffusive fluxes. It may be seen from Equations (2.4.2-3) that the diffusive fluxes which are proportional to to prssure gradients and are inward for the normally negative main ion density gradients, can become

Table 8.4.2 Comparison of flows in ITER

Ion	$v_{th,i}$	$v_{\phi,i}$	$v_{th,z}$	$v_{\phi,z}$	
He	$1.32 \times 10^6$	$2.62 \times 10^4$	$1.04 \times 10^6$	$4.47 \times 10^3$	m/s
C	$1.32 \times 10^6$	$2.38 \times 10^4$	$6.02 \times 10^5$	$6.92 \times 10^3$	m/s
Fe	$1.32 \times 10^6$	$1.40 \times 10^4$	$2.79 \times 10^5$	$1.67 \times 10^4$	m/s

positive for helium ions because of the effects of low- $z$  in Equations (2.4.2-3).

### 8.5 Summary

In view of the prospect of the impurity flow reversal theory in providing an effective impurity control mechanism, it was considered instructive to apply the theory to predict the behavior of impurity transport in the future thermonuclear reactors. Three design concepts, namely, INTOR, TIBER II, and ITER were considered in this investigation. The reference parameters of these designs span the range appropriate to the next-generation engineering test reactor.

With reference parameters, and representative profiles, the impurity flux was modeled for INTOR in the co-injected neutral beam power range of 25, 50, 75 and 100 MW, and beam energies of 100, 200 and 500 keV. It is clear from this investigation that 50 to 75 MW of co-injected neutral beam power is sufficient to prevent the accumulation of impurities in central plasmas.

The transport of helium and carbon impurities was modeled with TIBER II reference parameters. The predicted flow reversal results for helium were found to be sensitive to the assumed helium profile. However, it was found that for more realistic profiles, 50 to 75 MW of co-injected beam power would be adequate to drive helium out of the central plasmas. In the case of carbon, it was found that 50 MW of co-injected beam power would be needed to remove carbon from the center.

With the reference parameters and representative profiles, flow reversal did not take place in the case of iron and carbon impurities. This is because the rate of beam momentum deposition per plasma ion is so small that plasma rotation remains negligible as compared to thermal velocities. Some flow reversal was seen to take place in case of helium mainly because of the outward contribution of diffusive fluxes.



## CHAPTER IX

## CONCLUSIONS

The impurity flow reversal theory and the gyroviscous theory of momentum confinement were applied to carry out a detailed analysis of the neutral beam driven impurity accumulation and rotation experiments in the PLT, ISX-B, and the PDX tokamaks. The theories were also applied to predict impurity transport trends in INTOR, TIBER II and ITER, the reference designs for the future thermonuclear reactors.

The impurity flow reversal theory developed by Stacey and Sigmar predicts an outward flow of impurities with co-injection, and an enhancement in the normally inward flow of impurities with counter-injection. There is a large experimental data base from the PLT and the ISX-B tokamaks that qualitatively supports these theoretical predictions. The theory was applied to analyze the representative experimental data from the PLT and the ISX-B tokamaks with intrinsic as well as injected impurities over a wide range of parameters.

An experimental study inferred tungsten fluxes from measured chordal distribution of the ultra-soft x-rays radiated from the PLT deuterium discharges with tungsten limiters. The general tendency of the tungsten flux with co-injection was to change from an inward to an outward direction. The tungsten flux for counter-injection was always directed inward, was an order of magnitude greater than the flux during co-injection, and increased substantially with time. It was further observed that the co- plus counter-discharges were similar to co-discharges instead of to counter-discharges. Thus, if the counter-beams were responsible for an increased tungsten density due only to knocking tungsten off the limiter, then co- plus counter-discharges should have at least as much tungsten as in the counter-discharge. It implies that the observed results are due to the effects of neutral beam injection on impurity transport. The impurity flow reversal theory was applied to model the experimental results using the measured quantities as far as possible. Both the steady-state and the time-dependent formulations of the theory were found to model the experimental data quite well. It is concluded that neutral

beam co-injection drives impurities outward, while, counter-injection enhances the normally inward impurity flow in tokamak plasmas.

There is a considerable data from the ISX-B tokamak that demonstrates that impurity transport is sensitive to the direction of neutral beam injection. The measured quantity in these experiments is usually the radiative emission rate which is proportional to the corresponding impurity concentration. Two sets of experimental data were chosen for modeling purposes. In the first type of experiments, neutral beam injection took place from 80 to 240 ms in the co-injection case, and from 125 to 240 ms in the counter-injection case, with 1 MW of neutral beam power in each case. The temporal radiative emission profiles were found to be relatively flat in co-discharges. In contrast, the emission increased so rapidly in the counter case that the discharge disrupted around 174 ms due to impurity accumulation and rapid cooling. The increase in the central ion radiation was 10 to 30 times higher in the case of counter-discharge as compared to the co-discharge. In the second type of experiments, two co-beams, each with 1.2 MW power, were injected sequentially at 80 and

160 ms respectively. The concentration of the interior ions decreased appreciably after the second beam was turned on. This implies that impurities are actually driven out of the center when the second co-beam is turned on. Thus, the beam induced transport effects can overwhelm the increased edge source rate of impurities. Using the data files from the ZORNOC data analysis code, and the ORNL atomic physics code, the theory was found to model the experimental data remarkably well.

The next set of data selected for investigation came from the PLT tokamak with intrinsic iron. The chordal brightness, which is proportional to the corresponding impurity concentration along the line of sight, was inferred in these experiments from the measured spectral signals originating from the PLT deuterium discharges with neutral beam injection. The experimental results clearly indicate differences in the iron concentrations between the co- and counter-discharges, being more than twice in the latter case. The soft x-ray measurements also support these conclusions. The bolometric measurements indicate a substantial central peaking with counter-injection, but a fairly broad distribution with

co-injection. The radial emissivity profile predicted by theory was converted to chordal brightness distribution to compare with experiment. The agreement between theory and experiment was generally excellent.

An experimental study on the effects of neutral beam injection on laser-ablated scandium and molybdenum has come up with some novel but interesting results. In terms of absolute measurements, significant and reproducible quantitative differences were found in the experiments with co- versus counter-injection. With a given amount of the injected impurity, the ion densities that reach the interior of the plasmas were found to be two to three times larger in the counter-discharge as compared to co-discharge. This observation was, however, attributed by the experimental group to the peripheral plasma conditions, and was assumed to be of no consequence in terms of the impact of neutral beam direction on impurity transport. Unfortunately, the data in terms of absolute measurements were not published.

The measured chordal brightness of injected impurities in these experiments was Abel-inverted by the experimental group to yield the radial emissivity profile. The local emissivities normalized to their maxima were then used to compare the effects of neutral beam injection on impurity transport. No noticeable difference was found in the normalized radial profiles of emissivities with co- versus counter-injection. This observation was invoked to propose that transport properties were almost identical with co- and counter-injection.

As a first step to investigate the experimental results, the sensitivity of these results was studied in terms of the atomic physics alone. Very different impurity profiles used did not show any appreciable effect on the normalized emission profiles. This indicates that normalized emission profiles are indeed insensitive to impurity transport, and hence impurity transport is not a driving mechanism in these results. In contrast to insensitivity of normalized profiles to impurity density, the results were very sensitive to electron temperature. This implies that the normalized results reported are a manifestation of the atomic physics

rather than the details of the transport effects. Since the measured electron temperature profiles reported are not very different in the co- and counter-discharges, it is not very surprising that atomic physics considerations lead to similar normalized profiles irrespective of the beam direction as was indeed noted by the experimental group. In any case, the experimental data lacks details to reach any definite conclusions. Thus, in the absence of more detailed measurements under less restrictive conditions, it does not seem justified to conclude that impurity transport is insensitive to neutral beam direction.

In view of the general success of the impurity flow reversal theory in modeling the neutral beam driven impurity transport experiments in the PLT and the ISX-B tokamaks, it was considered motivating to apply the theory to predict impurity flow reversal trends in future thermonuclear reactors. Three reactor design concepts, namely, INTOR, TIBER II, and ITER were investigated. With the reference design parameters, and representative profiles, the iron impurity flux was modeled for INTOR in co-injected neutral beam power range of 25, 50, 75, and 100 MW, and beam energies of 100, 200, and 500 keV. The

investigations demonstrated that 50 to 75 MW of co-injected neutral beam power would be sufficient to prevent the accumulation of impurities in central plasmas. The transport of helium and carbon impurities was modeled with TIBER II reference parameters. It was found that 25 to 50 MW of co-injected beam power would be adequate to drive helium out of the central plasmas. In the case of carbon, it was determined that 50 MW of co-injected beam power would be needed to remove carbon from center. With the reference parameters, and representative profiles, flow reversal did not take place in the case of iron and carbon impurities in ITER. This is because the rate of neutral beam momentum deposited per plasma ion was so small that plasma rotation was negligible. Some flow reversal was predicted in the case of helium ions in ITER mainly because of the outward contribution of diffusive fluxes in the case of helium ions.

The impurity flow reversal theory includes a term to account for the radial transfer of toroidal and parallel momentum. Such a term is needed to match the rotation results from experiments. The experimental evidence indicates that some of the momentum that is input to the center of the plasma



with neutral beam injection is transferred radially outward. However, the momentum confinement times inferred from toroidal rotation measurements in tokamaks with unbalanced neutral beam injection are about two orders of magnitude shorter than could be accounted for by theoretical estimates based on standard neoclassical perpendicular viscosity. The momentum transport with unbalanced neutral beam injection was, therefore, generally considered to be anomalous in the neutral beam driven rotation experiments. The Stacey-Sigmar gyroviscous theory shows that the gyroviscous force is of the right order of magnitude to correctly explain the experimentally inferred momentum confinement time. The gyroviscous theory was applied to analyze rotation data from the PLT and the PDX tokamaks with exact experimental conditions. Both the steady-state and the decay measurements of the toroidal rotation velocities were modeled. The theory was found to be in excellent agreement with experiment over a wide range of parameters. The theory is also known to agree well with rotation data from ISX-B. The agreement of the gyroviscous theory of momentum confinement with experiment provided confidence in using this theory to predict external drag in the impurity flow reversal calculations.

The detailed analysis of the fairly large experimental data base carried out in this study of neutral beam driven particle and momentum transport brings us to the following conclusions.

1. The impurity flow reversal theory can model experimental data quite well in PLT and ISX-B tokamaks. It has been established that neutral beam co-injection can drive impurities outward to achieve clean central plasmas, while counter-injection significantly enhances the normal inward transport.
2. The external drag, which is an important element in impurity flow reversal theory, is correctly predicted in PLT and ISX-B tokamaks by gyroviscous theory of momentum confinement. It is possible, therefore, to calculate impurity transport in PLT and ISX-B tokamaks entirely from first principles.

## REFERENCES

1. C. L. Longmire and M. N. Rosenbluth, Phys. Rev. 103 , 507 (1956).
2. J. B. Taylor, Phys. Fluids 4 , 1142 (1961).
3. S. I. Braginskii, in Reviews of Plasma Physics, edited by M. A. Leontovich, Consultants Bureau, New York, Vol. 1, p. 205 (1965)
4. J. W. Connor, Plasma Phys. 15 , 765 (1973).
5. T. B. Moore and F. L. Hinton, Nucl. Fusion 14 , 639 (1974).
6. P. H. Rutherford, Phys. Fluids 17 , 1782 (1974).
7. F. L. Hinton and R. D. Hazeltine, Rev. Mod. Phys. 48 , 239 (1976).
8. S. P. Hirshman and D. J. Sigmar, Nucl. Fusion 21 , 1079 (1981).
9. D. M. Meade, Nucl. Fusion 14 , 289 (1974).
10. R. W. Conn and J. Kesner, Nucl. Fusion 15 , 775 (1975).
11. D. L. Jassby, Nucl. Fusion 15 , 453 (1975).
12. R. V. Jensen, D. E. Post, and D. L. Jassby, Princeton Plasma Physics Lab (PPPL) report, PPPL-1350 (1977).
13. T. Ohkawa, Kakuyugo-kenkyo 32 , 67 (1974).
14. K. H. Burrell, Phys. Fluids 19 , 401 (1976).

15. M. S. Chu, and J. M. Rawls, Phys. Fluids 20 , 1787 (1977).
16. J. W. Wong, Phys. Fluids 21 , 299 (1978).
17. T. Ohkawa, Report GA-A12926 (1974).
18. Z. El-Derini, and G. A. Emmert, Nucl. Fusion 16 , 342 (1976).
19. J. W. Connor, and J. C. Cordey, Nucl. Fusion 14 , 185 (1974).
20. J. D. Callen et al., in Plasma Physics and Controlled Nuclear Fusion, (Proc. Int. Conf., Tokyo), IAEA, Vol. 1, p.645 (1975).
21. W. M. Stacey, Jr., Phys. Fluids 21 , 1404 (1978).
22. W. M. Stacey, Jr., and D. J. Sigmar, Phys. Fluids 22 , 2000 (1979).
23. W. M. Stacey, Jr., and D. J. Sigmar, Nucl. Fusion 19 , 1665 (1979).
24. W. M. Stacey, Jr., Phys. Fluids 23 , 2332 (1980).
25. D. R. Eames, Ultra-soft X-ray Emission from the Princeton Large Torus, Ph. D. Thesis, Princeton University, (1981).
26. R. C. Isler, E. C. Crume, and D. E. Arnurius, Phys. Rev. Lett. 26 , 2105 (1982).
27. C. E. Bush et al., Nucl. Fusion 23 , 67 (1983).
28. S. Suckewer et al., Phys. Rev. Lett. 43 , 207 (1979).
29. S. Suckewer et al., Nucl. Fusion 21 , 1301 (1981).

30. K. Brau, Impurity Poloidal Asymmetries, and Plasma Rotation in PDX tokamak, Ph. D. Thesis, Princeton University, (1983).
31. K. Brau et al., Nucl. Fusion 23 , 1643 (1983).
32. R. C. Isler et al., Nucl. Fusion 23 , 1017 (1983).
33. R. C. Isler et al., Nucl. Fusion 26 , 391 (1984).
34. S. D. Scott et al., Bul. Am. Phys. Soc. 30 , 1387 (1985).
35. K. H. Burrell, T. Ohkawa, and S. K. Wong, Phys. Rev. Lett. 47 , 511 (1981).
36. E. C. Crume, and D. E. Arnurius, Simulation of Impurity Transport in ISX-B Tokamak with Directed Neutral Beam Heating, Sherwood Meeting, 1P15, (1984).
37. A. A. Ware, and J. C. Wiley, Phys. Fluids 24 , 936 (1981).
38. R. D. Hazeltine, and A. A. Ware, Phys. Fluids 19 , 1163 (1976).
39. R. D. Hazeltine, and A. A. Ware, Phys. Fluids 20 , 1880 (1977).
40. C. S. Chang, and R. D. Hazeltine, Phys. Fluids 25 , 536 (1982).
41. C. S. Chang, Phys. Fluids 26 , 2140 (1983).
42. W. M. Stacey, Jr., and D. J. Sigmar, Phys. Fluids 27 , 2076 (1984).
43. W. M. Stacey, Jr. et al., Nucl. Fusion 25 , 25, 463 (1985).

44. W. M. Stacey, Jr., R. B. Bennett, and D. J. Sigmar, J. Nuc. Mater. 121 , 82 (1984).
45. R. B. Bennett, Neutral Beam Driven Impurity Flow Reversal in Tokamaks, Ph. D. Thesis, Georgia Tech., (1984).
46. R. B. Bennett, and W. M. Stacey, Jr., Nuc. Sc. Eng., 88 , 475 (1984).
47. S. Suckewer et al., Nucl. Fusion 21 , 981 (1981).
48. S. Suckewer et al., Nucl. Fusion 24 , 815 (1984).
49. R. C. Isler, F. D. Morgan, and N. J. Peacock, Nucl. Fusion 25 , 386 (1985).
50. M. N. Rosenbluth et al., in Plasma Physics and Controlled Fusion, (Proc. 4th Int. Conf., Madison), Vienna, Vol. 1, p.495 (1971).
51. R. D. Hazeltine, Phys. Fluids 17 , 961 (1974).
52. K. T. Tsang, and E. A. Frieman, Phys. Fluids 19 , 747 (1976).
53. J. T. Hogan, Phys. Fluids 27 , 2308 (1984).
54. W. M. Stacey, Jr., and D. J. Sigmar, Phys. Fluids 28 , 2800 (1985).
55. INTOR Group, "International Tokamak Reactor, Phase Two A, Part 2", Nucl. Fusion 25 , 1791 (1985).
56. C. D. Henning et al., "TIBER II Status Report", Lawrence Livermore National Laboratory, UCID-20863, (1986).

57. N. A. Uckan et al., "Physics Analysis of the TIBER-II Engineering Test Reactor", ORNL/TM-10611, (1987).
58. S. P. Hirshman, Phys. Fluids 19 , 155 (1976).
59. S. P. Hirshman, Phys. Fluids 21 , 224 (1978).
60. R. D. Hazeltine, and A. A. Ware, Nucl. Fusion 16, 342 (1976).
61. C. D. Boley, E. M. Gelbard, and W. M. Stacey, Jr., Phys. Fluids 19 , 2051 (1976).
62. A. N. Kaufman, Phys. Fluids 3 , 610 (1960).
63. R. C. Grim, and J. L. Johnson, Plasma Phys. 14 , 617 (1972).
64. A. B. Mikhailovskii, and Tsypin, Sov. J. Plasma Phys., 10 , 51 (1984).
65. V. Shafranov, Plasma Phys. 8 , 314 (1966).
66. K. C. Shaing, and J. D. Callen, Phys, Fluids 26 , 1526 (1983).
67. A. W. Bailey, and W. M. Stacey, Jr., Time-dependent Impurity Transport, GTFR-56 (1985); also A. W. Bailey, R. B. Bennett, A Users' Manual for the Time-dependent Inertia Code, (1985).
68. J. P. Roache, "Computational Fluid Dynamics", Hermosa Publishers (1982).
69. H. Hsuan, K. Bol, and R. A. Ellis, Nucl. Fusion 15 , 657 (1975).

70. E. Hinnov et al., "Radiated Energy and Impurity Density Changes during Intensive Hydrogen Influx in the PLT Tokamak, PPPL-1865 (1981).
71. J. Schivell et al., "Bolometer for Measurements of High Temperature Plasmas, PPPL-1910 (1982).
72. K. Bokasten, J. Opt. Soc. Am. 51, 943 (1961).
73. R. W. P. McWhirter, in Plasma Diagnostic Techniques, edited by R. H. Huddleston and S. L. Leonard, Academic Press, New York (1965).
74. P. C. Efthimion et al., "Electron Energy Balance during Neutral Beam Injection", Status of Neutral Beam Heating in PLT, Vol. 2, Princeton (1978).
75. R. C. Hulse, Nucl. Technol./Fusion 3, 259 (1983).
76. D. Grove et al., "Experimental Results of the PLT Tokamak", Proc. 6th Intl. Conf. on Plasma Physics and Controlled Nuclear Fusion, Berchtesgaden, IAEA, Vienna, Vol. 1, p. 26, (1977).
77. D. E. Post et al., Atomic Data and Nuclear Data Tables 20, 397 (1977).
78. H. C. Howe, "Physics Models in the Tokamak Transport Code PROCTR", ORNL/TM-9537 (1985).
79. J. A. Rome, J. D. Callen, and J. F. Clarke, Nucl. Fusion 14, 141 (1974).
80. P. E. Stott, Plasma Phys. 18, 251 (1976).



81. H. Eubank et al., "PLT Neutral Beam Heated Results",  
Proc. 7th Intl. Conf., Innsbruck, 1978, IAEA, Vienna,  
Vol. 1, p.167 (1979).
82. H. Eubank et al., Phys. Rev. Lett. 43 , 270 (1979).
83. W. Stodiek et al., "Transport Studies in the PLT", Proc.  
8th Intl. Conf., Brussels, 1980, IAEA, Vol. 1, p. 9  
(1981).
84. R. Goldston et al., "Confinement Studies During Neutral  
Beam Injection in PLT", Proc. 2nd Joint  
Grenoble-Varennas Intl. Symp., Heating in Toroidal  
Plasmas II, (1980).
85. W. M. Heidbrink, J. Lovberg, J. D. Strachan, R. E. Bell,  
"Fusion Product Measurements of the Local Ion Thermal  
Diffusivity in the PLT Tokamak", PPPL-2315 (1986).
86. A. J. Wootan et al., "Experimental Results on Finite  
Beta Limits and Transport in the ISX-B Tokamak",  
ORNL/TM-8750 (1983).
87. B. Zurro et al., ZORNOC: A 1 1/2-D Tokamak Data Analysis  
Code for Studying Noncircular High Beta Plasmas",  
ORNL/TM-7146 (1980).
88. R. C. Isler et al., Phys. Rev. Lett. 47 , 333 (1981).
89. R. C. Isler et al., Phys. Rev. Lett. 47 , 649 (1981).
90. R. C. Isler et al., "Impurity Transport during Neutral  
Beam Injection in the ISX-B Tokamak", ORNL/TM-7472  
(1980).

91. E. C. Crume, D. E. Arnurius, and R. C. Isler, Bul. Am. Phys. Soc. 25, 867 (1980).
92. E. C. Crume, personal communication (1984).
93. C. Breton, C. D. Michelis, M. Mattioli, "Ionization Equilibrium and Radiation Cooling of a High Temperature Plasma", EURATOM-CEA Association Fontenay-aux-Roses, Report EUR-CEA-FC-853 (1976).
94. W. M. Stacey, Jr., Fusion Plasma Analysis, John Wiley and Sons, p.231, (1981).
95. E. C. Crume, and D. E. Arnurius, "Numerical Calculation of Impurity Charge State Distribution", ORNL/TM-6050 (1977).
96. R. H. Fowler, J. A. Holmes, and J. A. Rome, "NFREYA - A Monte Carlo Beam Deposition Code for Noncircular Tokamak Plasmas", ORNL/TM-6845, Oak Ridge National Laboratory (1979).
97. S. L. Milora, J. Vac. Sci. Technol. 20, 1246 (1982).
98. F. Wagner et al., "Confinement and  $\beta_p$ -Studies in Neutral Injection Heated ASDEX Plasmas", IPP-III/86 (1983).
99. S. Suckewer, and E. Hinnov, personal communication (1985).
100. E. Hinnov, and F. W. Hufmann, J. Opt. Soc. Am., 53, 1253 (1983).

101. E. Hinnov, "Iron Radiation in Tokamak Discharges", in  
Diagnostics for Fusion Experiments, edited by E.  
Siddoni and C. Wharton, Pergamon Press, p.139, (1979).
102. B. Denne and E. Hinnov, J. Opt. Soc. Am., B1 , 655  
(1984).
103. H. Hsuan et al., Bul. Am. Phys. Soc., 24 , 1107 (1978).
104. H. Hsuan et al., Proc. Joint Varenna-Grenoble Int.  
Symp. on Heating in Toroidal Plasmas, Grenoble (1978).
105. S. Suckewer et al., "Ion Transport Studies on the PLT  
Tokamak During Neutral Beam Injection", PPPL-2063  
(1983).
106. S. Suckewer, personal communication (1984).
107. H. Eubank, PDX and PLT Groups, in Heating in Toroidal  
Plasmas, Proc. 3rd Joint Grenoble-Varenna Int. Symp.  
Grenoble, CEC, Brussels, p.15 (1982).
108. R. C. Isler, and L. E. Murray, Appl. Phys. Lett. 42 , 355  
(1985).
109. M. N. Rosenbluth et al., in Plasma Physics and  
Controlled Nuclear Fusion Research, Proc. 4th Intl.  
Conf. Madison, Vol. 1, p. 495, IAEA (1971).
110. W. M. Stacey, Jr., C. M. Ryu, and M. A. Malik, Nucl.  
Fusion 26 , 293 (1986).
111. H. Eubank et al., in Plasma Physics and Controlled  
Nuclear Fusion Research, Proc. 7th Int. Conf.  
Innsbruck, p. 167, IAEA (1979).

- 112. H. P. Eubank, personal communication (1985).
- 113. R. J. Fonck et al., J. Nucl. Mater. 111, 112 , 343 (1982).
- 114. R. J. Hawryluk et al., Phys. Rev. Lett. 49 , 326 (1982).
- 115. S. L. Davis, D. Mueller, C. J. Keane, "The Mass Resolving Charge-Exchange System on PDX", PPPL-1940 (1982).
- 116. FED Group, The Fusion Engineering Device, USDOE Report DOE/TID-1110 (1981).
- 117. TFCX Preconceptual Design Report, PPPL, F-AXXX-8406-006 (1984).
- 118. J. A. Schmidt, and H. P. Furth, "Compact Ignition Tokamak", Conceptual Design Report, PPPL, A-860606-P-01, (1986).
- 119. D. J. Sigmar et al., "Alpha-Particle Diffusion in Tokamak Reactors", Proc. 5th Int. Conf. Plasma Physics and Controlled Nuclear Fusion, Tokyo, Japan, Vol. 1, p. 595, IAEA (1975).